# SYNTHESIS AND ISOLATION OF 2D COVALENT ORGANIC FRAMEWORKS AND AN EXAMINATION OF THE INITIAL STAGES OF CRYSTALLIZATION

A Dissertation
Presented to
The Academic Faculty

by

Cameron Hill Feriante

In Partial Fulfillment
of the Requirements for the Degree
Doctor of Philosophy in the
School of Chemistry and Biochemistry

Georgia Institute of Technology
August 2020

# SYNTHESIS AND ISOLATION OF 2D COVALENT ORGANIC FRAMEWORKS AND AN EXAMINATION OF THE INITIAL STAGES OF CRYSTALLIZATION

Approved by:

Dr. Seth Marder, Advisor
School of Chemistry and Biochemistry
*Georgia Institute of Technology*

Dr. Will Gutekunst
School of Chemistry and Biochemistry
*Georgia Institute of Technology*

Dr. John Reynolds
School of Chemistry and Biochemistry
*Georgia Institute of Technology*

Dr. Kristina Walton
School of Chemical Engineering
*Georgia Institute of Technology*

Dr. Jean-Luc Bredas
School of Chemistry and Biochemistry
*Georgia Institute of Technology*

Date Approved: April 20th, 2020

To Dr. Dennis Hill and Carson Hill Feriante

# ACKNOWLEDGEMENTS

The pursuit of a Ph.D. is not a trivial endeavor, and I have been very fortunate to have the unfailing support of family, friends, mentors and colleagues throughout my efforts. I wish first to thank my academic advisor, Dr. Seth Marder for his consistent guidance and wisdom during my time in his research group. I thank the other faculty and research scientists at the Georgia Institute of Technology, including the members of my graduate committee for their advice and guidance; This includes Dr. John Reynolds, Dr. Jean-Luc Bredas, Dr. Will Gutekunst, and Dr. Kristina Walton as committee members, as well as Dr. Steve Barlow, Dr. Tim Parker, and Dr. Raghunath Dasari. Dr. Will Dichtel at Northwestern University and his research group have been consistent collaborators throughout this work and deserve thanks as well.

Research is a highly collaborative effort, and I wish to thank the colleagues who have helped me along the way. Dr. Samik Jhulki, Austin Evans, Khaled Al-Kurdi, Dr. Matthew Cooper, Declan McCarthy, Theo Hicks, Ian Pelse and Ioannina Castano to name some.

I wish to thank my loving family for their support during my time at Georgia Tech. Thank you to my parents, Mark and Stephanie Feriante, my grandparents Dennis and Kathleen Hill, and my sister Sydney for your help and support. Finally I wish to thank my loving wife Ashley, and my son Nicholas for their patience, love and support, without which this would not have been possible.

# TABLE OF CONTENTS

# LIST OF TABLES

# LIST OF FIGURES

# LIST OF SYMBOLS AND ABBREVIATIONS

| | |
|---|---|
| COF | Covalent Organic Framework |
| 2D | Two-Dimensional |
| 3D | Three-Dimensional |
| TAPB | 1,3,5-tris(4-aminophenyl)benzene |
| PDA | Terephthalaldehyde |
| MOF | Metal Organic Framework |
| hcb | Honeycomb (COF Topology) |
| sql | Square (COF Topology) |
| kgm | Kagome (COF Topology) |
| hxl | Hexagonal (COF Topology) |
| kgd | Dual Kagome (COF Topology) |
| TAPPy | Tetrakis(4-aminophenyl)pyrene |
| UHV | Ultra-high Vacuum |
| $scCO_2$ | Supercritical Carbon Dioxide (Activation) |
| XRD | X-Ray Diffraction |
| AFM | Atomic Force Microscopy |
| SEM | Scanning Electron Microscopy |
| TEM | Transmission Electron Microscopy |
| STM | Scanning Tunneling Electron Microscopy |
| PXRD | Powder X-Ray Diffraction |
| $n$ | An integer in the Bragg Equation |
| $\lambda$ | Wavelength |

| | |
|---|---|
| $d$ | Lattice spacing in Å between planes of atoms |
| $\theta$ | Angle of diffraction |
| $a$ | Cartesian x-axis in Miller indices |
| $b$ | Cartesian y-axis in Miller indices |
| $c$ | Cartesian z-axis in Miller indices |
| FWHM | Full width at half-maximum |
| $\tau$ | Crystallite diameter in the Scherrer equation |
| $K$ | Dimensionless Shape factor in the Scherrer equation |
| $\beta$ | FWHM of diffraction peak in radians in Scherrer equation |
| GIWAXS | Grazing incidence wide-angle X-ray scattering |
| BET | Brunauer-Emmett-Teller (Theory) |
| P | Pressure |
| $P_0$ | Initial pressure during adsorption/desorption measurement |
| $S_{BET}$ | BET Surface Area in $m^2/g$ |
| PSD | Pore size distribution |
| DFT | Density functional theory |
| AcOH | Acetic acid |
| DI | Deionized |
| OMePDA | 2,5-dimethoxyterephthaldehyde |
| TFP | Triformylphloroglucinol |
| BDBA | Benzene 1,4-diboronic acid |
| OBuPDA | 2,5-dibutoxyterephthaldehyde |
| OOctPDA | 2,5-dioctyloxyterephthaldehyde |
| OHPDA | 2,5-dihydroxyterephthaldehyde |

| | |
|---|---|
| NDI-DA | 4,9-bis(4-aminophenyl)-2,7-dihexylbenzo[lmn][3,8]phenanthroline-1,3,6,8(2H,7H)-tetraone |
| TII | Thienoisoindigo, (E)-4,4'-dibutyl-5,5'-dioxo-4,4',5,5'-tetrahydro-[6,6'-bithieno[3,2-b]pyrrolylidene]-2,2'-dicarbaldehyde |
| BDT | Benzene-dithiophene dialdehyde |
| APS | Advanced Photon Source at Argonne National Laboratory |
| IPA | Isopropyl Alcohol |
| DMF | Dimethylformamide |
| THF | Tetrahydrofuran |
| ODodecPDA | 2,5-didodecyloxyterephthalaldehyde |
| *t* | Time |
| A | Amorphous phase |
| C | Crystalline phase |
| SAXS | Small-angle X-ray scattering |
| WAXS | Wide-angle X-ray scattering |
| OD | Outer diameter |
| M | Molar |
| LCTEM | Liquid-Cell Transmission Electron Microscopy |
| TFPPy | Tetrakis(4-formylphenyl)pyrene |
| PD | Phenylene diamine |

# SUMMARY

Covalent organic frameworks (COFs) are crystalline network polymers with permanent porosity and a range of potential applications including gas storage and separation, molecular separations, catalysis, charge transport and others. This thesis focuses on two principal aspects of two-dimensional imine-linked COF synthesis; First, the activation process used to isolate the synthesized COF material and remove guest molecules such as solvent, catalyst, or oligomers, and second, the initial stages of the COF synthesis process where crystalline material first forms. In the first research Chapter a series of three 2D imine-linked COFs are examined after vacuum activation, activation with supercritical carbon dioxide and activation with nitrogen flow and heat. The crystallinity and porosity of the resulting materials is assessed to determine the structural changes induced by each activation method and to provide insight into the best methods for COF activation. In the second research Chapter 2D imine-linked COFs are examined during the initial stages of the COF synthesis through a variety of *in situ* and *ex situ* methods to monitor the development of crystallinity during the reaction, and to assess how different structural features of the COF affect this process. The overall ambition of the thesis is to expand the foundational knowledge pertaining to the formation of 2D imine-linked COFs allowing for the synthesis and isolation of higher quality materials.

# CHAPTER 1. INTRODUCTION

## 1.1 Introduction to Covalent Organic Frameworks

Covalent organic frameworks (COFs) are an emerging class of polymeric material that are crystalline two-dimensional (2D) or three-dimensional (3D) network polymers composed of organic monomers linked by strong covalent bonds.[1-2] Because of their ordered structure and crystallinity, COFs are distinct from other cross-linked polymer networks, which do not display long-range order. Covalent organic frameworks generally display crystallinity, reversible covalent bond formation/breakage between monomers under the reaction conditions which allows for error correction during synthesis, and high surface area and permanent porosity. These properties are illustrated in Figure 1.1 below, which shows the reversible imine bond formation reaction between 1,3,5-tris(4-aminophenyl) benzene (TAPB) and terephthalaldehyde (PDA), leading to the so-called TAPB-PDA COF.[3]

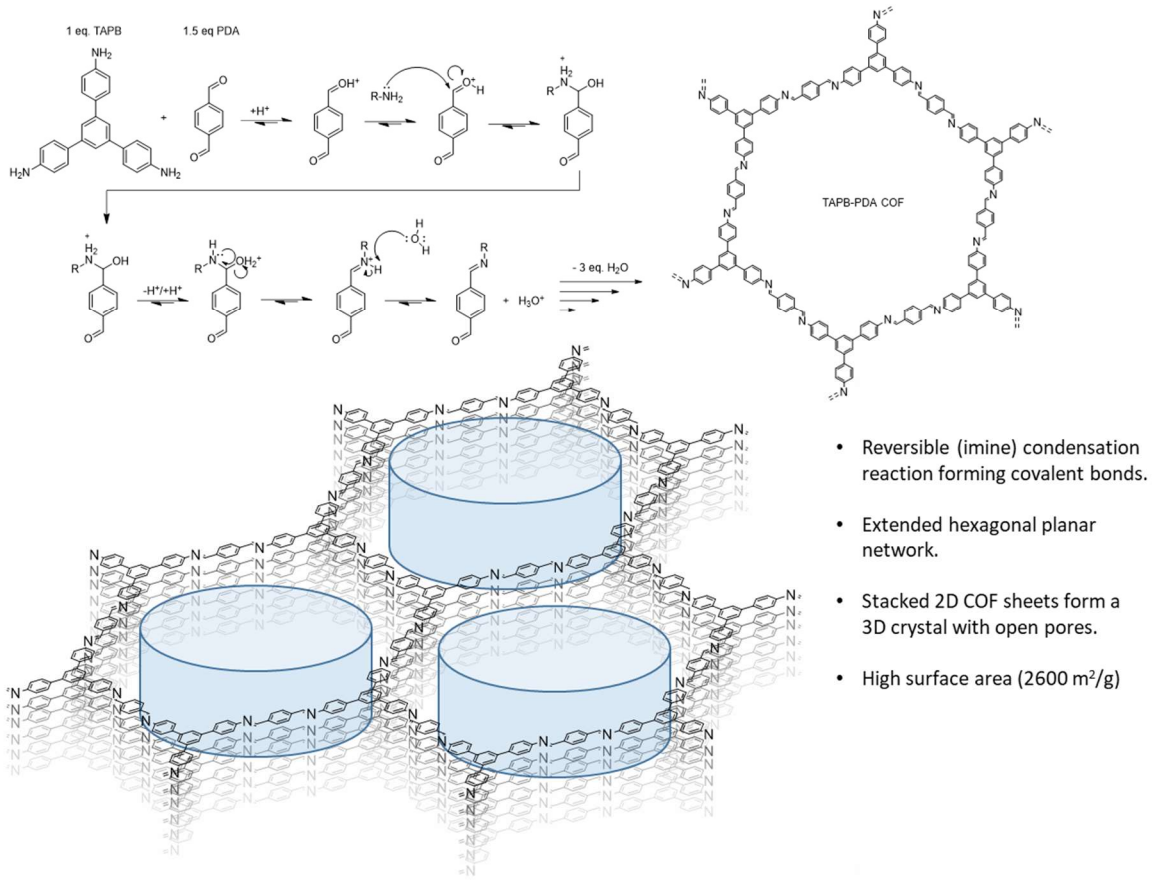


**Figure 1.1: Reversible imine bond formation leading to TAPB-PDA COF, a typical imine-linked two-dimensional covalent organic framework and a conceptual image showing the columnar pores formed by the framework.**

As framework materials, the rational design of COFs falls within the discipline of reticular chemistry. The term 'reticular chemistry' was coined by Yaghi *et al.* to define the chemical discipline of designing framework materials through the selection of monomer units with well-defined directional bonding, and connecting these units using strong chemical bonds.[2] Reticular chemistry incorporates metal organic frameworks (MOFs) in addition to COFs.

Reticular chemistry allows for the rational design of new materials by understanding the bonding geometry of monomers.

While at the University of Michigan, Omar Yaghi and Adrian Cote published the first paper on covalent organic frameworks in 2005, reporting two 2D COF materials linked via the self-condensation of boronic acids to form boroxine rings, and the condensation of boronic acids with catechols to form boronic esters.[1] Since this seminal work, the range of chemical linkages motifs used for the construction of COFs has expanded rapidly, as seen in Figure 1.3. The first imine linked COF was reported by Uribe-Romo *et al.* in 2009, and was synthesized via the acetic acid catalyzed condensation of tetra-(4-anilyl)methane and terephthaldehyde, yielding a 3D interpenetrated network with a tetrahedral framework geometry analogous to diamond.[4] Since the first publication reporting covalent organic frameworks, interest in COFs has expanded significantly, with over 1000 publications in 2019, as seen below in Figure 1.2.

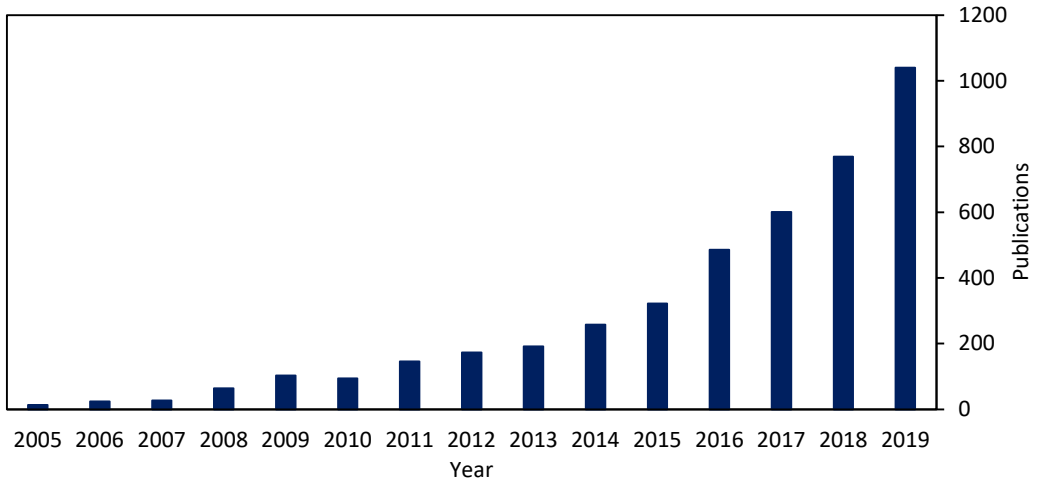


**Figure 1.2: Publications on the topic "Covalent Organic Frameworks" per year, source: Web of Science on March 18th, 2020.**

Today, covalent organic frameworks are a dynamic research area, with interest in COFs for a variety of potential applications ranging from gas storage and separation, catalysis, to sensing and organic electronics. This introduction will present some of the linkage chemistries that have been used to assemble COFs in Section 1.2, followed by a brief exploration of the interesting properties that arise from COFs ordered porous structures in Section 1.3. The common synthesis methods reported in the COF literature are presented in Section 1.4, followed by a literature review examining the most common synthetic methods reported. In Section 1.5, the most relevant characterization methods for COFs, X-ray diffraction and gas adsorption are discussed as they apply to COFs, followed by a brief overview of other characterization methods that have been used for COF characterization. Finally, in Section 1.6, the research aims of this thesis are briefly described, the relevant literature and context for each research Chapter is covered in their respective introductions.

## 1.2 Linkages and Topologies of Covalent Organic Frameworks

Covalent organic frameworks are distinct from metal organic frameworks (MOFs) in that the monomer units used link together via covalent bonds between the second period elements such as boron, carbon, nitrogen, and oxygen, as opposed to metal-ligand coordination. This results in increased stability and solvent tolerance but generally requires that the covalent bond formation be reversible under the reaction conditions in order to allow for error correction during the formation of the COF. The first COFs were synthesized via the condensation of boronic acids, which is a reversible reaction when water is present to hydrolyze the newly formed boroxine rings or boronic esters. Imine-linked COFs, which are the focus of Chapter 2 and Chapter 3 of this thesis, are formed through the reversible condensation of an aldehyde and an amine monomer. Various other

linkage chemistries have been explored and Figure 1.3 below, adapted from a review by Zhu *et al.,* shows some of the many reversible covalent bond chemistries which have been used to synthesize COFs.[5]

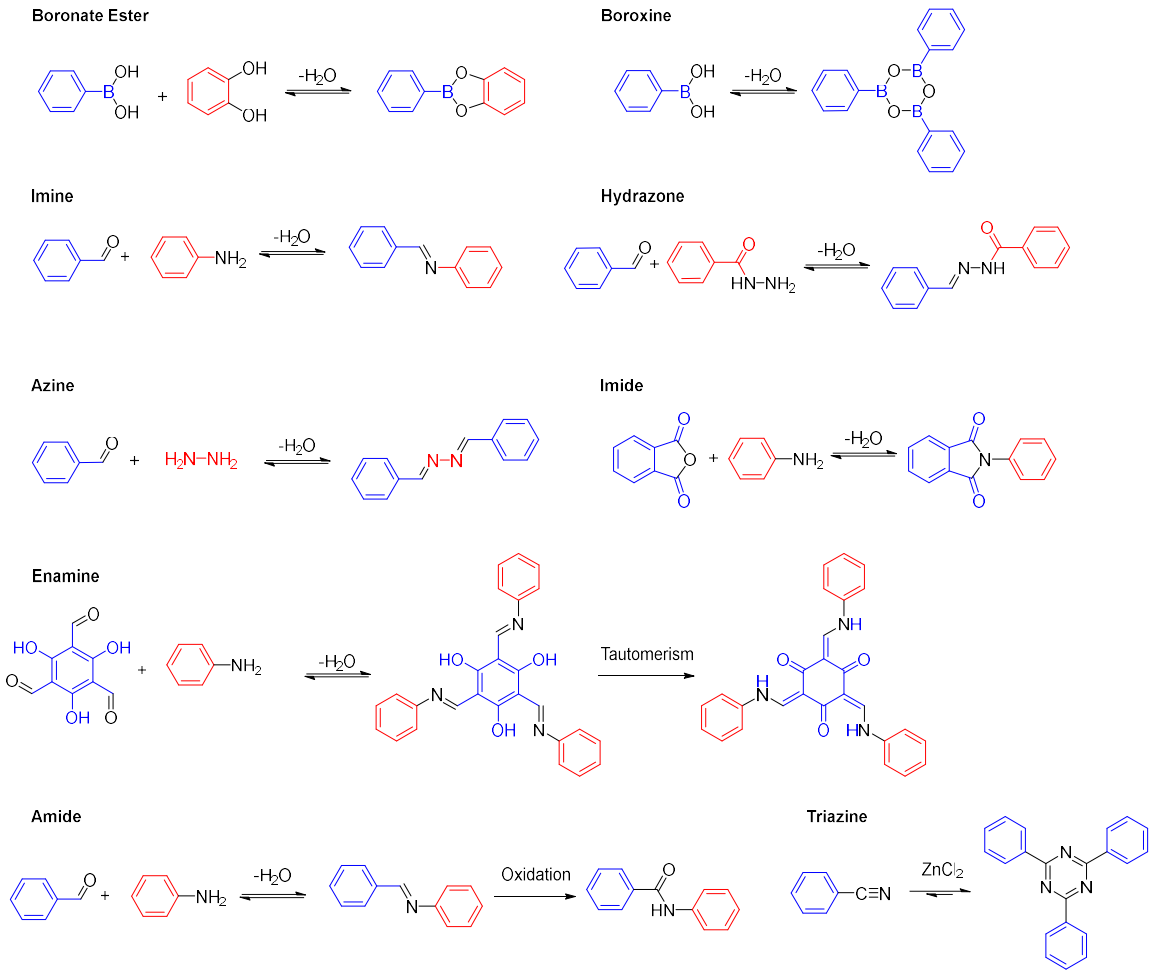


**Figure 1.3: A selection of reversible linkage chemistries used for constructing COFs.[5]**

By judiciously selecting monomer units, five different 2D COF topologies with identical sides can be accessed; honeycomb (hcb), square (sql), kagome (kgm), hexagonal (hxl), and

dual kagome (kgd), shown in Figure 1.4.[6] Generally the 2D COFs reported are the augmented form of these topologies, which are also shown in Figure 1.4, since the molecules serving as the network's vertices have lateral dimensions. Examples of monomer combinations yielding examples of these topologies from Chapters 2 and 3 of this thesis, and from literature reports appear below in Figure 1.5.

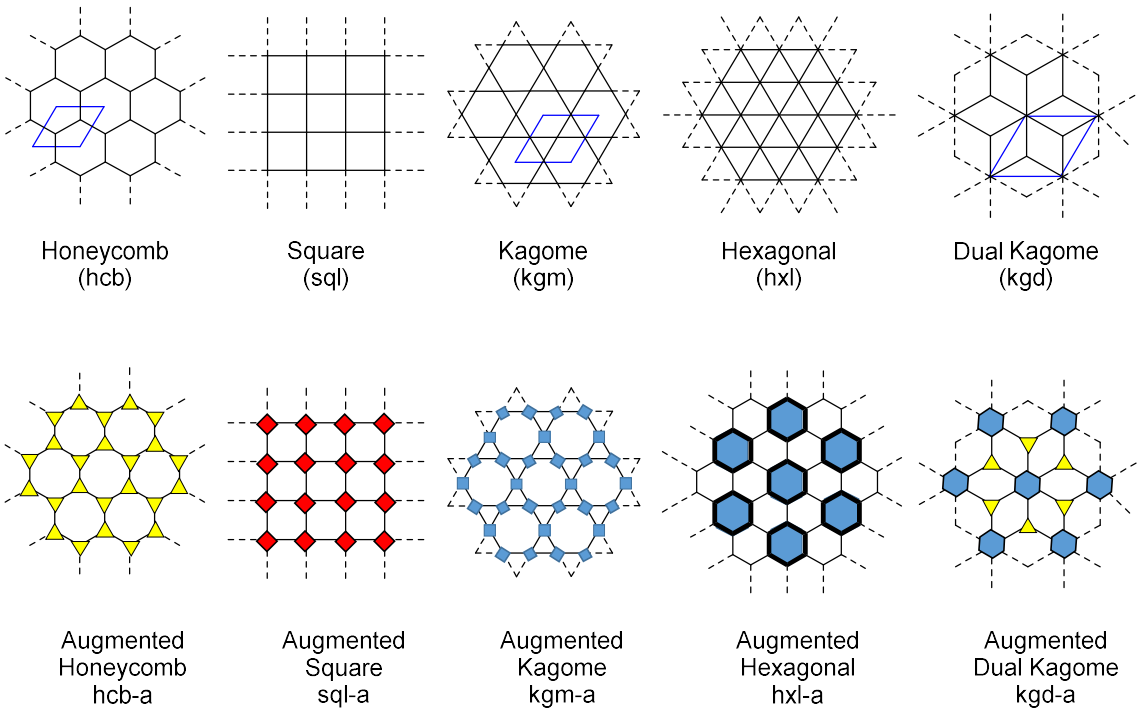


**Figure 1.4: Possible 2D COF topologies.[6]**

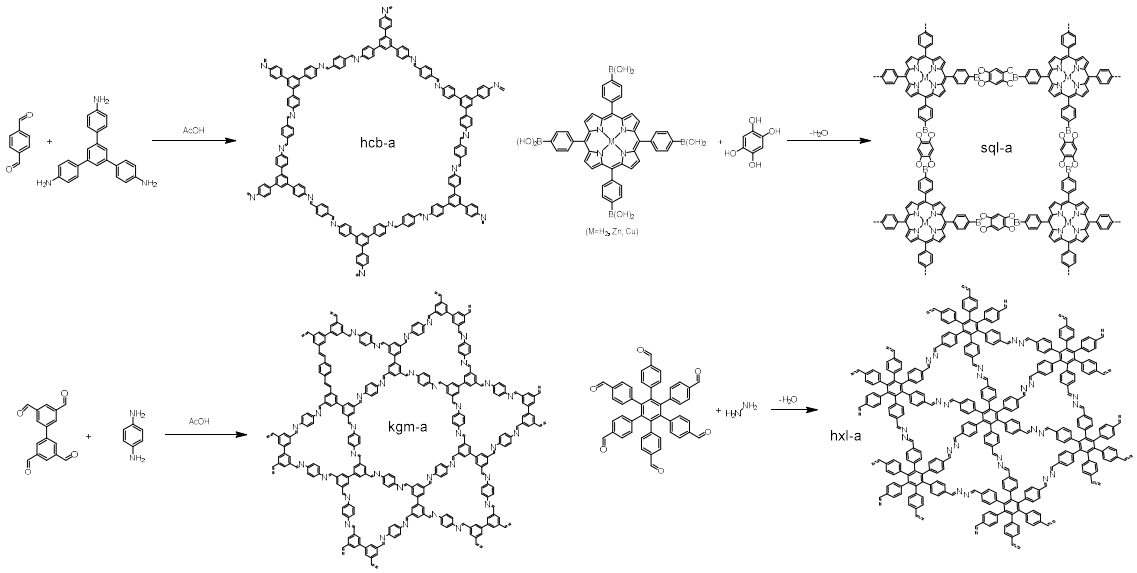


**Figure 1.5: Examples of monomer combinations yielding augmented honeycomb, square,[7] kagome[8] and hexagonal[9] COF topologies.**

In this manuscript, the COF topologies examined include augmented honeycomb (hcb-a), such as the COF formed via the condensation of TAPB and PDA shown in Figure 1.4, and augmented square (sql-a), an example of which is the COF formed by 1,3,6,8-*tetra*(4-aminophenyl)pyrene (TAPPy) and PDA which is examined in Chapter 2. 2D COFs are exclusively studied in this thesis, for additional information on 3D COFs, the review published by Zhu and Zhang is suggested.[5]

## 1.3 Potential Applications of Covalent Organic Frameworks

Covalent organic frameworks offer an attractive combination of designability, thermal stability, chemical stability, and permanent porosity that leads to a variety of potential applications, seen in Figure 1.6 below. COFs have been examined as materials for gas

storage and separation,[10-12] molecular separations,[13-15] catalysis,[16-21] molecular sensing,[22-23] metal chelation,[24-25] ion-conduction,[26-28] charge transport,[29-31] and charge storage.[32-35]


**Figure 1.6: Properties and applications of COFs arising from the regular arrangement of monomers and bonds.**

This thesis focuses on 2D imine-linked covalent organic frameworks, which garner attention for potential electronics applications due to the conjugation through the imine bond, which is in contrast to some other classes of COF materials such as boronic ester linked COFs which do not have the potential for in-plane conjugation through the COF linkage. The planar, 2D structure combined with the in-plane conjugation of the imine bond makes it possible for 2D imine COFs to display large degrees of in-plane conjugation leading to potentially useful properties.

## 1.4 Imine-Linked Covalent Organic Framework Synthesis Methods

Imine covalent organic frameworks can be synthesized as crystalline materials through a variety of methods. Some reported methods applicable to imine COFs, as well as other COF chemistries, include:

- Solvothermal synthesis: One or more COF monomers are sealed in a reaction vessel with organic solvent(s) and a catalyst and reacted at temperatures which exceed the boiling point of the solvents, resulting in pressures higher than 1 atm.[1]
- Solution synthesis: One or more COF monomers are dissolved in an organic solvent or mixture of solvents and reacted with a catalyst at temperatures less than or equal to the boiling point of the solvent mixture.
- Solid phase synthesis: COF monomers are subjected to physical forces such as grinding or ball milling with or without a catalyst.[36]
- Interfacial synthesis: COF monomers in an organic phase are reacted with a catalyst in an immiscible aqueous layer, forming a thin film of COF material.[37] Alternatively, COFs can be synthesized at the solvent/air interface.

- Surface synthesis: COF monomers are deposited on a surface under ultra-high vacuum (UHV) conditions and reacted to form single or few-layer materials.[30, 38]
- Microwave Synthesis: COF monomers and catalyst are combined in a glass vial and heated using microwave radiation.[39]

The synthesis method used to produce a covalent organic framework can have significant effects on the properties of the material. For instance, TAPB-PDA COF can be synthesized as microcrystalline powders using solution and solvothermal methods,[3] as thin films via interfacial polymerization using scandium triflate catalyst,[40] or as discrete nanoparticles[41] by varying the solvent system used.

Additional niche methods of COF synthesis have been reported as well. Garzon *et al.* report a spray coating synthesis method where a trifunctional aldehyde and trifuctional amine (TAPB in this case) were atomized along with an acid catalyst in a three-stream nozzle, yielding hollow, spherical COF nanoparticles.[42] Zhang *et al.* reported the use of a 3D printing nozzle to polymerize a solution of COF monomers into a cm scale COF monolith with high surface area and crystallinity.[43] Karak *et al.* make use of a terracotta process alongside a trifluoroacetic acid catalyst to produce porous, molded COF beads, cylinders and spheres.[36]

### *1.4.1 The "Standard" Solvothermal Synthesis of Imine-Linked COFs*

The majority of reported COFs are synthesized via solution or solvothermal methods. The typical COF synthesis reaction dissolves the COF monomers in equimolar ratios, according to the number of functional groups on each monomer, in an organic solvent or solvent system. This generally is degassed by freezing the sample in liquid nitrogen, pumping

under high vacuum, then sealing the vial under vacuum. The container is then heated at 120 °C for three days, after which the COF is isolated and activated to remove remaining monomers, soluble oligomers and solvent. In literature, vacuum is generally used to remove residual solvent, though air drying, drying with heat, and critical point drying with supercritical carbon dioxide ($scCO_2$) are alternative methods. The topic of COF activation is explored at length in Chapter 2.

A review of the imine COF literature focused on COF synthesis methods reveals a broad array of different structures, but not a corresponding variety in the synthesis methodology. A literature search was performed using Scifinder.cas.org. Keywords used were "Imine Covalent Organic Framework" resulting in 233 references as of May 25$^{th}$, 2019. These were examined individually to gain specific insight into the methods used for solvothermal imine-linked COF synthesis. References reporting beta-keto enamine-based COFs, or non-solvothermal synthesis methods such as grinding, or 3D printing were excluded from this count. This resulted in 69 applicable references.[3-4, 17, 20, 32, 34, 40, 44-105] The results of this search show that 70% of reported solvothermally synthesized imine-linked COFs were synthesized in 72 hours, 80% of these were heated at specifically 120 °C. Of the COFs examined, 90% were vacuum activated. The initial reports on COF synthesis appear to have set a strong precedent in the field and may have artificially limited the explored synthesis possibilities for solvothermal imine linked COFs. In Chapter 2 of this manuscript, the effects of the activation method used for COF isolation is explored, and it is shown that the standard literature method of vacuum activation can have deleterious effects of COF structure, and can drastically affect the obtained crystallinity and surface area of isolated COF materials. In Chapter 3, the initial stages of COF synthesis are explored for imine-

linked COFs, and the traditional 72-hour COF reaction time is shown to be unnecessarily long in some cases.

## 1.5 Characterization of Covalent Organic Frameworks

Due to their insolubility, many characterization methods commonly used for organic compounds and polymers are difficult to apply to covalent organic frameworks. However, there is a suite of routine characterization methods used to provide structural, chemical, and electronic characterization of covalent organic frameworks. In Table 1.1 below, these techniques are broadly categorized into three groups. Structural characterization methods provide information into the structure of the covalent organic framework, giving insight into interlayer spacing, pore sizes, surface areas and other factors. Chemical characterization methods provide information on the chemical bonds present in the COF and can shed light onto chemical changes during COF synthesis, or investigate how the COF interacts with its chemical environment. Finally, electronic characterization methods examine the electronic properties of the COF, including features like redox activity, conductivity, or charge transfer.

**Table 1.1: Various analytical methods useful for probing the structure, chemical behavior, and electronic characteristics of COFs.**

| Structural Characterization | Chemical Characterization | Electronic and Spectroscopic Characterization |
|---|---|---|
| **X-Ray Diffraction (XRD):** Crystal Structure.[106]<br><br>**Gas Adsorption/Desorption:** Surface area, pore size distribution.[107-108]<br><br>**Atomic Force Microscopy (AFM):** Microscopic structure and morphology.[109]<br><br>**Scanning Electron Microscopy (SEM):** Microscopic structure and morphology[110]<br><br>**Transmission Electron Microscopy (TEM):** Microscopy structure and morphology, direct visualization of COF lattice.[111]<br><br>**Scanning Tunneling Microscopyw:** Atomic resolution imaging of COF lattice | **IR Spectroscopy:** Chemical bonds and functional groups.<br><br>**Solid-State NMR:** Chemical structure, functional groups, connectivity.[112]<br><br>**Thermogravimetric Analysis:**Thermal stability. | **UV-Vis Spectroscopy:** Light absorption, intra-layer delocalization.[113]<br><br>**Cyclic Voltammetry:** Oxidation/reduction behavior.[114]<br><br>**X-Ray Photoelectron Spectroscopy:** Elemental composition, chemical state, density of electronic states.[115]<br><br>**Ultraviolet Photo-Electron Spectroscopy:** Ionization energy and electronic structure.[116]<br><br>**Conductivity:** Electron/hole transport properties of the bulk material.[117] |

Of the techniques listed in Table 1.1, powder x-ray diffraction (PXRD) and gas adsorption/desorption measurements are the most heavily relied on for the routine analysis of the structure of COF powders, and are discussed in more detail in the following sections. For details on the other analytical methods applicable to COFs presented in Table 1.1, the reader is directed to the reviews cited within Table 1.1. Many of the cited reviews focus on the application of the respective technique towards metal-organic frameworks which are a more mature field of chemistry with a larger body of literature than COFs. The application of these methods to COFs does not differ significantly from these methods use in other areas of chemistry.

### *1.5.1 X-Ray Diffraction*

X-ray diffraction is a useful technique for the analysis of solid materials, providing information on crystal structures, phases and orientations. In 1912, Max von Laue theorized and discovered that crystals can act as 3D diffraction gratings for x-rays with wavelengths similar to the spacing of planes of atoms within the crystal lattice. X-ray diffraction analysis is based on the constructive interference of monochromatic x-rays interacting with the crystal lattice. Constructive interference occurs when Bragg's law, shown in equation 1 below, is satisfied.[106]

$$n\lambda = 2d\sin\theta \quad (1)$$

Where $n$ is an integer, $\lambda$ is the wavelength of the incident X-ray radiation, $d$ is the lattice spacing of the crystal planes, and $\theta$ is the angle of the diffraction. When Bragg's law is satisfied, constructive interference occurs, and a diffracted X-ray is produced and

subsequently detected by the diffractometer. In solid matter, the onset of destructive interference occurs very rapidly as θ moves away from the refractive angle and thus the observed diffraction peak is sharp. X-ray diffractometers are composed of three principal components:

- X-ray tube: A cathode tube which produces electrons, which are accelerated towards a target material (often copper), which produces X-ray radiation when the bombarding electrons excite inner shell electrons which then emit characteristic X-rays when they relax.
- Sample Holder: Holds the solid sample in place.
- X-ray detector: Measures and records the X-ray intensity produced by the sample diffraction. This is reported as a plot of the intensity versus the diffraction angle 2θ (or the reciprocal space *q)*, called a diffractogram or powder diagram.

Powder X-ray diffraction, or PXRD identifies all the possible X-ray diffractions of the sample material because each possible crystal orientation is represented in the finely dispersed and randomly oriented powder sample. PXRD does not provide the same quantity of data as single crystal XRD for structure determination, though recent advances are narrowing this capability gap. Because covalent organic frameworks are most often synthesized as microcrystalline powders, PXRD is the most commonly applied XRD method. In this manuscript, PXRD is most often used to assess the structure of synthesized COFs, though *in-situ* XRD, operating on the same principles is used for analyzing COF formation during the reaction.

For powder COF samples synthesized here, Bragg-Brentano sample geometry, shown below in Figure 1.7, is used. This analysis method allows for measurement at low $2\theta$ values (as low as 1 °2θ in this thesis), which correspond to the large *d* spacings of the COF pores. The exact limits of the technique depend on the specific instrument in use, as well as the wavelength of X-ray radiation used.

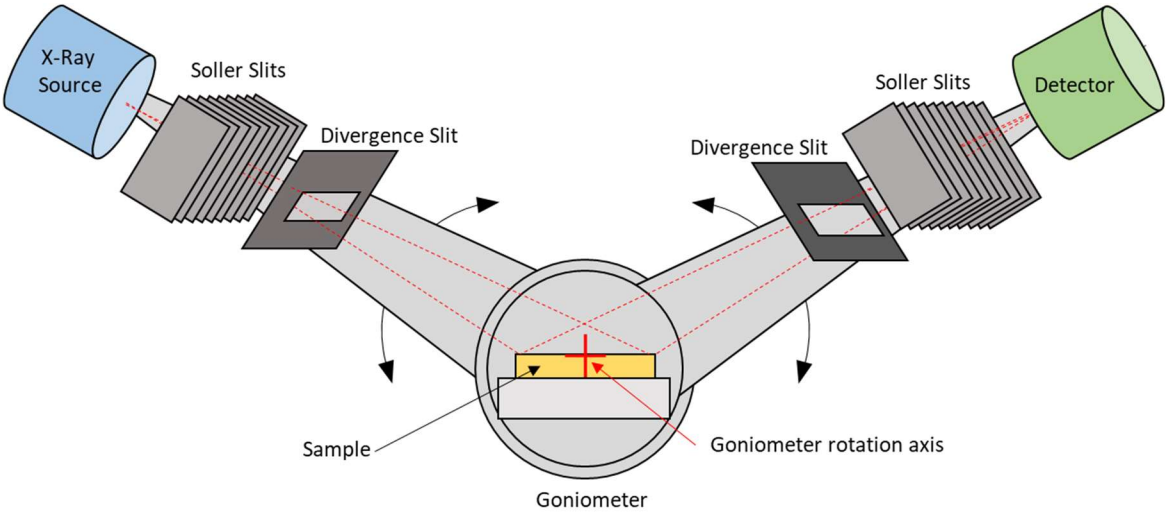


**Figure 1.7. Schematic of Bragg-Brentano sample geometry in a PXRD instrument.[106]**

The diffractogram, or PXRD pattern obtained for a typical TAPB-PDA COF sample is shown below in Figure 1.8. Lower $2\theta$ values correspond to larger *d* spacings., while higher $2\theta$ values correspond to smaller *d* spacings within the COF structure. The Miller indices are a vector representation for the diffracting planes in the crystal lattice. The indices are defined as the reciprocal of the fractional intercepts the plane makes with the crystal axis. The Cartesian x-axis is defined as *a*, the y-axis as *b*, and the z-axis as *c*. A Miller index of (100) represents a plane that intersects the *a*-axis at one unit length (the length of the crystal

cell), but does not intersect *b* or *c*. In hexagonal COFs like TAPB-PDA this diffraction originates from the parallel sides of the hexagonal COF pore, and thus measures the width of the pore. The (001) peak originates from the interlayer spacing between the stacked 2D COF sheets. In the PXRD patterns for COFs, the (100) peak is often the most intense signal observed, while the (001) signal is less intense and broadened.

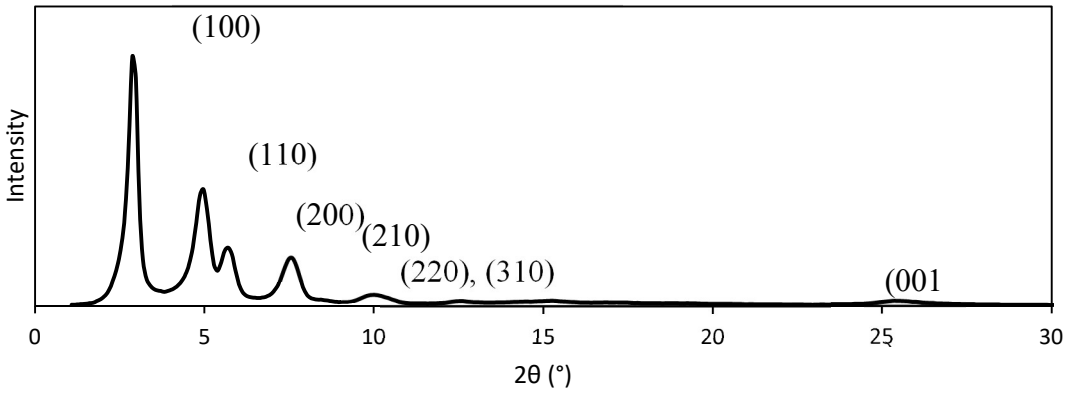


**Figure 1.8: An example PXRD pattern for TAPB-PDA COF[118] with Miller indices over their respective peaks.[40]**

New COF structures are often confirmed using PXRD by first modeling the predicted COF structure computationally. Software, such as Materials Studio, can provide predicted PXRD patterns based on an input COF unit cell, which can then be compared to experimentally obtained PXRD patterns. An example is the TAPPy-NDI-DA COF PXRD comparison below in Figure 1.9., which shows the predicted PXRD pattern computed for the COF, and the experimental PXRD pattern that confirms the predicted structure. This COF is examined further in Section 2.9.

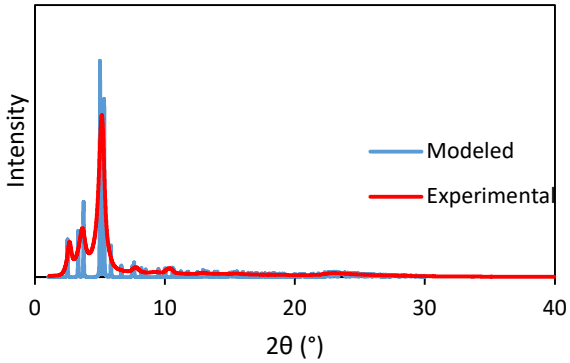


**Figure 1.9. TAPPy-NDI-DA COF computationally predicted PXRD pattern (blue), compared to the experimental PXRD pattern (red).[118]**

The Scherer equation relates the full width of the PXRD peak at half of its maximum value (FWHM) to the crystallite size according to:

$$\tau = \frac{K\lambda}{\beta \cos\theta} \tag{2}$$

Where τ is the crystallite diameter, $K$ is a dimensionless shape factor depending on the crystallite shape which is often close to 1 (usually 0.9), λ is the wavelength of the X-ray radiation, β is the FWHM of the peak in radians after subtracting instrumental broadening, and θ is the angle of the diffraction. The Scherer equation allows for the measurement of the COF crystallite size based on the X-ray diffraction characteristics, and was used by Evans *et al.* to confirm that COF nanoparticles were single COF crystals by comparing the XRD data to the nanoparticle size based on scanning electron microscopy measurements, and dynamic light scattering measurements.[119]

As a non-destructive, rapid technique that requires no additional preparation of the activated COF sample, PXRD is a critical characterization technique when studying

framework materials. PXRD provides information on the pore size of the COF, the crystallite size, the interlayer spacing of the COF sheets, as well as the overall sample quality and crystallinity.

Grazing incidence wide-angle x-ray scattering (GIWAXS) uses high intensity x-ray radiation to probe a thin layer of material at the analyte surface. At small angles, only a very small amount of material is present in the beam path, and thus high intensity x-ray sources, such as synchrotron radiation, are necessary for reasonable analysis times. GIWAXS has been used to examine COF films, giving insight into the crystallite size and orientation relative to the substrate surface. Matsumoto *et al.* used GIWAXS to examine 100 nm thick TAPB-PDA COF films grown interfacially and transferred to a silicon/silicon oxide substrate.[37]

Single crystal XRD is applicable to COFs that have been obtained as single crystal samples, and these COFs can be examined to provide precise crystal structures. Zhang *et al.* determined a COF crystal structure of a 3D imine linked COF, using agitation in THF to separate individual COF crystals for rotational electron diffraction analysis.[120] Ma *et al.* used mono-functional terminating groups in excess in order to grow single crystals of 3D imine COFs over the course of 30 to 40 days. These 100 micrometer long crystals were examined via single crystal XRD and the resulting crystal structure was the first single crystal COF structure reported.[121] Evans *et al.* later reported the first such example of a 2D COF single crystal through a seeded growth strategy.

### *1.5.2 Surface Analysis*

In 1916, Irving Langmuir, who would later receive the Nobel Prize in 1932 for his work on surface chemistry, presented his model for the adsorption of gases on surfaces as a single layer of adsorbed molecules.[122] This work was later expanded upon by Stephen Brunauer, P. H. Emmett, and Edward Teller who extended Langmuir's treatment of the single molecular layer to multi-molecular layers.[108] The eponymous Brunauer-Emmet-Teller (BET) theory is commonly used today to model and calculate the BET surface area ($S_{BET}$) of porous materials such as activated carbons, clays, zeolites, sol-gels, and in the case of this work, COFs. [108] The adsorption process is explained conceptually in Figure 1.10, below:

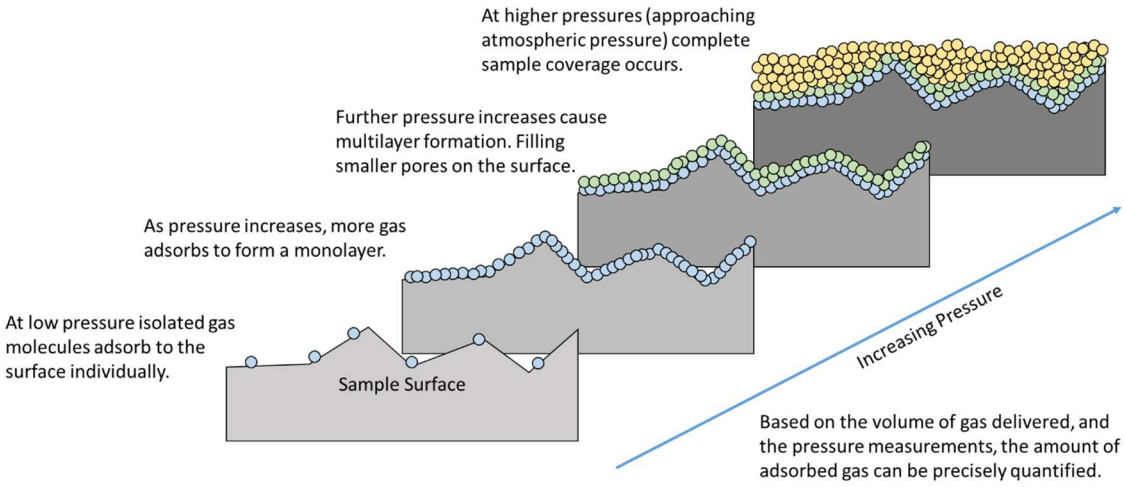


**Figure 1.10: Stages of gas adsorption on an analyte surface.**

The instrument is set up so that gas can be precisely dosed into or removed from the sample tube using a calibrated manifold and various valves, vacuum pumps and gas inputs. A

simplified instrument diagram is shown below in Figure 1.11, along with the general steps of the adsorption/desorption measurement.

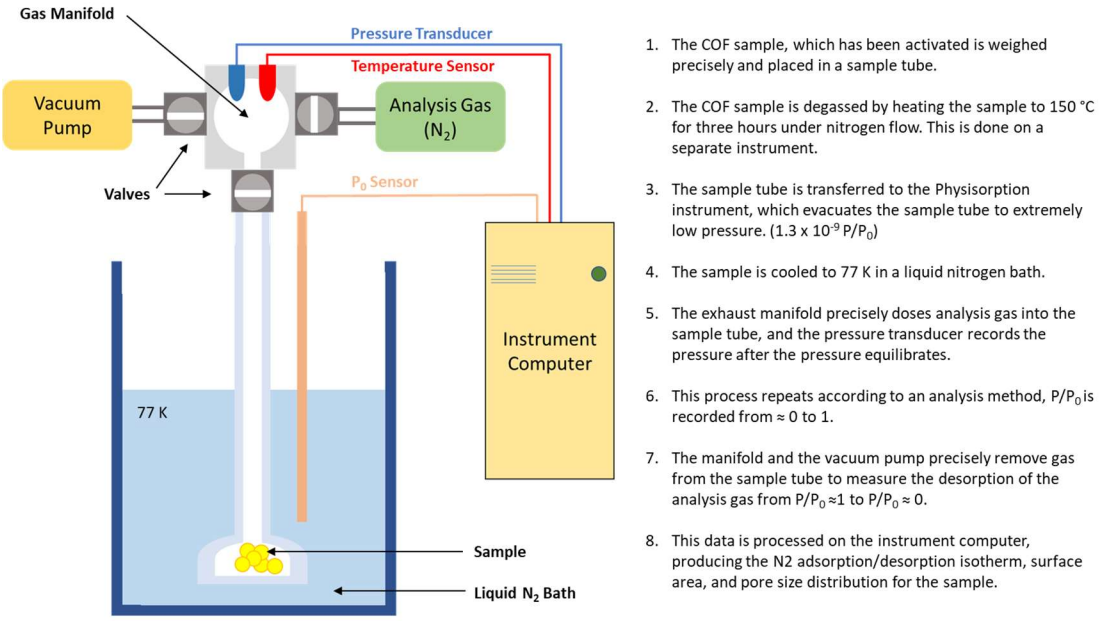


**Figure 1.11: Instrument diagram for $N_2$ adsorption/desorption measurements**

In practical use, BET theory allows for the calculation of $S_{BET}$ through a BET plot, which is a plot of: $1/([(p_0/p)-1)$ on the y-axis, and $p/p_0$ on the x-axis.[108] An example of a TAPB-PDA COF sample $N_2$ isotherm, and its corresponding linear plot used to calculate $S_{BET}$ are shown below in Figure 1.12.

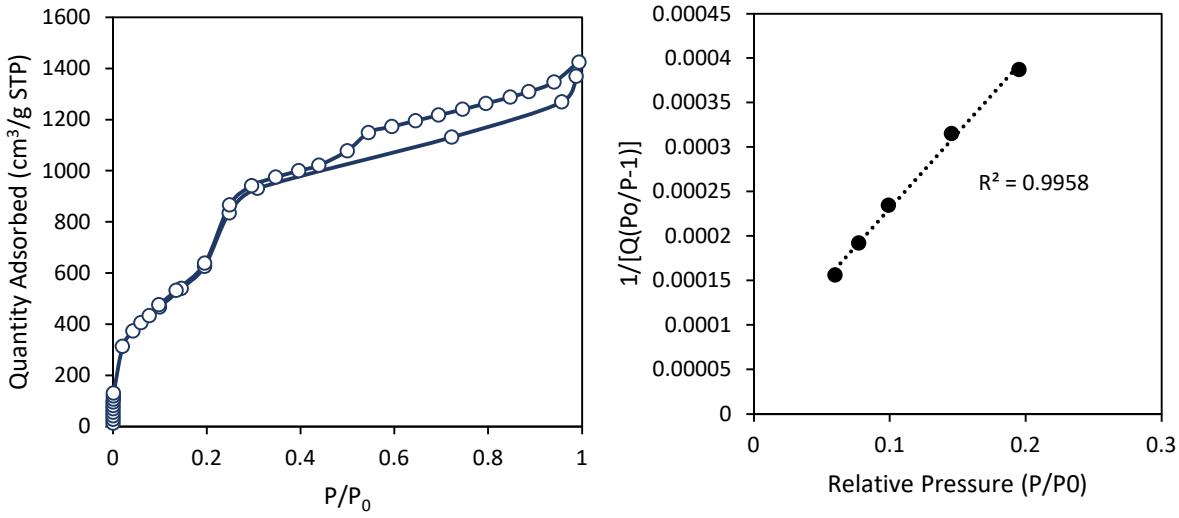


**Figure 1.12: Left: Experimental $N_2$ isotherm for TAPB-PDA COF. Right: BET plot showing the linear region with calculated $S_{BET}$ inset.**

Within the linear regime of this relationship, from approximately $p/p_0 > 0.05$ to $p/p_0 > 0.3$, the y-intercept of the plot and the slop of the line yield the monolayer adsorbed gas quantity $v_m$ according to $v_m=1/(A+I)$ where $A$ is the slope and $I$ is the y-intercept. The total surface are is related to $v_m$ by; $S_{total}=(v_m \cdot N \cdot s)/V$, where $N$ is Avogadro's number, $V$ is the molar volume of the analyte gas, and $s$ is the adsorption cross section of the analysis gas. The specific surface area $S_{BET}$ is related to $S_{total}$ by; $S_{BET}=S_{total}/a$, where $a$ is the sample mass.[108] During this analysis, the sample mass and the sample's available surface area are easily affected by leftover solvent molecules, or oligomeric monomer condensation products, or residual catalysts, therefor it is crucial that the sample be rigorously cleaned and dried through an activation process, which is discussed in detail in Chapter 2.

The isotherm obtained for mesoporous samples can be used to generate data on the pore size distribution (PSD) of the sample through various mathematical techniques. Density

functional theory (DFT) can be used to accurately model the behavior of fluids adsorbing to surfaces, in pores, and the condensation of gases inside the pores of a sample.[123] The DFT model is used to relate the pore filling pressure of the pore to the PSD. This capability has been integrated into modern surface analysis instruments, such as the Micromeritics 3Flex used extensively during this work. A sample PSD is shown below in Figure 1.13.

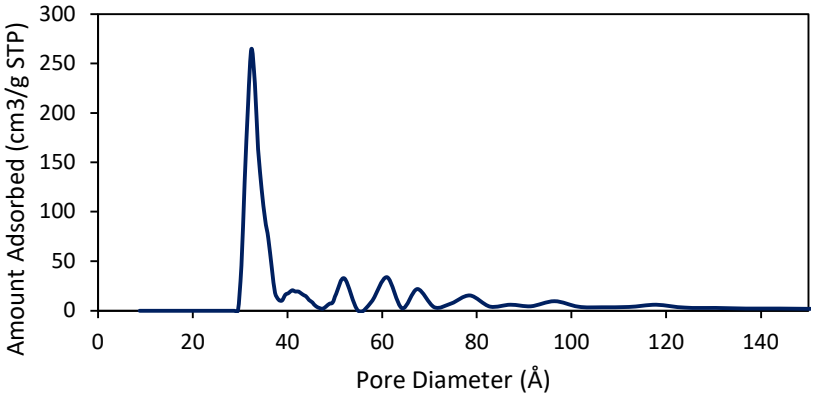


**Figure 1.13: Example pore size distribution of TAPB-PDA COF**

Surface characterization is a powerful tool in the analysis of framework materials, yielding information on the material's surface area, pore diameter and pore volume. This can be compared to theoretical Connolly surface areas, which are modeled by "rolling" a spherical solvent molecule along the molecule or framework's calculated surface in order to determine the surface area.[124] Connolly surfaces are often calculated for COFs to provide a theoretical comparison to the measured $S_{BET}$ values obtained for COF samples.

## 1.6 Research Summary

The synthesis, characterization, and application of covalent organic frameworks is an ever-broadening topic. This thesis focuses primarily on the synthesis and characterization of imine-linked covalent organic frameworks due to their potential applications in organic electronics. The application of imine-linked COFs in this area is heavily reliant on the growth of high-quality COF samples to minimize defects in the crystal lattice, thus providing material properties close to those predicted for various electronically interesting imine COFs.

Towards this end, Chapter 2 of this thesis focuses on the activation process, where reaction solvents, remaining monomers and oligomers and other contaminants are removed from the COF framework prior to characterization. This stage in COF synthesis is ubiquitous, since solvent and other guest molecules interfere with subsequent structural and chemical characterization. Despite this ubiquity, the effects of different activation methods which had been reported was unstudied. After examining the effects of vacuum activation compared to critical point drying with supercritical carbon dioxide and a new nitrogen-flow activation method, the chapter demonstrates that gentle activation techniques allow for more rapid isolation of imine-linked COF samples during the COF synthesis. The study into the effects of activation on different COF linkages is then examined to see if the discoveries for imine-linked COFs are generalizable to a greater percentage of the COF field.

Chapter 3 of this thesis similarly focuses on the synthesis of imine-linked COFs, using a combination of *ex-situ* and *in-situ* techniques to study the initial formation of crystalline

COFs. Here the lessons learned from Chapter 2 are applied to more accurately assess the initial precipitates from the COF polymerization, which are highly susceptible to distortions during the activation process. TAPB-PDA COF initially serves as a model COF, and the effect of acid and monomer concentration on COF formation is assessed using *in-situ* XRD. The effect of COF topology on the rate of formation is assessed by comparing hexagonal TAPB-based COFs to square COFs based on tris-1,3,5,7-(4-aminophenyl)pyrene (TAPPy). This is further expanded when the effects of alkoxy substituents of increasing chain length on the initial crystallization on TAPB/2,5-dialkoxyterephthaldehyde-based COFs is investigated. The findings here help to shed light on the initial processes of COF crystallization. An understanding of these initial stages is likely to be critical to the development of the COF field, especially in endeavors to synthesize single-crystal 2D imine-linked COF samples for further study.

The fourth and final chapter contextualizes the new research presented here within the COF field, states the impact of the work contained here, and suggests potential future research paths which could provide additional insight and knowledge about COF materials.

# CHAPTER 2. STUDYING THE EFFECTS OF ACTIVATION ON TWO -DIMENSIONAL COVALENT ORGANIC FRAMEWORKS

## 2.1 Chapter Introduction

Solvothermally synthesized COFs are synthesized in a solvent mixture that dissolves each monomer component and a catalyst, often acetic acid. This reactive mixture is removed prior to *ex situ* analysis of the isolated covalent organic framework as guest solvent molecules, residual catalyst, and oligomeric species will occupy the COF pores. These impurities can lead to errors in surface measurements, and lead to broad interference in X-ray diffraction measurements among other characterization issues. Prior to the work described in this chapter and the related papers, the activation process for COFs was not extensively studied, and most reported COF synthesis methods utilized vacuum activation to remove guest solvents after rinsing the COF.

In this chapter, the role of activation in COF isolation, and the resulting differences in material properties, namely X-ray diffraction and BET surface area are examined for several COF species previously reported in literature. The initial discoveries leading to the recognition of the important of activation are detailed, followed by a series of experiments, which identified the activation method as a key parameter that can be responsible for the quality of isolated COF materials, depending on their the intrinsic robustness of their structure. Next an experiment where three COF species were subjected to different solvent

rinses, then activated either via vacuum drying or critical point drying with $scCO_2$ is presented.

Critical point drying is shown to be the most effective method of activation for all COFs studied here, but the technique requires specialized and potentially costly equipment, and thus an alternate method was developed that uses gentle heating and nitrogen flow to effectively activate various COF materials. This method, which can be accomplished with common laboratory equipment is shown to be a useful procedure for researchers to activate potentially fragile COF materials without investing in specialized equipment.

Stepping back from activation itself, the role of COF structure and functional groups within the COF are examined. We used combinations of data obtained during these experiments (*vide infra.*), as well as specific literature examples where COFs were activated via vacuum drying, yet still displayed high surface areas and crystallinity, in order to identify factors that lead to increased stability towards vacuum drying. Specifically, from this collection of COFs, general trends and structural features are identified that may increase the interlayer interactions between 2D COF sheets, and allow for structural stability when using less gentle activation methods, such as vacuum drying. The reversibility of the structural changes caused by vacuum activation is examined, then the effects of activations on other COF linkages, such as azine-linked COFs, beta-keto enamine-linked COFs, and boroxine linked COFs is assessed using example COF materials from literature.

Finally, the use of $scCO_2$ allows COFs to be isolated as crystalline materials after shorter periods of time than the most widely reported literature procedures that suggest a reaction time of 72 hours at 70 °C. A variety of COF structures, including materials containing

electronically active monomers were synthesized in 4 hours, as crystalline materials exhibiting high surface areas. These COF materials are characterized using a combination of PXRD, $N_2$ adsorption/desorption.

The chapter concludes with an overview of the potential impact and importance of this work, before presenting the materials and methods used for the presented experiments, data analysis, and literature reviews.

## 2.2 Observing Rapid Synthesis of TAPB-PDA COF

In the process of performing COF reactions as a function of time, it was observed that the synthesis method used produced crystalline TAPB-PDA COF in 4 hours, with crystalline diffraction signals shown by PXRD as early as three minutes after adding acetic acid catalyst solution. This finding contrasted strongly with related work by Smith *et al.,* which reported that TAPB-PDA COF initially formed amorphous material, which then became crystalline after two to three days at the 70 °C reaction temperature.[3] Because the synthesis method used differed slightly from the method reported by Smith *et al.* several experiments were performed in order to identify the key parameter(s) responsible for the change in results.

### *2.2.1 Comparison of Reported TAPB-PDA COF Synthesis Method to a Literature Method*

The method used by Smith *et al.* for the acetic acid catalysed synthesis of TAPB-PDA COF is compared to the similar method reported here for this COF. Table 2.1, shown below,

compares key features of the synthesis methods including acid and monomer concentrations, reaction time, and other factors.

**Table 2.1: Comparison of reaction parameters between the presented TAPB-PDA COF synthesis and the method reported by Smith *et al.*[3]**

| Reaction Parameter | Method | Smith *et al.* Method[3] |
|---|---|---|
| mg TAPB | 33.5 mg, 0.095 mmol | 55 mg, 0.16 mmol |
| mg PDA | 19.2 mg, 0.143 mmol | 31, 0.23 mmol |
| M TAPB | 0.063 | 0.017 |
| M PDA | 0.095 | 0.024 |
| M AcOH | 3.5 | 3.37 |
| M $H_2O$ | 7.40 | 7.16 |
| Acid Addition Method | 0.5 mL 10.5 M AcOH in DI $H_2O$ | 1.2 mL DI $H_2O$, followed by 1.8 mL glacial AcOH |
| Solvent | 4:1 *p*-dioxane:mesitylene | 4:1 *p*-dioxane:mesitylene |
| Solvent Volume | 1 mL | 6.3 mL |
| Total Volume | 1.5 mL | 9.3 mL |
| Reaction Temp. | 70 °C | 70 °C |
| Initial Reaction Temp. | 70 °C | Room Temperature |

| | | |
|---|---|---|
| Reaction Time | 4 hours | 72 hours |
| Activation Method | $scCO_2$ | Room Temperature Vacuum |

As is seen in Table 2.1 above, the final glacial acetic acid concentration and water concentration in the final reaction mixtures are quite similar. The concentrations of the COF monomers are higher in the method reported here than in the method reported by Smith *et al.* Additional differences are present in the method of acid addition; here it is added as a solution with deionized (DI) water, and in the Smith *et al.* method the acid and water are added separately. [3] Additionally, in the method reported here the acid solution is added while the monomer solution is already preheated to the reaction temperature, while in the Smith *et al.* method the acid and water are first added, then the reaction is heated to 70 °C. The final difference apart from the reaction time, is the activation method; Smith *et al.* make use of vacuum activation at room temperature for an unspecified time (assumed to be overnight), while the method reported here relies on critical point drying with supercritical carbon dioxide ($scCO_2$). [3]

### *2.2.2 Isolating the Activation Procedure as the Key Parameter*

Initially, it was thought that the change where acid catalyst solution was added to the heated monomer solution, rather than room temperature solution as reported by Smith *et al.* was responsible.[3] It was initially postulated that the increased temperature during to the addition of the acid catalyst may allow for different monomer templation, with subsequent effects on the final COF. A series of four COFs were synthesized where the

initial temperature of the monomer solution was varied between 0 °C and 120 °C. After two minutes at the initial temperature, the reaction was heated or cooled to 70 °C, then allowed to react for four hours at 70 °C prior to isolation via filtration, rinsing with methanol, followed by $scCO_2$ activation. The resulting PXRD patterns, shown below in Figure 2.1, are effectively identical, indicating that the initial solution temperature is not a key parameter responsible for the drastic difference in crystallinity at four hours between the two COF synthesis methods.

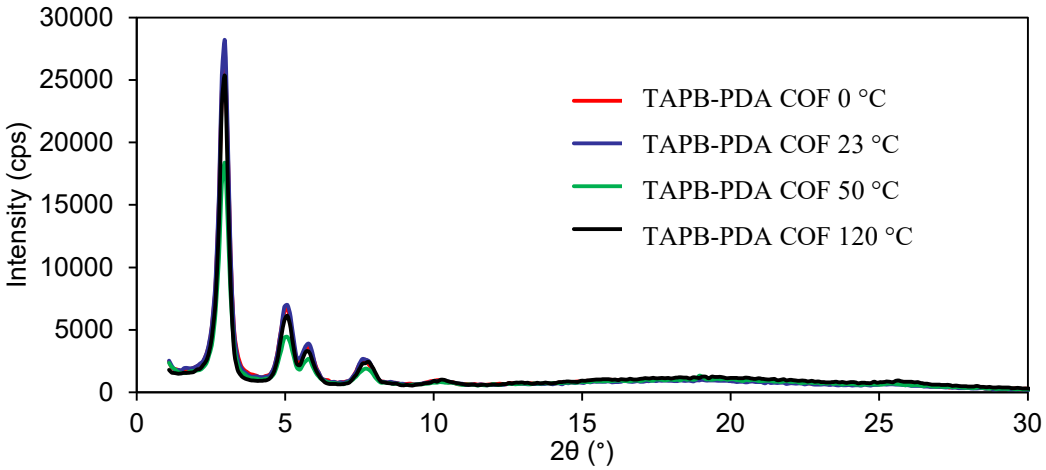


**Figure 2.1: PXRD patterns of TAPB-PDA COF samples synthesized using a range of initial starting temperatures before reacting for at 70 °C.**

Next, the concentration changes between the method used here and the reported method were examined. A COF was synthesized in four hours using the same concentration of monomers and acid that Smith *et al.* employed, followed by $scCO_2$ activation. [3] This trial resulted in an identical PXRD intensity compared to the method reported here as seen in Figure 2.2 below.

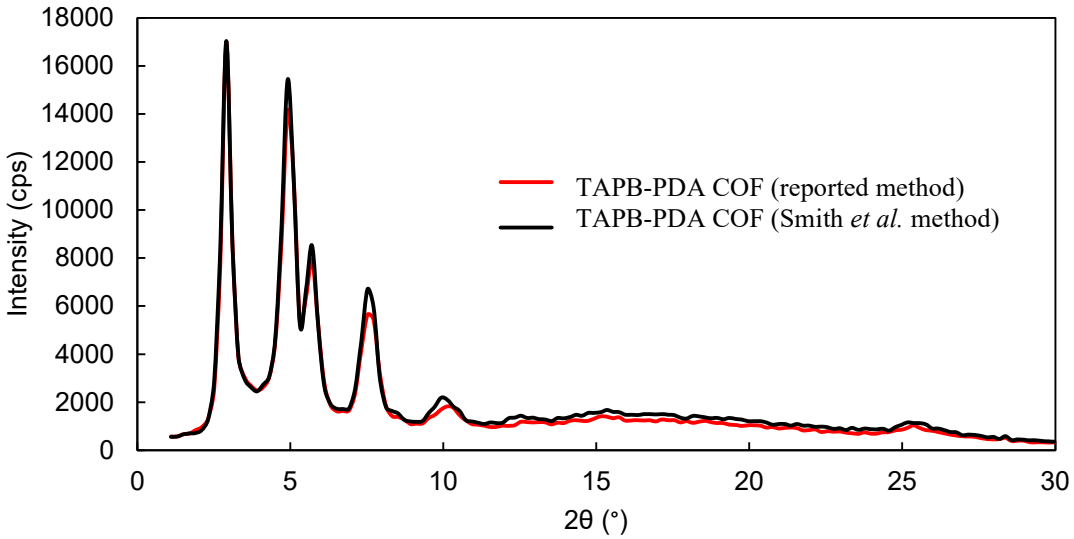


**Figure 2.2: Comparison of PXRD patterns from the TAPB-PDA COF synthesis method reported here (red), and the method reported by Smith *et al.* (black).[3]**

The order of acid catalyst solution components was also examined, because in the Smith *et al.* method, acetic acid and water are added separately, while in the method reported herein, they are added together as a solution.[3] The resulting PXRD patterns for the trials are shown in Figure 2.3, below. Adding the components together was equally effective as first adding the water, followed by glacial acetic acid. However, first adding glacial acid resulted in lower PXRD intensity, likely due to rapid precipitation of solid COF material

causing incomplete and inefficient mixing. The order of addition was not found to be the factor responsible for the observed differences.

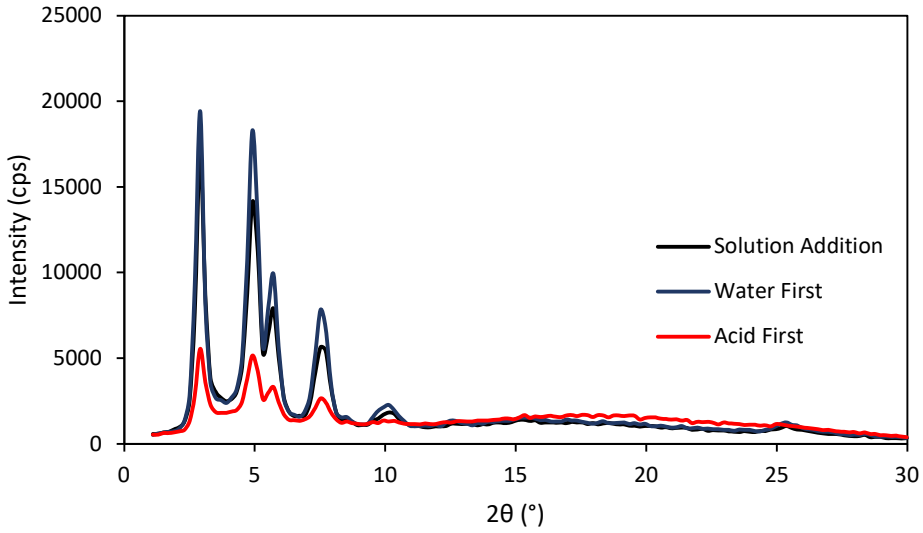


**Figure 2.3: Comparison of TAPB-PDA COF sample PXRDs with the order of acid and water addition varied.**

Finally, the activation method used to remove solvent and other guest molecules was examined. In the method reported by Smith *et al.* vacuum activation is used to remove the toluene rinse solvent, however in the method reported here, critical point drying with carbon dioxide is used to remove methanol. [3] The results of this direct comparison are shown in Figure 2.4 below, with the PXRD patterns at left, and the nitrogen adsorption isotherms shown at right with $S_{BET}$'s inset.

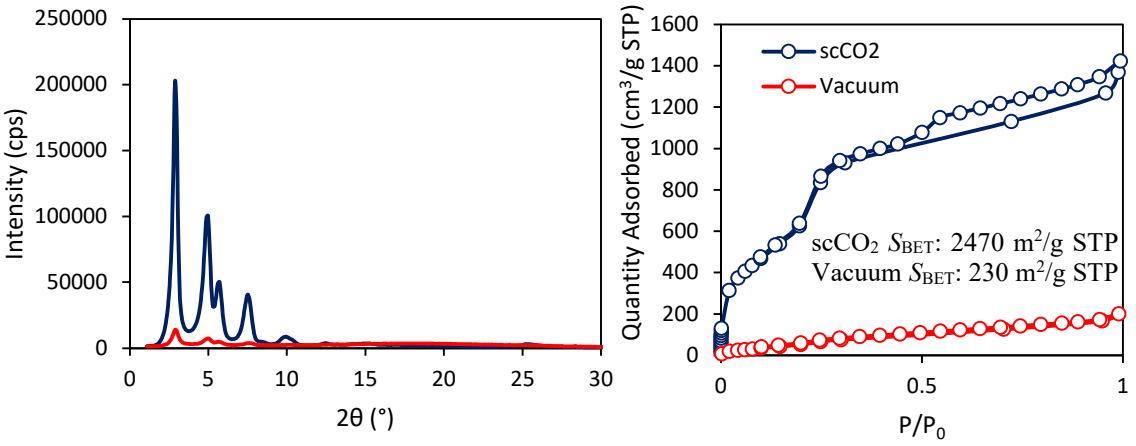


**Figure 2.4: Left: PXRD patterns for TAPB-PDA COFs isolated using critical point drying ($scCO_2$, blue) and vacuum (red). Right: $N_2$ adsorption/desorption isotherms for the same TAPB-PDA COF samples. Inset Right: $S_{BET}$ values obtained for the same TAPB-PDA COF samples.**

The activation method used has clearly had a drastic effect on the COF solids that were obtained. The vacuum activated COF displays far lower surface area, crystallinity and porosity than the $scCO_2$ dried COF. Additionally, the 32 Å pores characteristic of the COF material have vanished, as seen in the pore size distributions of the two material samples, shown below in Figure 2.5.

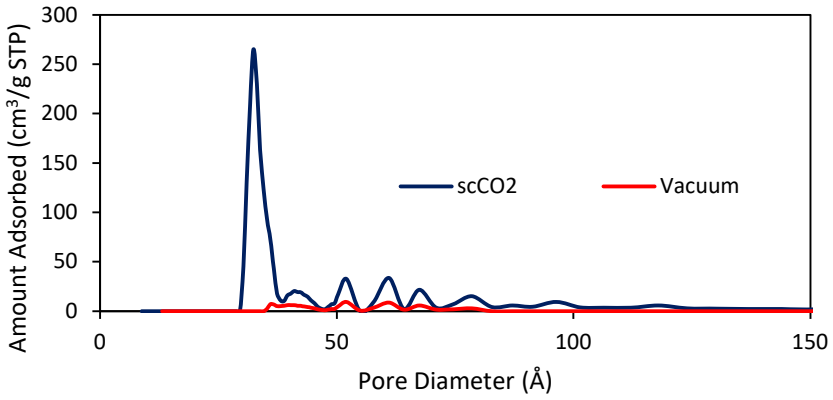


**Figure 2.5: Pore size distribution for TAPB-PDA COF samples isolated using critical point drying ($scCO_2$, blue) or vacuum activation (red).**

Based on the data obtained, the activation method used was identified as the key difference in the two procedures, and the vacuum activation is responsible for the low crystallinity and porosity observed at low time scales by Smith *et al.* This implies that the activation method used for COF isolation and preparation is of greater importance than has been previously recognized in the COF literature; a more general investigation of the impact of different COF activation methods is warranted. [3] Also warranted is an investigation of how different COF structures, and structural features affect a COF material's susceptibility to degradation during activation via vacuum drying.

## 2.3 Introduction to COF Activation Methods Reported in Literature

After the synthesis of a covalent organic framework via solution or solvothermal methods is complete, the COF pores are occupied by solvent, residual catalyst, and potentially unreacted monomer and oligomeric species. In order to prevent further reaction or

degradation, the catalyst must be removed. This is accomplished by rinsing the COF solids with additional solvents, Soxhlet extraction may also be employed if more thorough cleaning is desired. After rinsing, in order to accurately assess the crystallinity of the framework, or the surface area and pore size distribution, the COF pores must free of guest solvent molecules, residual catalyst, and oligomeric species. Several methods of accomplishing this have been reported:

- Vacuum activation, which uses reduced pressure, sometimes with the additional application of heat to evaporate residual solvents from the COF pores.
- Drying using heat.
- Drying under nitrogen or air flow.
- Critical point drying using super critical carbon dioxide ($scCO_2$).

During $scCO_2$ activation, the COF material is immersed in a solvent such as methanol, or isopropanol, then cooled to approximately 0 °C. The solvent is slowly displaced by liquid $CO_2$ at high pressure. Once the solvent has been completely removed and replaced by liquid $CO_2$, the temperature is increased past the critical point, at which point $CO_2$ transitions from a liquid to a supercritical fluid. Then, after an equilibration period, the pressure is reduced slowly, while maintaining the higher temperature. This causes the supercritical $CO_2$ to transition to a gas, without ever evaporating. By circumventing the liquid to gas phase boundary, critical point drying minimizes capillary forces within the COF pores and leads to little structural distortion. The COF then is removed from the pressure chamber, clean, dry, and ready for further analysis. This process is shown conceptually in Figure 2.6, below.

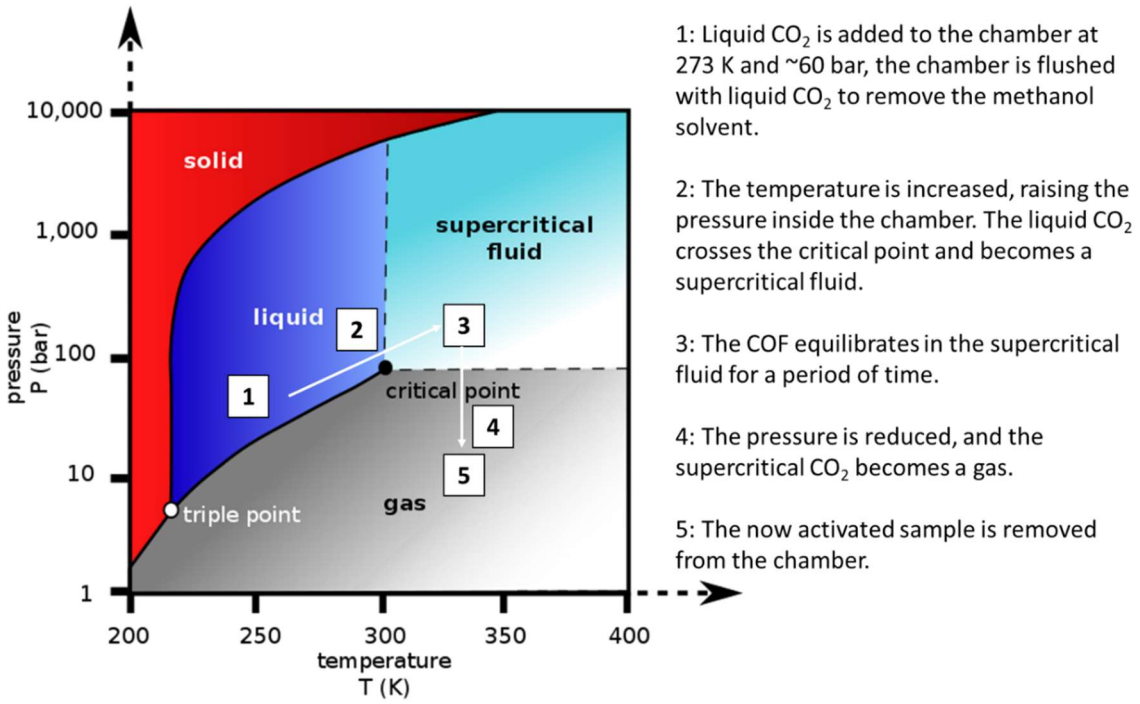


**Figure 2.6: Phase diagram of carbon dioxide sourced from Wikimedia commons. Arrows show the process steps for critical point drying. (https://commons.wikimedia.org/wiki/File:Carbon_dioxide_pressure-temperature_phase_diagram.jpg#/media/File:Carbon_dioxide_pressure-temperature_phase_diagram.svg accessed April 21st, 2020)**

As discussed earlier in Chapte 1, a literature search was performed using Scifinder.cas.org to examine the synthesis conditions and activation methods reported for imine-linked COFs.[3-4, 17, 20, 32, 34, 40, 44-105] An examination of these reports shows several clear trends. Vacuum activation is by far the most widely utilized method for COF activation, with 54 of the 61 (or 89%) examined works using vacuum activation in some capacity. Heating and air drying are used sparingly with two and four reports respectively. $ScCO_2$ activation features in five references, always in combination with vacuum drying. Some information however can be gained about the general efficacy of the activation methods by examining the $S_{BET}$ values reported for the COFs. In each of these works the highest reported $S_{BET}$ value was recorded, disregarding COF structure. The average $S_{BET}$ for all examined

references was 1080 $m^2/g$ STP. The average $S_{BET}$ reported for COFs which used vacuum activation at any point during the COF isolation process, was 1100 $m^2/g$, which agrees well with the average value since vacuum activation is so widely used. Interestingly however, the five references that reported using $scCO_2$ drying at any point in the COF activation process, had an average reported $S_{BET}$ of 2090 $m^2/g$, which is 90% higher than the average value for the vacuum activated COF reports. It is critical to note at this point, that several important factors were disregarded for this comparison. In examining the $S_{BET}$ values reported, the synthesis conditions, synthesis time, and even COF structure have been completely discounted. However, the fact remains that COF publications utilizing $scCO_2$ on average report nearly double the average surface area reported for imine COFs isolated using vacuum activation. This literature evidence agrees well with the initial conclusions reached by comparing the method reported by Smith *et al.* with the COF synthesis method reported here. [3] The used of critical point drying is clearly an important factor in determining the outcome of COF activation. The effect of vacuum activation has already been studied in the context of MOF materials, where it has been shown to cause structural distortion during activation.[125] When gas evaporates within highly porous structures, capillary forces can cause structural changes, including pore collapse.[125] This further supports that $scCO_2$ activation is beneficial and effective in the activation of other framework materials, such as COFs, through very similar mechanisms.[126-127]

## 2.4 The Effects of Activation Methods on Imine-Linked Covalent Organic Framework Crystallinity and Porosity

An experiment was designed to test the effect of rinse solvent, and the effect of the activation method used for COF activation on the resulting crystallinity and porosity. The

experimental design, shown below in Figure 2.7, takes a COF sample reacted under the standard conditions in four hours, and divides the filtered solid in half after it has been rinsed by one of four rinse solvents, methanol, toluene, acetone or dichloromethane. Half of the sample is subjected to vacuum activation at room temperature overnight, and the other half is activated via $scCO_2$. This methodology helps to account for slight variations during the synthesis process. After activation, the COF solids were analyzed via PXRD and $N_2$ adsorption.

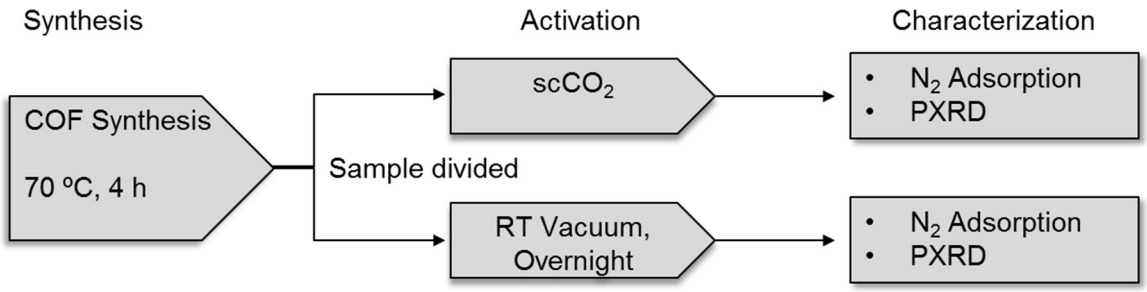


**Figure 2.7: Experimental design for testing the effects of vacuum activation versus $scCO_2$ activation on imine COFs.**

Three two-dimensional, imine-linked COFs that have been well documented in the COF literature were examined in this manner, TAPB-PDA COF, TAPB-OMePDA COF, and TAPPy-PDA COF. The structures of these COFs are shown below in Figure 2.8.

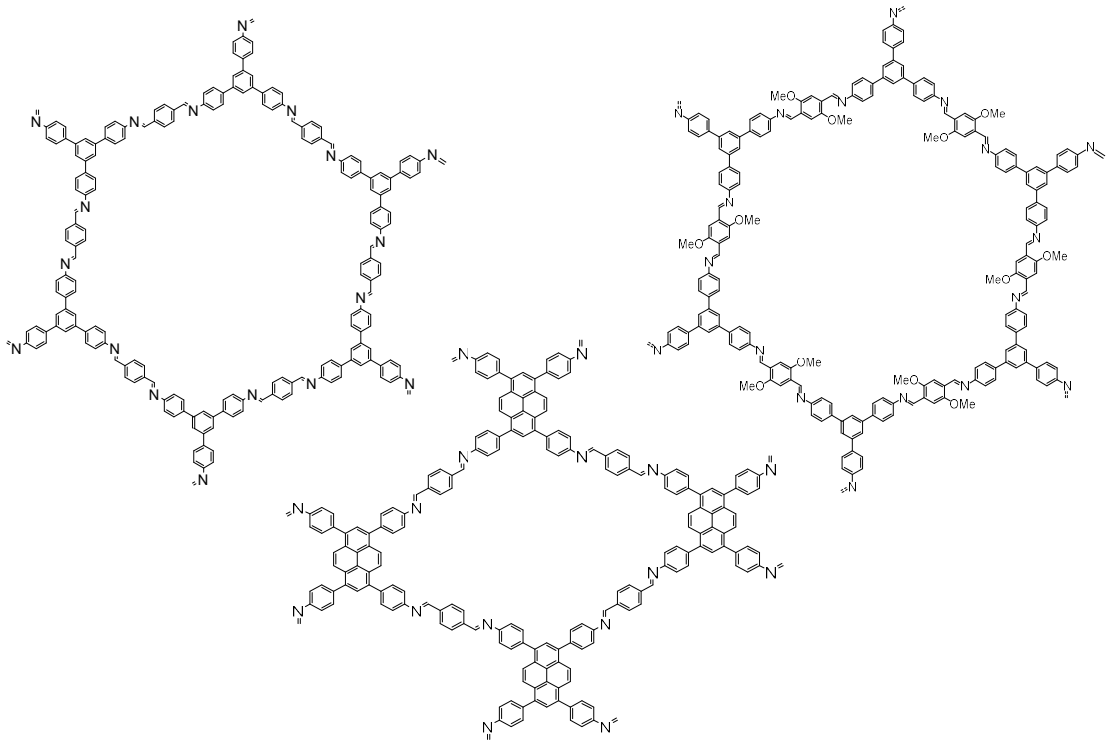

**Figure 2.8: Left: TAPB-PDA COF, Center: TAPPy-PDA COF, Right: TAPB-OMePDA COF.**

The basic TAPB-PDA COF is commonly used as a model system partly because of the commercial availability of the monomer components. [3, 20, 40, 118] In 2015, TAPB-OMePDA was reported by Xu *et al.* to form as a more crystalline COF than TAPB-PDA COF, which was attributed to charge delocalization caused by the pendant methoxy groups.[20] This increased interlayer interaction here is hypothesized to increase the resilience of the COF towards the capillary forces induced by evaporating solvents during vacuum activation. Similarly, TAPPy-PDA COF was selected because of its reported inter-layer interactions, in this case caused by the conformation of the four phenyl rings surrounding the pyrene core.[128] Auras *et al.* investigated the synchronized offset stacking behavior of this COF, which they posited was the reason for increased π-π interactions between the COF sheets,

and consequently the increased crystallinity they observed.[128] This synchronized offset stacking is shown in Figure 2.9, below.

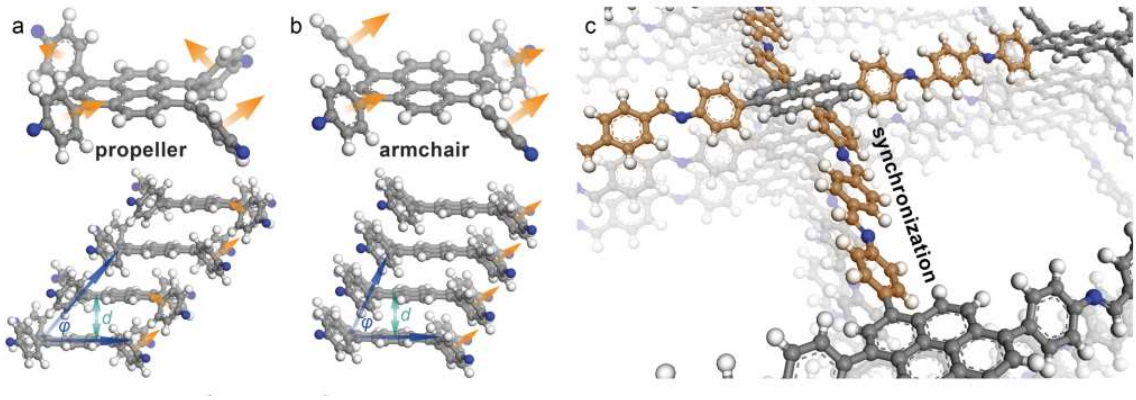


**Figure 2.9: Schematic drawing showing conformational synchronization in the phenyl spacers of TAPPy-PDA COF originally published by Auras *et al.* and used here with permission.[128]**

Again, these interlayer interactions are hypothesized to increase the resilience of the COF during the vacuum activation process. Figure 2.10 below shows the PXRD and $N_2$ adsorption results specifically for methanol rinsed COF samples. Corresponding data for toluene, acetone, and dichloromethane rinsed samples are available in the Section 2.11.8.

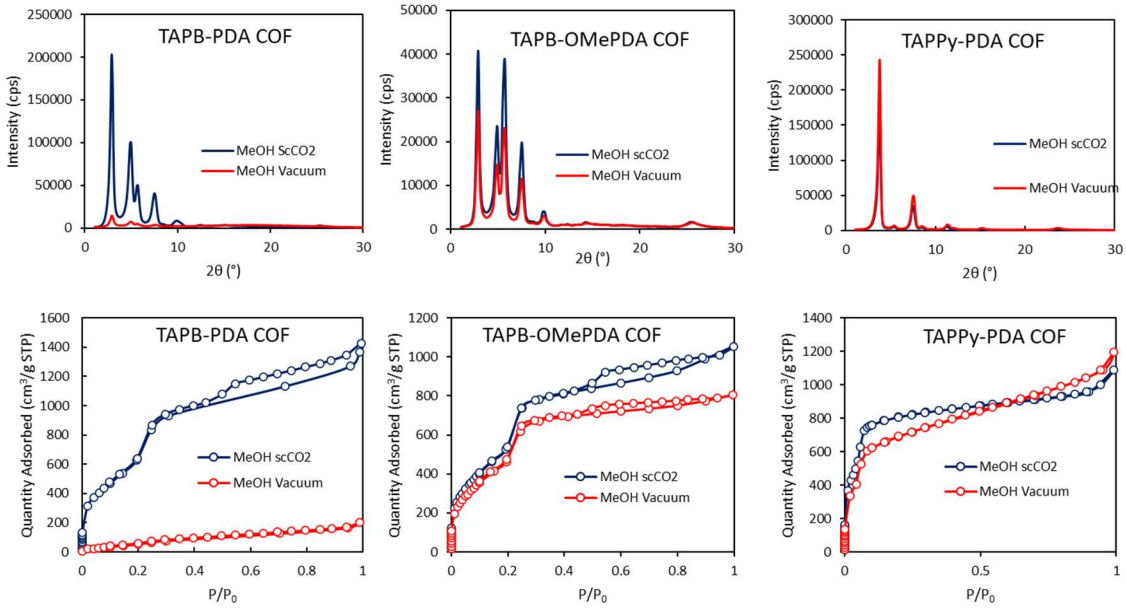


**Figure 2.10: Left Top: PXRD pattern of methanol rinsed TAPB-PDA COF activated by $scCO_2$ (blue) and vacuum (red). Left Bottom: $N_2$ adsorption/desorption isotherms of TAPB-PDA COFs. Center Top: PXRD pattern of methanol rinsed TAPB-OMePDA COF activated by $scCO_2$ (blue) and vacuum (red). Center Bottom: $N_2$ adsorption/desorption isotherms of TAPPy-PDA COFs. Right Top: PXRD pattern of methanol rinsed TAPPy-PDA COF activated by $scCO_2$ (blue) and vacuum (red). Right Bottom: $N_2$ adsorption/desorption isotherms of TAPPy-PDA COFs.**

After four hours, TAPB-PDA COF displays high surface area, and intense diffraction peaks indicative of high crystallinity when activated using $scCO_2$, with the rinse solvent used showing no significant effect on the COF properties obtained. In contrast, the vacuum activated samples of TAPB-PDA COF show markedly reduced diffraction intensity compared to the $scCO_2$ activated samples and show approximately 90% less accessible surface area. The differences in the pore size distributions for vacuum activated and $scCO_2$-activated samples are particularly telling. In vacuum activated samples there is no porosity corresponding to the 32 Å pores of the COF structure, see Figure 2.5, or Figure 2.46 in Section 2.11.8. This result shows that vacuum activation causes degradation of the COF

crystal structure, possibly through a pore collapse mechanism similar to MOFs.[126] There is also the possibility of lateral sheet displacement, as explored by Sick *et al.*, which could also explain the loss of porosity. This is further explored later in Section 2.6.[127]

After four hours of reaction time, TAPB-OMePDA COF shows high surface area, and intense diffraction peaks similar to TAPB-PDA COF. Again, the rinse solvent used to clean the filtered COF solids has no marked effect on the crystallinity or surface area obtained. However, when activated by vacuum activation overnight at room temperature, TAPB-OMePDA COF shows roughly 50% of the accessible surface area of $scCO_2$ activated samples. Similarly, the PXRD intensity decreases by a corresponding 50%. Here several causes can be posited for the increased stability of the methoxy group adorned TAPB-OMePDA COF compared to the bare TAPB-PDA COF. Xu *et al.* theorized that the charge delocalization caused by the inclusion of the methoxy groups on the COF lead to lower inter-layer repulsive forces due to the polar imine bond, and consequently an increase in COF crystallinity.[20] If a lateral sheet displacement mechanism is assumed, as presented by Sick *et al.*, then the inclusion of the methoxy groups could sterically inhibit the sliding of COF sheets relative to one another.[127] Regardless, the key result is that the inclusion of the methoxy group has some stabilizing effect, which consequently helps the COF to withstand vacuum activation.

After four hours of reaction time, TAPPy-PDA COF shows very high surface area, and sharp diffraction peaks irrespective of activation method. Here, the vacuum activated samples show approximately 90% of the crystalline diffraction intensity, and approximately 90% of the accessible surface areas found for the $scCO_2$ activated samples. This COF is particularly robust towards vacuum activation, to such a degree that $scCO_2$

activation is not necessary for crystalline materials after a four-hour synthesis. Presumably, the stability of this COF is due to the "synchronized offset stacking" mechanism presented by Auras *et al.*, where the phenyl rings attached to the pyrene core orient in a uniform fashion.[128] This stacking behavior increases π-π interaction between the COF sheets, resulting in highly crystalline materials.[128] Here it is theorized that these same interactions increase the stability of TAPPY-PDA COF during vacuum activation. Alternatively, the smaller pores of the TAPPy-PDA COF (23 Å vs 32 Å for TAPB-PDA COF) are more structurally rigid, and may be better able to resist pore collapse due to the evaporation of solvents within the confined pores.

Activation using $scCO_2$ was effective for all the COFs studied, and is the ideal method for activating a COF which is not known to be resilient towards vacuum activation. Vacuum activation by contrast has been demonstrated to have the potential to severely disrupt the crystallinity and porosity of susceptible COFs such as TAPB-PDA. The specific structural characteristics that lead to stability, or the lack thereof, are of interest. This limited examination of three COF structures, in combination with a thorough examination of the current literature on imine-linked COFs synthesized solvothermally provides some insight into the COF features and characteristics that may impart additional stability during vacuum activation.

## 2.5 Nitrogen Flow Activation of Imine-Linked Covalent Organic Frameworks

While $scCO_2$ activation was found to be effective for each COF studied, and is a reasonable first choice for activation of a new COF material, the technique requires specialized equipment to handle the high pressures and temperature control necessary for proper and

safe activation. Because of the importance of gentle activation for accurately assessing COF material properties without disrupting the crystal structure or adversely affecting porosity, it was potentially valuable to identify methods that are more accessible than activation with $scCO_2$ to COF researchers.

A method using nitrogen flow and gentle heating developed.[118] This method uses sequential solvent exchange to replace the methanol used initially to rinse the COF solids, with dichloromethane, then finally hexanes before drying away the solvent under gentle nitrogen flow, at 150 °C for three hours.

This method was tested on samples of TAPB-PDA COF, TAPB-OMePDA COF, and TAPPy-PDA COF. The resulting $S_{BET}$ values for the samples are shown below in Table 2.2, with the $scCO_2$ and vacuum activated $S_{BET}$ values included for comparison.

**Table 2.2: $S_{BET}$ values for COFs activated using nitrogen flow.**

| COF | $N_2$ Flow $S_{BET}$ ($m^2/g$ STP) | $scCO_2$ $S_{BET}$ ($m^2/g$ STP) | Vacuum $S_{BET}$ ($m^2/g$ STP) |
|---|---|---|---|
| TAPB-PDA | 2060 | 2470 | 230 |
| TAPB-OMePDA | 2060 | 2080 | 820 |

| | | | |
|---|---|---|---|
| TAPPy-PDA | 2080 | 2530 | 2400 |

As seen in Table 2.2, above, each COF is activated effectively by the nitrogen flow method, though $S_{BET}$ values obtained are slightly lower than those obtained via $scCO_2$ activation. The benefit in the nitrogen flow method, is that COF activation can be accomplished with ubiquitous laboratory supplies and any appropriate nitrogen gas source, rather than a highly specialized high-pressure system.

## 2.6 Structural Features in Imine-Linked Covalent Organic Frameworks Leading to Stability During Vacuum Activation

The realization that COFs are susceptible to degradation during vacuum activation is of critical importance, especially when considering that approximately 90% of the references examined in the literature search performed on 2D imine linked COFs utilize vacuum activation at some point during the isolation of their COF materials. However, there are still several examples of COFs isolated as highly crystalline materials despite being subjected to vacuum activation. Here, all COFs found during the course of the literature review that have reported $S_{BET}$ values greater than 1500 $m^2/g$ STP are examined, with the specific goal of elucidating structural or chemical similarities which may help to explain their observed robustness to vacuum activation through the lens of the activation studies on TAPB-PDA COF, TAPB-OMePDA COF, and TAPPy-PDA COF presented in Section 2.4.

Of the 61 references examined in the literature review, 11 reported COF materials were found that were activated using vacuum activation, and displayed $S_{BET}$ values greater than 1500 $m^2/g$. The COF monomer combinations are shown below in Figure 2.11, with their respective $S_{BET}$ values.

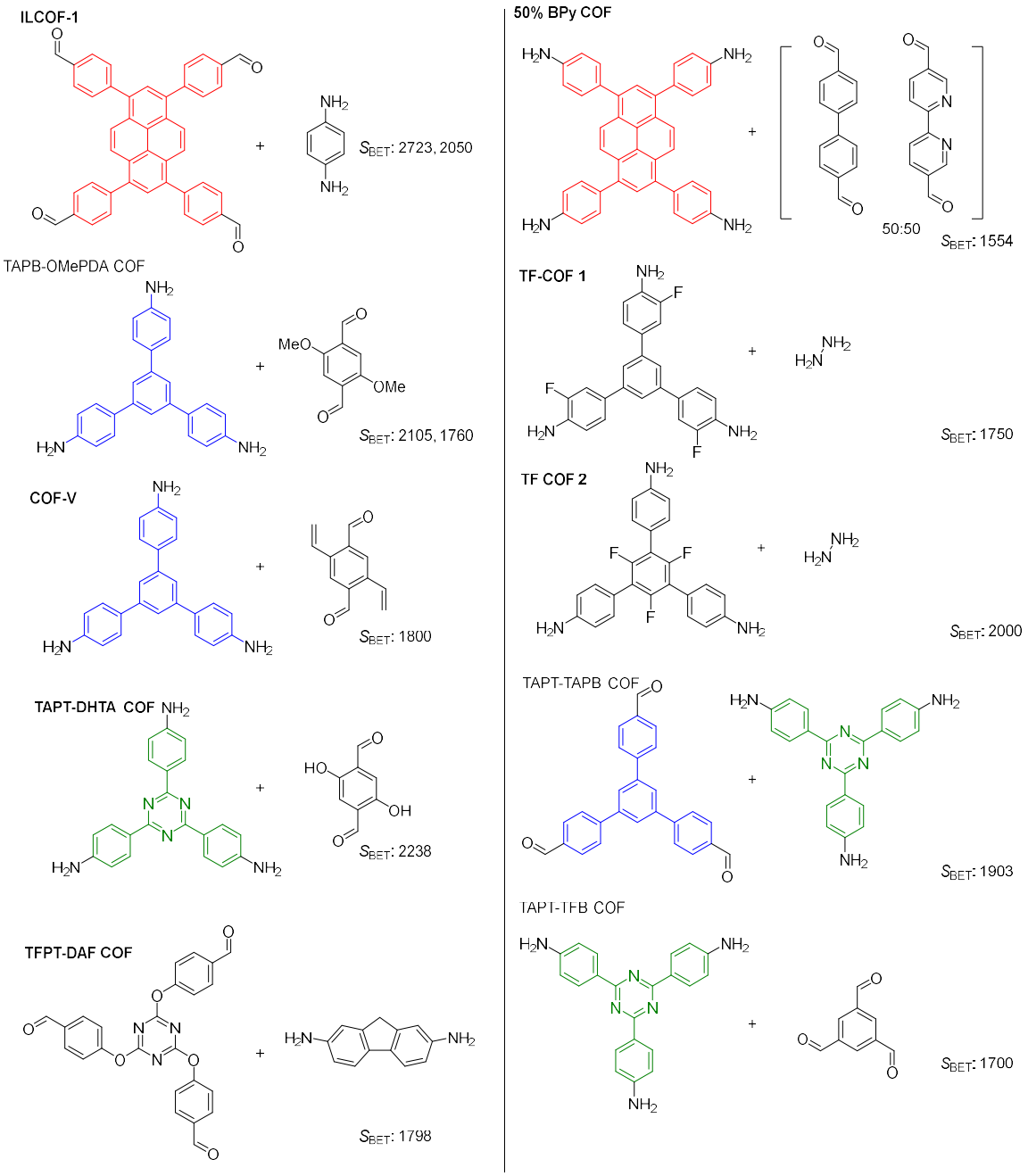


**Figure 2.11: COFs reported with high $S_{BET}$ values (> 1500 $m^2/g$) despite vacuum**

**activation.[17, 20, 32, 45, 47, 57, 63, 72, 87] Common monomer structures are color coded for emphasis.**

Similarly to TAPPy-PDA COF studied in previous sections, ILCOF-1 reported by Rabbani *et al.*, and 50% BPy-COF reported by Zhang *et al.*, shown in Figure 2.11 above, both utilize the pyrene core as a four-armed linker in vacuum-stable COFs with high reported surface areas.[45, 57] Both ILCOF-1 and 50% BPy-COF also utilize linear aromatic linkers, phenylene diamine and a 1:1 mixture of (1,1'-biphenyl)-4,4'-dicarbaldehyde and (2,2'-bipyridine)-5,5'-dicarbaldehyde respectively. [45, 57] Based on the work presented by Auras *et al.*, it is presumed that the same synchronized offset stacking mechanism is active in both pyrene-based COFs and the resulting increased inter-layer interactions may help explain these COFs stability despite vacuum activation.[128]

TAPB-OMePDA COF, which was described in previous sections herein, also appeared twice in this literature examination. Reported by Xu *et al.* with a $S_{BET}$ of 2105 $m^2/g$, and by Li *et al*. with a $S_{BET}$ of 1760 $m^2/g$.[20, 87] These results are similar to the $S_{BET}$ value of 2080 $m^2/g$ found for the 4 hour synthesis of TAPB-OMePDA COF reported in this work, and shows that this COF is reproducibly stable to vacuum activation even when synthesized in different labs via different, albeit similar methods. Two additional COFs that are structurally similar to TAPB-OMePDA COF also appear among the vacuum-stable COFs found in the literature. COF-V was reported by Jiang *et al.* and substitutes 2,5-divinylterephthaldehyde for PDA, yielding a $S_{BET}$ of 1800 $m^2/g$.[32] Additionally, TAPT-DHTA, reported by Mu *et al.,* displays a similar skeletal structure to TAPB-OMePDA

COF, and is composed of tris-1,3,5-(4-aminophenyl)triazine (TAPT), and 2,5-dihydroxyterephthaldehyde (OHPDA).[63] TAPT-DHTA was reported with an $S_{BET}$ of 2238 $m^2/g$.[63] Each of these COFs pairs either TAPT or TAPB, relatively planar 3-armed linkers, with a 2,5-difunctionalized terephthaldehyde derivative. Here similar effects to those reported for TAPB-OMePDA COF by Xu *et al*. are likely responsible for the improved stability of these COFs to vacuum activation compared to TAPB-PDA, which does not have substituents on the terephthaldehyde linker.[20] Xu *et al*. propose delocalization of the partial positive charge induced by the polar imine bond as the reason for improved crystallinity of TAPB-OMePDA COF, which would also be a plausible mechanism for TAPT-DHTA COF, since the oxygen atoms of the hydroxyl groups are similarly resonant with the COF π system.[20] However, this mechanism is also applicable to COF-V with its vinyl substituents, that are also capable of π-donation into the aromatic system. A possible alternative or additional mechanism to charge delocalization could be that the inclusion of substituent groups restricts the ability of COF sheets to easily slide relative to each other, which could also aid in maintaining the COF structure during activation processes. Without the benefit of high-resolution crystal structures, or advanced modeling, this is difficult to examine further.

Two examples of COFs without pyrene's stacking behavior, or stabilizing substituent chains are present in the data set. TAPT-TAPB COF reported by He *et al.* and TAPT-TFB COF reported by Gao *et al.* are both COFs composed of trifunctional planar cores that are isolated with high $S_{BET}$ values after vacuum activation; $S_{BET}$ values are 1900 and 1700 $m^2/g$ respectively.[17, 47] It is possible that the smaller pore structure, as compared to a COF like TAPB-PDA COF, caused by the compact 3+3 hexagonal ring structure imparts additional

rigidity to the COF structure. Additionally, due to the smaller pore structure, there is a larger extent of π-π interaction per unit area of COF sheet, which conceptually agrees with the trend exhibited by pyrene-based imine COFs, where increased π-π interactions due to the stacking behavior appear to impart stability.

An additional strategy employed for the synthesis of more crystalline COFs is fluorination of the building blocks explored by Alahakoon *et al.* with COFs TF-COF 1 and TF-COF 2 reported.[72] These fluorinated COFs show $S_{BET}$ values of 1750 and 2000 $m^2/g$ respectively. [72] In these structures, fluorinated derivatives of TAPB are combined with hydrazine to form a hexagonal covalent organic framework.[72] Empirically, electron deficient aromatic rings are know to prefer face-to-face orientations. [72] This methodology resulted in highly crystalline COFs where each sheet stacks closely to the adjacent COF sheet. Additionally, in a mechanism similar to TAPT-TFB COF and TAPT-TAPB COF, smaller pore sizes relative to the more extended TAPB-PDA COF may impart additional stability due to the exceptionally short hydrazine monomer used as the linear linker in both TF-COF 1 and TF-COF 2. [72]

The final example found was TFPT-DAF COF where a flexible triamine linker combined with diaminofluorene provide a $S_{BET}$ value of 1798 $m^2/g$ STP.[101] Here it is likely that the smaller pore size (1.5 nm), due to the spiral shape adopted by the flexible TFPT core, and potential for extensive π-π stacking interaction between the fluorene linkers both contribute to a vacuum-stable COF.

From all of these literature examples, and the lessons learned from the three COFs studied in the activation experiments, several trends begin to emerge which may be helpful in

specifically designing and selecting monomer systems that will have a tendency to produce highly crystalline, and stable COF systems, which can be easily analyzed and studied. The identified structural features all seem to maximize interlayer interactions between the COF sheets, while minimizing the COF networks potential to shift and rearrange during activation. Two features of the literature COFs stand out; small pore size, and strong π-π interactions between layers.

A recent work by Sick *et al.* also examines COF stability to vacuum, though they rationalized the changes observed as being due to solvent exposure rather than the exposure of the COFs studied to vacuum drying.[127] By examining a series of TAPB-based imine linked COFs they identified COFs that were robust to solvent vapor exposure, and COFs that were sensitive to solvent vapor exposure. Based on the results presented in Section 2.3 of this work however, it is suggested that the changes observed were due to the vacuum drying used to dry the COF between solvent exposure and analysis. [127] Viewing their results through this lens, it is possible to relate the structural features they identified to the literature data presented above, and with the activation studies on TAPB-PDA COF, TAPB-OMePDA COF, and TAPPy-PDA COF. Figure 2.12, below, shows the COFs studied by Sick *et al.*, which were identified as susceptible or robust towards their analysis conditions. [127]

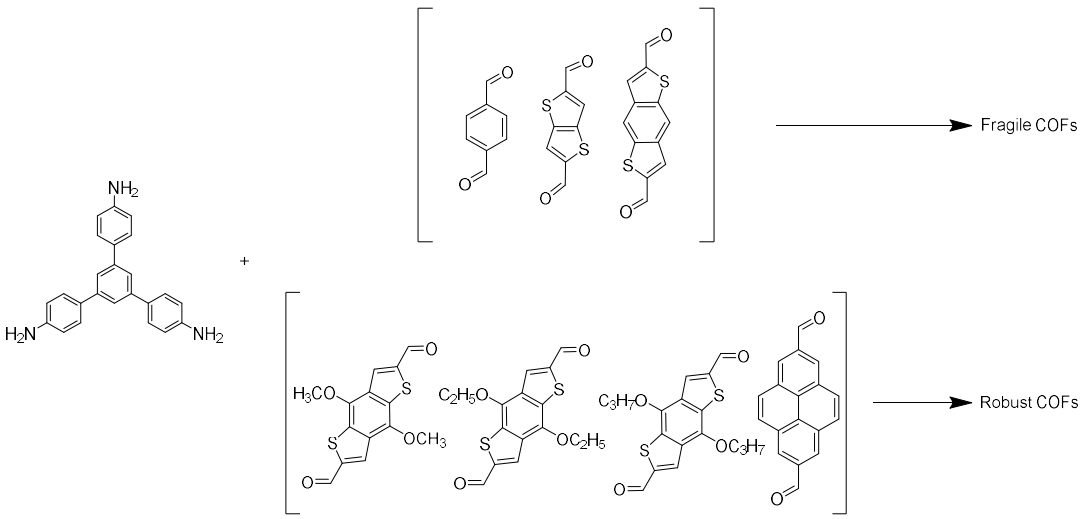


**Figure 2.12: TAPB and linear dialdehyde based COFs studied by Sick *et al.* to determine susceptibility to disruption of COF layers by solvent exposure and subsequent vacuum drying. [127]**

In viewing Figure 2.12, and interpreting the disorder between layers observed by Sick *et al*. after solvent exposure and subsequent vacuum drying, conclusions can be drawn about the activation stability of the TAPB-based COFs that they studied. The TAPB based COFs using terephthaldehyde, thieno(3,2-b)thiophene-2,5-dicarbaldehyde, or benzo(1,2-b:4,5-b')dithiophene-2,6-dicarbaldehyde as linear linkers are not stable to the method of solvent exposure followed by vacuum drying technique used in this work. [127] Their result for TAPB-PDA COF corroborates the observations on TAPB-PDA COF activation presented in Section 2.4. TAPB, with linear aromatic linkers does not appear to offer sufficiently strong interlayer interactions to withstand activation using vacuum. [127]

However, the work by Sick *et al.* does present four COFs that the authors deem robust to solvent exposure, which is here interpreted as the COFs actually being robust towards the vacuum drying method used in this study. Alkoxy-substituted derivatives of benzo(1,2-b:4,5-b')dithiophene-2,6-dicarbaldehyde show improved stability relative to the unsubstituted COF, mirroring the TAPB-PDA and TAPB-OMePDA COFs, which display

the same trend. [127] This result shows that alkoxy substituents could be a reliable avenue for increasing COF stability. The other stable COF they report combines TAPB with pyrene-2,7-dicarbaldehyde, and here the increased π-π interactions between the pyrene linkers in adjacent layers are likely responsible for the increased stability. [127]

To conclude, based on the results presented in Section 2.3, the review of vacuum activation stable COFs in the existing literature, and a reinterpretation of the thorough work by Sick *et al.* clear trends and design motifs for stable COFs emerge. [127] COFs with extensive π-π interactions, mostly utilizing pyrene derived monomers show increased stability. COFs with alkoxy substituents, or other π-donating substituents on the linkers similarly resist vacuum activation. Fluorination was also demonstrated to improve crystallinity after a vacuum activation procedure by Alakahoon *et al*.[72] COFs with small pore sizes, either through the use of two trifunctional cores, or through short linear linkers may also offer improved stability compared to COFs with more expanded pore structures. These findings may be of use to researchers who specifically desire COFs that can be safely activated via vacuum, or need COFs that can be continually reactivated after use as catalysts or separation media.

## 2.7 Regeneration of Imine-Linked COFs Damaged by Vacuum Activation

After observing the degradation of COFs via vacuum activation explored in Section 2.4, an experiment was devised to examine if the degradation observed was reversible to gain insight into the mechanism of degradation. If the COF degradation was fully reversible, then a sheet displacement mechanism such as the one put forth by Sick *et al.* would be more likely. If a pore collapse mechanism, such as has been observed for MOFs was

occurring, then the COF degradation would likely be permanent and irreversible.[127] TAPB-PDA COF, as the most sensitive COF, was the ideal candidate for this experiment.

Vacuum activated TAPB-PDA COF samples isolated from methanol and toluene were rewetted with their respective solvent, then subjected to $scCO_2$ activation. The methanol rinsed sample showed improved crystallinity, and $S_{BET}$ improved from 230 $m^2/g$ to 950 $m^2/g$, indicating that mesoporosity could be partially restored. The toluene-wetted sample showed no change in the PXRD pattern seen in Figure 2.13 below, however, the $S_{BET}$ obtained was 430 $m^2/g$ compared to the initial 250 $m^2/g$. Unlike in the work by Sick *et al.*, we do not observe complete recovery of crystallinity for vacuum damaged COFs.

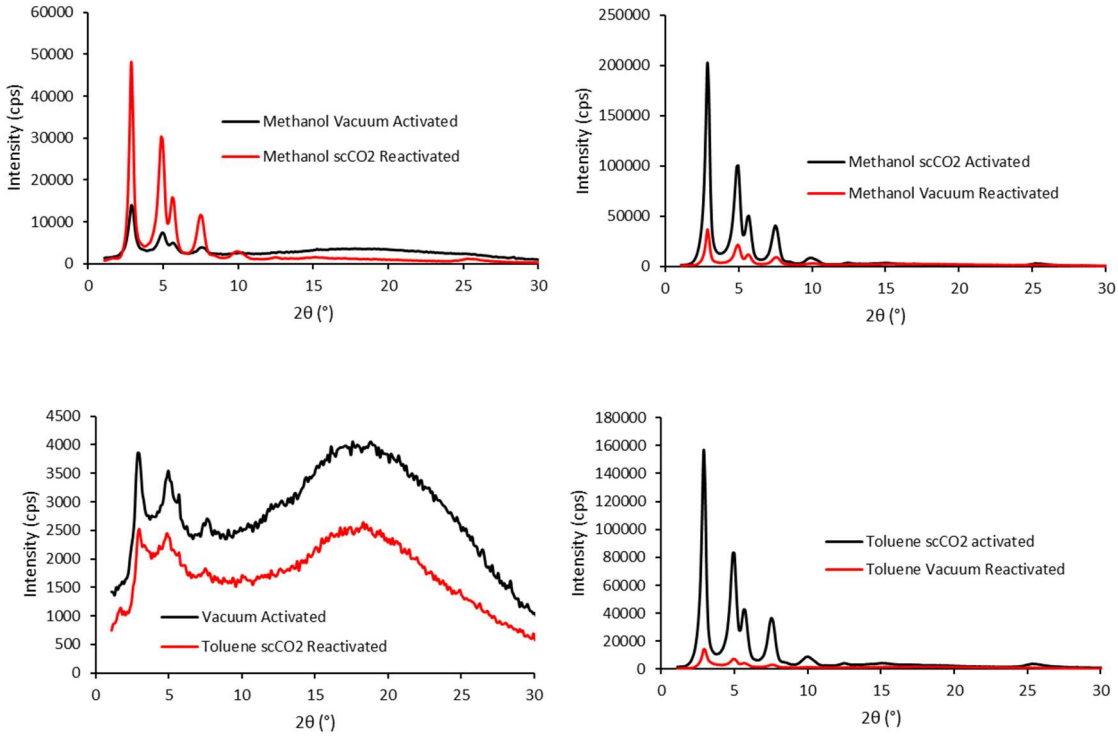


**Figure 2.13: Top Left: PXRD patterns of TAPB-PDA COF rinsed with methanol then vacuum activated (black) then rewetted and reactivated via $scCO_2$ (red). Top Right: TAPB-PDA COF rinsed with methanol then activated with $scCO_2$ (black) then**

**rewetted and reactivated via vacuum (red). Bottom Left: TAPB-PDA COF rinsed with toluene then activated with vacuum (black) then rewetted and reactivated via $scCO_2$ (red). Bottom right: TAPB-PDA COF rinsed with toluene then activated with $scCO_2$ (black) then rewetted and reactivated via vacuum (red).**

Conversely, $scCO_2$-activated TAPB-PDA COFs isolated with high $S_{BET}$ and crystallinity were rinsed again and subjected to vacuum activation. The methanol rinsed, $scCO_2$ activated TAPB-PDA COF showed significant reduction in $S_{BET}$ from 2470 $m^2/g$ to 440 $m^2/g$ after it was reactivated using vacuum. The toluene rinsed, $scCO_2$ activated TAPB-PDA COF showed a similar reduction in $S_{BET}$ from 2890 $m^2/g$ to 330 $m^2/g$ after being subjected to vacuum drying. Nitrogen adsorption/desorption isotherms at 77 K for the methanol rinsed samples are shown below in Figure 2.14

.

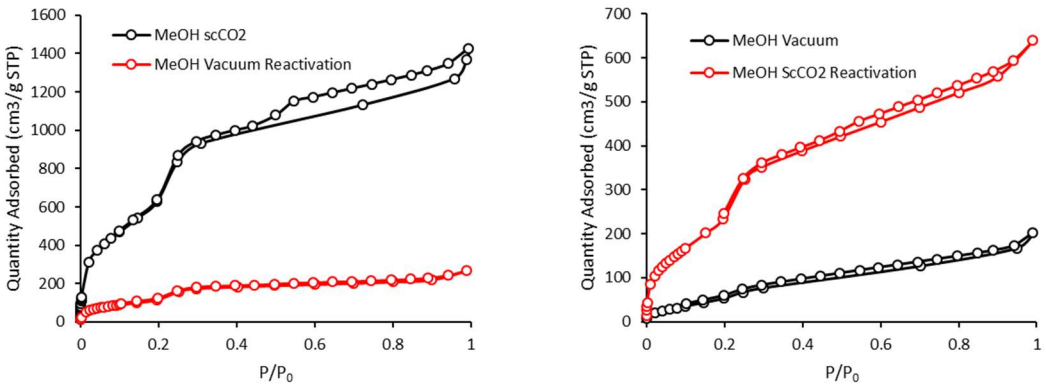


**Figure 2.14: Left: Nitrogen adsorption/desorption isotherm at 77 K for methanol rinsed TAPB-PDA COF initially activated with $scCO_2$ (black) then reactivated via vacuum (red). Right: Nitrogen adsorption/desorption isotherm at 77 K for methanol rinsed TAPB-PDA COF initially activated with vacuum drying (black) then reactivated with $scCO_2$ (red).**

Based on the partial reversibility of the COF disruption caused by vacuum activation it is possible that a pore collapse mechanism is occuring, which could be partially reversible when the COF is resubjected to $scCO_2$ activation conditions. It is also possible that both pore collapse and sheet displacement are occuring, and the portion of COF degradation due to pore collapse is irreversible, while the portion due to sheet displacement is reversible, leading to the observation of incomplete recovery of crystallinity and porosity.

## 2.8 Examining the Effects of Activation Method on the Porosity and Crystallinity of Non-Imine COFs

After demonstrating that vacuum activation can have detrimental effects on the porosity and crystallinity measured for susceptible imine COF species, the question remained of whether other COF linkage chemistries were similarly affected. Additionally, the question remained if this phenomenon is endemic to two dimensional COFs, or if three dimensional COFs are equally susceptible. To this end an effort was made to generalize these findings to other COF classes.

### *2.8.1 Examining the Effects of Activation Methods on a Beta-Keto Enamine-Linked Covalent Organic Framework*

Beta-keto enamine COFs are similar to imine COFs, but are linked via an enamine rather than an imine. The most common monomer yielding beta-keto enamine COFs is triformylphloroglucinol (TFP), a three-fold symmetric monomer which reacts initially to

form an imine linkage, then tautomerizes to a stable enamine COF. The specific COF tested was the so called TAPB-TFP COF reported by Daugherty *et al.*, where it was polymerized both directly, and through a linker exchange method.[85] The COF structure is shown below in Figure 2.15. The linker exchange method reported by Vitaku *et al.* yields a higher quality COF based on the measured $S_{BET}$, but since the purpose of this series of experiments is to compare the effects of $scCO_2$ activation, vacuum activation and nitrogen flow activation, the simpler direct condensation is employed.

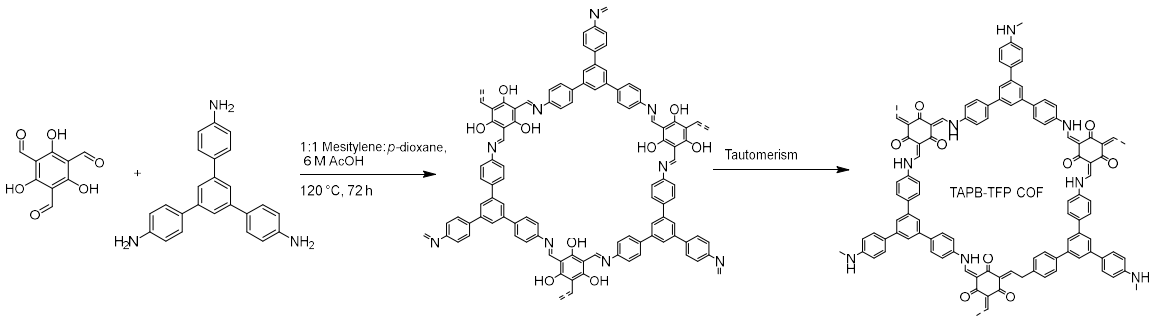


**Figure 2.15: TAPB-TFP COF synthesis and structure.**

Three samples of TAPB-TFP were prepared according to the literature method. Similar to earlier experiments presented in Section 2.3, prior to activation each COF sample was split into two halves. In this case, the effect of nitrogen flow activation was tested as well, therefore the samples were split as shown in Table 2.3, below. This experimental method yielded two vacuum activated samples, two $scCO_2$ activated samples, and two $N_2$ flow

activated samples, which were all analyzed via PXRD while one sample of each type was analyzed using $N_2$ adsorption/desorption.

**Table 2.3: Sample division for TAPB-TFP activation experiment**

| COF Reaction | COF Samples | Activation Method |
|---|---|---|
| CF-III-111-A (TAPB-TFP COF) | CF-III-111-A1 | $scCO_2$ |
| | CF-III-111-A2 | Vacuum |
| CF-III-111-B (TAPB-TFP COF) | CF-III-111-B1 | $scCO_2$ |
| | CF-III-111-B2 | $N_2$ Flow |
| CF-III-111-C (TAPB-TFP COF) | CF-III-111-C1 | Vacuum |
| | CF-III-111-C2 | $N_2$ Flow |

The six samples were analyzed via PXRD producing the patterns shown below in Figure 2.16. The PXRD patterns obtained show material crystallinity somewhere between the two methods reported by Daugherty *et al.*; the samples synthesized here show more crystallinity

than the directly condensed COFs reported, but are more amorphous than those that Daugherty *et al.* obtained with their reported monomer exchange method. The PXRD patterns show roughly similar PXRD patterns for all activation methods, showing that the beta-keto enamine linked COF does not demonstrate the same vacuum activation sensitivity as TAPB-PDA COF.

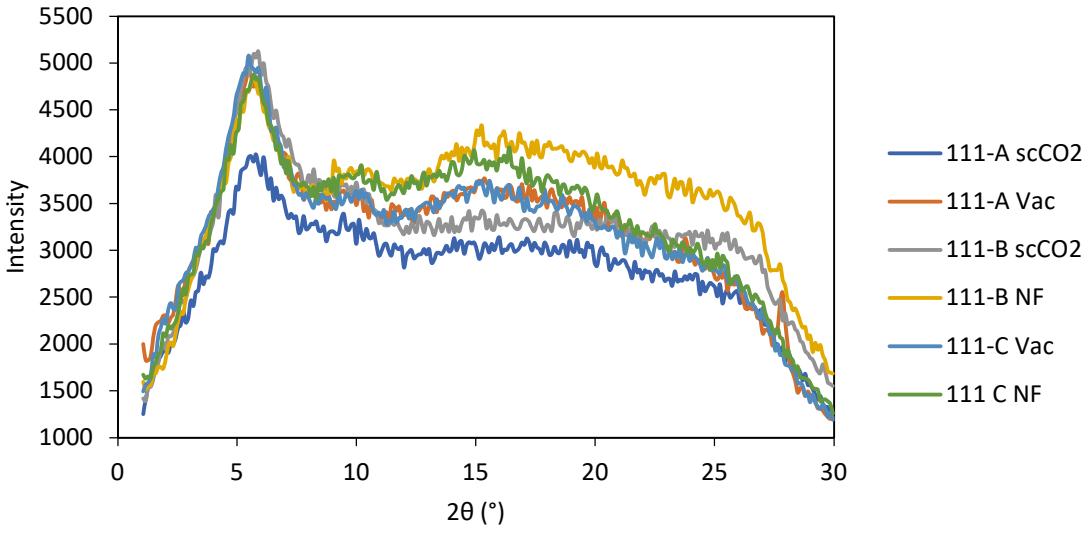


**Figure 2.16: PXRD patterns for TAPB-TFP COF samples activated using $scCO_2$, vacuum and $N_2$ flow methods.**

A representative sample of each activation type was also analyzed by $N_2$ adsorption/desorption, the isotherms for which are shown below in Figure 2.17, while the calculated $S_{BET}$ values are shown below in Table 2.4.

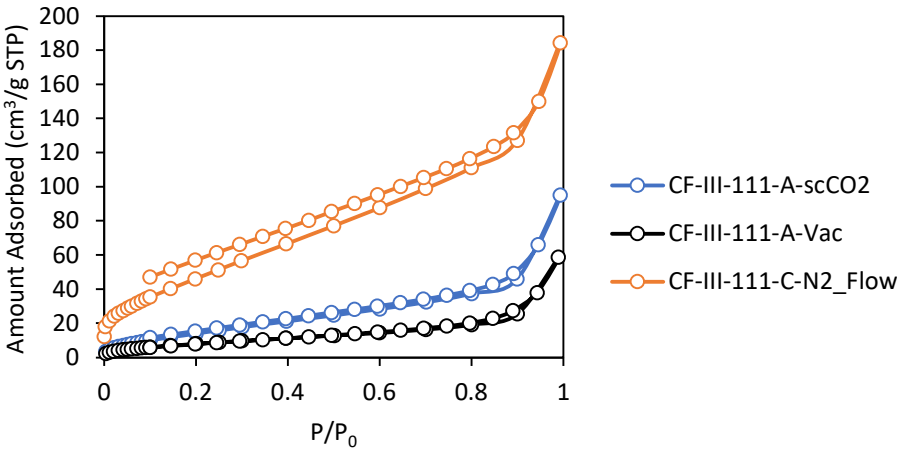


**Figure 2.17: $N_2$ adsorption/desorption isotherms for TAPB-TFP COF samples activated using $scCO_2$ activation, vacuum activation and $N_2$ flow activation.**

**Table 2.4: Measured $S_{BET}$ values for TAPB-TFP COF samples activated using scCO2 activation, vacuum activation and $N_2$ flow activation.**

| Activation Method | $scCO_2$ | Vacuum | $N_2$ Flow |
|---|---|---|---|
| Sample | CF-III-111-A1 | CF-III-111-B2 | CF-III-111-C2 |
| $S_{BET}$ ($m^2/g$) | 59.1797 ± 1.0929 $m^2/g$ | 32.1125 ± 0.2885 $m^2/g$ | 184.9440 ± 2.2165 $m^2/g$ |

The $S_{BET}$ values obtained for the TAPB-TFP COF samples show a different trend than the PXRD patterns obtained for TAPB-TFP COF. The nitrogen-flow activated sample showed a higher measured $S_{BET}$ of 185 $m^2/g$. $ScCO_2$ and vacuum activation provided low measured $S_{BET}$ values of 59 $m^2/g$ and 32 $m^2/g$ respectively. The pore size distributions were calculated for these COF samples, and show a very broad distribution of pore sizes consistent with a more amorphous material, which agrees well with the low $S_{BET}$ values and the severely

broadened diffraction signals in the PXRD patterns. The pore size distributions for the TAPB-TFP COF samples are shown below in Figure 2.18.

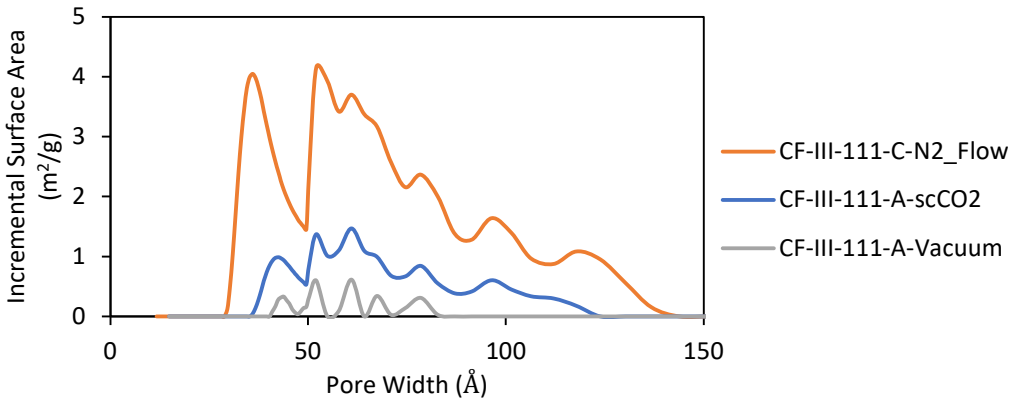


**Figure 2.18: Pore size distributions for TAPB-TFP COF samples activated with $scCO_2$, vacuum and nitrogen-flow activation.**

Based on the data presented here it can be concluded that vacuum activation and $scCO_2$ activation do not differ significantly in the quality of the COF material obtained, while nitrogen flow activation may show some advantages for this class of COFs. This result is drawn predominantly from the obtained PXRD data, which provided similar patterns for all COF samples. The materials obtained here all show lower measured $S_{BET}$ values compared to the 815 $m^2/g$ surface area reported for direct-condensation synthesized TAPB-TFP COF reported by Daugherty *et al.* The difference in surface area may be due to the differences in COF rinsing, here a simple rinse with methanol was employed to maintain consistency with the previously tested imine COF samples in Section 2.3, while in the literature procedure reported by Daugherty *et al.* and extensive rinsing procedure using hot

DMF, followed by hot acetone and hot ethanol is used to rinse the COF prior to vacuum activation. Despite the high reported surface area, the PXRD pattern reported for TAPB-TFP COF shows a less distinct diffraction signals that the PXRD patterns obtained here. Based on the results obtained here, and the reports of high surface area beta-keto enamine COFs activated using vacuum methods reported by Vitaku *et al.* and others, it is evident that beta-keto enamine-linked COFs are not as susceptible to degradation during vacuum activation as some imine-linked COFs.

### *2.8.2 Examining the Effects of Activation Methods on an Azine-Linked Covalent Organic Framework*

Azine linkages, shown below in Figure 2.19 below, can be formed through the condensation of hydrazine with a ketone or aldehyde. Azine-linked COFs have been reported, but the effects of various activation methods on the porosity and crystallinity of the activated COF materials have never been studied. HCOF-1, shown below in Figure 2.19, reported by Lu *et al.* was selected as an example of an azine-linked COF for this experiment.[129] Despite utilizing the same trifunctional TFP node as TAPB-TFP COF, HCOF-1 is not shown to display the same irreversible tautomerism as TAPB-TFP COF. Instead, Lu *et al.* report that the ATR-FTIR spectrum of the COF is consistent with the coexistence of both tautomers. HCOF-1 is shown in the imine form in Figure 2.19.

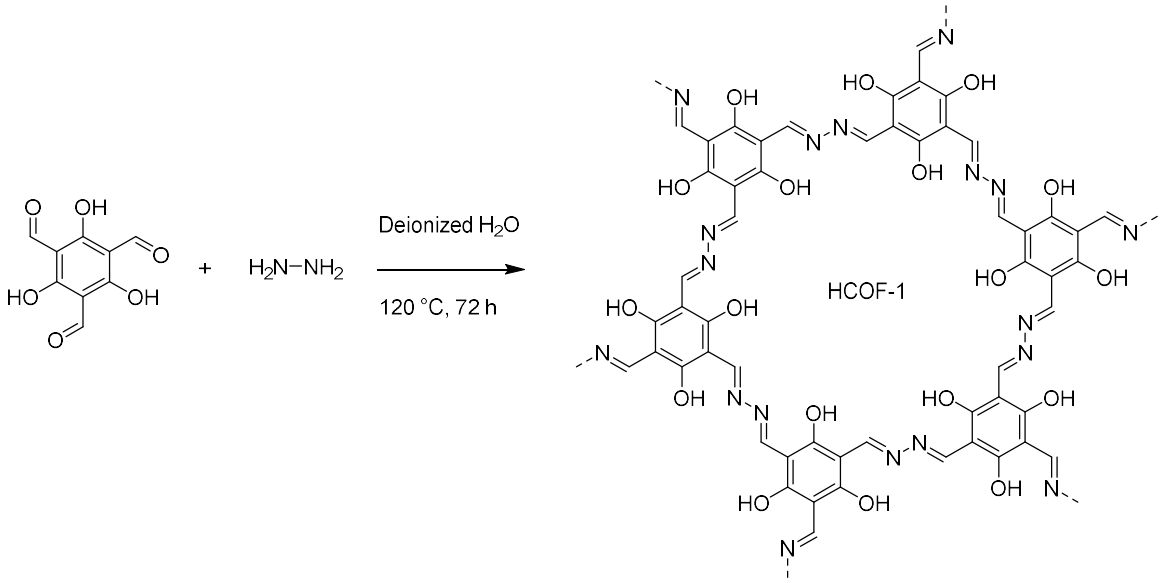


**Figure 2.19: Synthesis method and structure of HCOF-1**

The experimental design is identical to the experiment testing the activation of HCOF-1 in Section 2.8.1. Six samples of HCOF-1 were synthesized according to the method reported by Lu *et al.* then activated using identical conditions to the imine COFs examined in Section 2.3. Samples were divided according to the same method as Section 2.8.1, resulting in the samples shown below in Table 2.5 below.

**Table 2.5: Sample division for HCOF-1 activation experiment**

| COF Reaction | COF Samples | Activation Method |
|---|---|---|
| CF-III-112-A (HCOF-1) | CF-III-112-A1 | $scCO_2$ |
| | CF-III-112-A2 | Vacuum |
| CF-III-112-B (HCOF-1) | CF-III-112-B1 | $scCO_2$ |
| | CF-III-112-B2 | $N_2$ Flow |
| CF-III-112-C (HCOF-1) | CF-III-112-C1 | Vacuum |
| | CF-III-112-C2 | $N_2$ Flow |

PXRD patterns, which are shown below in Figure 2.20, were obtained for the six HCOF-1 samples. The PXRD patterns obtained for all six samples are consistent with the reported PXRD pattern for HCOF-1. The (100) peak intensities, used previously to assess the crystallinity of imine-linked COFs in Section 2.3 show that the vacuum activated samples show approximately 75% of the diffraction intensity of the $scCO_2$-activated samples and the nitrogen-flow activated samples.

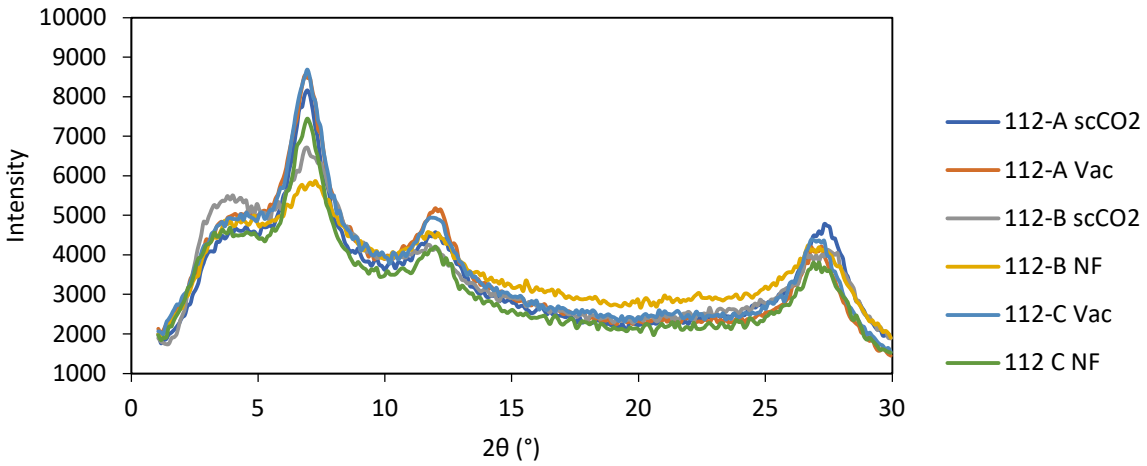


**Figure 2.20: PXRD patterns for TFP-Hydrazine COF samples activated using $scCO_2$, vacuum and $N_2$ flow methods.**

A representative sample of each activation method was analyzed by $N_2$ adsorption/desorption, the isotherms from which are shown below in Figure 2.21, and the measured $S_{BET}$ values obtained are shown below in Table 2.6.

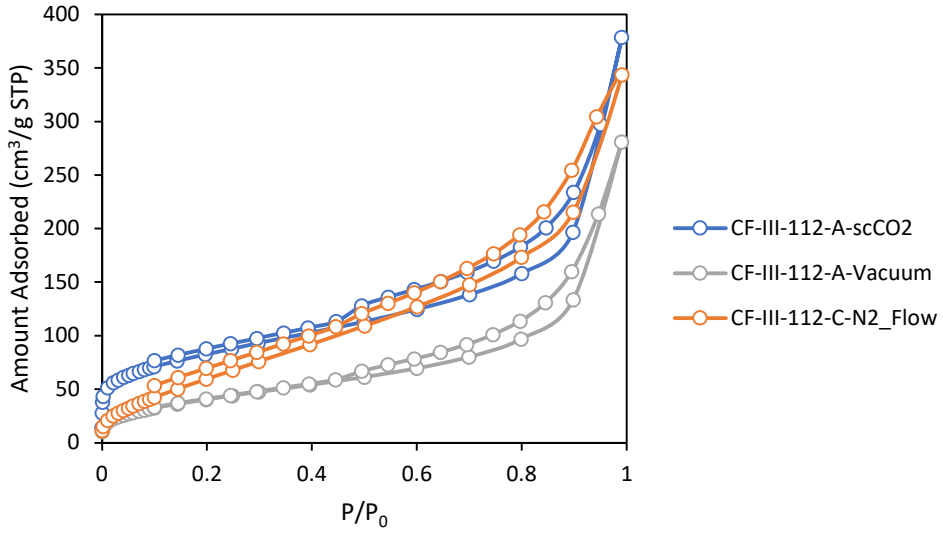


**Figure 2.21: $N_2$ adsorption/desorption isotherms for TFP-Hydrazine COF samples activated using $scCO_2$ activation, vacuum activation and $N_2$ flow activation.**

**Table 2.6. Measured $S_{BET}$ values for HCOF-1**

| Activation Method | $scCO_2$ | Vacuum | $N_2$ Flow |
|---|---|---|---|
| Sample | CF-III-112-A1 | CF-III-112-B2 | CF-III-112-C2 |
| $S_{BET}$ ($m^2/g$) | 290.8108 ± 1.8854 m²/g | 152.4511 ± 0.5703 m²/g | 259.1837 ± 4.7505 m²/g |

The measured $S_{BET}$ values for the HCOF-1 samples are lower than the 617 $m^2/g$ value reported by Lu *et al.* Similarly to TAPB-TFP COF presented earlier, this may be due to differences in the rinsing method. In the method reported by Lu *et al.* the filtered solid from the HCOF-1 reaction is rinsed with anhydrous 1,4-dioxane, while here the COF was rinsed with methanol for consistency with the imine-linked COF activation trials presented in Section 2.3. However, despite the lower than reported $S_{BET}$ measurements, a trend is evident in the data; the vacuum activated sample of HCOF-1 shows 52% of the surface area of the $scCO_2$ activated HCOF-1 sample, 152 $m^2/g$ as compared to 291 $m^2/g$. The nitrogen flow activated sample $S_{BET}$ was 260 $m^2/g$, indicating that this method was nearly as effective as $scCO_2$ activation. Pore size distributions for the HCOF-1 samples were calculated, and are shown below in Figure 2.22.

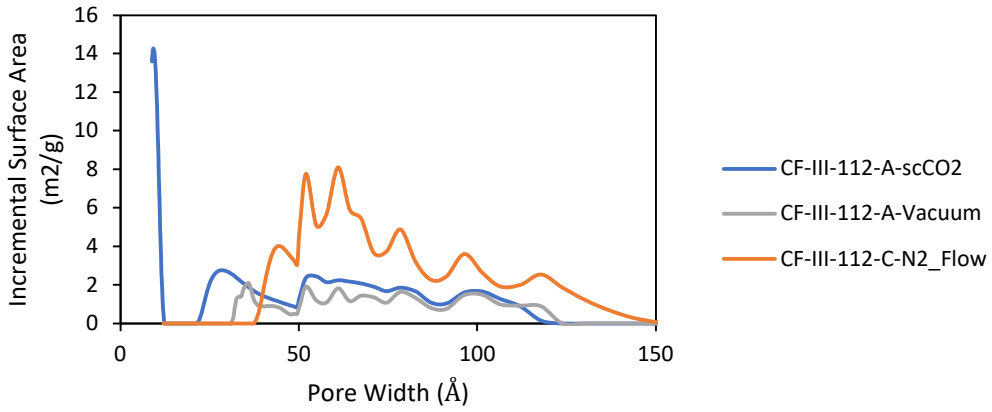


**Figure 2.22: Pore size distributions for HCOF-1 samples activated with $scCO_2$, vacuum, and nitrogen-flow activation.**

The pore size distributions show that only the $scCO_2$ activated sample has any pore volume corresponding to the 10.2 Å pore size measured by Lu *et al.* for HCOF-1. The pore size distributions here show a significant number of pores large than the expected pore size of the COF, which is consistent with the lower measured surface areas obtained for these samples.

These results indicate that azine linked COFs such as HCOF-1 may behave more similarly to imine-linked COFs during vacuum activation that beta-keto enamine COFs. HCOF-1 shows some degree of susceptibility to degradation during vacuum activation based on the lower measured surface area for the vacuum activated sample. Similarly to TAPB-PDA COF, nitrogen-flow activation is nearly as effective as $scCO_2$ activation, and may be a suitable substitute if $scCO_2$ equipment is unavailable for COF activation. Lu *et al.* do not

report a theoretical Conolly surface area for HCOF-1, so it is unknown how the $S_{BET}$ obtained for HCOF-1 in their work compares to the theoretical surface area of the COF.

### *2.8.3 Examining the Effects of Activation Methods on a Boroxine-Linked Covalent Organic Framework*

Boroxine linked COFs were the first COF linkage motif to be reported in 2005 by Côte *et al.*[1] This class of COFs, which can be produced through the condensation of boronic acids alone or with a boronic acid and a diol differ significantly from imine COFs in the hydrolytic stability of the COF. COF-1, produced by the self-condensation of 1,4-benzene diboronic acid (BDBA), and shown below in Figure 2.23 was selected as an example of a boroxine-linked COF for testing the effects of different activation methods on this type of COF.

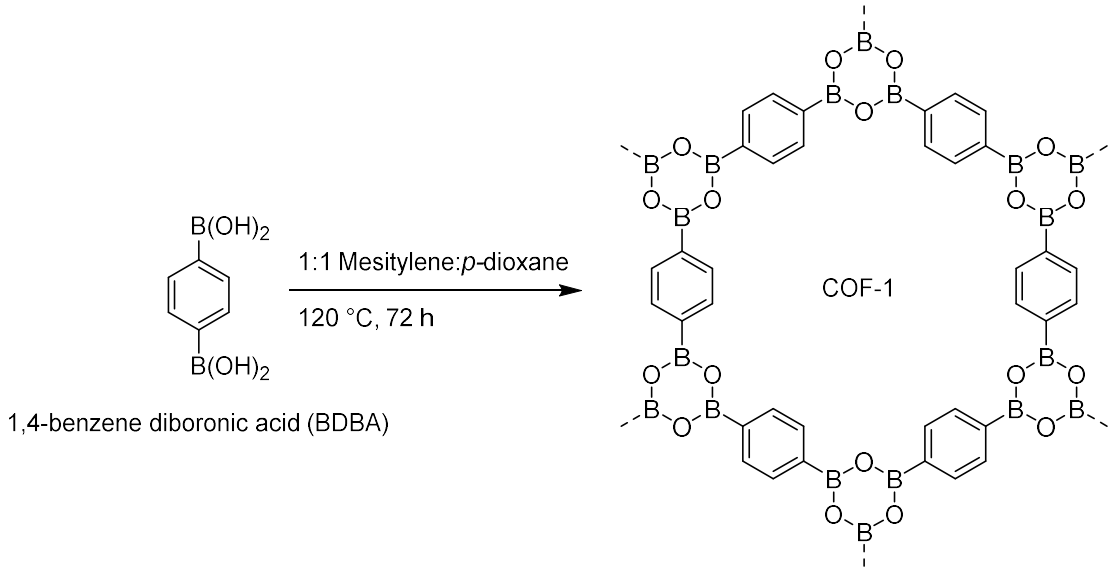


**Figure 2.23: Synthesis conditions and structure of COF-1**

The literature method reported in the seminal work on COFs was used to synthesize three identical samples of COF-1. Samples were divided according to the same method as Section 2.8.1, resulting in the samples shown below in Table 2.7. A significant difference between this experiment, and the activation experiments for the imine, azine, and beta-keto enamine COFs previously presented is the use of acetone as the transfer solvent for $scCO_2$ activation. This is due to the susceptibility of boroxine COFs to degradation in protic solvents such as methanol, which is used as the transfer solvent for $scCO_2$ for all other COFs tested.

**Table 2.7: Sample division for COF-1 activation experiment**

| COF Reaction | COF Samples | Activation Method |
|---|---|---|
| CF-III-110-A (COF-1) | CF-III-110-A1 | $scCO_2$ (acetone) |
| | CF-III-110-A2 | Vacuum |
| CF-III-110-B (COF-1) | CF-III-110-B1 | $scCO_2$ (acetone) |
| | CF-III-110-B2 | $N_2$ Flow |
| CF-III-110-C (COF-1) | CF-III-110-C1 | Vacuum |
| | CF-III-110-C2 | $N_2$ Flow |

PXRD patterns, which are shown below in Figure 2.24, were obtained for the six COF-1 samples. The measured PXRD patterns agree very well with literature, except for the peak located at 4.3 °θ which is not within the 2θ range shown in the PXRD pattern reported by Côte *et al.* This peak corresponds to a larger d-spacing than is calculated for COF-1, and its origin is not known. However, the (100) and (110) peaks of COF-1 are quite distinct. The (100) peak in the PXRD patterns for the nitrogen-flow activated COF-1 samples are significantly more intense than either the vacuum-activated or $scCO_2$ activated samples.

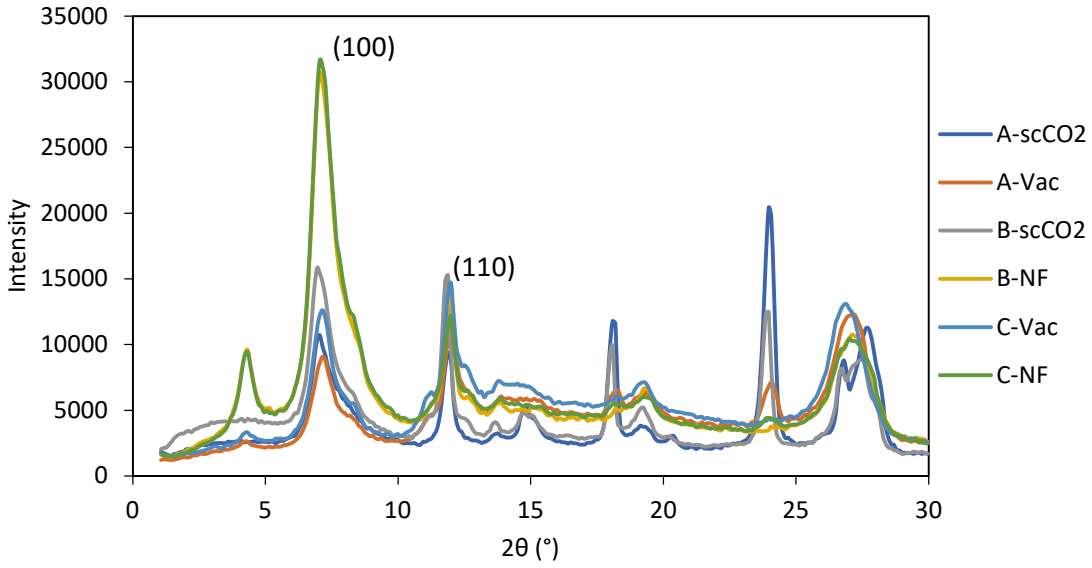


**Figure 2.24: PXRD patterns for COF-1 samples activated using $scCO_2$, vacuum and $N_2$ flow methods.**

A representative sample for each activation method was analyzed by $N_2$ adsorption/desorption, resulting in the isotherms shown below in Figure 2.25. The $S_{BET}$ values for these COF samples are shown below in Table 2.8.

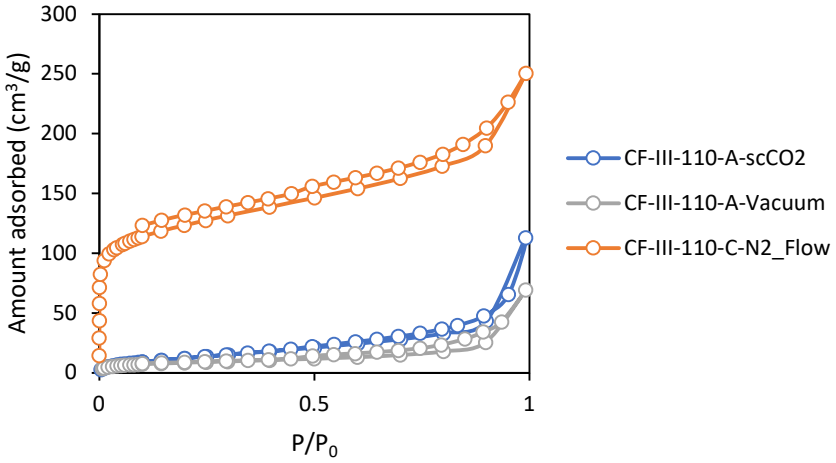


**Figure 2.25: $N_2$ adsorption/desorption isotherms for COF-1 samples activated with $scCO_2$, vacuum, and nitrogen-flow activation.**

**Table 2.8. Measured $S_{BET}$ values for COF-1**

| Activation Method | $scCO_2$ | Vacuum | $N_2$ Flow |
|---|---|---|---|
| Sample | CF-III-110-A1 | CF-III-110-B2 | CF-III-110-C2 |
| $S_{BET}$ ($m^2/g$) | 49.8978 ± 0.6452 $m^2/g$ | 29.9824 ± 0.2288 $m^2/g$ | 402.5091 ± 6.6574 $m^2/g$ |

Only the isotherm and $S_{BET}$ for the nitrogen-flow activated COF-1 sample compare favorably to the reported literature values from Côte *et al.* It is likely that the room-

temperature vacuum activation used resulted in effective removal of the acetone used to rinse the COF, but would not have been able to remove residual water as effectively as the 150 °C method reported by Côte *et al.* In a similar manner, super critical $CO_2$ can dissolve some amount of water throughout the temperature range utilized for $scCO_2$ activation. It seems that while $scCO_2$ activation is effective at removing residual water, it may not be able to purge the residual water away from the sensitive COF-1 structure rapidly enough to prevent hydrolysis of the framework. Here it seems that the hydrolytic stability of the COF was the driving factor in the efficacy of the activation method, rather than any structural change induced in the COF itself. The nitrogen flow activation method used here uses dry, high purity nitrogen, and elevated temperatures to activate the COF, and is the most effective method presented here. The pore size distributions measured for the three COF-1 samples, shown below in Figure 2.26, show that only the nitrogen-flow activated sample shows pore sizes consistent with COF-1.

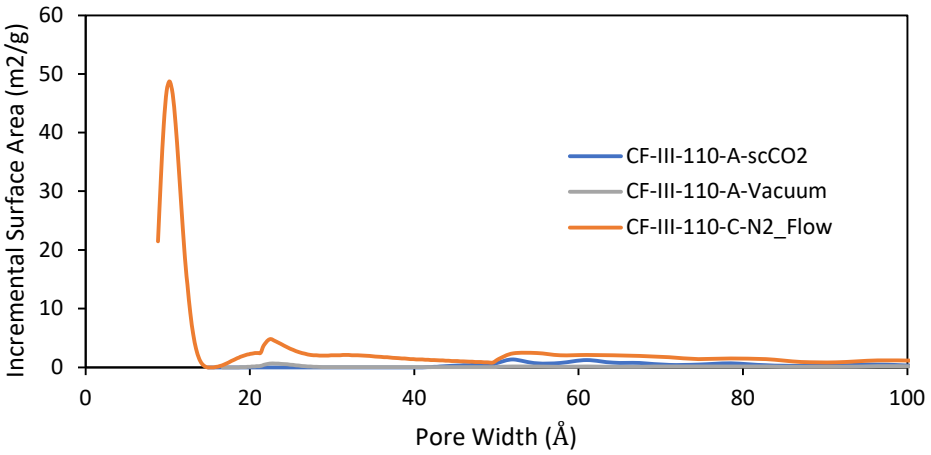


**Figure 2.26: Pore size distributions for COF-1 samples activated using $scCO_2$, vacuum, and nitrogen-flow activation.**

For sensitive boroxine COFs it seems that the activation method employed must remove residual water from the COF system as rapidly and thoroughly as possible in order to prevent hydrolysis of the framework. Through this work it is found that initial attempts at $scCO_2$ activation of the boroxine-linked COF-1 are unsuccessful. Through examination of the literature additional insight can be gained for another boronic ester-linked COF, COF-5 shown below in Figure 2.27.

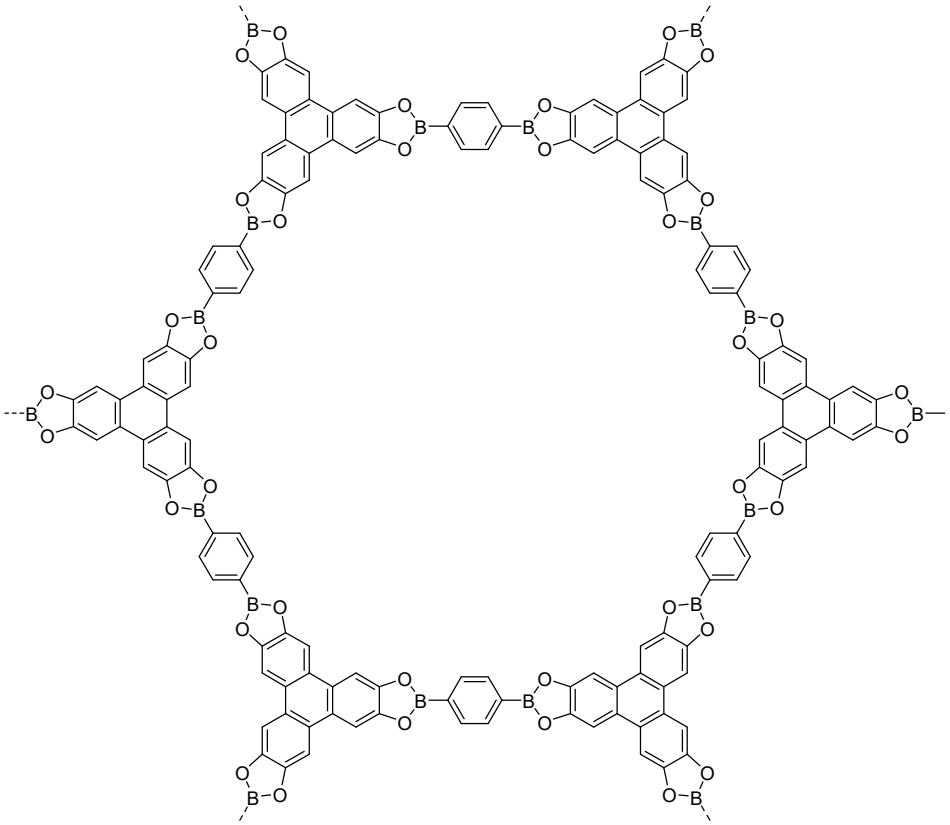

**Figure 2.27: Structure of COF-5[1]**

This COF was reported alongside COF-1 by Côte *et al.*, where it was activated via vacuum at 150 °C. The $S_{BET}$ reported for COF-5 activated in this way was 1590 $m^2/g$.[1] Later, Castano *et al.* reported the synthesis of single crystal COF-5 nanoparticles through a nucleation suppression technique.[130] These single crystal particles were vacuum activated prior to nitrogen adsorption/desorption measurements, which showed a $S_{BET}$ of 1990 $m^2/g$ which compares exceptionally well to the 2000 $m^2/g$ theoretical surface area for COF-5 also reported by Castano *et al.* in the same work.[130] Using this pair of reported values for COF-5, it can be concluded that COF-5 is not distorted by vacuum activation.

## 2.9 Generalizable Rapid Synthesis of Two-Dimensional Imine-Linked COFs Made Possible by Gentle Activation Methods

The realization that $scCO_2$ drying is significantly gentler for imine-linked COF activation allows for more insight into various areas of imine-linked COF synthesis due to the lower amounts of structural distortion occurring during COF activation. One area where this is applicable is in the rapid synthesis of COF materials. By utilizing $scCO_2$ drying instead of vacuum activation, TAPB-PDA COF can be isolated as a crystalline material after only four hours, far faster than the 72 hour synthesis methods that had been previously reported.[3] The use of $scCO_2$ drying to isolate other TAPB-based COFs as crystalline, high surface area materials after four hours was examined, shown in Figure 2.28, below.

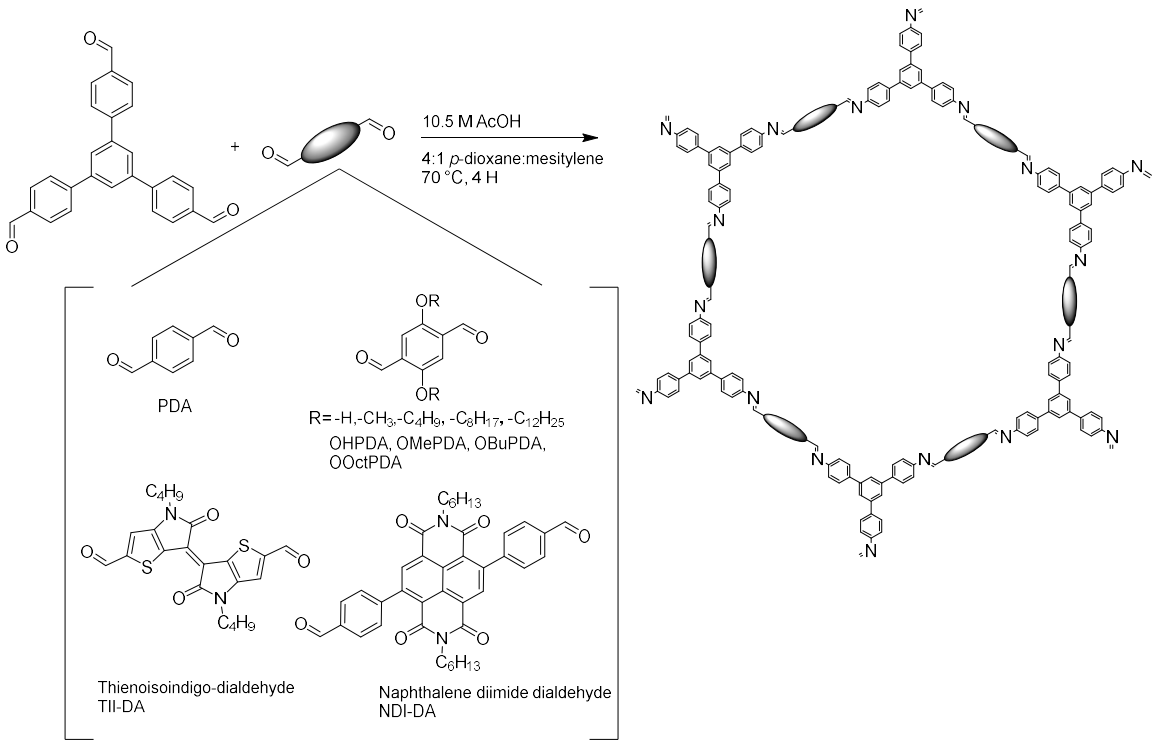


**Figure 2.28: TAPB-based COF materials synthesized in four hours using acetic acid catalysis followed by scCO$_2$ activation.**

TAPB-PDA COF and TAPB-OMePDA COF were previously presented in Section 2.3 where their activation behavior was investigated. As described in Section 2.3, TAPB-PDA COF and TAPB-OMePDA COF were successfully synthesized in 4 hours with $S_{BET}$ values of 2340 and 2080 m$^2$/g STP respectively. Additional 2,5-dialkoxy substituted COFs were synthesized using 2,5-dibutoxyterephthaldehyde (OBuPDA) and 2,5-dioctyloxyterephthaldehyde (OOctPDA). TAPB-OBuPDA COF and TAPB-OOctPDA COF showed crystalline PXRD patterns shown in Figure 2.29 below, and $S_{BET}$ values of 2060 and 490 m$^2$/g. Note that the inclusion of the long octyloxy chains inside the COF pores restricts the volume available for gas adsorption, and thus lowers the accessible surface area; For TAPB-OOctPDA COF, the intensity of the diffraction in the PXRD

pattern is a better gauge of COF crystallinity than a high measured $S_{BET}$. A hydroxyl functionalized COF was synthesized using 2,5-dihydroxyterephthaldehyde (OHPDA) which resulted in a crystalline PXRD pattern, shown in Figure 2.16, and a $S_{BET}$ value of 950 $m^2/g$ STP.[23] This result shows that for alkoxy and hydroxyl substituted TAPB-Based COFs, the four-hour synthesis method presented produces crystalline materials.

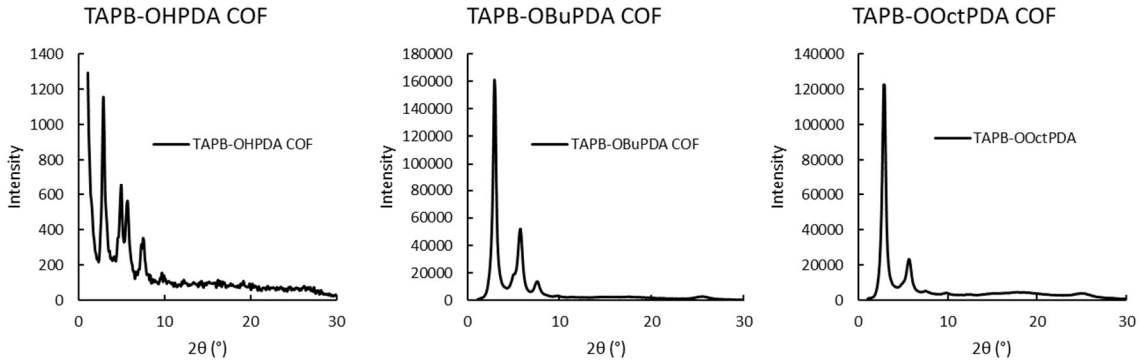


**Figure 2.29: Left; PXRD of TAPB-OHPDA COF, Center: PXRD of TAPB-OBuPDA COF, Right: PXRD of TAPB-OOctPDA COF.**

A TAPB based COF with a more exotic linear naphthalene diimide (NDI) based linker was also explored while investigating the generalizability of the four-hour synthesis method presented. NDI derived molecules and polymers have been studied as electronically active materials.[131] This particular COF has was studied as an electrode material for lithium ion batteries, and as a capacitive material in a work currently in preparation for publication. TAPB-NDI-DA COF, shown in Figure 2.15, was successfully synthesized in four hours and the characterization data is shown in Figure 30 below. This COF displayed $S_{BET}$ values of 1200 $m^2/g$ STP, and the 77 K $N_2$ adsorption/desorption isotherm is shown in Figure 2.30 below. This result shows that the four-hour synthesis method presented here is also applicable to larger aromatic linkers in addition to the simpler terephthaldehyde-derived linkers.

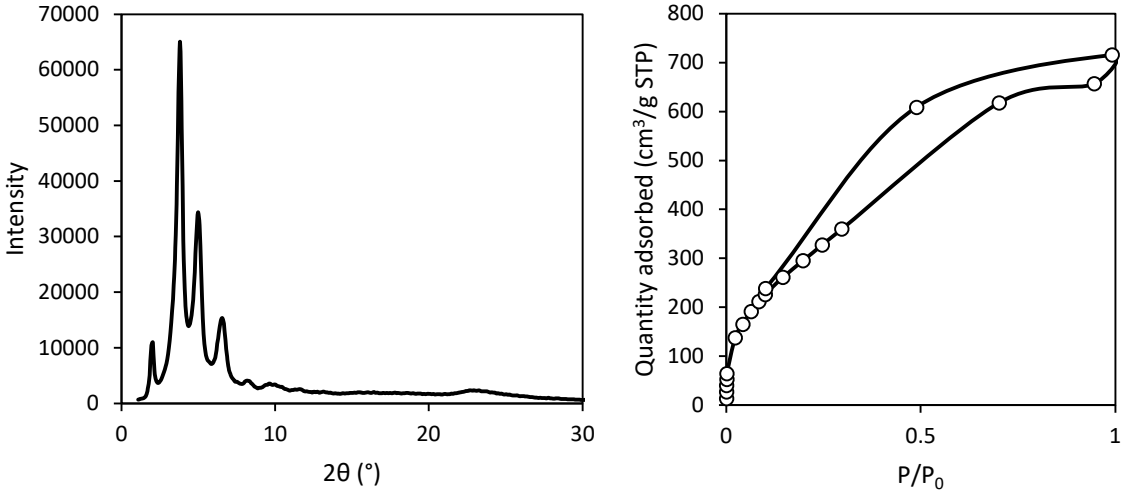


**Figure 2.30: Left: PXRD pattern of TAPB-NDI-DA COF synthesized in four hours followed by $scCO_2$ activation. Right: 77 K $N_2$ adsorption/desorption isotherm of TAPB-NDI-DA COF.**

In addition to TAPB based COFs, two additional pyrene-based COFs were examined to see if the four-hour method was generalizable across different amine core monomers. The

TAPPy-NDI-DA COF shown in Figure 2.31 below, was synthesized in four hours using a slightly modified acetic acid synthesis method to account for the lower monomer solubility. Additionally, TAPPy-TII COF, also shown in Figure 2.31 below was also synthesized successfully using the four-hour method.

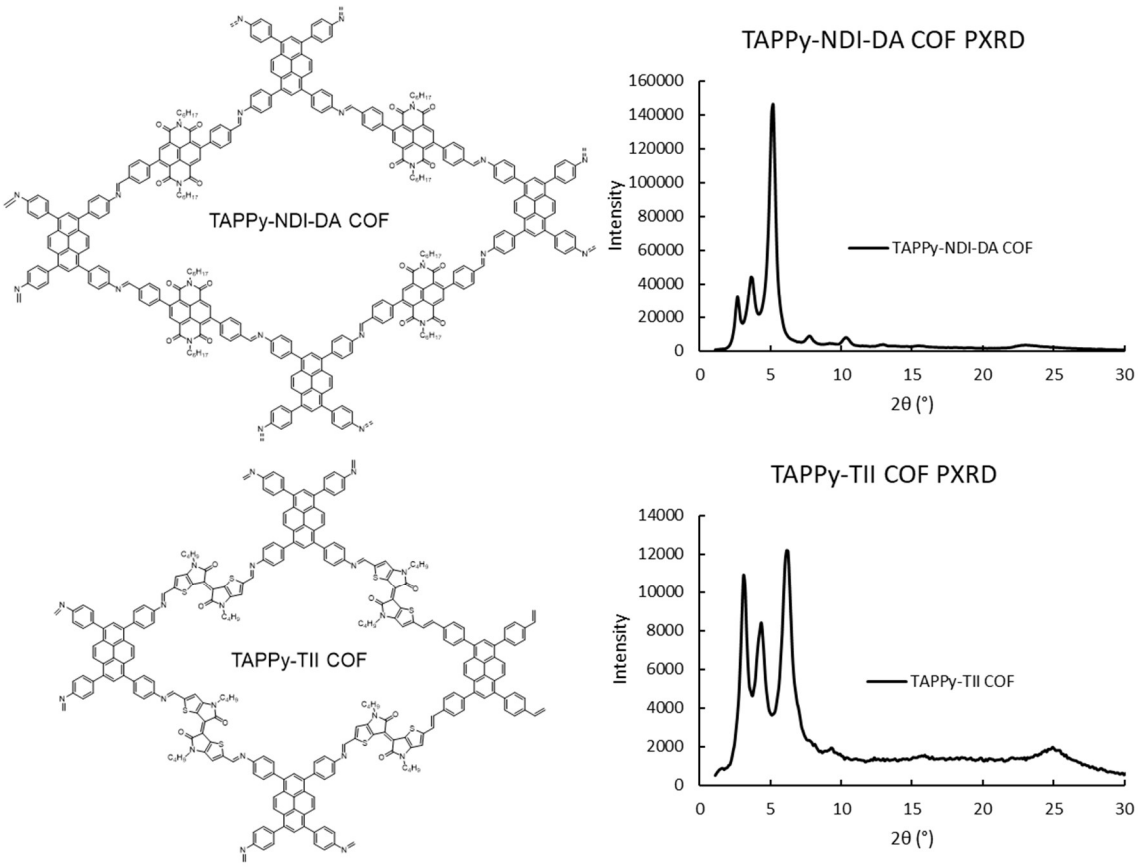


**Figure 2.31: Top Left: Structure of TAPPy-NDI-DA COF. Top Right: PXRD pattern of TAPPy-NDI-DA COF synthesized in four hours followed by scCO₂ activation. Bottom Left: Structure of TAPPy-TII COF. Bottom Right: PXRD pattern of TAPPy-TII COF synthesized in four hours followed by scCO₂ activation.**

## 2.10 Chapter Conclusion

Three imine-linked 2D COFs were examined thoroughly to determine the effects of vacuum and $scCO_2$ activation on the COF structure during isolation. The COF material properties were probed using PXRD to assess the crystallinity directly, and nitrogen adsorption/desorption to examine the $S_{BET}$ and pore size distributions. This series of experiments resulted in several new conclusions about the effect of the activation method used to isolate COF materials on their material properties.

Vacuum activation of imine-linked 2D imine COFs generally results in lower crystallinity and porosity in the isolated COFs. TAPB-PDA COF showed the most pronounced degradation upon exposure to vacuum activation. TAPB-OMePDA COF with pendant methoxy groups showed about 50% loss of crystallinity and porosity and TAPPy-PDA COF was largely unaffected, showing roughly 10% loss. These findings point to structural features which may improve stability.

The existing COF literature was examined to find examples of COFs that were isolated as crystalline materials via vacuum activation in order to identify other potential structural features which may improve COF stability during activation. Present among these examples were COFs with strong interlayer interaction, such as pyrene-based COFs, or COFs with π-donating substituents connected the linear linkers. COFs with smaller pore sizes may also be more robust. Fluorination of the COF monomers is also a potential strategy towards COFs with high stability towards vacuum activation.

This series of experiments allows for the proposal of some general guidelines for the isolation of new COF materials in their most crystalline state. Activation using $scCO_2$ was

exceptionally effective for all COFs examined here, and when examining the literature can be seen to result in higher isolated surface areas. When investigating new COF structures with unknown stability towards vacuum activation, $scCO_2$ activation is the optimal activation method for isolating COFs with minimal structural distortion. However, $scCO_2$ activation requires specialized equipment, and so an alternative method was examined. Drying COFs using nitrogen flow after solvent exchange to a low surface tension solvent is an acceptable alternative for the activation of sensitive COFs and provided COF samples with slightly lower isolated $S_{BET}$ values compared to $scCO_2$.

The effects of different activation methods on various COF linkages was also examined through the use of representative examples of beta-keto enamine-linked COFs, azine-linked COFs, and boroxine/boronic ester-linked COFs. The findings here implied that beta-keto enamine COFs are not as susceptible to vacuum activation as imine COFs were shown to be in Section 2.4, though the low overall crystallinity of the TAPB-TFP COF tested may mask the actual effects of activation. It was found that azine linked COFs, here represented by HCOF-1, were susceptible to degradation when isolated using vacuum activation. The vacuum activated sample prepared here showed approximately 50% of the $S_{BET}$ of the $scCO_2$ activated sample. Similar to the imine-linked COFs tested, nitrogen-flow activation performed nearly as well as $scCO_2$ activation for HCOF-1. For boroxine linked COFs, represented by COF-1, it was found that nitrogen-flow activation greatly outperformed either $scCO_2$ using acetone as a transfer solvent, or room temperature vacuum. It is posited here that in order to activate the hydrolytically unstable boroxine COF, the rapid removal of water is of utmost importance. Therefore, the heat assisted nitrogen-flow method, which uses a temperature of 150 °C, was most effective. Literature procedures for the synthesis

of COF-1 report vacuum activation at elevated temperature. Reports of boronic ester-linked COF-5 in literature demonstrate the isolation of highly porous and crystalline materials using vacuum activation.[1] It is evident that boroxine and boronic ester-linked COFs behave very differently during activation than imine and azine-linked COFs, here vacuum activation, or activation using nitrogen flow is far more effective that the $scCO_2$ activation method tested here.

This research has also opened new areas of investigation; The use of $scCO_2$ activation allows for the observation of crystallinity at earlier stages of the COF synthesis process. This is examined further in Chapter 3. Additionally, the use of $scCO_2$ activation allows for the isolation of a variety of different imine COF structures as highly crystalline materials with high surface areas. TAPB-based COFs with a variety of hydroxyl and alkoxy functionalized terephthaldehyde monomers were successfully synthesized in four hours using $scCO_2$ activation. Pyrene based COFs using electronically relevant NDI and thienoisoindigo monomers were also synthesized successfully in this way.

This more rapid synthesis is of interest and value to the COF community because the throughput speed when screening for COF materials for particular applications can be dramatically increased compared to the 72-hour synthesis time that is commonly reported. The additional insight into the role of activation in the isolation of high-quality materials is similarly important. Vacuum activation can drastically degrade the structure of the isolated COF, which then affects the conclusions drawn from subsequent analytical methods. Additionally, the repeated isolation of COFs that are meant to be reused, for example in separation or catalytic applications may over time dramatically reduce the efficacy of the material due to collapse of the porous structure.

Therefore, the research presented here has exposed a potential pitfall when isolating new COF materials and made this knowledge accessible to the COF community. Further, the research presents a modified COF synthesis method that can provide crystalline materials in four hours, rather than the usual 72 hours. These contributions may help other researchers to avoid misleading characterization of new COF materials due to degradation during vacuum activation and may allow for faster synthesis and identification of potentially useful imine COF materials.

## 2.11 Chapter 2 Experimental Details and Supplemental Data

### *2.11.1 Chemical and Solvent Sources*

All solvents were commercially sourced and used without additional drying or degassing. Terephthaldehyde was purchased from Sigma-Aldrich and used without additional purification. 2,5-dimethoxyterephthalaldehyde was purchased from Sigma-Aldrich and used without additional purification. Glacial acetic acid was purchased from Fischer Scientific and used without additional purification. Deionized water was used throughout all experiments. **NDI-DA:** 4,9-bis(4-aminophenyl)-2,7-dihexylbenzo[lmn][3,8]phenanthroline-1,3,6,8(2H,7H)-tetraone was synthesized by Dr. Samik Jhulki according to a literature method.[118] **TAPB:** 1,3,5-*tris*(4-aminophenyl)benzene was either synthesized according to a literature method, or purchased from TCI chemicals.[132] **TII:** (E)-4,4'-dibutyl-5,5'-dioxo-4,4',5,5'-tetrahydro-[6,6'-bithieno[3,2-b]pyrrolylidene]-2,2'-dicarbaldehyde (Thienoisoindigo) was synthesized according to literature.[40] **TAPPy:** 1,3,5,8-tetra(4-aminophenyl)pyrene (TAPPy) was synthesized by Dr. Dasari and Kaitlin Slicker according to reported literature

methods. [128, 133] 2,5-dibutoxyterephaldehyde and 2,5-dioctyloxyterephthaldehyde were synthesized according to a literature method.[134]

*2.11.2 Characterization Methods*

IR Spectroscopy was performed using a Shimadzu Prestige 21 FT-IR in ATR mode using solid COF powder after PXRD analysis and $N_2$ adsorption/desorption measurements had been performed. Spectra were taken using 16 scans. The $^{1}H$ and $^{13}C$ ($^{1}H$) NMR spectra were measured on Varian Mercury 300 MHz and Bruker 400 MHz spectrometers. The chemical shift values were referenced with the solvent residual proton signal or the solvent carbon signal as internal standard.

Powder X-ray diffraction patterns were recorded on a Malvern Panalytical Empyrean in 2θ Brag Brentano geometry employing Cu Kα line focused radiation at 40 kV, 45 mA power and equipped with a PIXcel Medipix3 3D detector by Malvern PANalytical. Samples were placed on a silicon zero background sample holder then the sample surface was leveled with a clean microscope slide. No sample grinding was used prior to analysis unless specifically mentioned. Samples were rotated as diffraction data were collected using a continuous 2θ scan from 1 – 40°. For all samples, no features are observed after 30°, and diffractograms are presented from 0° to 30° for visual clarity. Scherrer analysis was performed using a shape factor of 0.9, instrumental broadening is assumed to be minimal. The Scherrer equation used is $\tau = K\lambda / \beta\cos\theta$, where $\tau$ is the crystallite size, K is a unitless shape factor, $\beta$ is the peak width at half maximum, and $\theta$ is the Bragg angle.

Surface area measurements were conducted on a Micromeritics 3Flex Physisorption Surface Area and Porosimetry Analyzer using between 10 and 50 mg. Samples were degassed at 150 °C for 3 hours under nitrogen flow prior to analysis. Nitrogen isotherms analysis was carried out at 77 K in a liquid nitrogen bath. $N_2$ adsorption/desorption isotherms, BET surface areas, pore size distributions and other related data was generated using the instruments native software (3Flex Share Version 5.0k). Nitrogen adsorption method was as follows: From $P/P_0$=0.000 to 0.010, $N_2$ dose amount is 15.0000 $cm^3/g$ STP, with a 45 second equilibration time. From $P/P_0$=0.010 to 0.1000, pressure increment is 0.010 ($P/P_0$), with a 10 second equilibration time. From $P/P_0$=0.1000 to $P/P_0$=0.3000, pressure increment is 0.050 ($P/P_0$), with a 10 second equilibration time. From $P/P_0$=0.300 to 0.700, pressure increment is 0.100 ($P/P_0$), with a 10 second equilibration time. From $P/P_0$=0.700 to 0.995, pressure increment is 0.100 ($P/P_0$), with a 10 second equilibration time. Finally, from $P/P_0$=0.995 to 0.100, pressure increment is 0.050 ($P/P_0$), with a 10 second equilibration time.

Structural Modeling of COF Materials was performed by Austin Evans at Northwestern University. Crystal modeling of the COF structures was carried out using the Materials Studio (ver.5.0) suite of programs by Accelrys. The initial structures were constructed piecewise starting with either a primitive hexagonal (P6) or tetragonal (P4) unit cell which were determined based on the bonding geometries of the constituent monomers. The a (and b when relevant) cell parameter was estimated according to the distance between the center of the vertices for each COF, and the c parameter was estimated to be 3 Å which is consistent with the interlayer spacing of graphene. The structures were optimized using the Geometry Optimization routine including energy minimization with

cell parameters optimization, using parameters associated with the Universal Force Field method.

Calculation of the simulated powder diffraction patterns and Pawley refinements were performed by Austin Evans in the Materials Studio Reflex Plus Module using a Bragg-Brentano geometry. The observed diffraction patterns were subjected to a polynomial background subtraction and then to Pawley refinement wherein peak profiles were refined using the Pseudo-Voigt peak shape function and asymmetry was corrected using the Berar-Baldinozzi function. Crystallite size was then estimated for all materials by the full pattern LeBail method which was Pawley refined to the experimental data.

Theoretical surface area calculations were carried out by Austin Evans using a Connolly surface calculation using the appropriate parameters for nitrogen as the adsorbed gas. Due to the difficulty with properly predicting the location distribution of mobile side chains, we removed their contribution to the calculated Connolly surface areas.

### *2.11.3 Monomer Synthesis Methods*

**2,5-Dihydroxyterepthaldehyde (OHPDA).** This compound was synthesized by dealkylation of 2,5-dibutoxyterephthaldehyde. A 250 mL round-bottom flask was charged with 2.5-dibutoxy terephthaldehyde[S16] (2.0 g, 7.2 mmol) and 50 mL DCM. The solution was cooled to 0 °C and then $BBr_3$ (1 M in DCM) solution (21.6 mL, 21.6 mmol) was added dropwise. Subsequently the reaction mixture was warmed to rt and stirred for overnight. Upon completion of the reaction (confirmed by TLC), the mixture was cooled to 0 °C and quenched by very careful dropwise addition of water. The mixture was extracted with DCM, organic layer was dried over anhydrous $Na_2SO_4$ and solvent was removed *in vacuo*

to obtain a yellow solid (1.16 g, yield: 98%). $^{1}$H NMR[S17] ($CDCl_3$, 400 MHz): δ (ppm) = 10.24 (s, 2H), 9.98 (s, 2H). All other characterization is consistent with literature. [17]

*2.11.4 COF Synthesis Methods*

**Synthesis of TAPB-PDA COF.** For the synthesis TAPB-PDA COF shown in Figure 2.32 below, 33.5 mg of TAPB (0.095 mmol), and 19.2 mg (0.143 mmol) of PDA are weighed into a 4 mL vial. 1 mL of 4:1 *p*-dioxane:mesitylene was added to the vial, which was sonicated thoroughly (1-2 minutes). The vial was preheated to 70 °C using an aluminum heating block. To the preheated solution, 0.5 mL of 10.5 M acetic acid was added. The vial was capped securely, and then gently swirled to mix the acid into the reaction mixture, and then the reaction mixture was allowed to stand for 4 hours at 70 °C. After the specified reaction time, the COF solid was transferred to a filter paper, and rinsed thoroughly with methanol (approximately 100 mL). Care was taken at this stage to not allow the COF to become dry on the filter paper. After rinsing, the damp solid was subjected to $scCO_2$ activation. This results in a fluffy yellow solid in 80% yield.

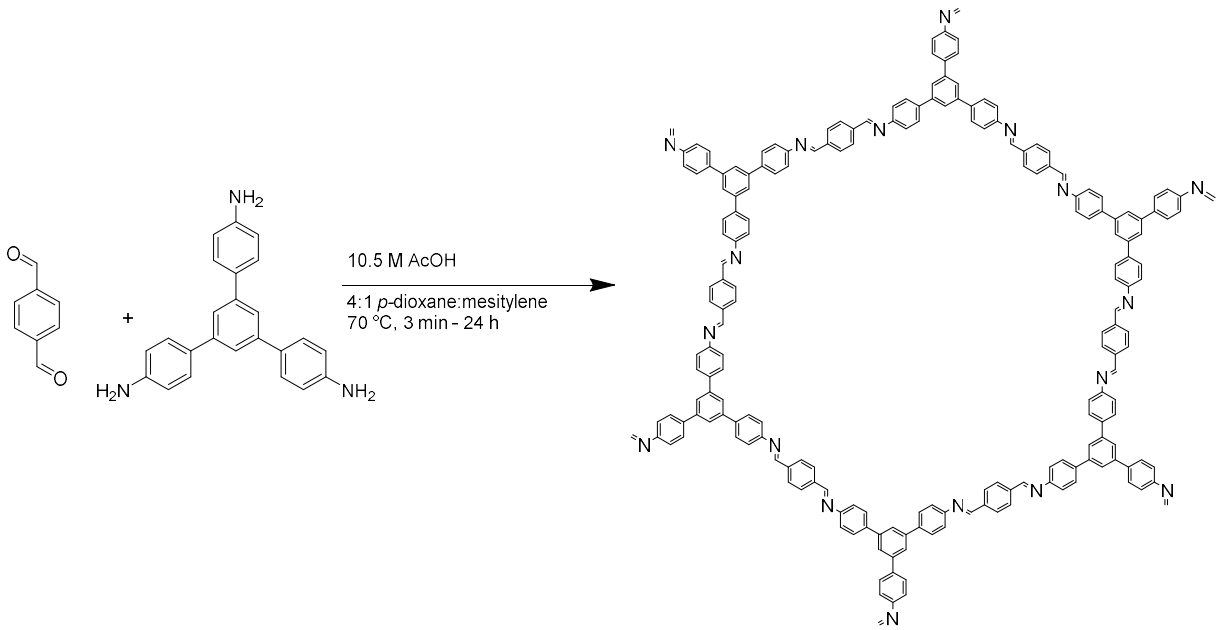


**Figure 2.32: Synthesis of TAPB-PDA COF**

**TAPB-OMePDA COF.** For the synthesis TAPB-OMePDA COF, shown in Figure 2.33 below, 55.0 mg of TAPB (0.156 mmol), and 45.6 mg (0.235 mmol) of OMePDA are weighed into a 4 mL vial. 3.33 mL of 4:1 *p*-dioxane:mesitylene was added to the vial, which was sonicated thoroughly (1-2 minutes). The vial was preheated to 70 °C using an aluminum heating block. To the preheated solution, 1.66 mL of 5 M acetic acid was added. The vial was capped securely, then gently swirled to mix the acid into the reaction mixture, then the reaction mixture was allowed to stand for 4 hours at 70 °C. After the specified reaction time, the COF solid was transferred to a filter paper, and rinsed thoroughly with methanol (approximately 100 mL). Care is taken at this stage to not allow the COF to become dry on the filter paper. After rinsing, the damp solid was subjected to $scCO_2$ activation. This results in a fluffy yellow solid in 75% yield.

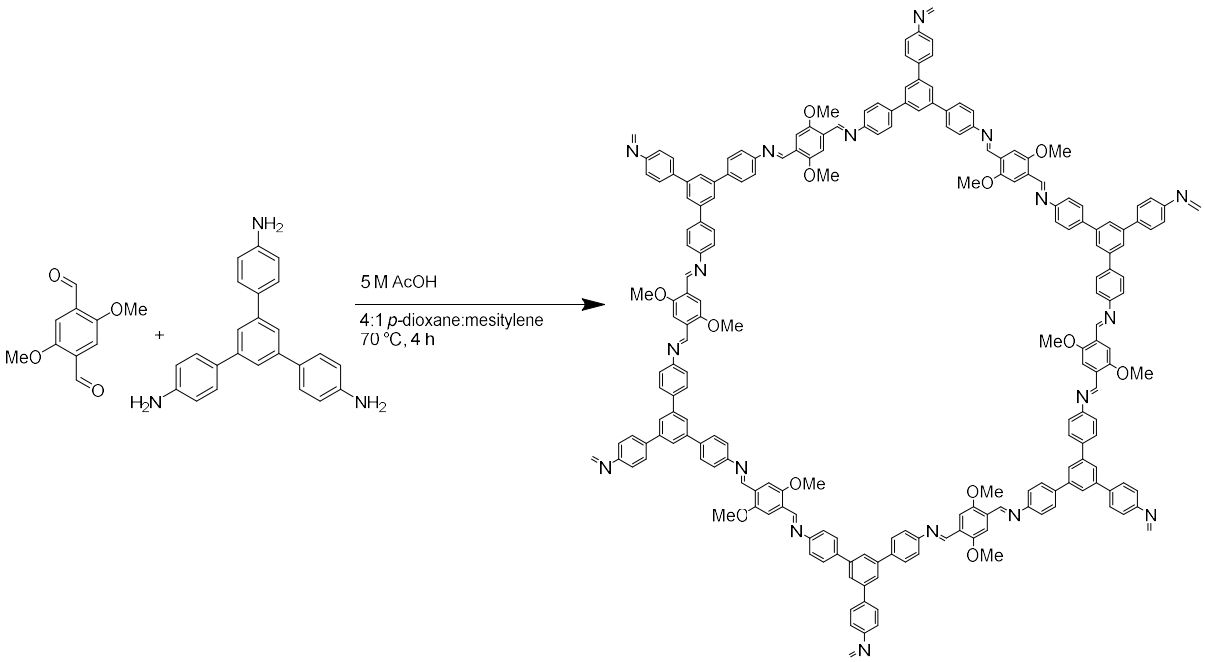


**Figure 2.33: Synthesis of TAPB-OMePDA COF**

**TAPB-OBuPDA COF.** For the synthesis TAPB-OBuPDA COF, 33.53 mg of TAPB (0.0954 mmol), and 39.3 mg (0.143 mmol) of OBuPDA are weighed into a 4 mL vial. 1 mL of 4:1 *p*-dioxane:mesitylene was added to the vial, which was sonicated thoroughly (1-2 minutes). The vial was preheated to 70 °C using an aluminum heating block. To the preheated solution, 0.5 mL of 10.5 M acetic acid was added. The vial was capped securely, then gently swirled to mix the acid into the reaction mixture, then the reaction mixture was allowed to stand for 4 hours at 70 °C. After the specified reaction time, the COF solid was transferred to a filter paper, and rinsed thoroughly with methanol (approximately 100 mL). Care is taken at this stage to not allow the COF to become dry on the filter paper. After rinsing, the damp solid was subjected to $scCO_2$ activation. This results in a fluffy yellow solid in 75% yield.

**TAPB-OOctPDA COF.** For the synthesis TAPB-OOctPDA COF, 33.53 mg of TAPB (0.0954 mmol), and 55.9 mg (0.143 mmol) of OOctPDA are weighed into a 4 mL vial. 1

mL of 4:1 *p*-dioxane:mesitylene was added to the vial, which was sonicated thoroughly (1-2 minutes). The vial was preheated to 70 °C using an aluminum heating block. To the preheated solution, 0.5 mL of 10.5 M acetic acid was added. The vial was capped securely, then gently swirled to mix the acid into the reaction mixture, then the reaction mixture was allowed to stand for 4 hours at 70 °C. After the specified reaction time, the COF solid was transferred to a filter paper, and rinsed thoroughly with methanol (approximately 100 mL). Care is taken at this stage to not allow the COF to become dry on the filter paper. After rinsing, the damp solid was subjected to $scCO_2$ activation. This results in a fluffy yellow solid in 75% yield.

**TAPPy-PDA COF.** For the synthesis TAPPy-PDA COF, shown in Figure 2.34 below, 40.5 mg of TAPPy (0.0715 mmol), and 19.2 mg (0.143 mmol) of PDA are weighed into a 4 mL vial. 1 mL of 4:1 *p*-dioxane:mesitylene was added to the vial, which was sonicated thoroughly (1-2 minutes). The vial was preheated to 70 °C using an aluminum heating block. To the preheated solution, 0.5 mL of 10.5 M acetic acid was added. The vial was capped securely, then gently swirled to mix the acid into the reaction mixture, then the reaction mixture was allowed to stand for 4 hours at 70 °C. After the specified reaction time, the COF solid was transferred to a filter paper, and rinsed thoroughly with methanol (approximately 100 mL). Care is taken at this stage to not allow the COF to become dry on the filter paper. After rinsing, the damp solid is subjected to $scCO_2$ activation. This results in a yellow solid in 90% yield.

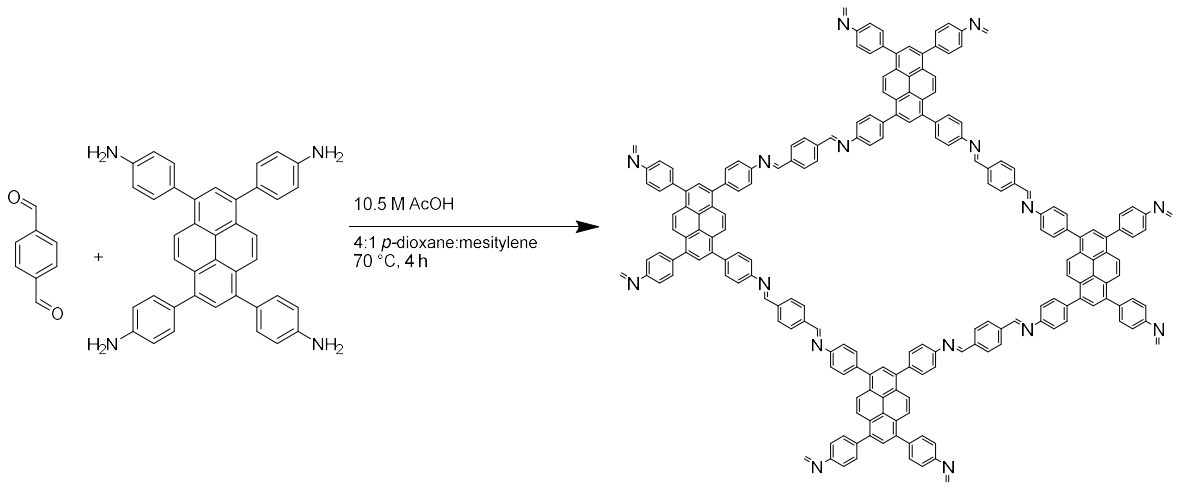


**Figure 2.34: Synthesis of TAPPy-PDA COF**

**TAPB-OHPDA COF.** For the synthesis TAPB-OHPDA COF, 20.0 mg of TAPB (0.057 mmol), and 14.0 mg (0.0842 mmol) of OHPDA are weighed into a 20 mL vial. 2 mL of 4:1 *p*-dioxane:mesitylene was added to the vial, which was sonicated thoroughly (1-2 minutes). The vial was preheated to 70 °C using an aluminum heating block. To the preheated solution, 0.4 mL of 10.5 M acetic acid was added. The vial was capped securely, then gently swirled to mix the acid into the reaction mixture, then the reaction mixture was allowed to stand for 4 hours at 70 °C. After the specified reaction time, the COF solid was transferred to a filter paper, and rinsed thoroughly with methanol (approximately 100 mL). Care is taken at this stage to not allow the COF to become dry on the filter paper. After rinsing, the damp solid is subjected to $scCO_2$ activation. The reaction produces a yellow/orange solid in 75% yield.

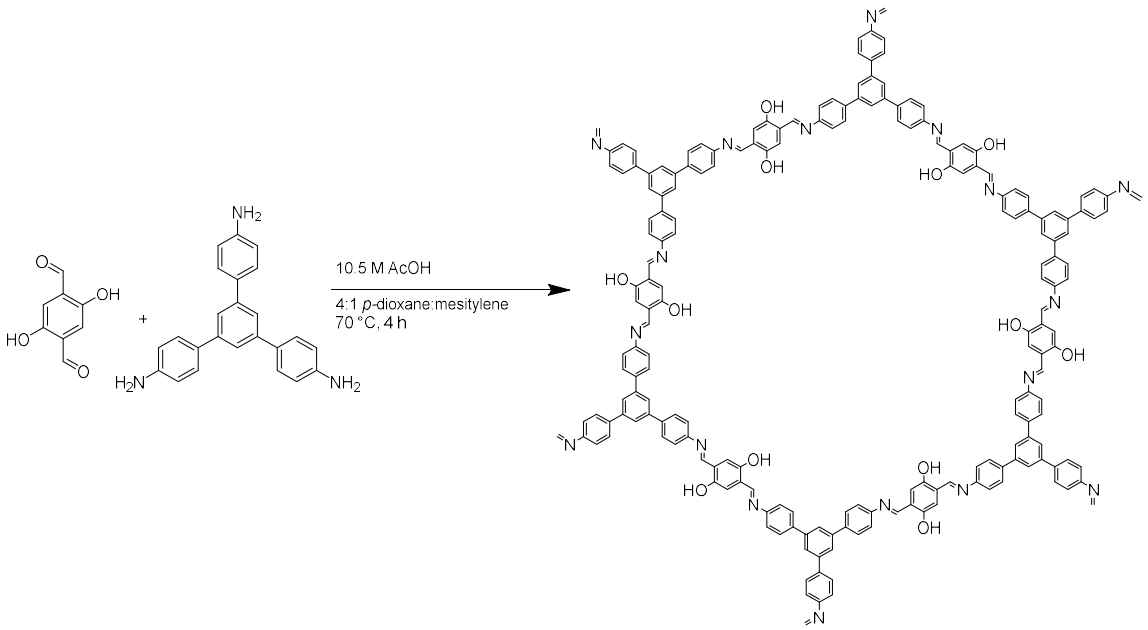


**Figure 2.35: Synthesis of TAPB-OHPDA COF**

**TAPB-NDI-DA COF:** For the synthesis TAPB-NDI-DA COF, shown in Figure 2.36 below, 33.53 mg of TAPB (0.0954 mmol), and 92.0 mg (0.1431 mmol) of NDI-DA are weighed into a 20 mL vial. 1 mL of 4:1 *p*-dioxane:mesitylene was added to the vial, which was sonicated thoroughly (1-2 minutes). The vial was preheated to 70 °C using an aluminum heating block. To the preheated solution, 0.5 mL of 10.5 M acetic acid was added. The vial was capped securely, then gently swirled to mix the acid into the reaction mixture, then the reaction mixture was allowed to stand for 4 hours at 70 °C. After the specified reaction time, the COF solid was transferred to a filter paper, and rinsed thoroughly with methanol (approximately 100 mL). Care is taken at this stage to not allow the COF to become dry on the filter paper. After rinsing, the damp solid is subjected to $scCO_2$ activation. The reaction produces a red solid in 75% yield.

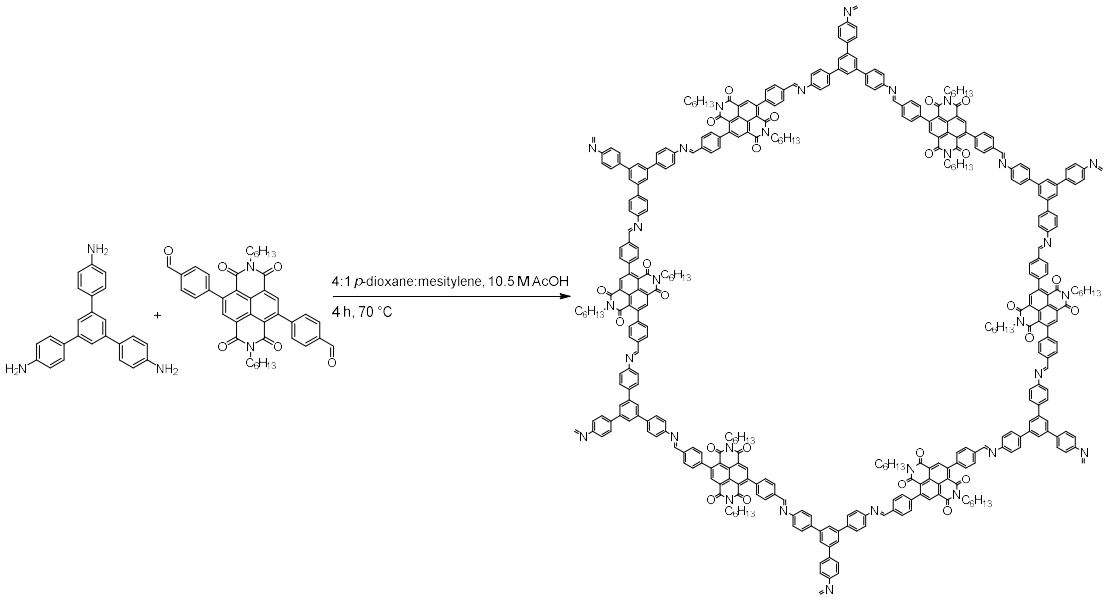


**Figure 2.36: Synthesis of TAPB-NDI COF**

**TAPPy-NDI-DA COF.** For the synthesis TAPPy-NDI-DA COF, shown in Figure 2.37 below, 70.8 mg of TAPPy (0.11 mmol), and 70.8 mg (0.11 mmol) of NDI-DA are weighed into a 4 mL vial. 2 mL of 4:1 *p*-dioxane:mesitylene was added to the vial, which was sonicated thoroughly (1-2 minutes). The vial was preheated to 70 °C using an aluminum heating block. To the preheated solution, 1.0 mL of 10.5 M acetic acid was added. The vial was capped securely, then gently swirled to mix the acid into the reaction mixture, then the reaction mixture was allowed to stand for 4 hours at 70 °C. After the specified reaction time, the COF solid was transferred to a filter paper, and rinsed thoroughly with dichloromethane (approximately 100 mL) then methanol (approximately 100 mL). Care is taken at this stage to not allow the COF to become dry on the filter paper. After rinsing, the damp solid is subjected to $scCO_2$ activation. The reaction produces a brown solid in 70% yield. This COF synthesis was found to produce the highest quality material when the amine was in excess.

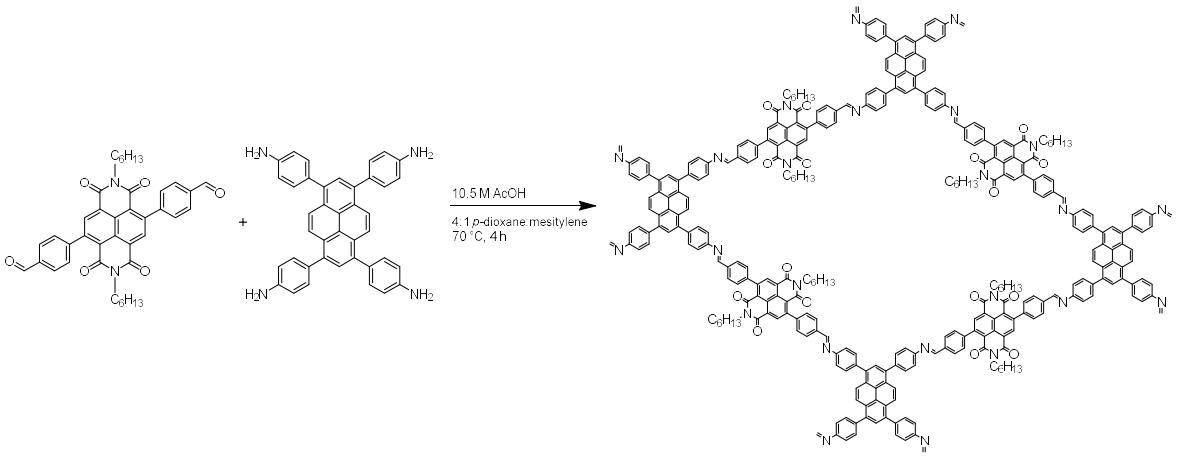


**Figure 2.37: Synthesis of TAPPy-NDI-DA COF**

**Synthesis of TAPPy-TII COF**

For the synthesis TAPPy-TII COF, shown in Figure 2.38 below, 70.81 mg of TAPPy (0.0716 mmol), and 63.33 mg (0.1431 mmol) of TII are weighed into a 4 mL vial. 1 mL of 4:1 *p*-dioxane:mesitylene was added to the vial, which was sonicated thoroughly (1-2 minutes). The vial was preheated to 70 °C using an aluminum heating block. To the preheated solution, 0.5 mL of 10.5 M acetic acid was added. The vial was capped securely, then gently swirled to mix the acid into the reaction mixture, then the reaction mixture was allowed to stand for 4 hours at 70 °C. After the specified reaction time, the COF solid was transferred to a filter paper, and rinsed thoroughly with dichloromethane (approximately 100 mL) then methanol (approximately 100 mL). Care is taken at this stage to not allow the COF to become dry on the filter paper. After rinsing, the damp solid is subjected to $scCO_2$ activation. The reaction produces a black solid in 70% yield.

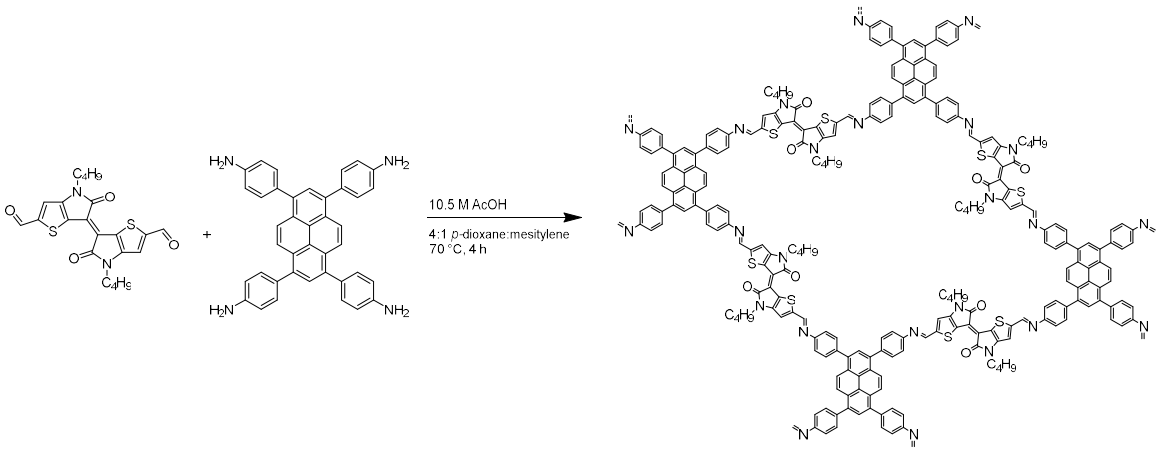


**Figure 2.38: Synthesis of TAPPy-TII COF**

*2.11.5 Method for COF Reaction Initial Temperature Trials with TAPB-PDA COF.*

For the trials studying the initial temperature during the synthesis of TAPB-PDA COF, 33.5 mg of TAPB (0.095 mmol), and 19.2 mg (0.143 mmol) of PDA are weighed into a 4 mL vial. 1 mL of 4:1 *p*-dioxane:mesitylene was added to the vial, which was sonicated thoroughly (1-2 minutes). The vial was preheated/cooled to 0 °C, 22 °C (room temperature), 50 °C, or 120 °C using an aluminum heating block or ice bath as appropriate. To the temperature-controlled solution, 0.5 mL of 10.5 M acetic acid was added. The vial was capped securely, then gently swirled to mix the acid into the reaction mixture, then the reaction mixture was allowed to stand for two minutes at the starting temperature before being heated/cooled to 70 °C, where the reaction stood for 4 hours at 70 °C. After the specified reaction time, the COF solid was activated via $scCO_2$ as described in Section 2.3.

*2.11.6 Supplemental Data for COF Reaction Initial Temperature Trials with TAPB-PDA COF.*

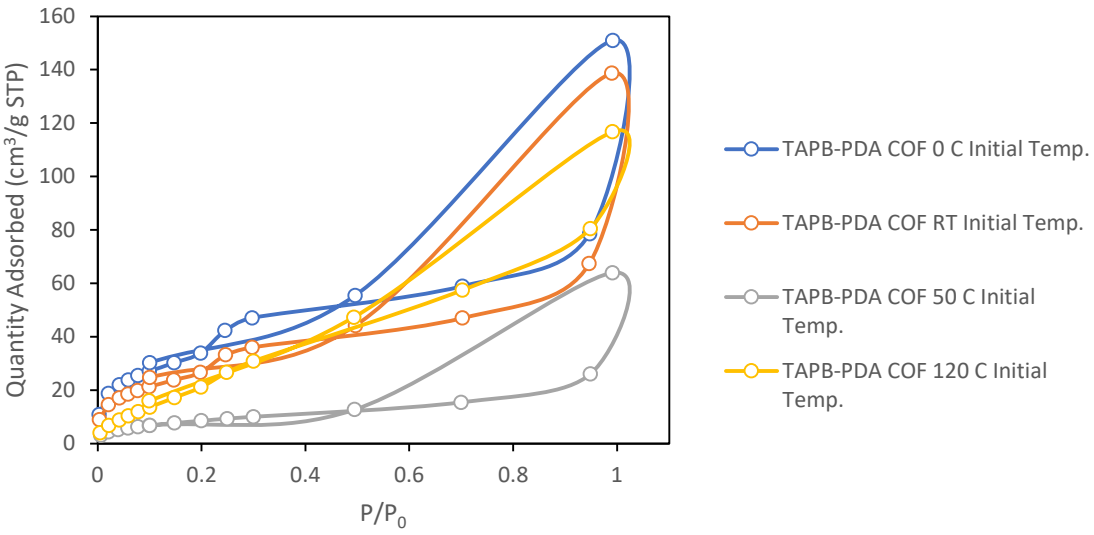


**Figure 2.39: TAPB-PDA COF $N_2$ adsorption/desorption isotherms from initial reaction temperature experiments.**

*2.11.7 Replication of TAPB-PDA Synthesis Method from Smith et al. using $scCO_2$ instead of vacuum.*[3]

**TAPB-PDA COF.** For the synthesis TAPB-PDA COF as synthesized by Smith *et al.*, 55 mg of TAPB (0.22 mmol), and 31 mg (0.33 mmol) of PDA are weighed into a 20 mL vial. 6.3 mL of 4:1 *p*-dioxane: mesitylene was added to the vial, which was sonicated thoroughly (1-2 minutes). To the solution 1.8 mL of DI water is added, followed by 1.2 ml of glacial acetic acid. The vial was capped securely, then gently swirled to mix the acid into the reaction mixture, then the reaction mixture was allowed to stand for 4 hours at 70 °C. After the specified reaction time, the COF solid was transferred to a filter paper, and rinsed thoroughly with methanol (approximately 100 mL)* Care was taken at this stage to not

allow the COF to become dry on the filter paper. After rinsing, the damp solid was subjected to $scCO_2$ activation. This resulted in a fluffy yellow solid in 80% yield.

*The activation method here is different than reported. The goal of the experiment was to determine if the preparation method reported by Smith *et al*. also produces crystalline material in four hours if activated with $scCO_2$ rather than the vacuum activation that was reported.

### *2.11.8 Supplemental PXRD Patterns, Isotherms, and Pore-Size Distributions for the Regeneration of Imine-Linked COFs Experiment*

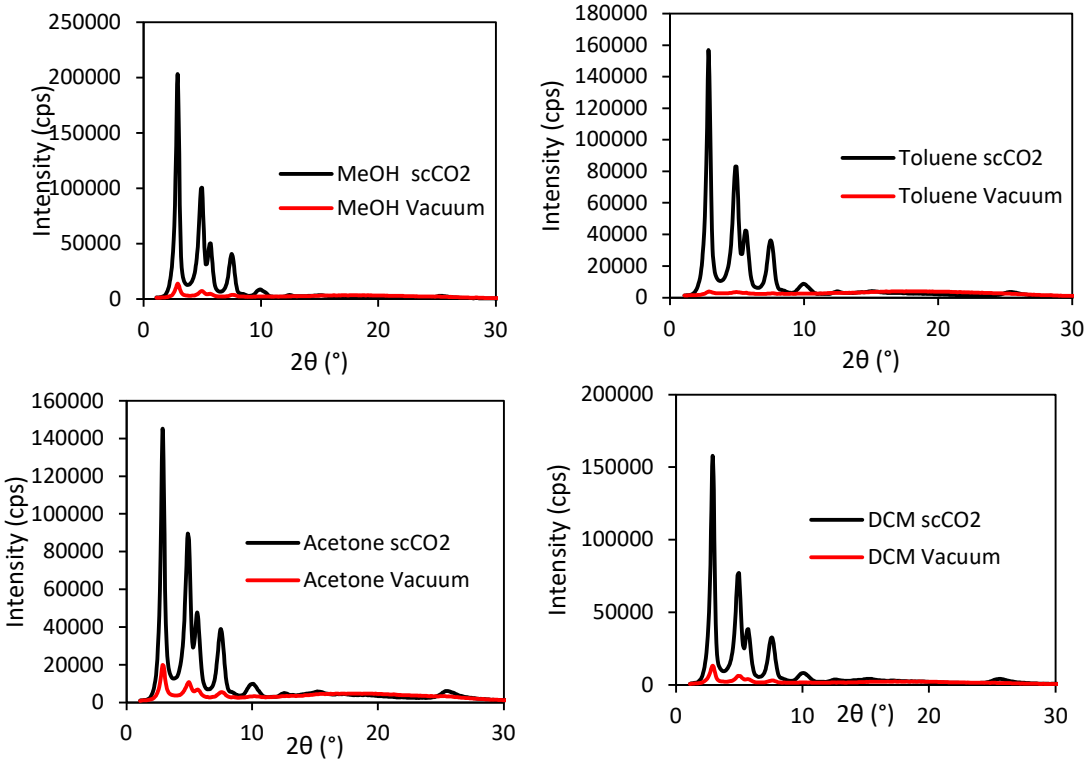


**Figure 2.40: Top Left: TAPB-PDA COF PXRDs for COFs rinsed in methanol then activated via vacuum or $scCO_2$. Top Right: TAPB-PDA COF PXRDs for COFs rinsed in toluene then activated via vacuum or $scCO_2$. Bottom Left: TAPB-PDA COF PXRDs for COFs rinsed in acetone then activated via vacuum or $scCO_2$. Bottom Right: TAPB-PDA COF PXRDs for COFs rinsed in dichloromethane then activated via vacuum or $scCO_2$.**

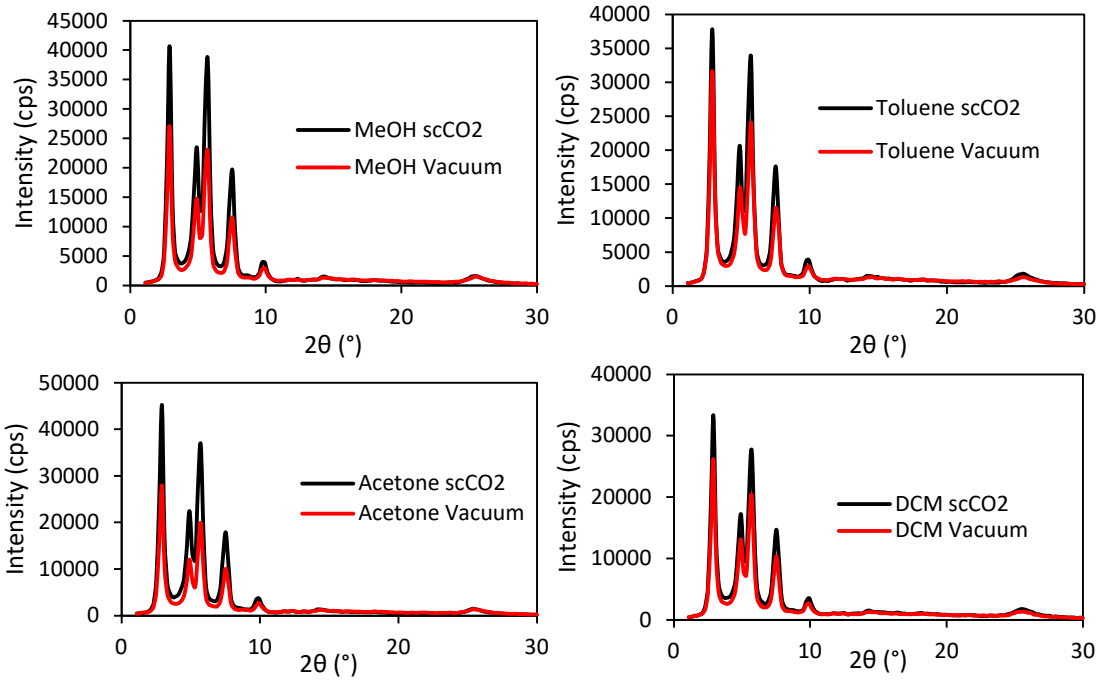


**Figure 2.41: Top Left: TAPB-OMePDA COF PXRDs for COFs rinsed in methanol then activated via vacuum or scCO₂. Top Right: TAPB-OMePDA COF PXRDs for COFs rinsed in toluene then activated via vacuum or scCO₂. Bottom Left: TAPB-OMePDA COF PXRDs for COFs rinsed in acetone then activated via vacuum or scCO₂. Bottom Right: TAPB-OMePDA COF PXRDs for COFs rinsed in dichloromethane then activated via vacuum or scCO₂.**

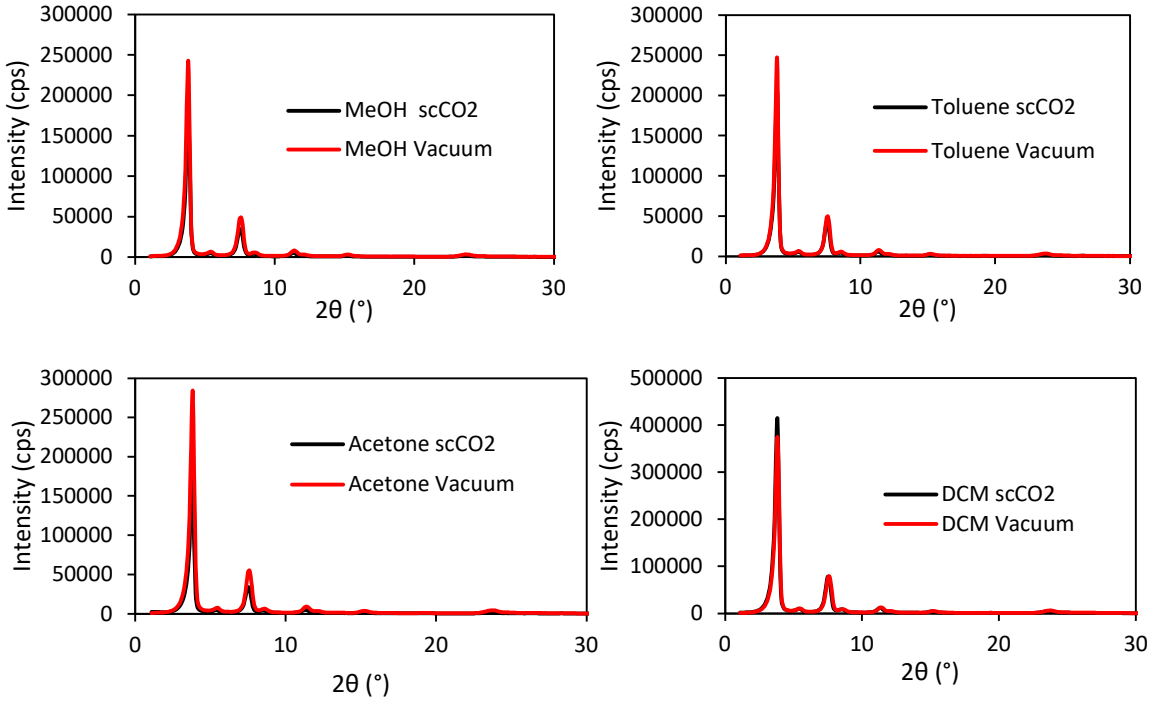


**Figure 2.42: Top Left: TAPPy-PDA COF PXRDs for COFs rinsed in methanol then activated via vacuum or $scCO_2$. Top Right: TAPPy -PDA COF PXRDs for COFs rinsed in toluene then activated via vacuum or $scCO_2$. Bottom Left: TAPPy -PDA COF PXRDs for COFs rinsed in acetonr then activated via vacuum or $scCO_2$. Bottom Right: TAPPy -PDA COF PXRDs for COFs rinsed in dichloromethane then activated via vacuum or $scCO_2$.**

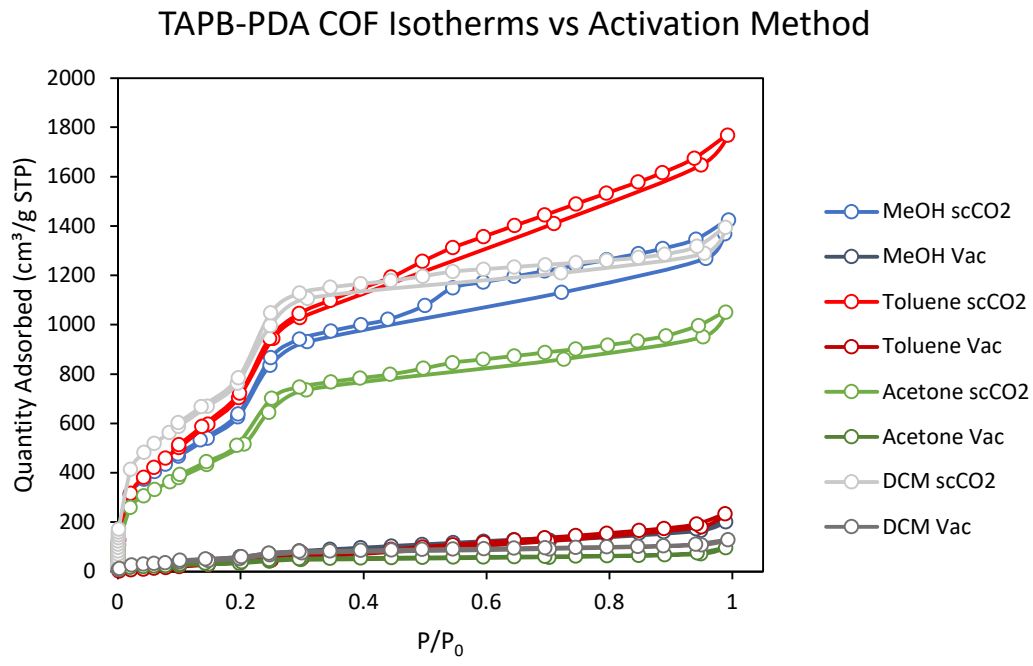


**Figure 2.43: TAPB-PDA COF 77 K $N_2$ adsorption/desorption isotherms for each tested activation method.**

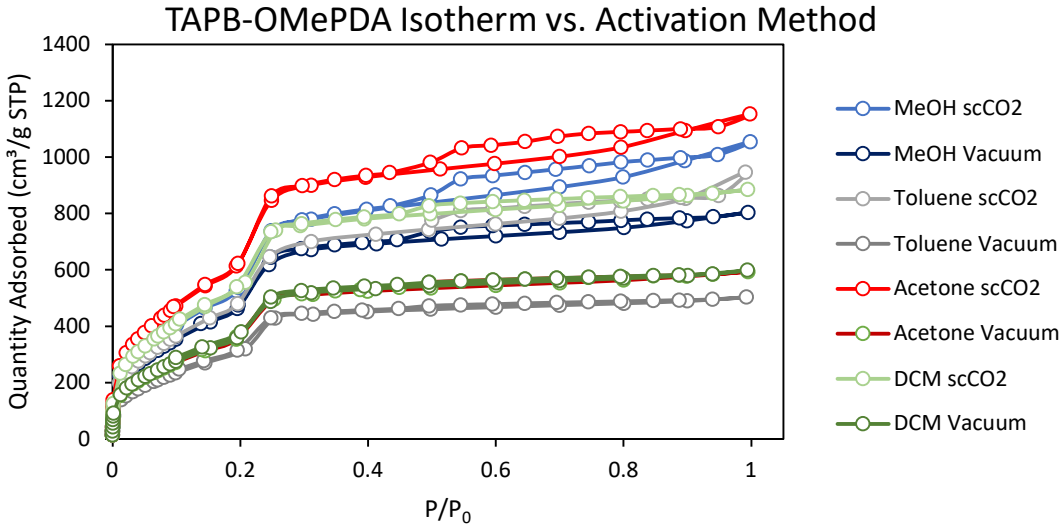


**Figure 2.44: TAPB-OMePDA COF 77 K $N_2$ adsorption/desorption isotherms for tested activation methods.**

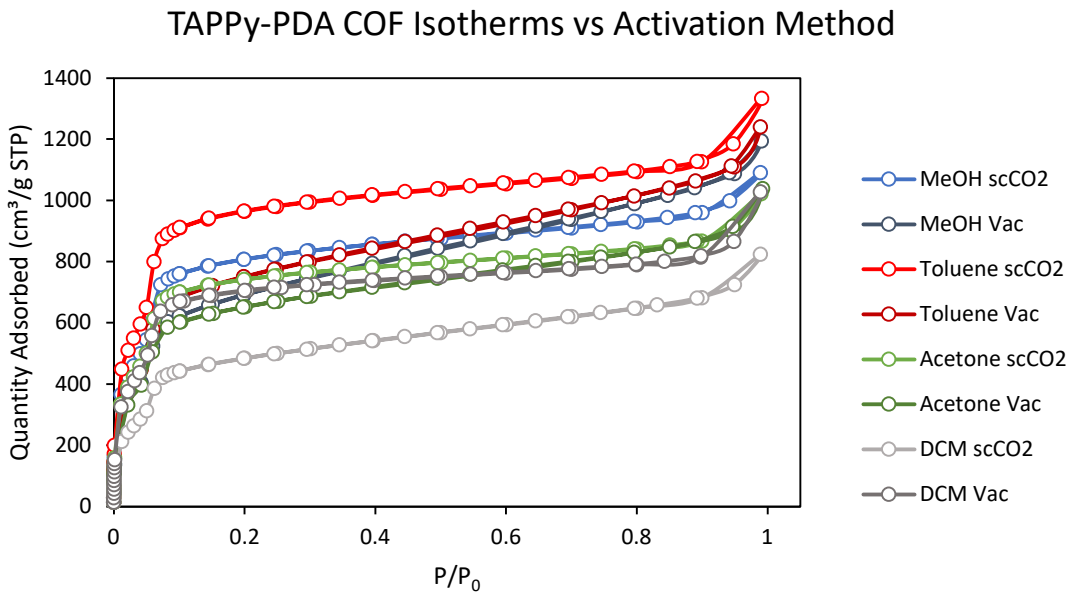


**Figure 2.45: TAPPy-PDA COF 77 K $N_2$ adsorption/desorption isotherms for each tested activation method.**

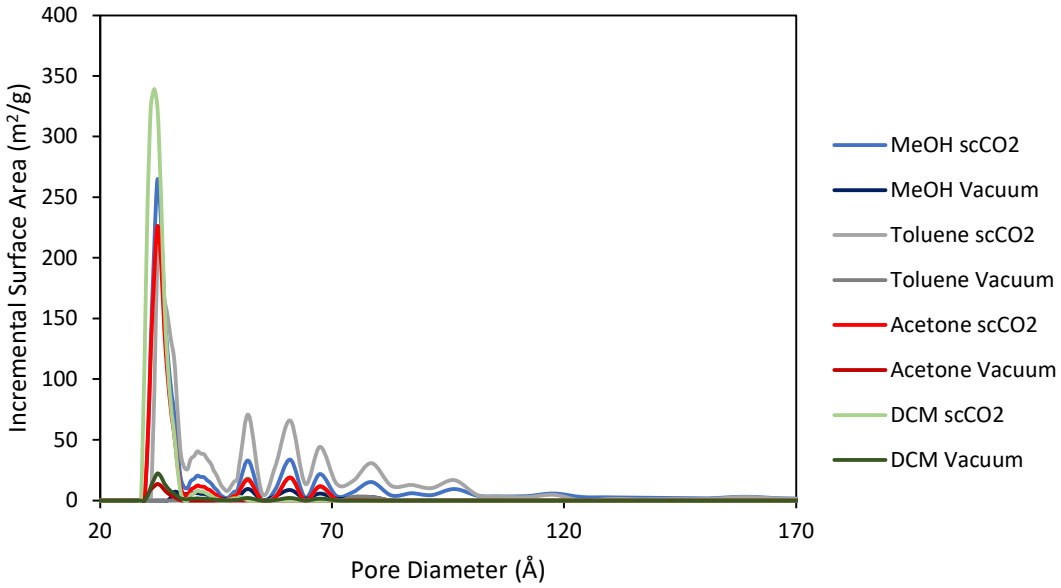


**Figure 2.46: TAPB-PDA COF pore size distributions for each tested activation method.**

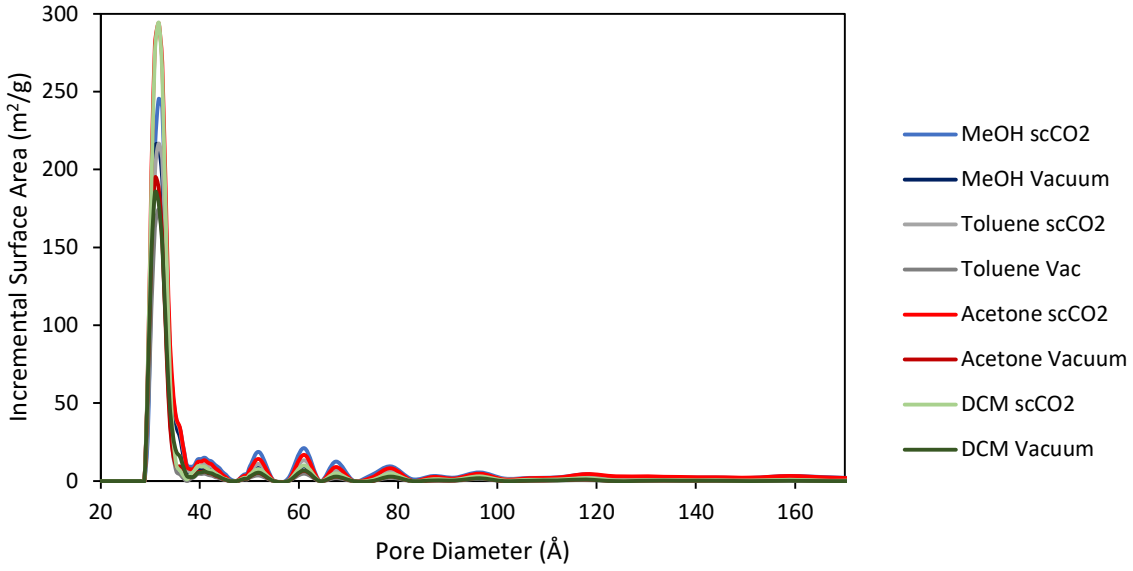


**Figure 2.47: TAPB-OMePDA COF pore size distributions for each tested activation method.**

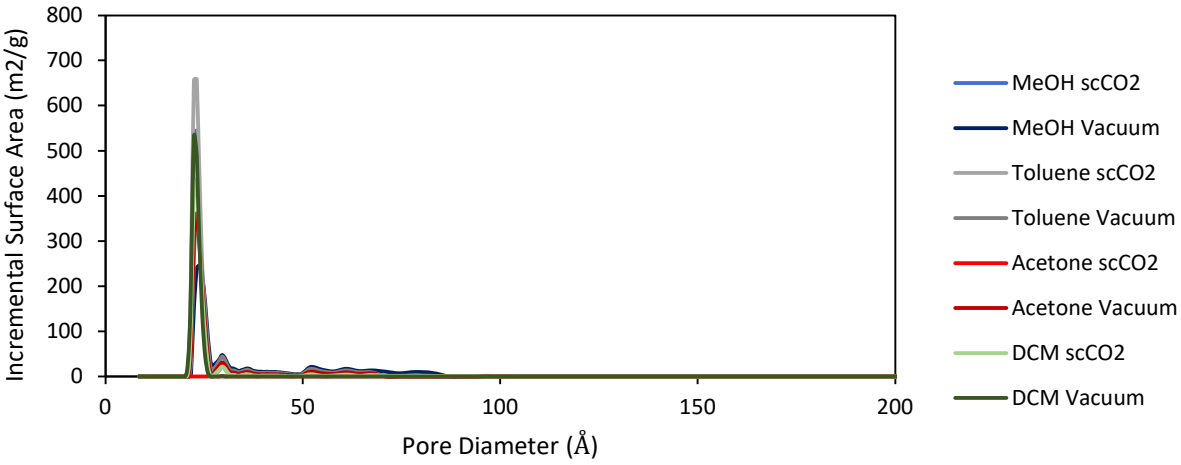


**Figure 2.48: TAPPy-PDA COF pore size distributions for each tested activation method.**

*2.11.9 Supplemental Data for TAPB-PDA COF isolated using Nitrogen-Flow Activation*

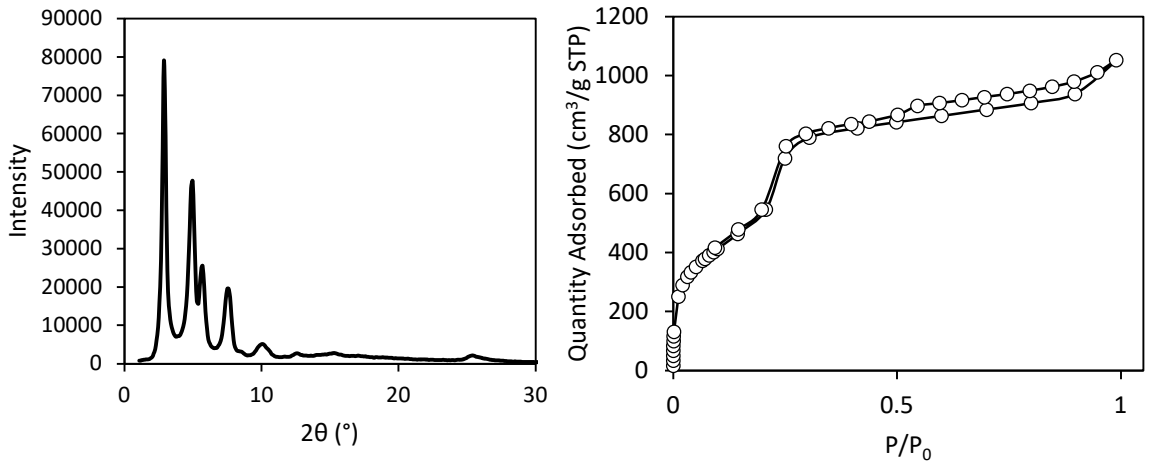


**Figure 2.49: Left: PXRD Pattern for TAPB-PDA COF isolated using nitrogen flow method. Right: $N_2$ adsorption/desorption isotherm for TAPB-PDA COF isolated using nitrogen flow methods.**

*2.11.10 Supplemental Data for Imine-Linked COFs Synthesized in Four Hours*

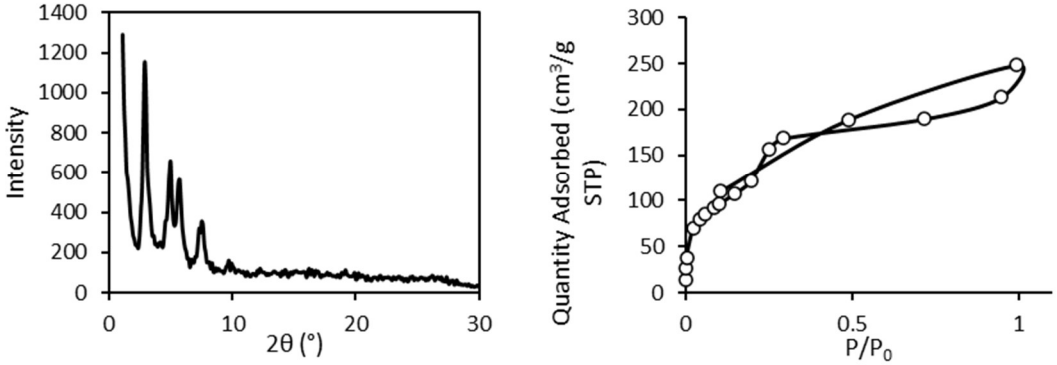


**Figure 2.50: Left: TAPB-OHPDA COF PXRD. Right: TAPB-OHPDA COF $N_2$ adsorption/desorption isotherm.**

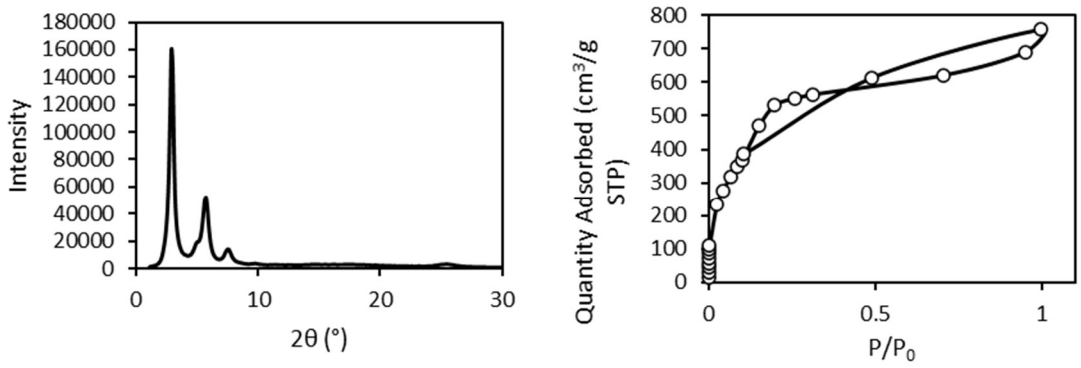


**Figure 2.51: Left: TAPB-OBuPDA COF PXRD. Right: TAPB-OBuPDA COF $N_2$ adsorption/desorption isotherm.**

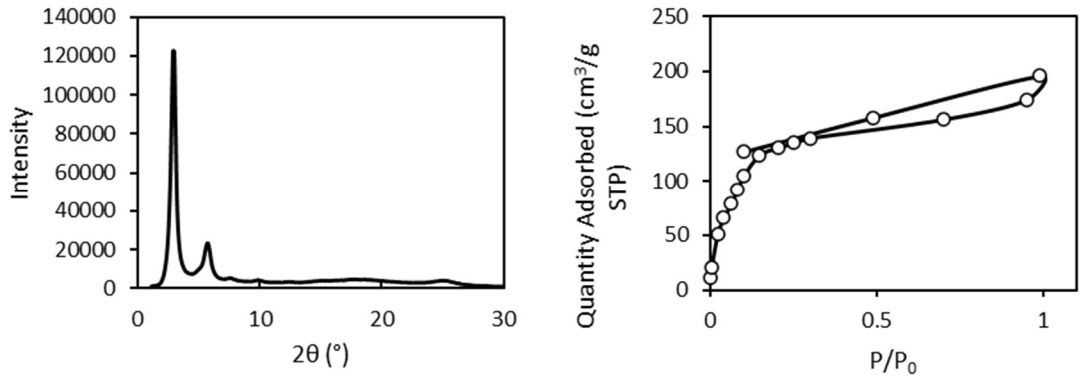


**Figure 2.52: Left: TAPB-OOctPDA COF PXRD. Right: TAPB-OOctPDA COF $N_2$ adsorption/desorption isotherm.**

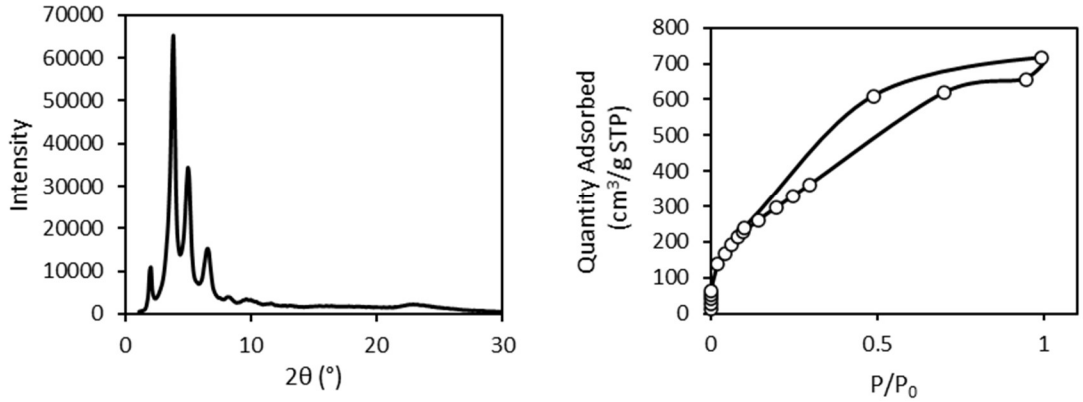


**Figure 2.53: Left: TAPB-NDI-DA COF PXRD. Right: TAPB-NDI-DA COF $N_2$ adsorption/desorption isotherm.**

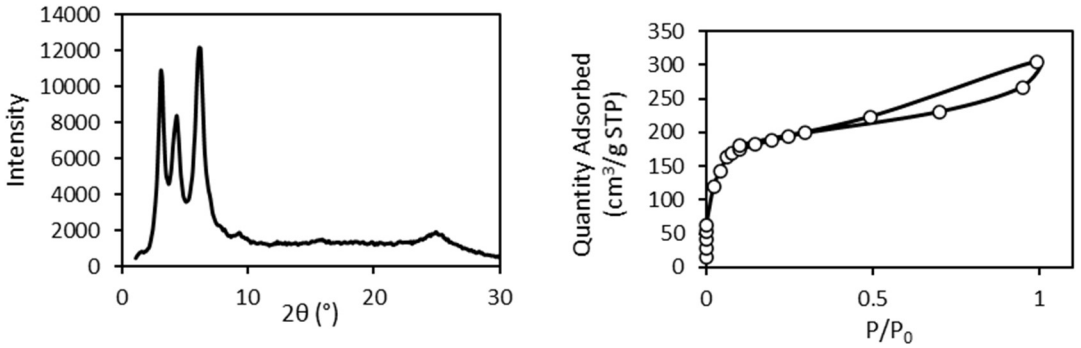


**Figure 2.54: Left: TAPPy-TII COF PXRD. Right: TAPPy-TII COF $N_2$ adsorption/desorption isotherm.**

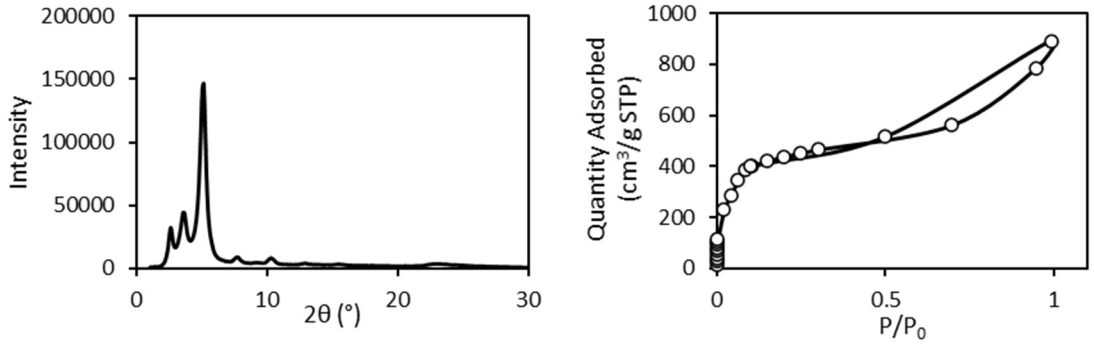


**Figure 2.55: Left: TAPPy-NDI-DA COF PXRD. Right: TAPPy-NDI-DA COF $N_2$ adsorption/desorption isotherm.**

# CHAPTER 3. INVESTIGATION OF THE INITIAL CRYSTALLIZATION OF TWO-DIMENSIONAL IMINE-LINKED COVALENT ORGANIC FRAMEWORKS

## 3.1 Chapter Introduction

Similarly to Chapter 2, this research chapter focuses on the synthesis of COF materials with the goal of better understanding the way COFs behave and assemble. Understanding the way COF materials assemble from individual monomers is a crucial step towards the synthesis of high-quality COF powders, films and even single crystal samples. Towards this end, this chapter focuses on the initial time period during COF synthesis immediately following the addition of an acetic acid catalyst. The use of $ScCO_2$ activation during 2D imine COF isolation was shown to result in more crystalline materials at earlier times during the synthesis process, due to the reduced disruption of the fragile initial COF structures during activation.[118] Vacuum activation, as seen in Chapter 2 can disrupt COF structures, and obscures the observation of crystalline materials on low time scales. By using $scCO_2$, it is also possible to gain greater insight into the mechanisms governing the formation of crystalline 2D imine COFs. Because of the revelation that $scCO_2$ allows for observation of early COF samples in greater detail is recent, the amount of prior work in the COF literature in the examination of the initial stages of imine COF formation is limited. Prior reports show that COFs were not isolated at sufficiently short time scales, or that vacuum activation was used, which would have damaged the initial solids and prevented observation of crystallinity. In Section 3.2 some relevant literature examples,

which report the formation of COFs at short time scales shorter than 12 hours, are presented for background context.

Following the brief literature examination, new work in examining the formation of various imine COFs at very short time scales via *in situ* and *ex situ* methods is presented in Sections 3.3 through 3.7, beginning with a thorough investigation of the formation of TAPB-PDA COF in Section 3.3.

In Section 3.5 and 3.6, several additional COF structures are examined in order to determine the effects COF skeletal arrangement, i.e. trifunctional nodes vs. tetrafunctional nodes by investigating the polymerization and crystallization of pyrene-based COFs compared to TAPB-based COFs. These COFs are examined *ex situ* via PXRD and gas adsorption/desorption at Georgia Tech, and then *in situ* using a synchrotron source in collaboration with Austin Evans at Northwestern University.

Section 3.7 specifically examines the effect of the amine and aldehyde monomer concentration on the initial crystallization of the TAPB-PDA Framework.

Finally in Section 3.8, the effects of bulky alkoxy side chains on the COF crystallization process is investigated by reacting TAPB with a series of 2,5-dialkoxyterephthaldehyde monomers. These COFs are examined *ex situ* via PXRD and gas adsorption/desorption, and then *in situ* using a synchrotron source in collaboration with Austin Evans at Northwestern University.

## 3.2 Literature Examples of Covalent Organic Frameworks Studied at Short Reaction Times

The work presented here is not the first example of a study on the crystallization behavior of 2D imine COFs. The first example of an investigation into the formation of 2D imine COFs to be presented here is a 2016 communication on the formation of TAPB-PDA COF by Smith *et al.*[3] In this work, the authors screened solvent and acid conditions to find the optimal conditions for imine COF growth and thus reported TAPB-PDA COF as a crystalline material with high surface area for the first time.[3] Prior to this work by Smith *et al.* TAPB-PDA COF had only been reported as an amorphous, low surface area material.[20] [18] The authors note, that upon addition of the acetic acid, the COF monomers form an extended network which precipitates rapidly, with 95% solid yield after only 15 minutes. These isolated solids showed no PXRD intensity corresponding to the COF, and a $S_{BET}$ of only 18 $m^2/g$. Subjecting these solids to the reaction conditions again without additional monomer for 48 hours resulted in crystalline material with a $S_{BET}$ of 287 $m^2/g$. [3] These results led the authors to the conclude that TAPB-PDA COF, and by extension 2D imine COFs in general initially form as amorphous materials, which then crystalize to give the COF framework through imine exchange reactions. The free amine and aldehyde monomers were said to play a very limited role after the initial precipitation, based on the ability of the COF to crystallize after isolation. [3]

This work by Smith *et al.* used exclusively vacuum activation, which was shown in Chapter 2 to severely degrade the TAPB-PDA COF structure during isolation. [3] Notably, $S_{BET}$ value of 287 $m^2/g$ obtained by Smith *et al.* agrees well with the $S_{BET}$ values found for TAPB-

PDA COF isolated via vacuum reported in Chapter 2.[3] It can therefore be concluded that the vacuum activation method used likely masked the true crystallinity of the COF formed.

Other works where the initial formation of 2D imine COFs is investigated are limited. Sick *et al.* report the PXRD patterns of a benzene-dithiophene dialdehyde (BDT) and TAPB based COF isolated after 12 hours, 24 hours, 48 hours and 72 hours, activated using $scCO_2$.[127] The authors note that activation with $scCO_2$ provides crystalline material at 12 hours, which is a similar result to those presented earlier in Chapter 2 of this work. However, in this reference, different structures were not examined, nor were COF synthesis times of less than 12 hours. [127]

Li *et al.* report on the synthesis of 2D imine COF colloidal nanoparticles using TAPB-PDA COF catalyzed with scandium triflate.[41] The synthesis of TAPB-PDA COF in acetonitrile solvent catalyzed by scandium triflate yields a stable suspension of imine nanoparticles, rather than a fully gelled precipitate as found for acetic acid catalyzed TAPB-PDA COF synthesis methods. These discrete nanoparticles allowed for comparison of the rates of crystallization, monitored via *in situ* XRD and gauged by the FWHM with the rate of particle growth monitored via dynamic light scattering DLS. [41] The authors report that the COF particles form faster than the framework crystallizes, which implies an amorphous initial solid that crystallized via transimination reactions. This result shows that, at least for scandium triflate catalyzed COFs, that an amorphous initial phase certainly exists. [41] Unfortunately, due to the tendency of acetic acid catalyzed COFs to rapidly precipitate the insoluble network, the rate of particle growth versus the rate of crystallization are not as easily studied as that of suspended nanoparticles.

Based solely on the reported literature there appears to be evidence that when catalyzed using scandium triflate, an initial amorphous phase does exist, however, this conclusion cannot be extended to acetic acid catalyzed COF synthesis due to the interference of vacuum activation in the experiments performed by Smith *et al.* Further investigation of the initial formation of TAPB-PDA COF and other 2D imine COFs is necessary to fully understand the crystallization behavior of the COF.

## 3.3 Synthesis and Isolation of TAPB-PDA Covalent Organic Framework after Short Reaction Times

The initial stages of COF synthesis and crystallization were first studied using TAPB-PDA COF because of the commercial accessibility of both monomer components, as well as its prior history as a model system in the existing COF literature.[3, 20, 40, 118, 127]

The COFs for this experiment were synthesized following the same procedure as presented in Chapter 2, with the reaction time after the addition of the 10.5 M acetic acid solution varied from 15 seconds for the shortest trials, up to 24 hours. The COF solids were isolated, activated, and analyzed following the same $scCO_2$ activation procedure as presented in Chapter 2. Using $scCO_2$ activation, crystallinity is observed *ex situ* as early as 3 minutes after the addition of acetic acid, as seen in Figure 3.1, below.

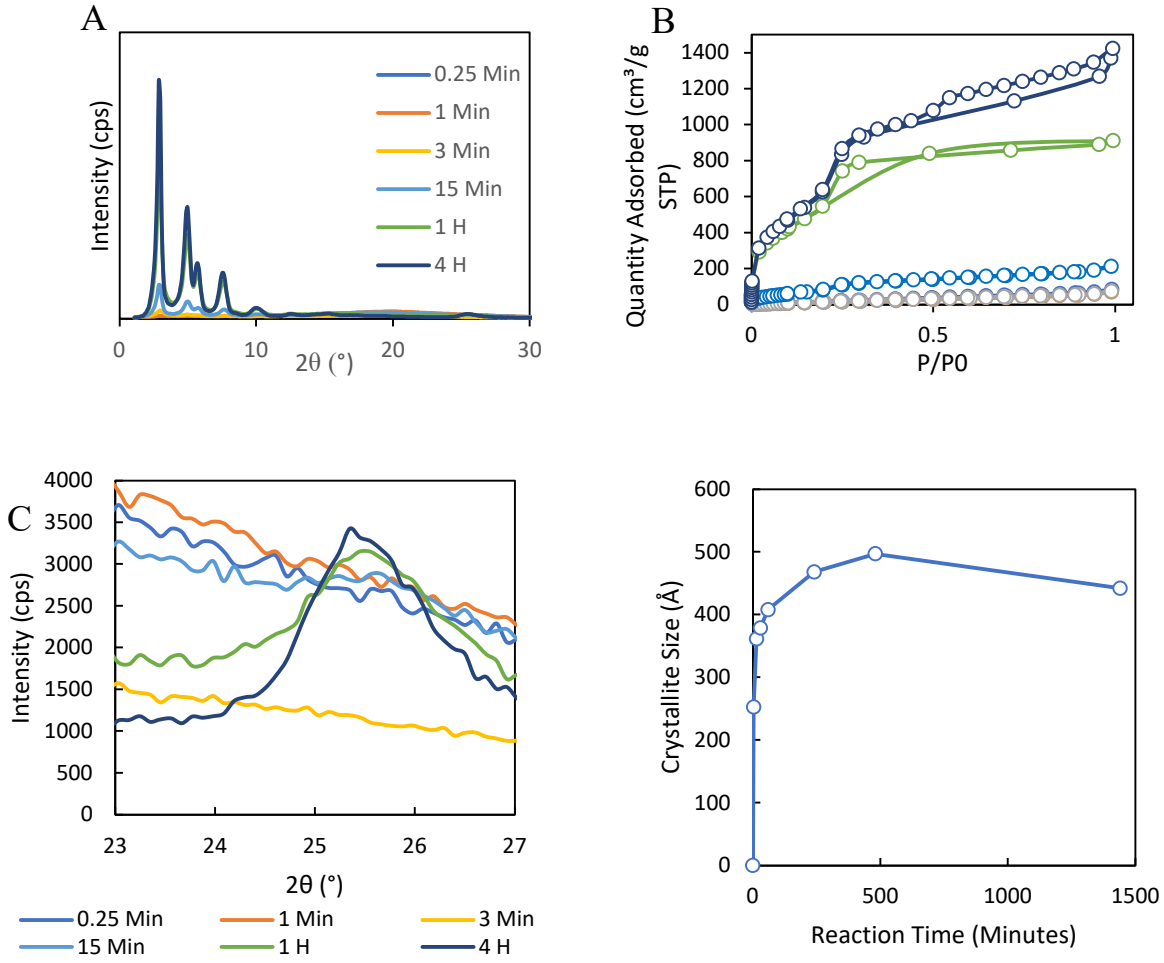


**Figure 3.1: A: PXRD patterns for TAPB-PDA COF samples isolated after different reaction times, B: 77 K $N_2$ adsorption/desorption isotherms for TAPB-PDA COF samples isolated after different reaction times, C: PXRD plot showing the development of the (001) peak (interlayer stacking) for TAPB-PDA COF samples, D: Crystallite size determined via the Scherer equation based on the (100) peak for TAPB-PDA COF samples.**

The measured COF crystallinity, as measured by the PXRD intensity of the isolated COF powder, increases over time and reaches its maximum value after 4 hours, after which increases in crystallinity and surface area and pore size homogeneity are minimal. Figure 3.1 above shows the development of the crystalline PXRD pattern as a whole, as well as the development of the (100) and (001) refractions specifically, which correspond to the

pore diameter within the COF sheet, and the interlayer spacing between the COF layers in the z direction. PXRD diffraction signals indicative of crystalline COF material are observable at three minutes, and are clear and distinct by 15 minutes. The PXRD patterns taken from TAPB-PDA solids synthesized in 15 or 60 seconds do not show crystalline (100) diffraction peaks corresponding to the COF pore size. The (001) peak corresponding to interlayer spacing is not observable by PXRD until one hour after the addition of acetic acid. This could represent some amount of disorder within the inter-sheet stacking at early stages in the reaction or could simply be due to the relatively lower intensity compared to the more prominent (100) peak.

This rapid crystallization is in direct contrast to the report by Smith *et al.* discussed earlier in Section 3.2, in which a sample synthesized in 15 minutes was reported as amorphous and effectively non-porous. Here the utility of $scCO_2$ activation is apparent. The gentler activation method has allowed for the *ex situ* observation of delicate crystalline material at very early stages of the reaction, as early as 3 minutes after addition of acetic acid.

The nitrogen adsorption/desorption isotherms and bet surface areas indicate that porosity increases linearly with the PXRD intensity. This relationship is plotted in Figure 3.27 in Section 3.10.4. After 4 hours TAPB-PDA COF obtains a BET surface area of 2340 $m^2/g$ STP, compared to a theoretical Connolly surface area of 2600 $m^2/g$ STP calculated by Austin Evans at Northwestern University. The pore size distribution shown in the Section 3.10.5 shows that the 32 Å pore characteristic of the TAPB-PDA COF becomes more apparent as the COF $S_{BET}$ and PXRD intensity increase.

In 2016, Smith *et al.* proposed a mechanism where TAPB-PDA COF initially rapidly polymerizes to an insoluble amorphous network which first precipitates, then error-corrects using the inherent reversibility of imine bond formation to form the crystalline network over extended periods of time.[3] Based on solely on the *ex situ* data obtained for TAPB-PDA COF, this mechanism can still be supported, though the time scale of one hour is clearly quite different than the multiple days reported there. However, it is possible that the activation of the COF used when first examining the formation of TAPB-PDA COF was insufficiently gentle to examine the initially formed precipitates accurately *ex situ*. Here however, $scCO_2$ activation is used. $ScCO_2$ activation is the gentlest method for activating porous solids currently known, however, it would be beneficial to examine the formation of COF materials without any activation as a confounding variable.[118]

To this end, a collaborative experiment was performed with the Dichtel group at Northwestern University, specifically Austin Evans. Here, 2D imine COFs were synthesized, and rapidly transferred into capillary tubes for analysis using the Advanced Photon Source (APS) at Argonne National Labs. Utilizing this method it was possible to obtain XRD data from the COF material present in the reaction only 90 seconds after the addition of acetic acid and it was possible to continually measure the formation of crystalline materials over the course of the next forty minutes. Shown below in Figure 3.2 is a surface plot of the (100) peak for TAPB-PDA COF measured using the APS.

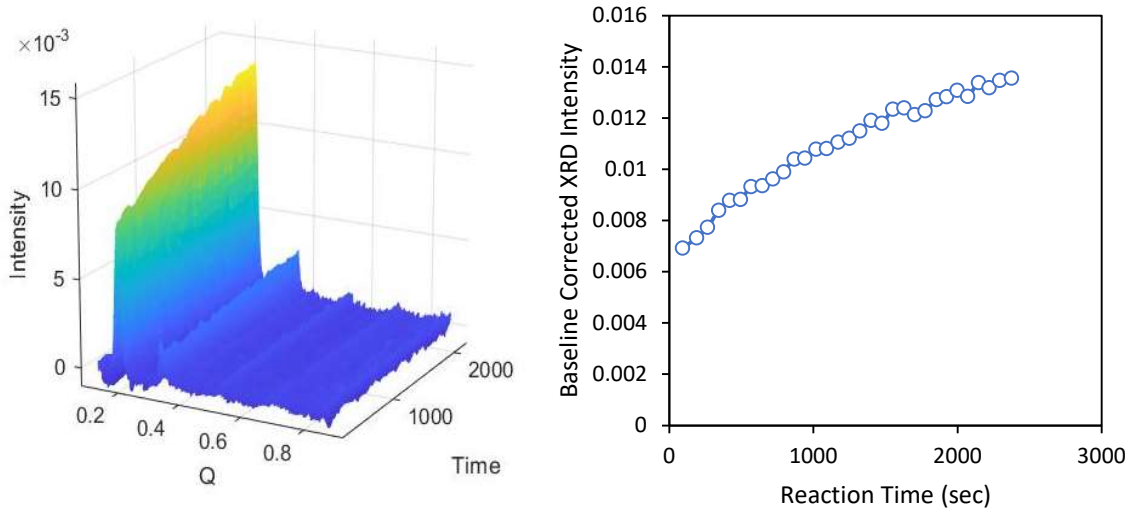


**Figure 3.2: Left: Baseline corrected surface plot of TAPB-PDA COF *in situ* (100) XRD intensity, baseline correction was performed according to the method presented in Section 3.10.2 Right: TAPB-PDA COF *in situ* (100) peak intensity plotted against reaction time.**

Also, in Figure 3.2 is a plot of the (100) peak intensity for each XRD scan which is shown in the surface plot. The data obtained shows that the COF has formed as early as 90 seconds after the addition of acetic acid, in contrast to the *ex situ* data in which is possible to observe evidence of crystallinity until 3 to 15 minutes after the addition of acetic acid. It is here posited, that the initial solids formed from the imine condensation may be crystalline, but insufficiently stable to survive any known activation process without severe disruption. This data prompted further investigation of the initial solids produced by the synthesis of TAPB-PDA COF.

## 3.4 Direct Transmission Electron Microscopy Observation of Initially Crystalline Imine-Linked Covalent Organic Frameworks via Sonication

TAPB-PDA COF was synthesized following the general protocol but was isolated 15 seconds after the addition of acetic acid. This material was activated using $scCO_2$, then

portions of a few milligrams of the COF solid were dispersed into each of several solvents. These samples were sonicated for five minutes, then the liquid was drop-cast onto clean silicon wafers. The exfoliated COF samples were analyzed by SEM. Solvents examined were acetone, isopropyl alcohol (IPA), dimethylformamide (DMF), and tetrahydrofuran (THF).

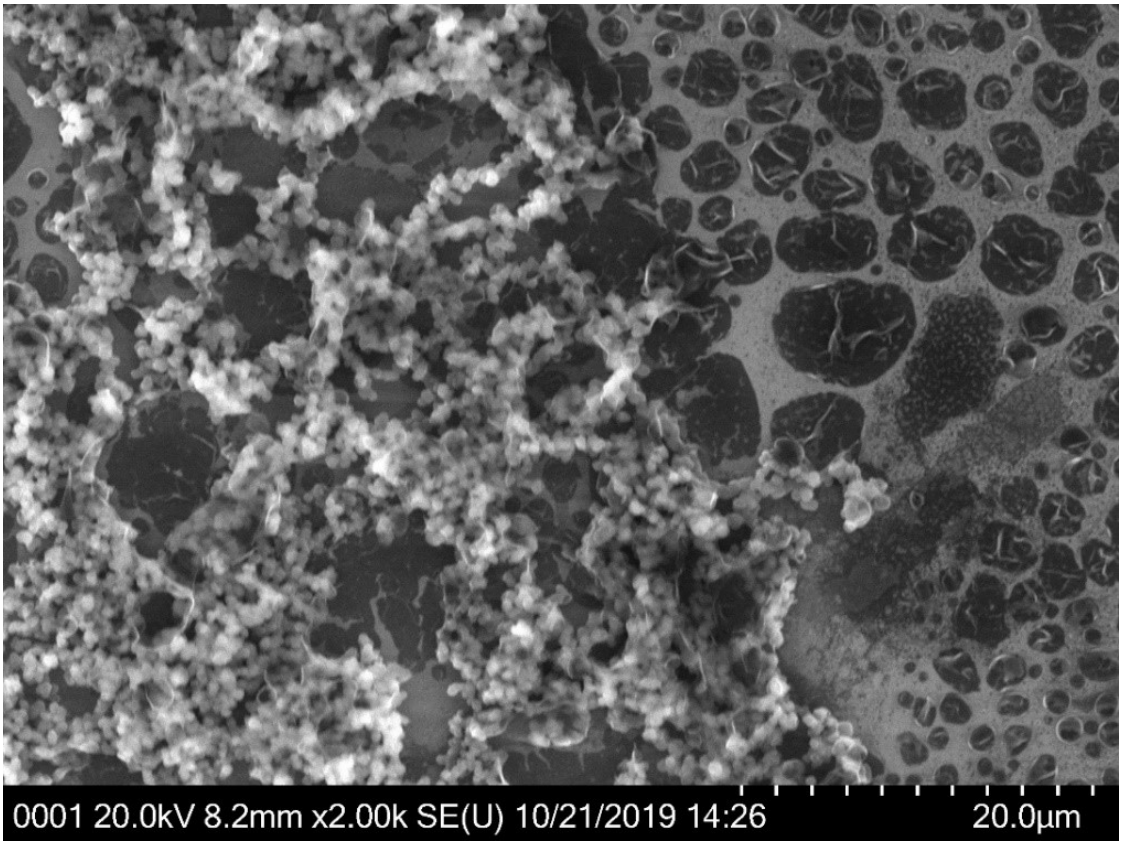


**Figure 3.3 SEM Image of TAPB-PDA COF synthesized in 15 seconds, sonicated in acetone and dropcast on silicon, showing features which may be due to large COF aggregates and other thin features tentatively assigned to COF sheets.**

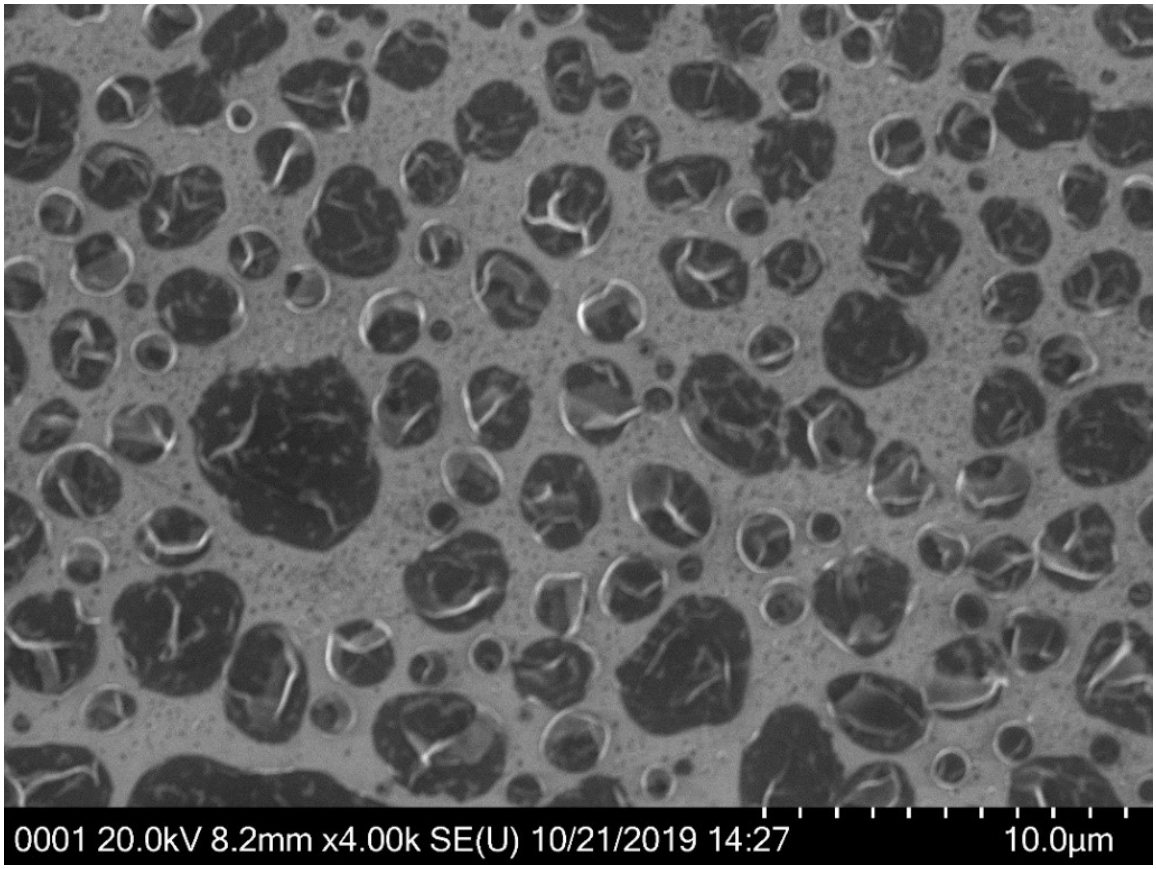


**Figure 3.4: SEM Image of TAPB-PDA COF synthesized in 15 seconds, sonicated in acetone and dropcast on silicon, showing features tentatively attributed to exfoliated COF sheets.**

Drop-casting the sonicated COF suspensions, and subsequent analysis using SEM provided images such as those shown in Figure 3.3 and 3.4, above. The sonicated COFs break apart into aggregated particles, and some isolated sheet-like structures as seen in Figure 3.3 and 3.4. Because of the large amount of large aggregated particles, the sonicated suspensions were centrifuged, leading to visually clear solutions with significant Rayleigh scattering when examined with a green laser (532 nm) as seen in Figure 3.5, below.

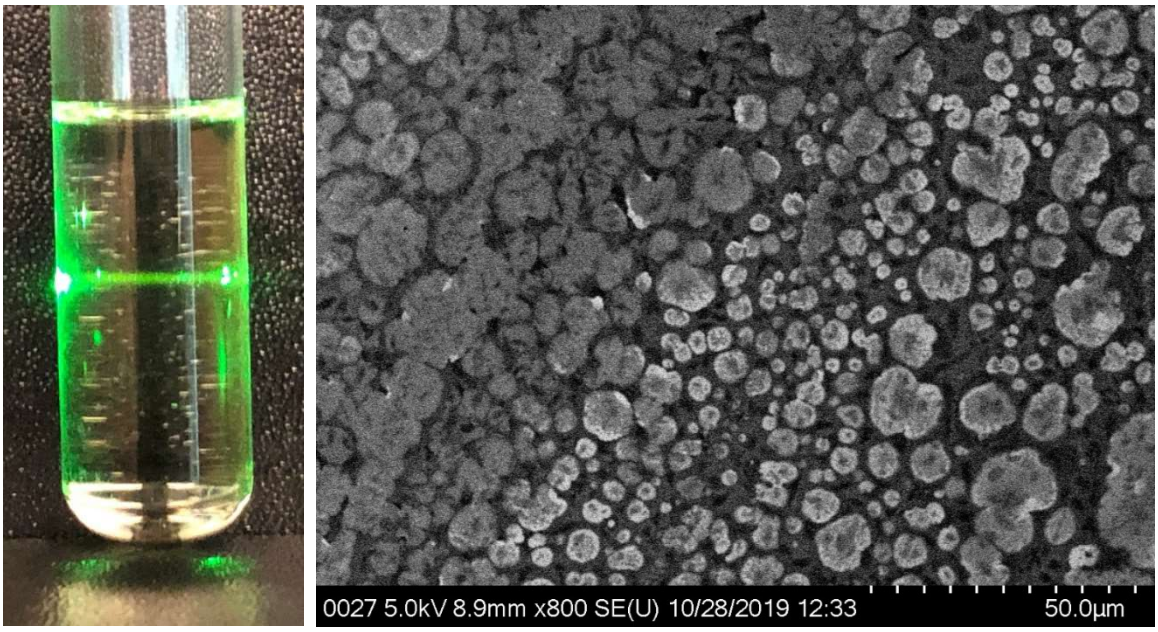


**Figure 3.5 Left: Sonicated TAPB-PDA COF in THF then centrifuged, showing distinct Rayleigh scattering when illuminated with a 532 nm laser. Right: SEM image of drop-cast TAPB-PDA COF supernatant after sonication and centrifugation in THF.**

The centrifuged TAPB-PDA COF suspensions drop-cast from THF showed structures that can be interpreted as nanosheets when viewed under the SEM, as seen in Figure 3.5, above. SEM does not provide the necessary resolution to confirm the crystallinity of these sheet-like structures, so the same procedure was repeated with the resulting centrifuged suspension drop-cast onto TEM grids instead. These were shipped to Northwestern University, and imaged by Ioaninna Castano in the Dichtel Group. Two representative images of TAPB-PDA COF nanosheets drop-cast onto a TEM grid are shown below in Figure 3.6. Experimental details for the TEM imaging conditions can be found in the Section 3.10.2.

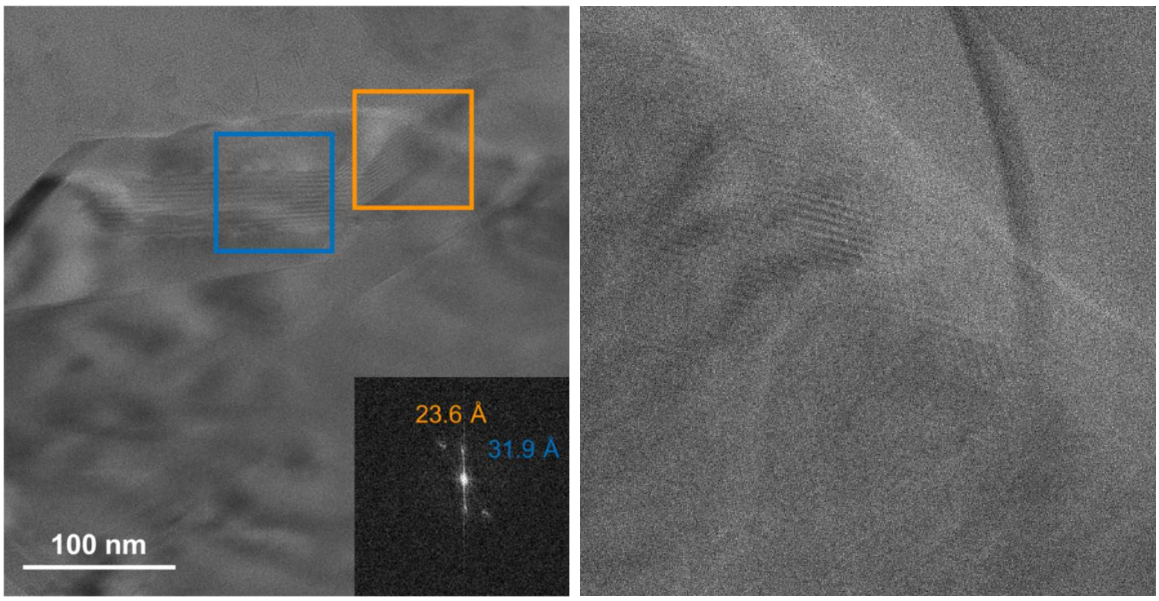


**Figure 3.6: TEM images of TAPB-PDA COF sonicated in THF and drop-cast onto a TEM grid. The left image shows inset areas where diffraction analysis was performed, showing a diffraction periodicity of 31.9 Å corresponding to the TAPB-PDA COF pore size.**

The hexagonal pores of the TAPB-PDA COF are visible, and diffraction analysis shows a periodicity of 31.9 Å, which agrees with the predicted COF structure. This shows that at 15 seconds after the addition of acetic acid, crystalline material has formed, though it is not visible to *ex-situ* measurement techniques.

The TEM images obtained by Ioaninna Castano, in combination with the *in-situ* XRD measurements obtained in collaboration with Austin Evans show that crystalline material forms very quickly after the addition of acetic acid. Based on the lack of change in the *in-situ* XRD intensity, and the lack of narrowing of the (100) peak, the crystalline domain size is not noticeably changing during the time period examined. A possible explanation for these observations, is that the aldehyde and amine monomers very rapidly condense to form

small nanosheets in solution, which loosely aggregate and precipitate, forming the initial solid material seen upon addition of the acetic acid catalyst. These sheets appear crystalline in the reaction solution, such as when viewed using *in-situ* XRD, but may be insufficiently oriented with each other to retain their crystallinity during isolation and activation. As the reaction continues uninterrupted, these sheets may reorient with each other, becoming more uniformly oriented with larger stacking domains, as indicated by the increasing intensity of the (001) peak after approximately one hour of reaction time. As more and more sheets stack in a single domain, the COF likely becomes more structurally rigid, and better able to withstand $scCO_2$ activation. TAPB-PDA COF, being relatively fragile towards activation as seen in Chapter 2, does not show signs of crystallinity after vacuum activation until the COF has had days to rearrange itself. This potential crystallization behavior is shown conceptually in Figure 3.7, below, and is compared to the amorphous-to-crystalline theory presented by Smith *et al.*

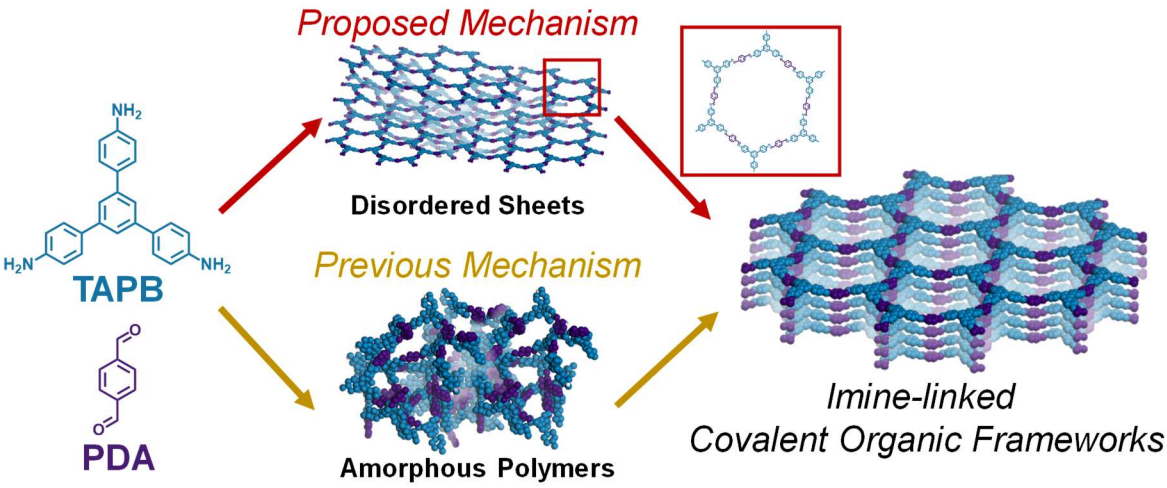


**Figure 3.7: Conceptual COF synthesis and crystallization mechanisms by Smith *et al.* (Bottom) and proposed here (Top).**

Based on the *ex situ*, *in situ* and TEM data obtained for TAPB-PDA COF, there is certainly crystalline material at very early stages of the reaction. However, while it is straightforward to detect the presence of crystalline material, proving the absence of amorphous material is significantly more challenging. Surface analysis is a very powerful technique for examining COF structure, but requires isolation and activation of the COF materials. Activation using $scCO_2$ is very gentle when applied to a 'mature' COF, but appears to be insufficiently gentle to activate the very first crystalline species that are detectable using *in situ* XRD, and visible via TEM after sonication. XRD is not sensitive towards amorphous species, and so the mechanism proposed by Smith *et al.* cannot be disproven at this point, though based on the saturation in the *in situ* XRD signal within 15 minutes it can be argued against. There is enough evidence to propose an alternate mechanism where the 2D imine-linked COF initially forms crystalline 2D sheets which then over time orient with one another in order producing the final layered COF structure composed of multiple stacked sheets. The stacked COF sheets together are then stable enough to be isolated and activated without experiencing significant structural distortions. The implications of this are expanded upon in Chapter 4.

An activation experiment was performed in order to further support this potential COF formation mechanism. A synthesis of TAPB-PDA COF was prepared in the usual manner presented in Section 2.11.4, then allowed to react for 60 seconds after the addition of the acetic acid catalyst. The COF solids were then isolated by filtration, rinsing thoroughly with methanol prior to $scCO_2$ activation. In contrast to other samples however, this sample was allowed to equilibrate in the supercritical phase of the $scCO_2$ activation process for 72 hours prior to depressurization and subsequent analysis. In the work by Sick *et al.* discussed

in Section 2.6, a lateral sheet displacement mechanism is proposed to explain the observed reorganization of COFs after disruption during solvent exposure (or vacuum activation). In their $scCO_2$ method however, the COFs are allowed to equilibrate in the supercritical phase for two hours, rather than the 15 minutes used for the samples presented here. It is clear that for fully-formed crystalline COF that $scCO_2$ activation does allow for reorganization of displaced COF sheets. If at the early stages of COF synthesis, the principal reorganization process yielding crystalline materials is organization of 2D sheets, then extended equilibration time in $scCO_2$ may improve the crystallinity of the material obtained. However, if the initial solids are an amorphous, highly-crosslinked gel-like material, then no amount of equilibration time is likely to be beneficial since the crosslinked gel cannot reorganize in the same way. The sample prepared using the 72-hour equilibration was analyzed via PXRD, and the resulting pattern was compared to another identically synthesized TAPB-PDA COF sample which was allowed to equilibrate for the standard 15 minutes during $scCO_2$ activation. These PXRD patterns are shown below in Figure 3.8.

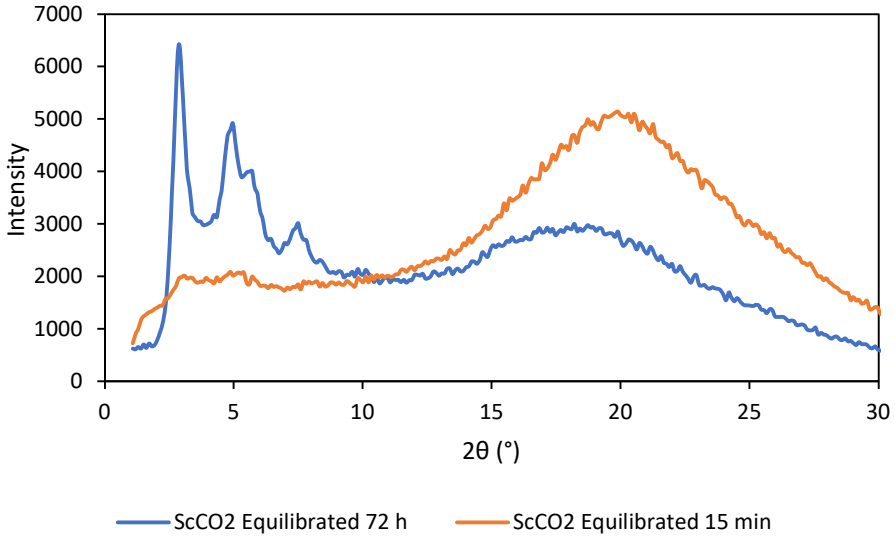


**Figure 3.8. PXRD pattern of a TAPB-PDA COF synthesized in 60 seconds and equilibrated for 72 hours in supercritical CO2 compared to a sample equilibrated for 15 minutes.**

The PXRD pattern clearly shows significant improvement in the diffraction intensity of the TAPB-PDA COF with the (100), (110), (200), and (210) peaks apparent. The PXRD pattern also shows a reduction in the broad signal indicative of amorphous material at 17 to 23 °2θ. The extended equilibration time has clearly improved the COF crystallinity, and implies a sheet reorganization mechanism like that reported by Sick *et al.* and others for fully formed COFs.[127, 135-136] This result, combined with the direct observation of COF sheets in early samples of TAPB-PDA COF and TAPB-OMePDA COF cast doubt on the notion that imine-linked 2D COFs precipitate as amorphous networks, and show that crystalline materials exist very early in the COF reaction.

## 3.5 *Ex Situ* Comparison of the Initial Formation of Covalent Organic Frameworks with Tri- and Tetra-Functional Monomer Nodes

A series of four COFs, TAPB-PDA COF, TAPB-OMePDA COF, TAPPy-PDA COF and TAPPy-OMePDA COF were synthesized in timed reactions and examined ex situ in order to examine several aspects of the formation of 2D imine COFs. The effect of alkoxy-substitution compared to the unsubstituted COF, the effect of node selection on COF formation, and the effect of competing lattice geometries on COF formation were examined.

The four COFs examined are shown below in Figure 3.9.

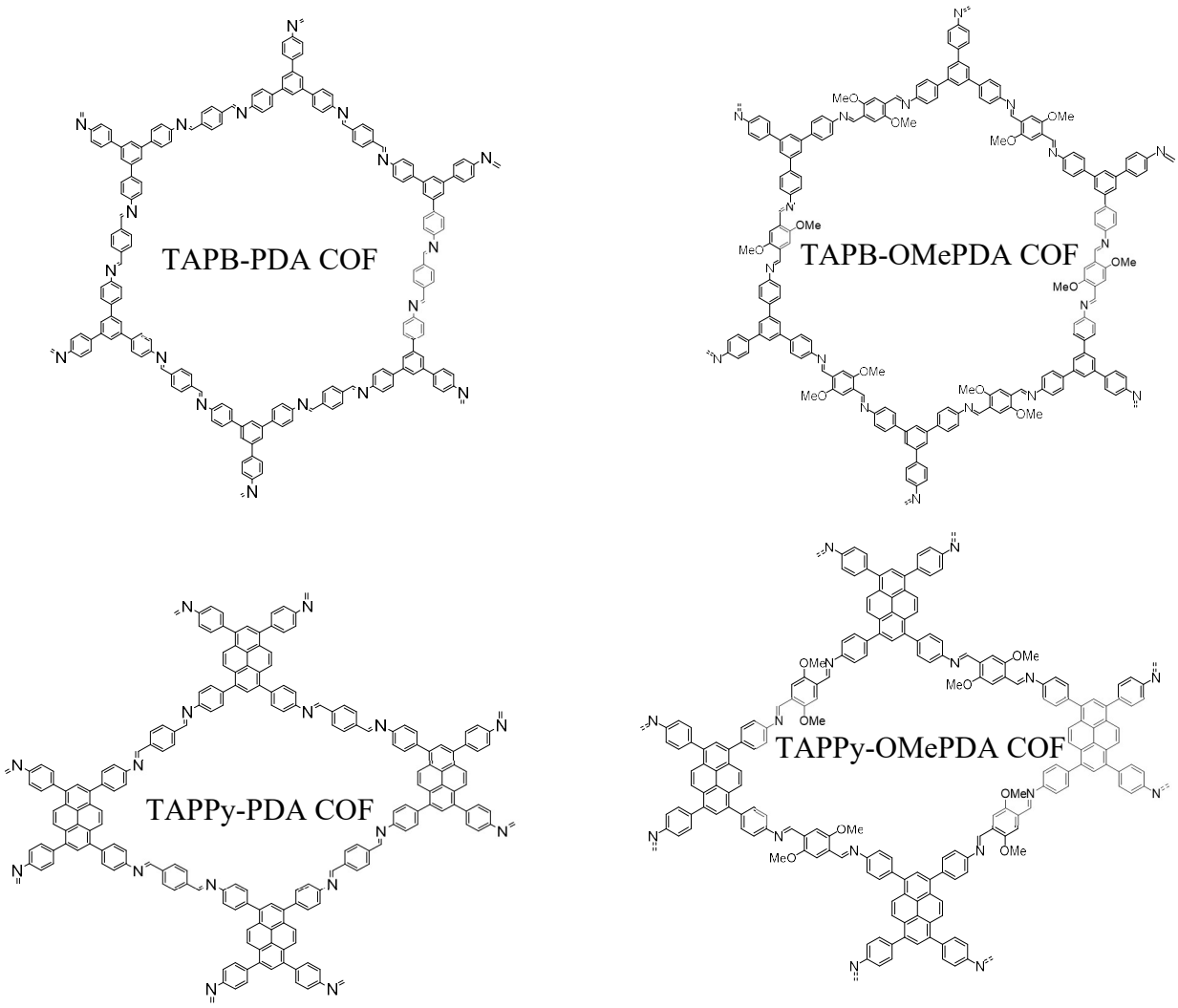


**Figure 3.9: Structures of TAPB-PDA COF, TAPB-OMePDA COF, TAPPy-PDA COF and TAPPy-OMePDA COF.**

TAPB-PDA COF, and the related TAPB-OMePDA COF are hexagonal pored COFs due to the trifunctional TAPB node and the linear dialdehyde monomers selected. TAPPy however is a tetrafunctional amine based on pyrene. This monomer can produce two different geometrically viable COF lattices when condensed with a linear dialdehyde, shown below in Figure 3.10, a tetragonal lattice with rectangular or rhombus shaped pores or a Kagome lattice with two distinct pore shapes, hexagonal and triangular.

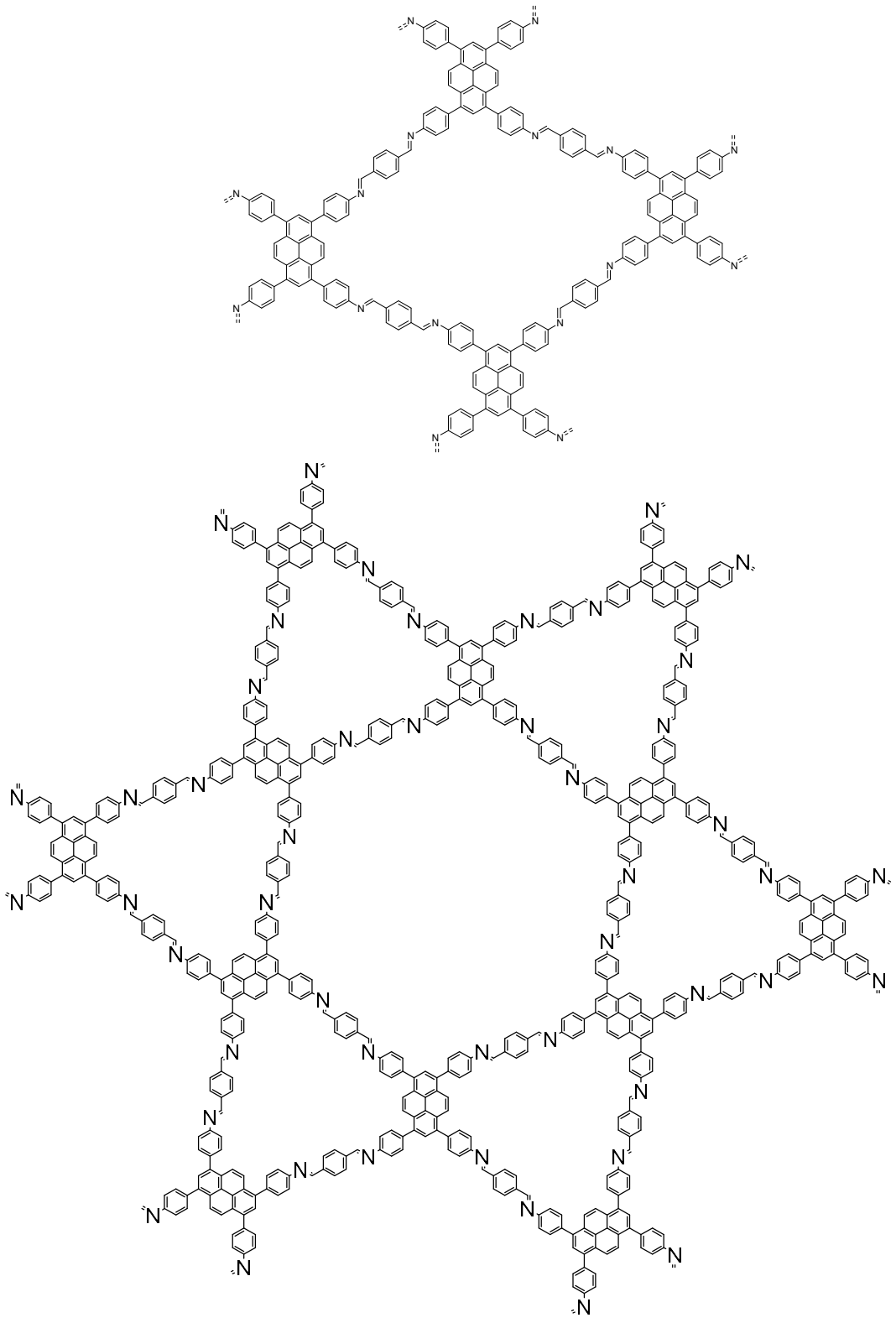

**Figure 3.10: TAPPy-PDA tetragonal lattice (top) and Kagome lattice (bottom)**

The presence of two possible lattices may complicate the initial formation of the COF depending on the favorability of the two structures relative to one another. If the lattices are equally favorable, the COF may even form as a mixture of crystal domains with either of the two lattice types. If one is slightly more favorable, both lattices may be present among the early COF domains, with the less favorable lattice slowly converting to the more favorable as the reaction continues. This exchange may cause COF samples isolated during this period to appear amorphous, or to display a combination of diffraction signals from both possible structures when analyzed using XRD.

COF samples were synthesized according to the standard method presented in Chapter 2, then the COF solids were isolated after 15 seconds, 60 seconds, 3 minutes, 15 minutes, 30 minutes, 1 hour, and 4 hours. These samples were analyzed via PXRD and nitrogen adsorption/desorption. PXRD patterns are shown in Section 3.10, in Figures 3.28 thorough 3.31. Nitrogen adsorption/desorption isotherms and pore size distributions are shown in the Section 3.10.5 as well, Figures 3.32 through 3.35 and Figures 3.36 through 3.39 respectively. Shown below in Figure 3.11 are plots of the (100) peak intensity versus reaction time for TAPB-PDA COF, TAPB-OMePDA COF, TAPPy-PDA COF and TAPPy-OMePDA COF, as well as the measured $S_{BET}$ values for the four COFs versus reaction time.

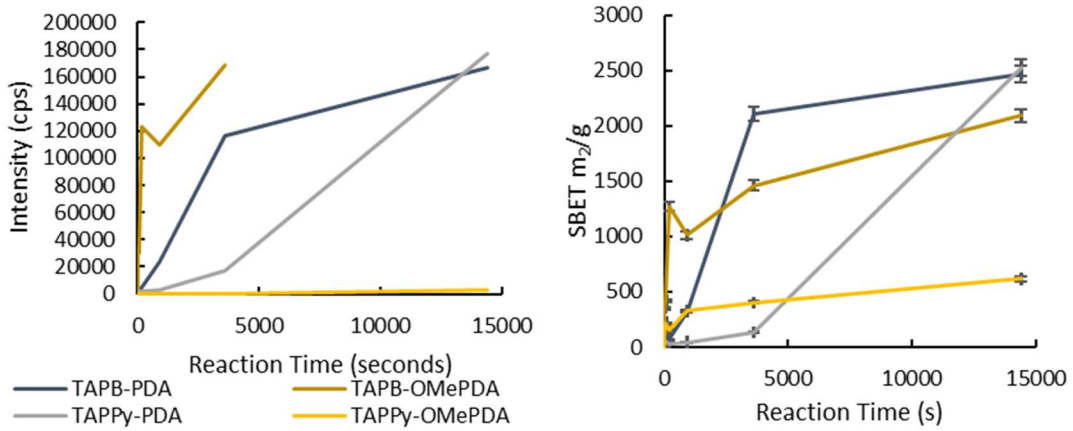


**Figure 3.11: Left: (100) diffraction peak intensity versus reaction time for TAPB-PDA COF, TAPB-OMePDA COF, TAPPy-PDA COF, and TAPPy-OMePDA COF. Right: Measured $S_{BET}$ values for the same four COFs. Error bars represent the 3% instrumental error in the measurement.**

From the data obtained it is evident that TAPB-PDA COF and TAPB-OMePDA COF initially crystallize much faster than the TAPPy-based COFs tested. The fastest crystallization, and fastest increase in $S_{BET}$ was observed for TAPB-OMePDA COF. Two factors may be at play here. Firstly, the aldehyde used, OMePDA, may be more reactive than the unsubstituted PDA due to resonance stabilization of the protonated aldehyde. Secondly, the increased crystal stacking energy of the TAPB-OMePDA COF versus TAPB-PDA COF, calculated by Xu *et al.* for the full COF, and by Wang *et al.* for structurally similar macrocycles, may cause more favorable interactions between the initial COF oligomers, resulting in faster orientation into the lattice.[20,137]

Both TAPPy-based COFs show a slower growth in the (100) diffraction peak, following a linear trend. If the amorphous to crystalline mechanism for COFs is invoked, this could be

due to slower reorientation of monomers due to the increased number of imine bonds per node. Alternately, if the COF initially forms a precipitate composed of a random mixture of Kagome and tetragonal network domains, the interconversion between the less favored Kagome lattice, and the more favored tetragonal lattice could explain the observed linear increase in the (100) peak intensity for the tetragonal lattice that is eventually isolated. The pore size distribution for the early TAPPy-PDA COF samples shown in Figure 3.38 in Section 3.10 show that there are a range of pore sizes from 14-30 Å during the early stages of COF formation, which then coalesce extremely rapidly to the 23 Å pore consistent with a purely tetragonal COF lattice.

*Ex situ* time trials become impractical for high temporal resolution experiments and are potentially complicated by structural distortions occurring during activation of the COF materials. To gain further insight into the differences in the initial formation of TAPB-PDA COF, TAPB-OMePDA COF, TAPPy-PDA COF and TAPPy-OMePDA COF, monomer samples were sent to collaborators at Northwestern University for *in situ* analysis.

## 3.6 *In Situ* Examination of the Initial Formation of Covalent Organic Frameworks with Tri- and Tetra-Functional Monomer Nodes

Monomer samples of TAPB, TAPPy, and OMePDA were sent to Austin Evans and Northwestern University. The COF synthesis reactions were set up as described in the Section 3.10.3, then a capillary full of the COF reaction material was placed in the beamline at the APS for X-Ray diffraction. The COF synthesis was monitored from a time of 90 seconds after the addition of acetic acid until 45 minutes after the acid addition, and the XRD data obtained for the (100) peak of each COF was baseline corrected and plotted as

a surface plot using MATLAB. This data is shown below in Figure 3.12. Note that the data for TAPPy-PDA COF and TAPPy-OMePDA COF is not baseline corrected due to the lack of an apparent (100) peak during the period examined.

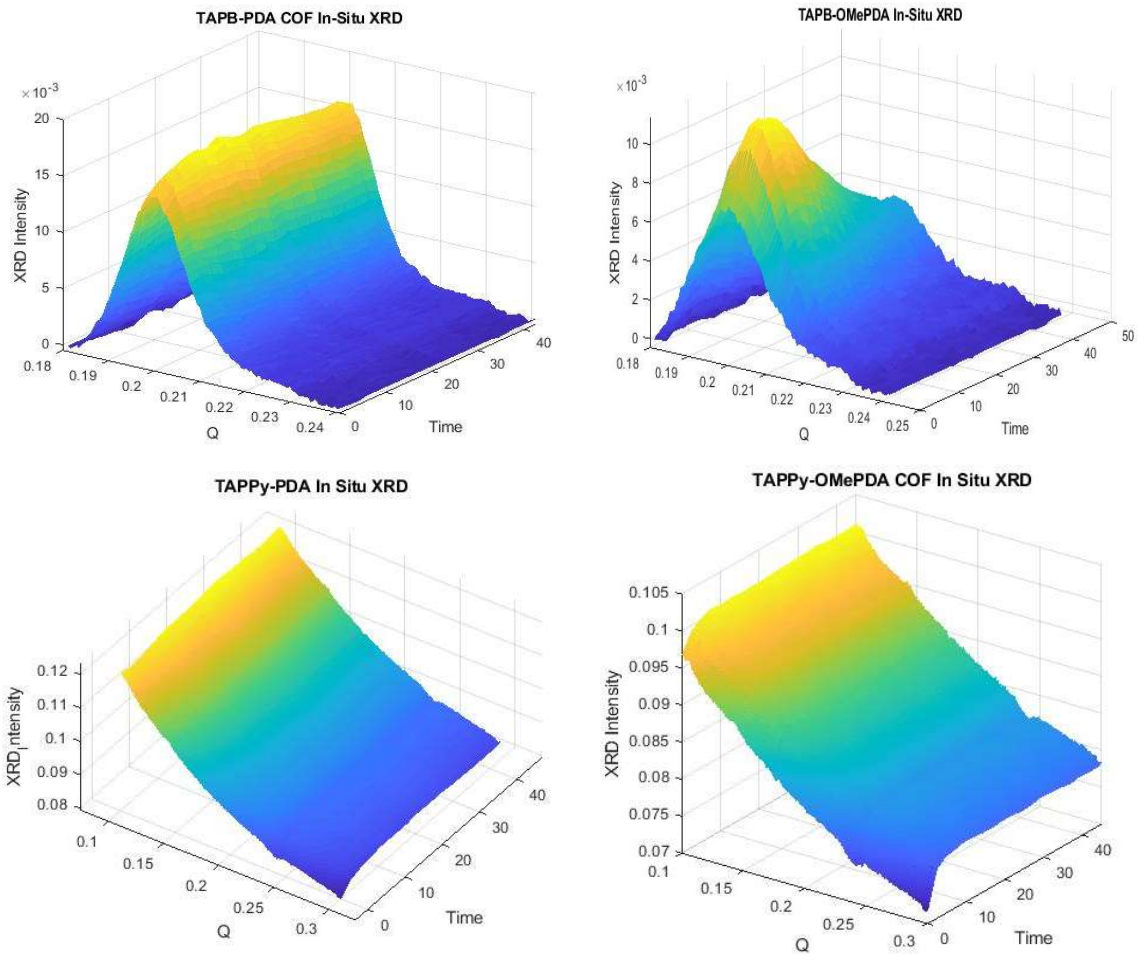


**Figure 3.12: Top Left: Surface plot of the baseline corrected TAPB-PDA COF (100) diffraction peak during the first 40 minutes of the COF synthesis reaction. Top Right: Surface plot of the baseline corrected TAPB-PDA COF (100) diffraction peak during the first 40 minutes of the COF synthesis reaction. Bottom Left: Surface plot of the un-corrected area where the (100) diffraction peak of TAPPy-PDA COF would appear during the first 40 minutes of the COF synthesis reaction. Bottom Right: Surface plot of the un-corrected area where the (100) diffraction peak of TAPPy-OMePDA COF would appear during the first 40 minutes of the COF synthesis reaction.**

Similarly to the *ex situ* results, TAPPy-based COF show the slowest formation of crystalline material, showing no observable diffraction within the time period measured. However, the TAPB-based COFs do show diffraction attributed the (100) peak, as seen in Figure 3.12. Here however, TAPB-PDA shows the fastest growth, having already attained its maximum measured diffraction intensity as soon as the measurement begins. TAPB-OMePDA COF shows increases in diffraction intensity for the first 10 to 15 minutes of the measurement, before beginning to lose intensity, possibly due to degradation of the COF structure due to the X-ray radiation. This result implies that TAPB-PDA COF forms faster, which contrasts with the *ex situ* results. Therefore, it is possible that TAPB-PDA COF forms faster, but is more susceptible to structural distortions during activation as seen in Chapter 2. This causes the *ex situ* measurements to underestimate the extent of crystallization of the COF during the early stages of the reaction, giving the appearance that the more robust TAPB-OMePDA COF is forming faster. This result highlights the importance of understanding the effect of isolation and activation on the COF structure, as well as the utility of *in situ* examination of the COF synthesis and crystallization process. *In situ* examination does not require any isolation of the COF material, and thus the potential for changes to the COF structure is avoided when the COF is examined directly. However, subjecting a COF to constant high-intensity X-ray irradiation, such as that from the synchrotron source used here, may cause degradation of the sample during longer scans. Unfortunately, *in situ* analysis of the surface area of the COF, which could provide additional insight, is not possible since surface analysis requires that the COF be dry and free of guest molecules. Regardless, *in situ* monitoring of COF formation could be a powerful tool for better understanding the formation of COFs.

## 3.7 *In Situ* Examination of the Effect of Monomer Concentration of TAPB-PDA COF Crystallization

The effect of the initial monomer concentration on the COF crystallization process was examined *in situ* by comparing the development of crystalline diffraction in diluted monomer solutions catalyzed by equal amounts of 10.5 M acetic acid. The original COF monomer concentration was examined at its original concentration, and at half, one quarter, and one eighth of the original concentration. These samples were analyzed in a similar manner as the TAPB-PDA COF samples presented in Section 3.3, however, the timing of the XRD scans is different. Bursts of five scans separated by two seconds were taken, each burst was separated by a time of approximately two minutes, this is clearly visualized later in Figure 3.14. The monomer concentrations used in this series of reactions is shown below in Table 3.1.

**Table 3.1: *In Situ* TAPB-PDA COF monomer concentrations**

| Sample | Dilution Factor | TAPB mM | PDA mM | Solvent Volume | Acid Volume/M | Total Volume |
|---|---|---|---|---|---|---|
| 3.7.A | 1X | 63.3 | 95.0 | 1.0 mL | 0.5 mL / 10.5 M | 1.5 mL |
| 3.7.B | 2X | 31.7 | 47.5 | 1.0 mL | 0.5 mL / 10.5 M | 1.5 mL |
| 3.7.C | 4X | 15.8 | 23.8 | 1.0 mL | 0.5 mL / 10.5 M | 1.5 mL |
| 3.7.D | 8X | 7.9 | 11.9 | 1.0 mL | 0.5 mL / 10.5 M | 1.5 mL |

The raw XRD data for each sample was baseline corrected using a polynomial fit, resulting in the XRD patterns shown in Figure 3.53 through Figure 3.56 in Section 3.10.5. The surface plots of these scans are shown below in Figure 3.13.

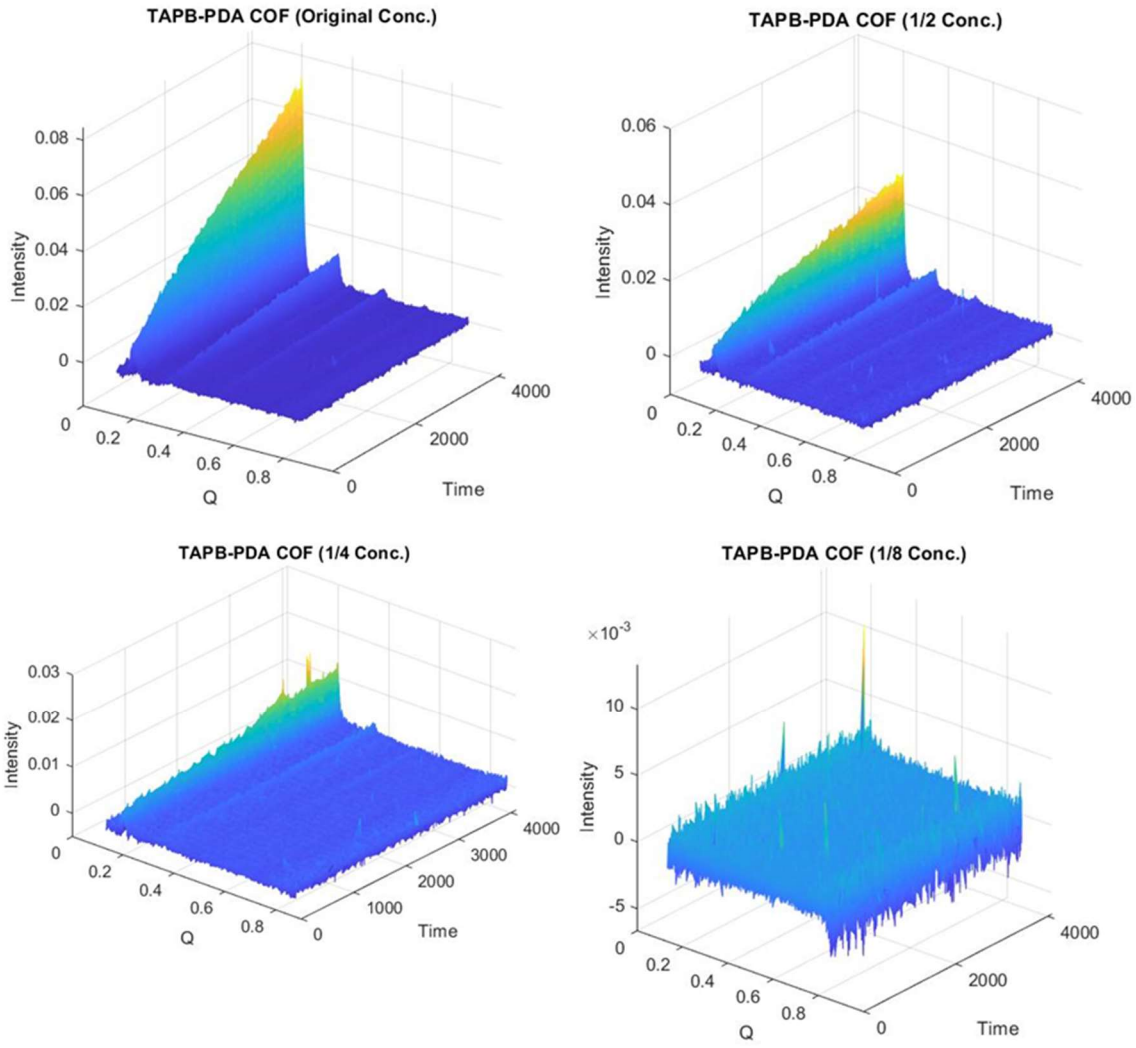


**Figure 3.13: Surface plots of TAPB-PDA COF *in situ* XRD data. Top left: TAPB-PDA COF synthesis at original concentration (sample 3.7.A). Top Right: TAPB-PDA COF synthesis at half concentration (sample 3.7.B) Bottom Left: TAPB-PDA COF synthesis at one-quarter concentration (sample 3.7.C) Bottom Right: TAPB-PDA COF synthesis at one-eighth concentration (sample 3.7.D)**

The intensity of the (100) peak for each sample was plotted against the reaction time, resulting in the linear-appearing plots shown below in Figure 3.14.

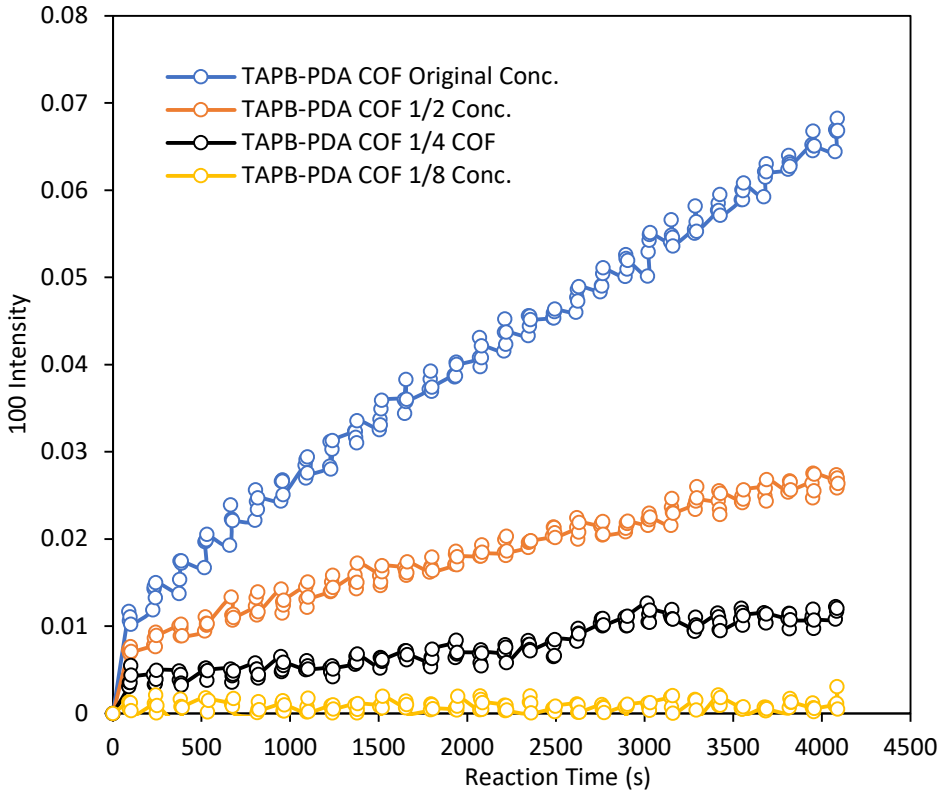


**Figure 3.14: TAPB-PDA COF baseline-corrected *in situ* (100) peak intensity plotted against reaction time for samples with different initial monomer concentrations.**

Linear fits of the resulting (100) intensity versus reaction time plots show that the monomer concentration is proportional to the slope of the (100) intensity. It is critical to note here, that the total concentration of the COF resulting from the monomer condensation is also decreasing by a proportional amount. The diffraction signal will be proportional to the amount of crystalline material in the x-ray beam, meaning that the maximum diffraction

obtained for each diluted sample will be reduced by a proportional amount. The sample that is diluted by half will show half of the maximum diffraction of the undiluted sample.

This behavior is consistent with a theoretical model for imine-linked COF formation where the amine and aldehyde monomers initially condense rapidly into a non-diffracting precipitate species, which then orients to the crystalline diffracting form through a process which is only dependent on the acid concentration and the temperature of the reaction medium.

From a COF synthesis standpoint this is interesting, since it means that so long as there is some critical concentration of monomers to initially react and precipitate, the COF crystallization process will follow the same pathway regardless of the actual monomer concentration. From this experiment, it is not clear what effect imbalances in monomer stoichiometry will have on the formation of the COF, but it is shown that the initial concentration of monomers does not affect the crystallization process.

The initial concentration of the amine and aldehyde monomers may influence other COF properties such as the crystallite size. To probe this, the (100) peak was integrated using the integral width method, which calculates the width of a rectangle of equal area to the peak integral. Peak integrals were estimated using the rectangle method, also known as the midpoint rule. In crystallographic analysis, the integral width can be used in place of the peak-width at half maximum (FWHM) when applying the Scherrer equation, which is described in Section 1.5.1. This analysis resulted in a lower bound for the crystallite size for each XRD scan in the dataset shown in Figure 3.13. The crystallite minimum size is

shown in Figure 3.15 below, on the left is the individual calculated crystallite sizes plotted against reaction time, on the right is the averaged values for each burst of 5 scans.

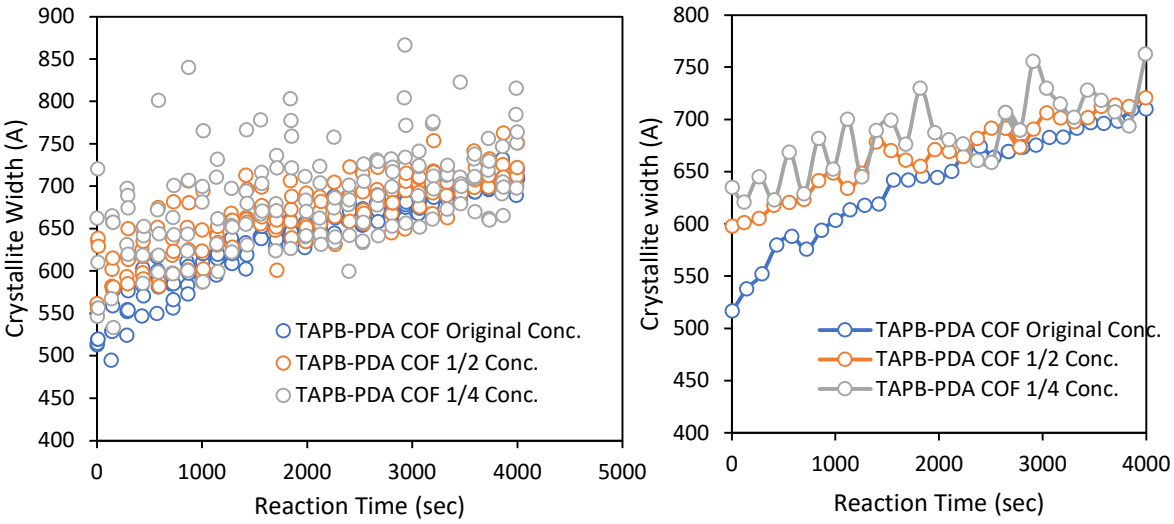


**Figure 3.15: Minimum crystallite width of TAPB-PDA COF at different initial monomer concentrations plotted against reaction time. Left: Calculated crystallite width for individual *in situ* scans. Right: Averaged crystallite widths from each burst of five *in situ* XRD scans.**

Based on the calculated crystallite widths from Figure 3.15, it is seen that the concentrated TAPB-PDA COF synthesis initially produces smaller COF crystallites than the half and quarter concentration TAPB-PDA COF samples, though all the experiments eventually produce similarly sized crystallites of approximately 700 Å in width. This corresponds to COF crystallites which are on average approximately 27 pores wide. Lower initial monomer concentrations may allow newly nucleated COF sheets to remain isolated in solution for a longer time before aggregating with additional COF sheets, resulting in larger sizes. Once aggregated the solid-state rearrangement of the COF results in further growth

and orientation of COF domains relative to one-another. Before concrete conclusions about the true nature of the initial stages of the crystallization of TAPB-PDA, additional experiments are needed to corroborate the conclusions drawn from the Scherrer analysis performed here. Direct observation of the newly formed COF crystallites would be ideal, though difficult to realize experimentally. Potential future research paths for further elucidating these initial conclusions and observations are discussed further in Chapter 4.

## 3.8 Examination of the Formation of Alkoxy-Substituted Two-Dimensional Imine-Linked Covalent Organic Frameworks

Pore surface engineering is a useful technique for imparting additional functionality to covalent organic frameworks.[138] Pendant groups within the pore of the COF can impart catalytic, separation, or sensing capabilities.[19, 139] However, the effect of adding potentially bulky side chains on the COF monomers on the formation and crystallization of COF materials has not been systematically studied. To this end, a series of 2,5-dialkoxyterephaldehyde monomers was synthesized following a literature method and polymerized into modified TAPB-based COFs following the methods presented earlier.[134] The synthetic route to the modified PDA monomers is shown below in Figure 3.16.

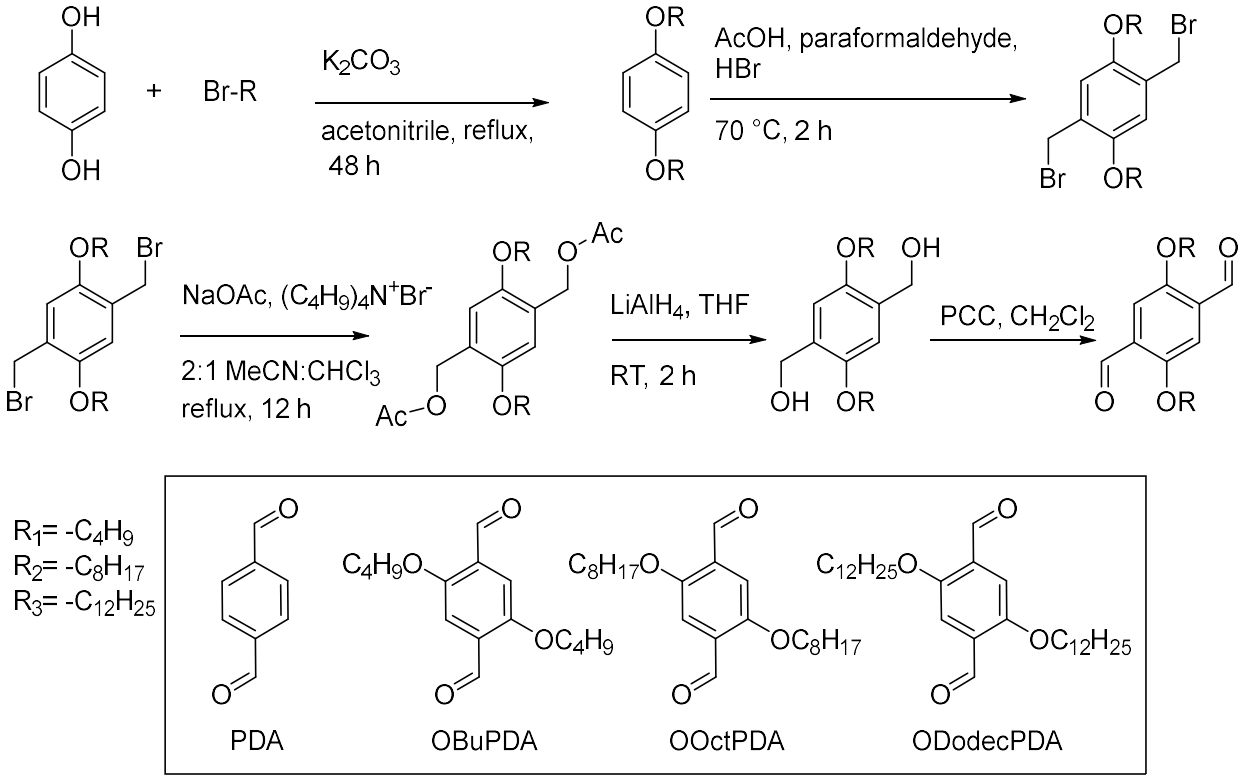


**Figure 3.16: Synthetic route yielding 2,5-dialkoxyPDA monomers[134]**

These four monomers, 2,5-dimethoxyPDA (OMePDA), 2,5-dibutoxyterephthaldehyde (OBuPDA), 2,5-dioctyloxyterephthaldehyde (OOctPDA), and 2,5-didodecyloxyterephthaldehyde (ODodecPDA) incorporate increasingly larger alkoxy groups, and were polymerized into COFs using TAPB as a node. The COF synthesis method is shown below in Figure 3.17.

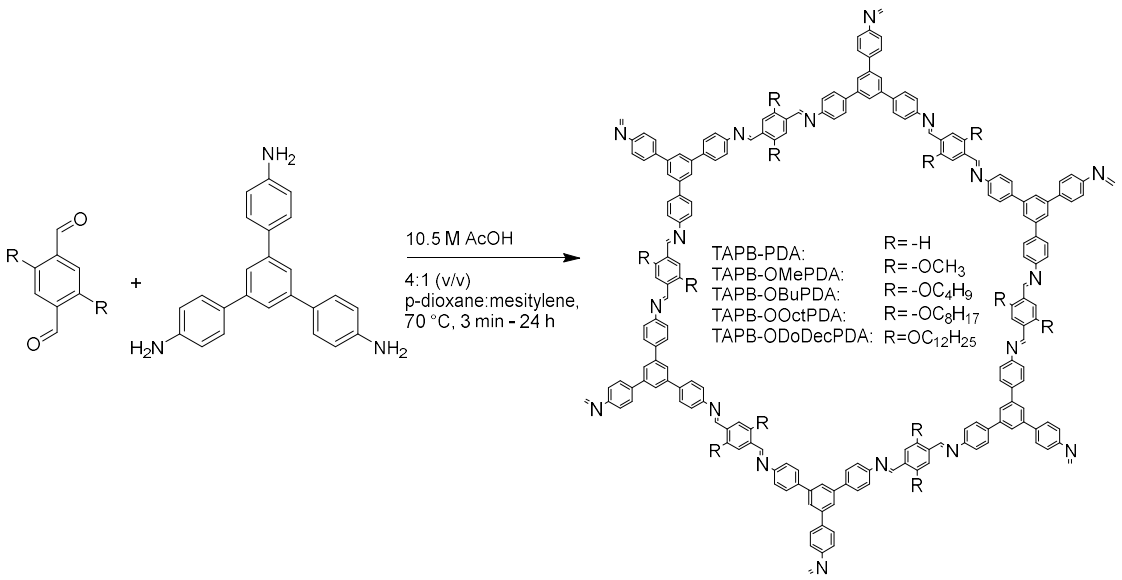


**Figure 3.17: Synthesis of dialkoxy-functionalized TAPB-PDA COFs**

The purpose of this series of experiments was to examine the effect of the inclusion of alkoxy groups of increasing size on the COF crystallization process, and on the properties of the resulting network. If COFs undergo an amorphous-to-crystalline transition as proposed by Smith *et al.*, then the inclusion of side chains with significant steric bulk may inhibit the error correction during the amorphous to crystalline transition by restricting rotation and rearrangement.[3] If this is the case, then the larger alkoxy chains may cause the resulting COF to take a longer time to rearrange from the initial amorphous species to the crystalline COF. Additionally, the inclusion of large side chains may inhibit the stacking between adjacent COF layers, resulting in disruption to the COF structure. This may be detectable via PXRD if the interlayer spacing is affected, either by the broadening or disappearance of the (001) diffraction peak corresponding to the interlayer spacing of the

COF. Additionally, disruption of the interlayer stacking behavior of the COF may also allow for easier exfoliation of the material into single or few-layer structures.

These COFs were isolated at different times during the reaction and analyzed using PXRD and nitrogen adsorption/desorption. The results for TAPB-PDA COF and TAPB-OMePDA COF were discussed previously and are found in the Section 3.4. The resulting PXRD patterns for TAPB-OBuPDA COF, TAPB-OOctPDA COF, and TAPB-ODodecPDA COF are included in the Section 3.10.5, as Figures 3.40 through 3.42. The corresponding nitrogen adsorption/desorption isotherms are included as Figures 3.43 through 3.45 and the corresponding pore size distributions are included as Figures 3.46 through 3.48. Below in Figure 3.18, the intensity of the (100) diffraction peak is plotted against reaction time for the four COFs, with TAPB-PDA COF included for context. The measured $S_{BET}$ values for the COFs are also included in Figure 3.18.

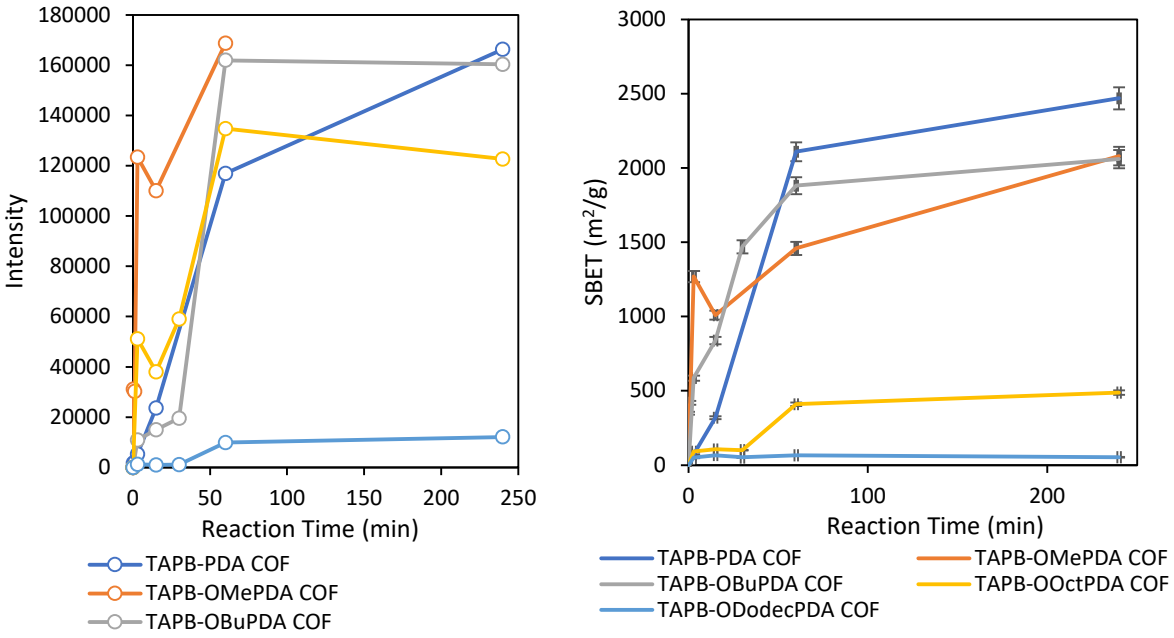


**Figure 3.18: Left: (100) peak intensities versus reaction time for TAPB-PDA COF, TAPB-OMePDA COF, TAPB-OBuPDA COF, TAPB-OOctPDA COF, and TAPB-ODodec PDA COF. Right: Measured $S_{BET}$ values for COFs. Error bars are the 3% instrumental error in the $S_{BET}$ measurement.**

Based on the *ex situ* data presented in Figure 3.18 several statements can be made: TAPB-OMePDA COF appears to form the most rapidly of the COFs measured here, rapidly producing a highly crystalline structure within 1 hour based on the (100) diffraction. TAPB-PDA COF, TAPB-OBuPDA COF, and TAPB-OOctPDA COF show similar crystallization behavior when examined *ex situ.* One expected trend is that the inclusion of alkoxy chains of increasing size restricts the available pore volume of the COF, and thus lowers the measured $S_{BET}$ in the case of TAPB-OOctPDA, and especially in the case of TAPB-ODodecPDA. The relationship between the alkoxy group chain length, and the measured $S_{BET}$ of the COF is shown below in Figure 3.19.

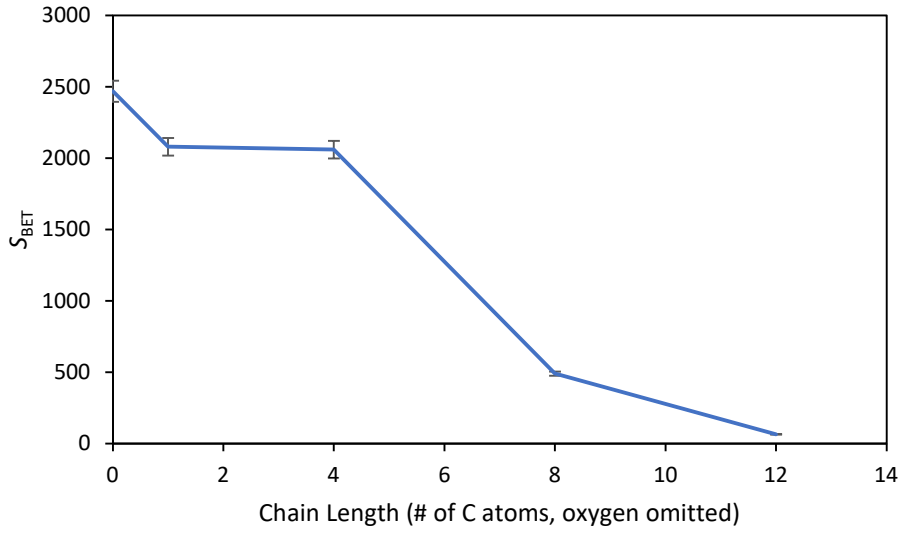


**Figure 3.19: Length of pendant alkoxy chain vs measured $S_{BET}$ in TAPB-2,5-dialkoxyPDA COFs. Error bars are the 3% instrumental error in the $S_{BET}$ measurement.**

The large dodecyloxy chains in TAPB-ODodecPDA seem to greatly inhibit the formation of the COF network. The diffraction intensity is dramatically reduced, as seen in Figure 3.42 in Section 3.10.5, and the diffraction peaks are broadened, indicating either smaller domain sizes in the COF crystallites, or disorder within the structure. Also prominent is a feature at 17 to 22 °θ indicative of amorphous material.[140] Based on this data obtained for TAPB-ODodecPDA COF the inclusion of large alkoxy groups on the PDA linker has affected the COF structure.

Further evidence that the larger alkoxy chains affect the COF structure comes from analysis of the (001) peak in the *ex situ* PXRD. Here it can be seen that the larger alkoxy chains such as the octyloxy and dodecyloxy chains shift the (001) peak to smaller 2θ values, indicating a larger *d* spacing between the COF layers as seen in Figure 3.20, below.

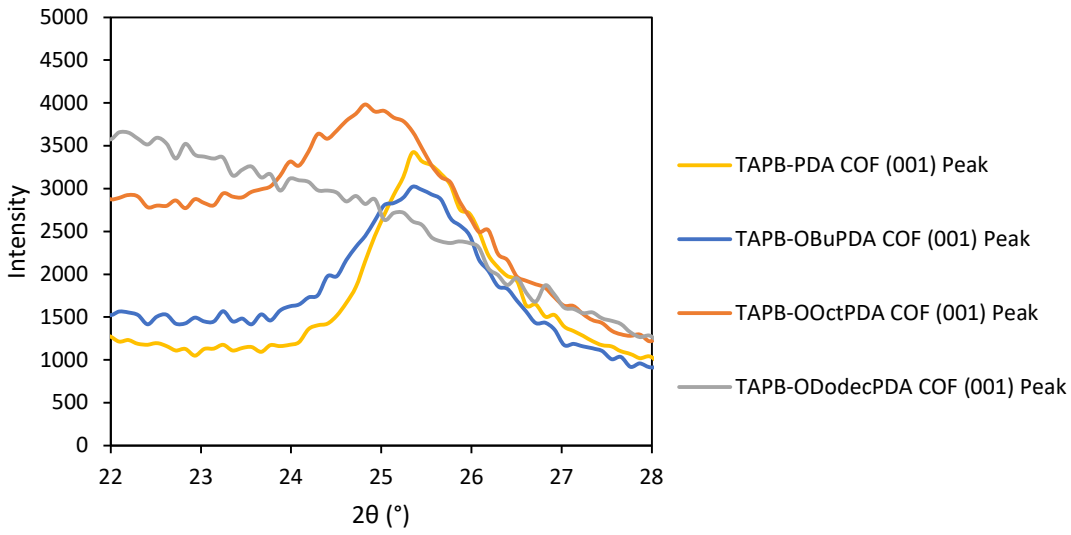


**Fig 3.20: TAPB-PDA COF, TAPB-OBuPDA COF, TAPB-OOctPDA COF and TAPB-ODodecPDA COF (001) PXRD peak showing broadening of the peak and a shift to lower 2θ values.**

The (001) peak for the TAPB-ODodecPDA COF is severely broadened but can be very roughly estimated at approximately 24 °2θ based on the asymmetric nature of the broad peak from 17° to 26° in the PXRD pattern. Using the Bragg equation, the *d*-spacing between the COF layers can be calculated, and the calculated d-spacings for TAPB-PDA COF, TAPB-OBuPDA COF, TAPB-OOctPDA COF, and TAPB-ODodecPDA COF are shown in Table 3.2, below.

**Table 3.2: Changes in COF interlayer spacing due to large alkoxy side chains.**

| COF | Pendant Group | Inter-layer spacing |
|---|---|---|
| TAPB-PDA | -H | 3.51 Å |
| TAPB-OBuPDA | $-OCH_2CH_2CH_2CH_3$ | 3.54 Å |
| TAPB-OOctPDA | $--OCH_2CH_2CH_2CH_2CH_2CH_2CH_2CH_3$ | 3.66 Å |
| TAPB-ODodecPDA | $-OCH_2CH_2CH_2CH_2CH_2CH_2CH_2CH_2CH_2CH_2CH_2CH_3$ | ~3.7 Å |

Based on the changes in the (001) peak, it shown that increasing the size of the pendant group attached to the COF linker, the spacing between layers can be increased by approximately 5%. However, this strategy also seems to have detrimental effects on the COF structure based on the broadened diffraction signals measured for TAPB-ODodecPDA COF.

*In Situ* XRD was applied in order to gain additional insight into the formation of the alkoxy-modified TAPB-PDA COFs. By avoiding isolation of the COF material, multiple data points can be obtained for the same sample. This avoids both activation induced measurement errors, and sample-to-sample variations. COF samples were prepared according to the synthetic procedure presented in the Section 3.10.3, and were analyzed using the beamline at APS in the same way as the TAPB and TAPPy-based COFs

presented in Section 3.4. Data from the *in situ* XRD scans processed using MATLAB, and the (100) peak for each sample was baseline corrected in order to obtain an accurate (100) peak intensity measurement. Surface plots of the baseline corrected (100) peaks for each COF are shown below in Figure 3.21, and plots of the full diffraction patterns are shown in Section 3.10.5 as Figures 3.49 through 3.52. The surface plot for TAPB-PDA COF is found earlier in Section 3.4 in Figure 3.12.

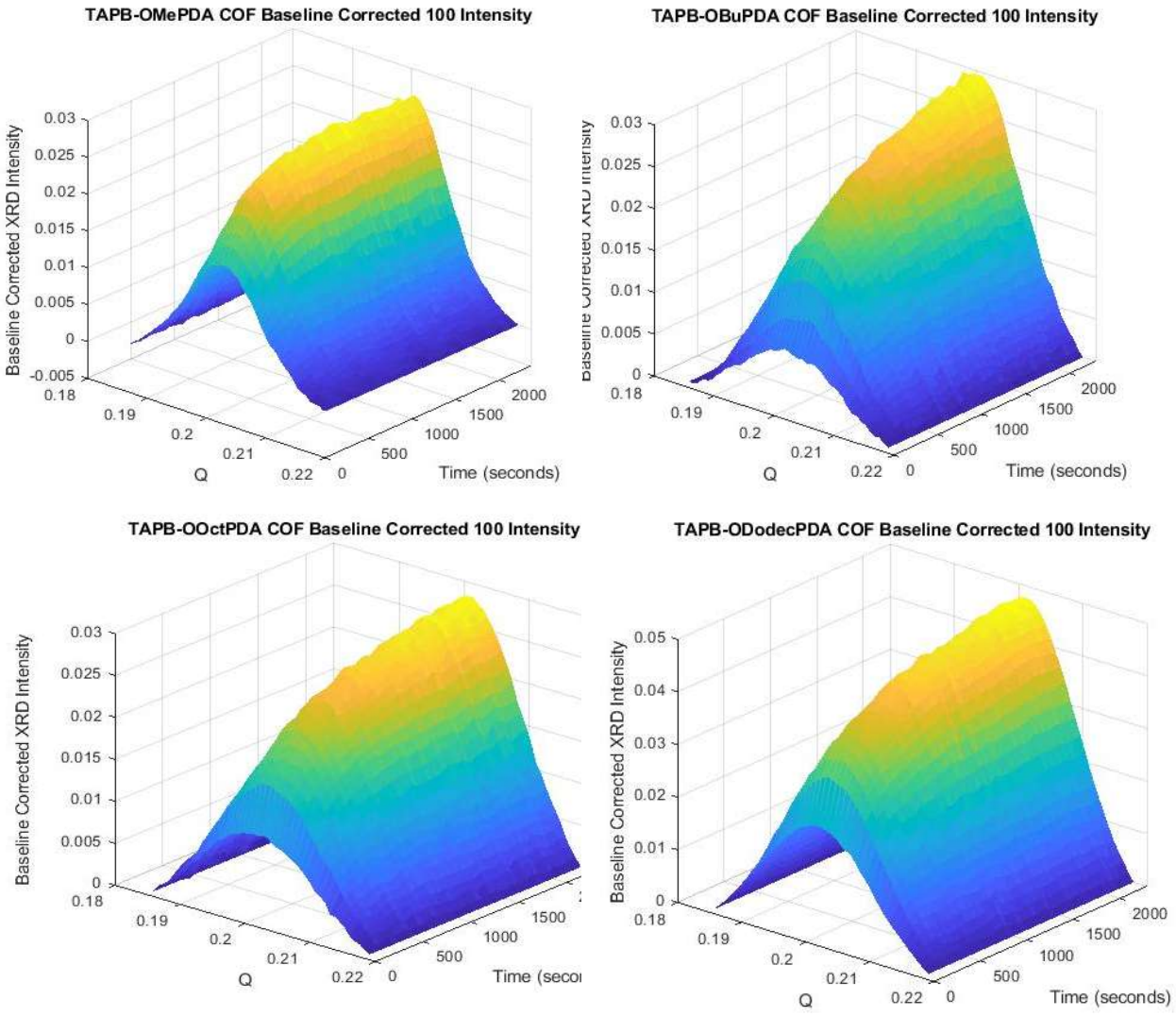

**Figure 3.21: Top Left: Surface plot of baseline-corrected TAPB-OMePDA COF (100) peak. Top Right: Surface plot of baseline-corrected TAPB-OBuPDA COF (100) peak. Bottom Left: Surface plot of baseline-corrected TAPB-OOctPDA COF (100) peak. Bottom Right: Surface plot of baseline-corrected TAPB-ODodec COF (100) peak.**

The baseline corrected intensity of the (100) peak versus reaction time for each of the 2,5-dialkoxy substituted COFs appear to follow first-order kinetics. The synthesis of the COF can be rationalized as a rapid condensation of free imine and aldehyde monomers into a non-diffracting species, which could be either an amorphous gel-like network, or a material composed of disordered COF sheets as discussed earlier. As the reaction progresses, this material reorders itself into the COF network which is visible using XRD. As shown before in Figure 3.19, the intensity of the (100) peak of the COF has a linear relationship with the $S_{BET}$ of the COF, which in turn is the most accurate measure of the quality of the COF. Therefore, for *in situ* measurements, it can be assumed that the intensity of the (100) peak is analogous to the degree of order of the COF structure as a whole. Monitoring the development of the (100) peak therefore allows for kinetics data on the COF reorganization process to be obtained.

The reaction for the reorganization of the COF can be simplified into two main processes: the condensation of imine and aldehyde monomers into the initial COF precipitate, and the reorganization of this initial precipitate, (through stacking, bond breaking and reformation, and other processes) into the final crystalline form of the COF. Each of these processes will have different rate constants, so the pathway shown in Figure 3.22, below is simplified.

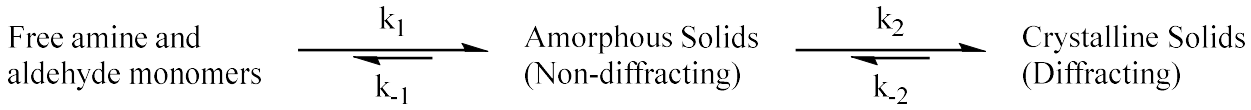


**Figure 3.22: Reaction pathway during COF formation**

Because of observations on how COFs form, two additional assumptions and simplifications can be made. The rate constant for the initial precipitation of COF solids, $k_1$ must be larger than the rate constant for the hydrolysis of the imine-linked oligomers formed, otherwise there would not be the rapid formation of solids as is observed during COF synthesis. Similarly, the overall rate constant for the conversion of amorphous COF precipitates to the crystalline COF network, $k_2$ must be larger than the reverse process, since the system does eventually form the crystalline network. Furthermore, it is inferred from observation that the effective rate constant for the formation of initial solids must be far larger than the effective rate constant for the crystallization process. This is concluded from qualitative observations, the initial precipitation takes seconds, while the crystallization processes takes minutes or hours depending on the COF and reaction conditions. Therefore, when considering the *in situ* data, the initial condensation of monomers can be disregarded since that stage of the reaction will be finished by the time the samples are first scanned.

Additionally, in Section 3.3 two separate potential COF formation mechanisms were discussed. For the purposes of this comparison of the rates of crystallization, any COF material which does not measurably diffract during the *in situ* experiment is considered amorphous material. The identity of this material could be a crosslinked, amorphous network as previously proposed by Smith *et al*. Or could be disordered sheets suspended in the reaction medium. Therefore, for the purposes of this section, amorphous material is

used to describe the portion of the COF reaction that is not explicitly crystalline as measured by *in situ* diffraction, without drawing distinctions between oligomer species, crosslinked networks, or other non-diffracting structures which could be present.

The intensities of the (100) peaks for each COF behave asymptotically during the time period measured during the *in situ* experiment. The maximum (100) peak intensity observed for each COF was therefore assumed to correspond to the fully crystalline COF, and the (100) intensities were normalized to a value of 1 to allow for comparison between the four different COF species: TAPB-OMePDA COF, TAPB-OBuPDA COF, TAPB-OOctPDA COF, and TAPB-ODodecPDA COF. TAPB-PDA COF formed very rapidly under these conditions, and since it produces a consistently crystalline material that does not vary during the time period measured, as seen in Figure 3.12, it is not included in Figure 3.23. The normalized (100) peak intensity data for the alkoxy-functionalized COFs is shown below in Figure 3.23.

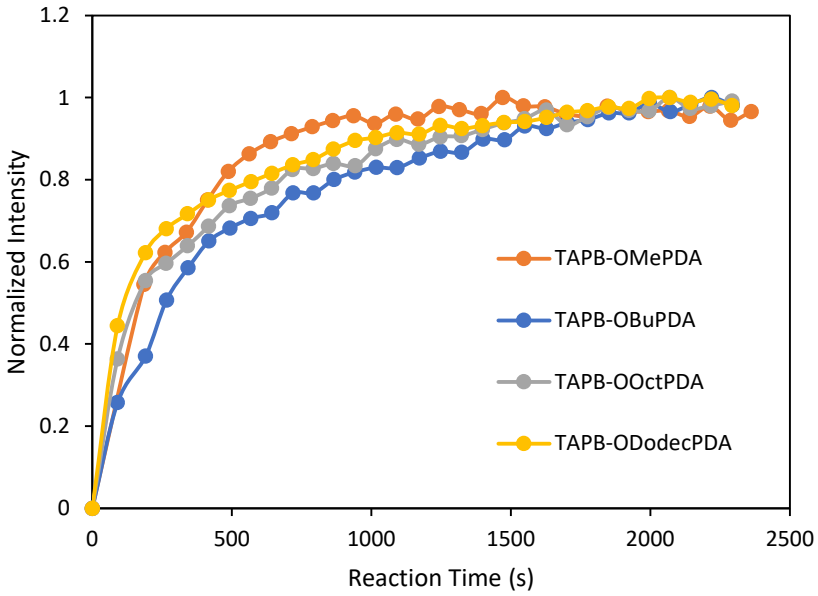


**Figure 3.23: Baseline corrected and normalized (100) peak intensity versus reaction time for TAPB-OMePDA COF, TAPB-OBuPDA COF, TAPB-OOctPDA COF, and TAPB-ODodecPDA COF.**

These data can be plotted linearly as:

$$n\big(1-(normalized\ intensity)\big)\ vs\ t \tag{3}$$

Here the normalized intensity being set to a value of 1 is convenient because the plotted curve is therefore equivalent a measure of the molar fraction of the COF material which is crystalline. The maximum value of 1, therefore, corresponds to the completely crystalline system that the COF approaches asymptotically. The molar fraction of the amorphous phase, which cannot be probed directly using XRD, is therefore:

$$[\boldsymbol{A}morphous] = 1 - [\boldsymbol{C}rystalline]$$

$$[A] = 1 - [C] \tag{4}$$

Whatever portion of the COF is not crystalline, therefore, is considered amorphous in these calculations. The data shown in Figure 3.23 was plotted linearly according to a first order reaction, shown in Figure 3.24. The linear fit of each COF series is included in the plot. Here the slope of the line corresponds to the effective rate constant for the COF reorganization from the amorphous phase to the crystalline phase. The *y*-intercept for the linear fit has been set to zero for each COF data set because at *t*=0 there should be no crystalline phase present.

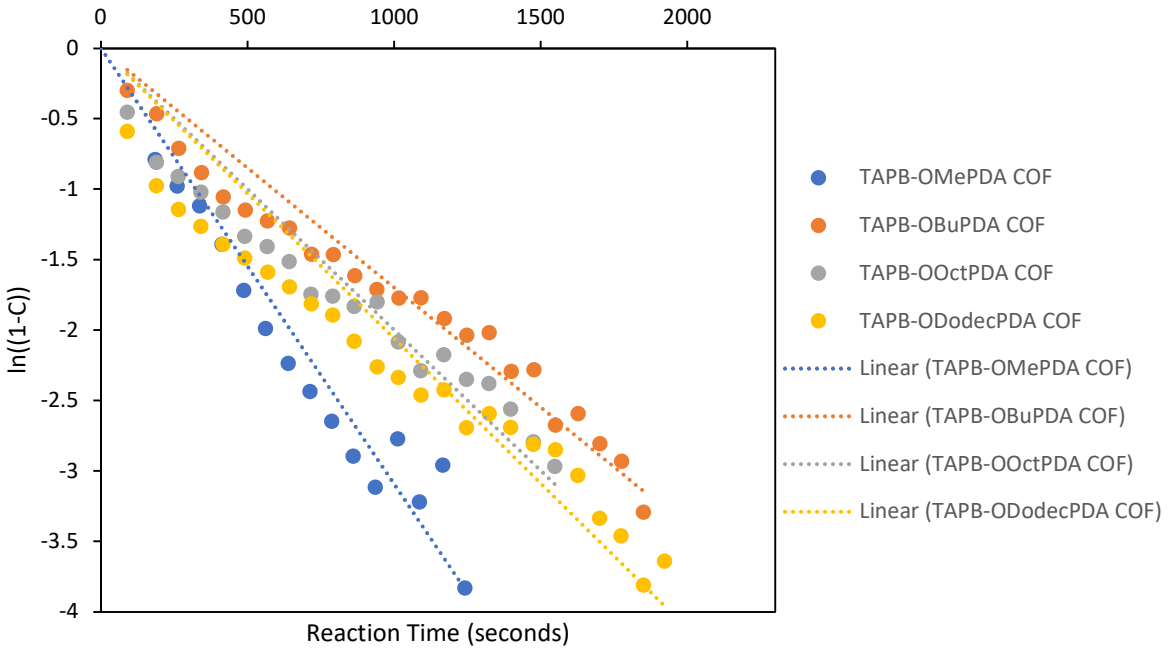


**Figure 3.24: Linearized first order plot for TAPB-OMePDA COF, TAPB-OBuPDA COF, TAPB-OOctPDA COF, and TAPB-ODodecPDA COF.**

This data shows that the effective rate constant for the crystallization process for each of the dialkoxy-substituted COFs are similar. Regression analysis from Figure 3.24 is found in Table 3.4 in Section 3.10.5. This indicates that the size of the alkoxy chain does not significantly affect the rate of crystallization of the COF network from the initially precipitated amorphous species. This result disproves with the original supposition that alkoxy chains of increasing size would interfere with this process by restricting rotation during reorganization or disrupting interactions between layers.

There is, however, an additional method of determining the effective rate constant for each COF by directly fitting the normalized (100) intensity data according to the first order rate law. The rate law for the COF reorganization process under investigation can be presented as:

$$-\frac{d[A]}{dt} = k[A] \tag{5}$$

Where [A] is the molar ratio of the amorphous phase and $k$ is the effective rate constant. The integrated rate law would therefore be:

$$[A] = [A]_0 e^{-kt} \tag{6}$$

Unfortunately [A] cannot be directly probed via diffraction measurements, so the integrated rate law must be rewritten in terms of [C] via the relationship [A]=1-[C]:

$$[C] = [C]_{\infty}(1 - e^{-kt}) \quad (7)$$

$[C]_{\infty}$ is the maximum molar ratio of the crystalline phase attained by the system at $t=\infty$, ideally 1. This modified first order integrated rate law was used as a fitting function using the curve fitting toolbox in MATLAB. Because COF synthesis is not an ideal system, and $[C]_{\infty}$ cannot be measured by definition, $[C]_{\infty}$ was included along with $k$ as a variable for the curve fitting toolbox. The obtained values obtained for $[C]_{\infty}$ and $k$ are shown in Table 3.3, below.

**Table 3.3: Fitted values for $[C]_{\infty}$ and $k$ from the MATLAB curve fitting toolbox for normalized (100) peak intensities vs reaction time measured *in situ* for TAPB-OMePDA COF, TAPB-OBuPDA COF, TAPB-OOctPDA COF, and TAPB-ODodecPDA COF.**

| COF | TAPB-OMePDA COF | TAPB-OBuPDA COF | TAPB-OOctPDA COF | TAPB-ODodecPDA COF |
|---|---|---|---|---|
| $[C]_{\infty}$ with 95% confidence bounds | 0.97 ± 0.01 | 0.95 ± 0.02 | 0.94 ± 0.02 | 0.94 ± 0.02 |

| | | | | |
|---|---|---|---|---|
| $k$ with 95% confidence bounds | 0.0039 ± 0.0002 | 0.0024 ± 0.0002 | 0.0033 ± 0.0004 | 0.0044 ± 0.0006 |
| $R^2$ | 0.9934 | 0.9763 | 0.9550 | 0.9403 |

The fitted curves are shown in comparison to the *in situ* XRD data for each COF in Figure 3.25, below.

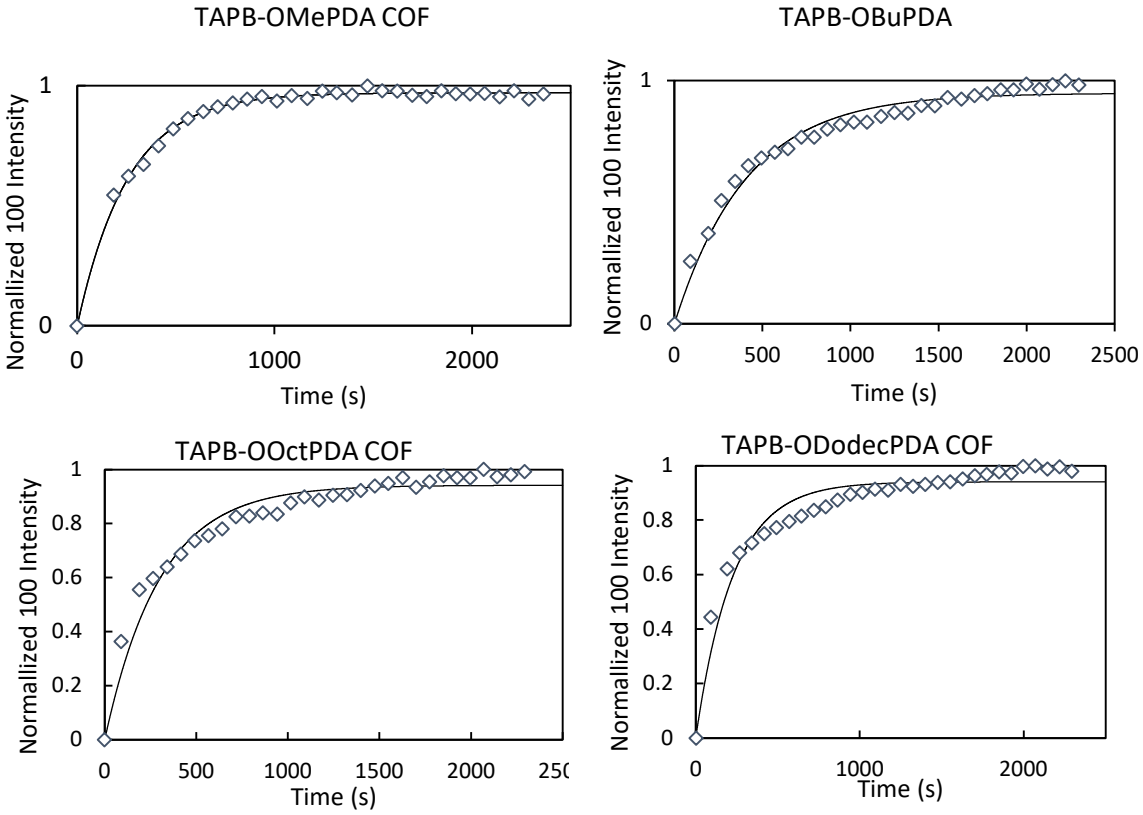


**Figure 3.25: Top Left: Plot of TAPB-OMePDA COF baseline corrected and normalized (100) peak intensity versus fitting equation. Top Right: Plot of TAPB-OBuPDA COF baseline corrected and normalized (100) peak intensity versus fitting equation. Bottom Left: Plot of TAPB-OOctPDA COF baseline corrected and normalized (100) peak intensity versus fitting equation. Bottom Right: Plot of TAPB-ODodecPDA COF baseline corrected and normalized (100) peak intensity versus fitting equation.**

From the data obtained from *in situ* XRD, it can be seen that the inclusion of longer and longer alkoxy chains does not meaningfully affect the rate of crystallization of the COF. This conclusion thoroughly disproves the original supposition that the alkoxy chains would inhibit this process, leading to slower crystallization rates for COFs with longer chains. However, the longest dodecyloxy chains do seem to have an effect during the COF isolation process. Figure 3.26 below shows a side by side comparison of the *ex situ* TAPB-ODodecPDA COF PXRD pattern from the one-hour synthesis sample, with the forty-minute scan from the *in situ* experiment.

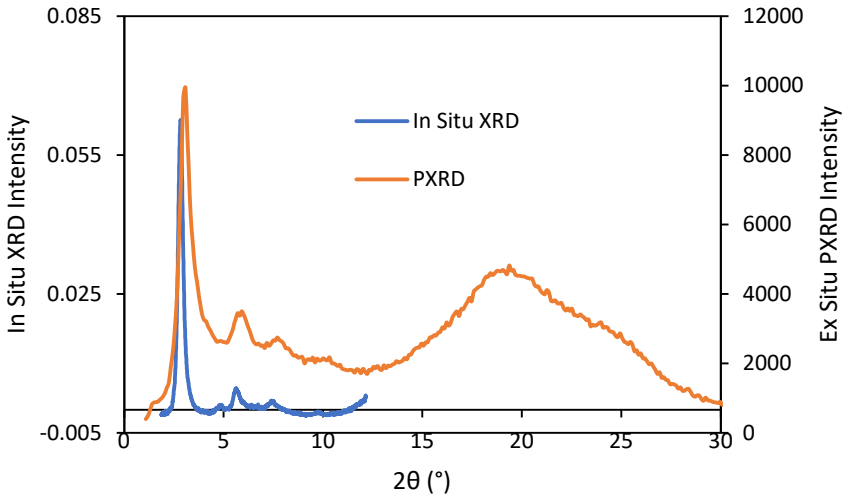


**Figure 3.26: Comparison of in situ XRD versus ex situ PXRD measurements for TAPB-ODodecPDA COF**

This comparison shows that the *in situ* diffraction pattern shows a proportionally more intense (100) peak than the isolated COF, as well as a lower baseline underneath the visible (100), (110), and (210) peaks, indicating a more ordered COF structure while the COF remains suspended in the reaction solvent. Unfortunately, the (001) peak corresponding to the interlayer stacking is not distinct in either XRD pattern, due to amorphous material in the PXRD pattern, and due to solvent scattering the *in situ* XRD pattern. This result implies that the inclusion of such long alkoxy chains causes structural changes in the COF during the isolation and activation processes, resulting in a more amorphous material that is not observed for any of the COFs synthesized with smaller alkoxy chains. This result shows that there is an upper limit on the size of the functional group that can be included in the COF structure without causing structural distortions, which has implications for COF pore surface engineering and COF applications reliant on pendant groups such as separations or sensing.

## 3.9 Chapter Conclusion

In the efforts to study the initial formation of COFs described in this chapter, several key conclusions were reached. Firstly, the crystallization behavior of COFs can be investigated using traditional *ex situ* methods, which require isolation of the COF after the synthesis reaction prior to analysis. This process puts distance between the crystallization and formation processes of interest and the actual analysis of the material and can cause misinterpretation of results as was seen in the comparison of TAPB-PDA COF to the related TAPB-OMePDA COF. When examined *ex situ*, it could be concluded that TAPB-OMePDA COF formed a crystalline network faster. However, when the formation of the COFs was monitored using *in situ* XRD, which is able to monitor the development of

crystallinity without affecting the reaction in progress, it was clear that the opposite was true; TAPB-PDA COF forms faster, but is more affected by the activation and isolation processes used. These efforts show the advantages of *in situ* XRD analysis for examining the formation of COFs. An additional advantage is the removal of sample-to-sample variation, since a single COF sample can be observed from the start to the end of the reaction, removing the need for multiple time trials and reducing monomer usage. This could be key in examining the synthesis of COFs composed of scarce or synthetically complex monomer components. However, the high X-ray intensities used to obtain rapid XRD scans on during the *in situ* experiment limit the accessibility of this technique to synchrotron x-ray sources.

*In situ* analysis was applied to a series of 2,5-dialkoxy functionalized COFs to test the theory that bulky side chains could affect the crystallization kinetics of COFs and affect their material properties. In examining the *in situ* data, effective rate constants were extracted showing no significant difference between the inclusion of small methoxy groups, or large dodecyloxy groups. This disproved the theory that the size of the alkyl chain would affect crystallization kinetics, though there were differences in the final material properties of the COFs. The larger alkoxy chains reduce the porosity of the COF, which is not unexpected since the pendant groups occupy space within the pores. This relationship must be considered for COF applications that rely both on the porosity of the COF for mass transfer, or the inclusion of pendant groups for imparting functionality to the COF, such as in catalysis, sensing or separations. Additionally, the inclusion of large dodecyloxy chains appear to cause disruption of the COF structure during isolation and activation based on differences in the *in situ* diffraction and the *ex situ* diffraction

measurements obtained. The exact mechanism for this is currently unknown, but possible causes include restricting the movement of solvents and liquid CO2 into and out of the COF during isolation and activation, or disruption of the interlayer stacking between COF sheets resulting in irregular sheet stacking and inconsistent interlayer distances.

Perhaps the most interesting result obtained is the insight into the speed of the crystallization process itself. Prior to this work it was reported that COFs required several days for proper crystallization while here it is shown that many COFs can form highly crystalline an porous materials within hours. This has implications for the future of COFs as functional materials since faster synthesis of high-quality COFs is desirable from a processing standpoint.

Additional insight was gained into the initial formation of COFs by directly examining exfoliated COF sheets from very short COF synthesis methods. COF material synthesized in only 15 seconds was subjected to sonication, and then centrifuged. The supernatant was drop-cast and examined via SEM and TEM revealing the presence of COF sheets that showed clear diffraction consistent with the expected hexagonal lattice. The presence of crystalline material at such an early stage of the COF synthesis casts doubt on a previously proposed COF formation mechanism that suggested that imine-linked COFs initially form as an amorphous, disordered network, which then reorients to the crystalline network due to the reversibility of the imine bond. This result suggests that COFs may instead initially form as discrete sheets, which are not ordered relative to one another, which then produce the crystalline network by rearranging and stacking. In the context of the synthesis of bulk COF powders this distinction is of limited interest, however, if accurate this new mechanism has implications for other areas of COF study. The growth of 2D imine-linked

COF crystals is as of yet unreported. If 2D imine linked COFs initially form crystalline sheets, stabilization of these sheets in solution may aide in the synthesis of single crystal COF samples. Additionally, if 2D imine-linked COFs are forming through a sheet stacking and rearrangement mechanism, prior computational studies which have been performed on boronic ester-based COF systems are more applicable to imine-linked COFs than if the original amorphous to crystalline mechanism is assumed. This is discussed fully in Chapter 4.

## 3.10 Chapter 3 Experimental Methods and Supplemental Data

### *3.10.1 Chemical and Solvent Sources*

All solvents were commercially sourced and used without additional drying or degassing. Terephthaldehyde was purchased from Sigma-Aldrich and used without additional purification. 2,5-dimethoxyterephthalaldehyde was purchased from Sigma-Aldrich and used without additional purification. Glacial acetic acid was purchased from Fischer Scientific and used without additional purification. Deionized water was used throughout all experiments. **TAPB:** 1,3,5-*tris*(4-aminophenyl)benzene was either synthesized according to a literature method, or purchased from TCI chemicals.[132] **TII:** (E)-4,4'-dibutyl-5,5'-dioxo-4,4',5,5'-tetrahydro-[6,6'-bithieno[3,2-b]pyrrolylidene]-2,2'-dicarbaldehyde (Thienoisoindigo) was synthesized according to literature.[40] **TAPPy:**

1,3,5,8-tetra(4-aminophenyl)pyrene (TAPPy) was synthesized by Dr. Dasari and Kaitlin Slicker according to reported literature methods. [128, 133] 2,5-dibutoxyterephaldehyde, 2,5-dioctyloxyterephthaldehyde, and 2,5-didodecyloxyterephthaldehyde were synthesized according to a literature method.[134]

### *3.10.2 Characterization Methods*

PXRD measurements and gas adsorption/desorption measurements were carried out according to the methods described in Section 2.11.

*In situ* XRD measurements were carried out by Austin Evans (Northwestern University). Small- and wide-angle X-ray scattering (SAXS/WAXS) patterns were collected at Argonne National Lab's Advanced Photon Source at both sectors 5-ID-D (DND-CAT) using a custom multicapillary heated sample stage in transmission geometry. Experiments conducted at 5-ID-D were collected at a beam energy of 13.3 keV. COF reactions were prepared in dram vials (same as SI-III), with acetic acid being added as a final step, shaken quickly and placed into capillaries. The sample was then aligned on the lower portion of the capillary. Diffusion of COF powders (after formation) was not observed on the time scales probed. Additionally, long-term static exposure X-ray exposure did not seem to impact any of the COF materials. While heating, frames were collected for 1 second apiece, continually, on a set of Pilatus detectors, which was then radially integrated to produce a linear XRD pattern using proprietary software available at the APS. Scattering intensity is reported as a function of the modulus of the scattering vector q, related to the scattering angle $2\theta$ by the equation $q = (4\pi/\lambda) \sin \theta$, where $\lambda$ is the X-ray wavelength. The sample-to-detector distance was adjusted to measure across relevant detection ranges. Capillary

experiments were conducted using 2.0 mm OD borosilicate capillaries with 0.2 mm wall thicknesses purchased from Hilgenberg GmbH. These capillaries then were sealed with sealing putty, which helped to prevent evaporation while measuring.

*In situ* COF XRD data processing and normalization: The (100) peak data from the *in situ* XRD scans was obtained by linearly background correcting the (100) peak manually. The points where the peak returned to the baseline scattering were used to determine the line for each scan using the point-slope formula. This baseline corrected data was normalized to a maximum value of 1 providing the data presented in Figure 3.18. These data points were used in the curve fitting toolbox in MATLAB to provide the fits seen in Table 3.3 and Figure 3.21.

TEM was performed using a JEOL (JEOL USA, Inc., Peabody, MA) ARM200CF Aberration-Corrected STEM/TEM operated at 200 keV equipped with a Gatan (Gatan, Inc., Pleasanton, CA) K2 "direct electron" detector (FEG Emission: 15 μA, spot size 3, 150 μm CL aperture). The ARM200CF was aligned for low-dose imaging, measuring the dose rate on the K2 detector through vacuum (no grid inserted). The dose rate was measured to be 1.41-11.35 $e^{-}$ $Å^{-2}$ $s^{-1}$ (3710 x 3838 pixels) with an image exposure times of 1 s (1.39-11.17 $e^{-}$ $Å^{-2}$ cumulative dose per image). All image acquisition was done using the Gatan Microscopy Suite (GMS), Digital Micrograph (Gatan, Inc., Pleasanton, CA).

### *3.10.3 COF Synthesis Methods:*

TAPB-PDA COF, TAPB-OMePDA COF, TAPB-OBuPDA COF, and TAPB-OOctPDA COF, and TAPPy-PDA COF were synthesized according to the method presented in Section 2.9. For the *in situ* TAPB-PDA COF experiments investigating the monomer

concentration presented in Section 3.7, monomer solution was prepared as described in Section 2.9, this solution was diluted by a factor of 2, 4, 8, or 16 using 4:1 *p*-dioxane:mesitylene solution in order to maintain a constant reaction volume.

**TAPB-ODodec PDA COF.** For the synthesis TAPB-ODodecPDA COF, 33.53 mg of TAPB (0.0954 mmol), and 71.9 mg (0.143 mmol) of ODodecPDA are weighed into a 4 mL vial. 1 mL of 4:1 *p*-dioxane:mesitylene was added to the vial, which was sonicated thoroughly (1-2 minutes). The vial was preheated to 70 °C using an aluminum heating block. To the preheated solution, 0.5 mL of 10.5 M acetic acid was added. The vial was capped securely, then gently swirled to mix the acid into the reaction mixture, then the reaction mixture was allowed to stand for 4 hours at 70 °C. After the specified reaction time, the COF solid was transferred to a filter paper, and rinsed thoroughly with methanol (approximately 100 mL). Care is taken at this stage to not allow the COF to become dry on the filter paper. After rinsing, the damp solid was subjected to $scCO_2$ activation. This results in a fluffy yellow solid in 75% yield.

**TAPPy-OMePDA COF.** For the synthesis TAPPy-OMePDA COF, 20.3 mg of TAPPy (0.0357 mmol), and 13.89 mg (0.0715 mmol) of OMePDA are weighed into a 4 mL vial. 0.5 mL of 4:1 *p*-dioxane:mesitylene was added to the vial, which was sonicated thoroughly (1-2 minutes). The vial was preheated to 70 °C using an aluminum heating block. To the preheated solution, 0.25 mL of 10.5 M acetic acid was added. The vial was capped securely, then gently swirled to mix the acid into the reaction mixture, then the reaction mixture was allowed to stand for 4 hours at 70 °C. After the specified reaction time, the COF solid was transferred to a filter paper, and rinsed thoroughly with methanol (approximately 100 mL).

Care is taken at this stage to not allow the COF to become dry on the filter paper. After rinsing, the damp solid was subjected to $scCO_2$ activation. This results in a yellow solid in 70% yield.

### *3.10.4 The Linear Relationship between $S_{BET}$ and (100) Diffraction Intensity for TAPB-PDA COF*

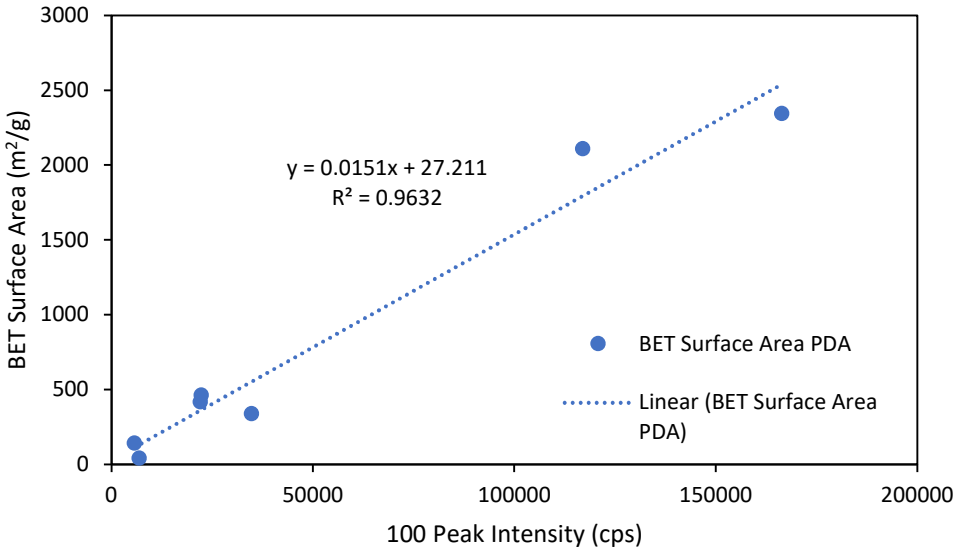


**Figure 3.27: Linear relationship between (100) peak intensity and $S_{BET}$ in TAPB-PDA COF samples.**

### *3.10.5 Supplemental PXRD Patterns, Isotherms, and Pore Size Distributions*

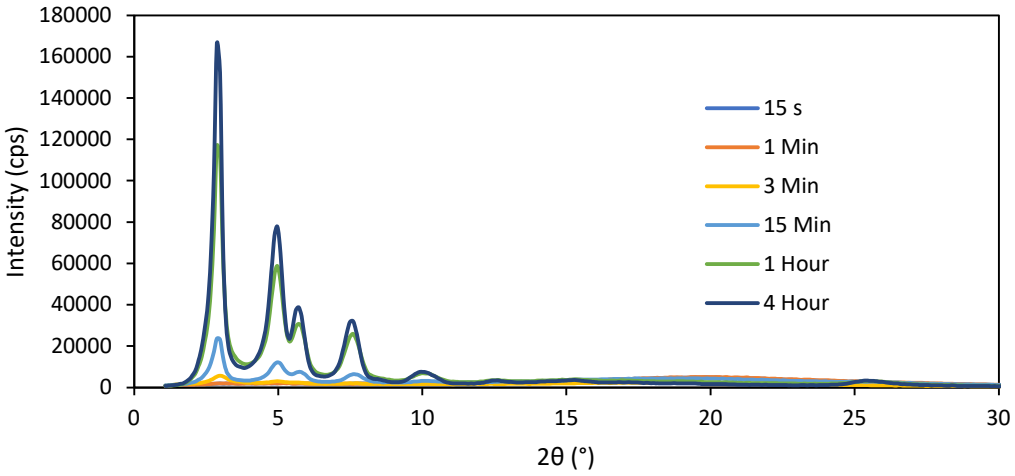


**Figure 3.28: TAPB-PDA COF PXRD patterns versus reaction time.**

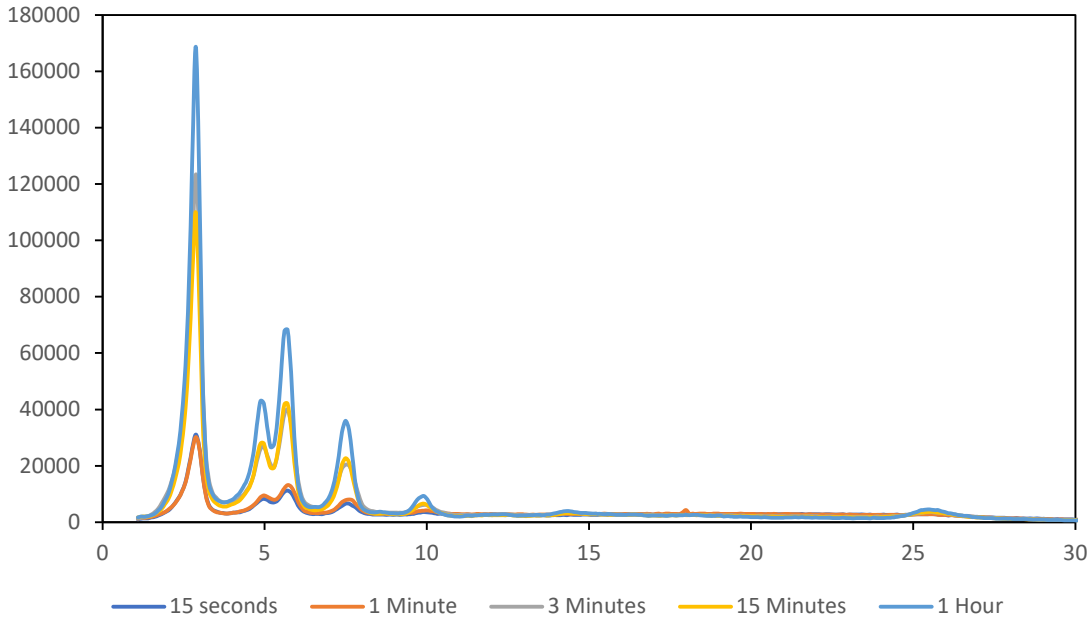


**Figure 3.29: TAPB-OMePDA COF PXRD patterns versus reaction time.**

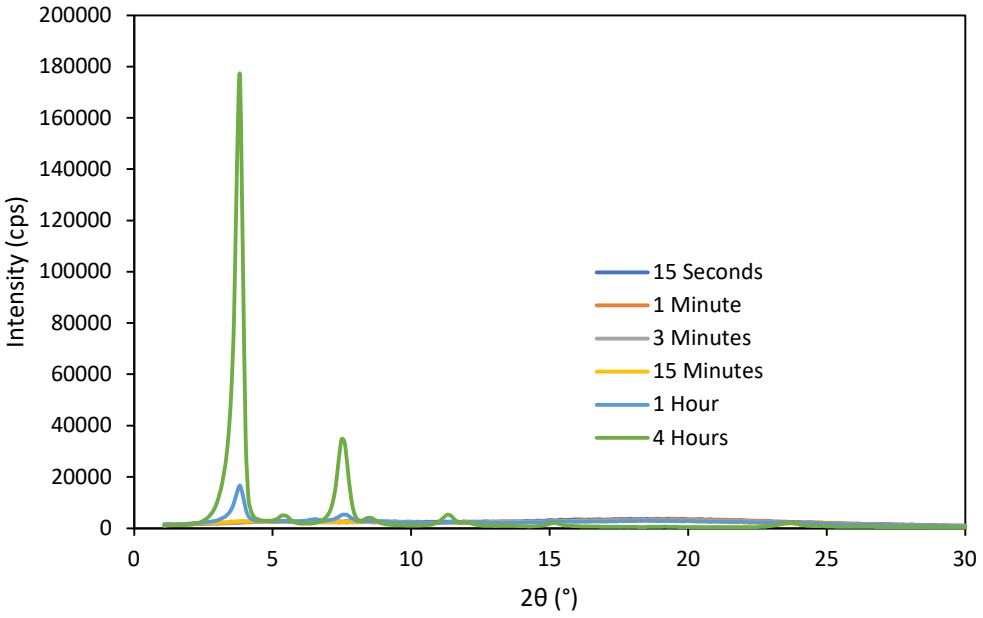


**Figure 3.30: TAPPy-PDA COF PXRD patterns versus reaction time.**

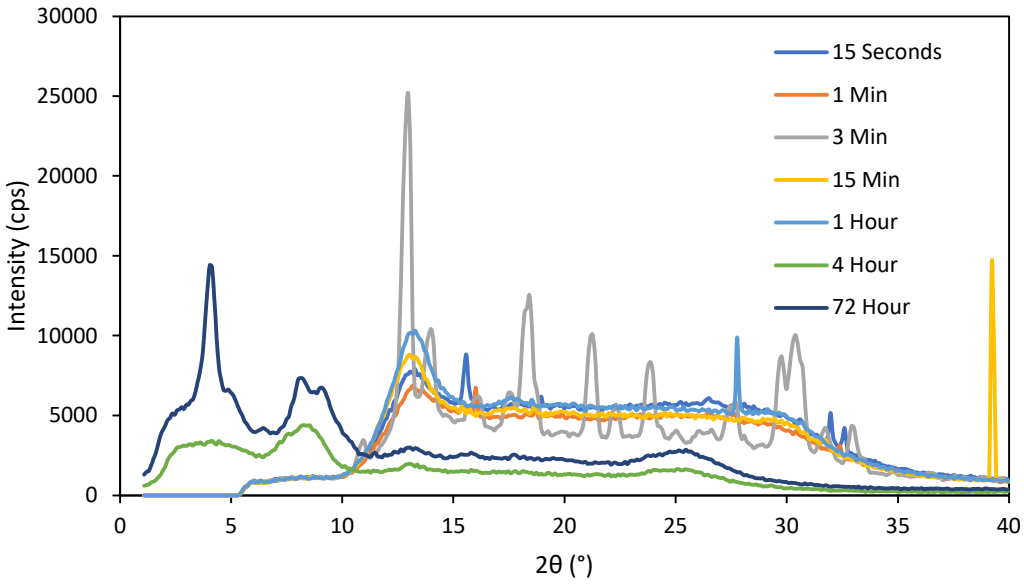


**Figure 3.31: TAPPy-OMePDA COF PXRD patterns versus reaction time.**

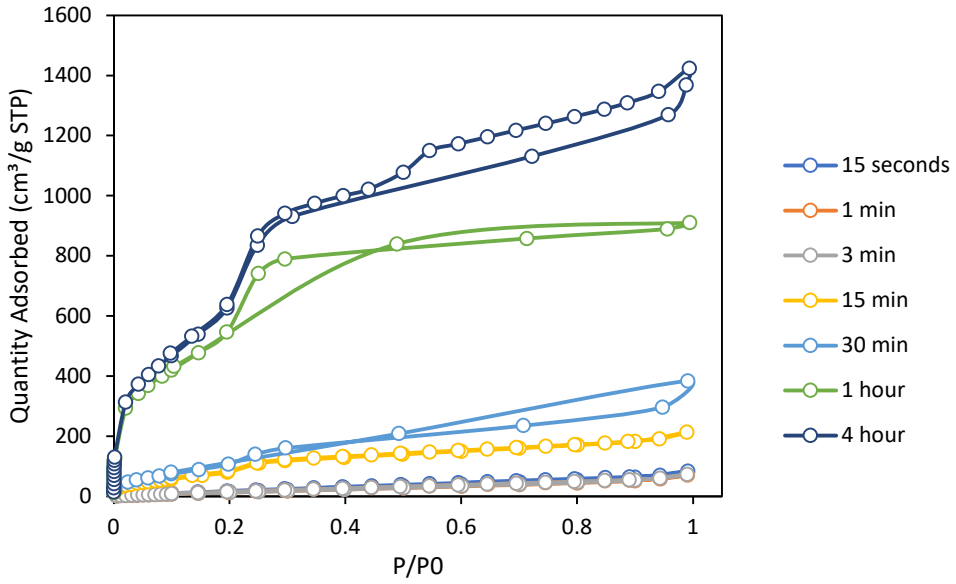


**Figure 3.32: TAPB-PDA COF nitrogen adsorption/desorption isotherms versus reaction time.**

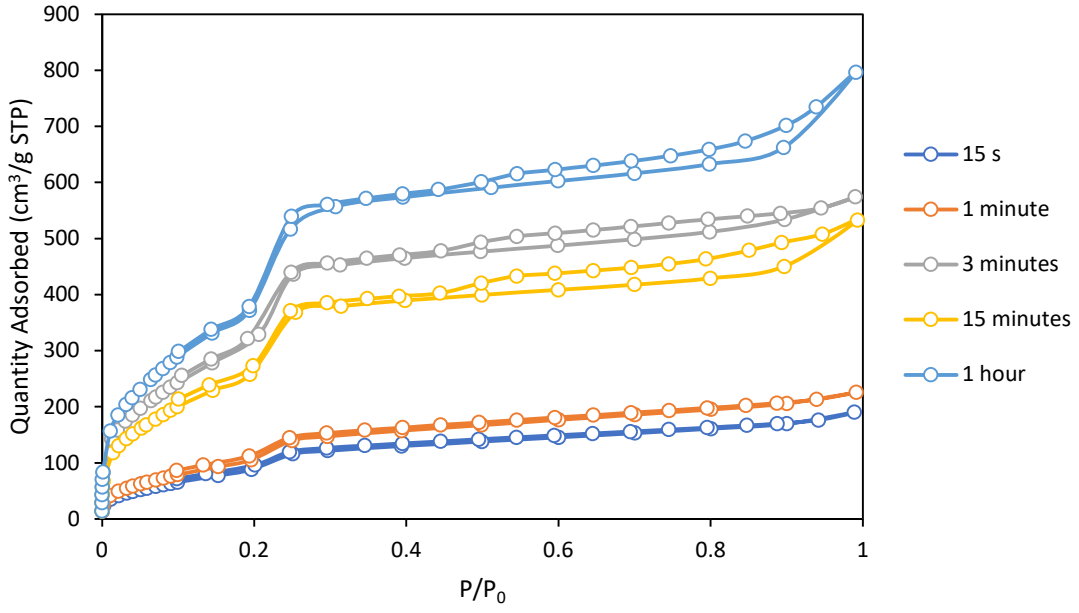


**Figure 3.33: TAPB-OMePDA COF nitrogen adsorption/desorption isotherms versus reaction time.**

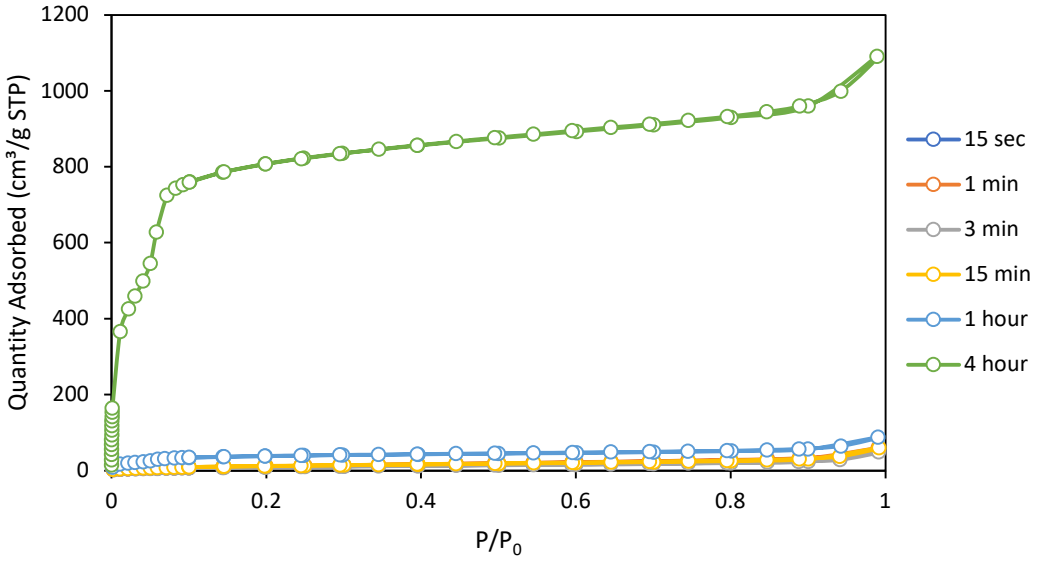


**Figure 3.34: TAPPy-PDA COF nitrogen adsorption/desorption isotherms versus reaction time.**

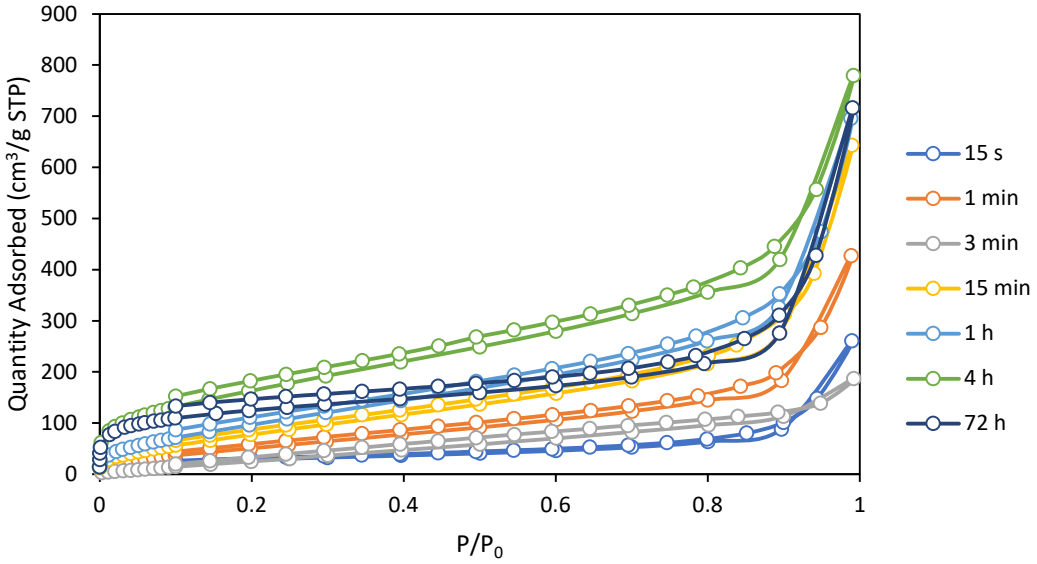


**Figure 3.35: TAPPy-OMePDA COF nitrogen adsorption/desorption isotherms versus reaction time.**

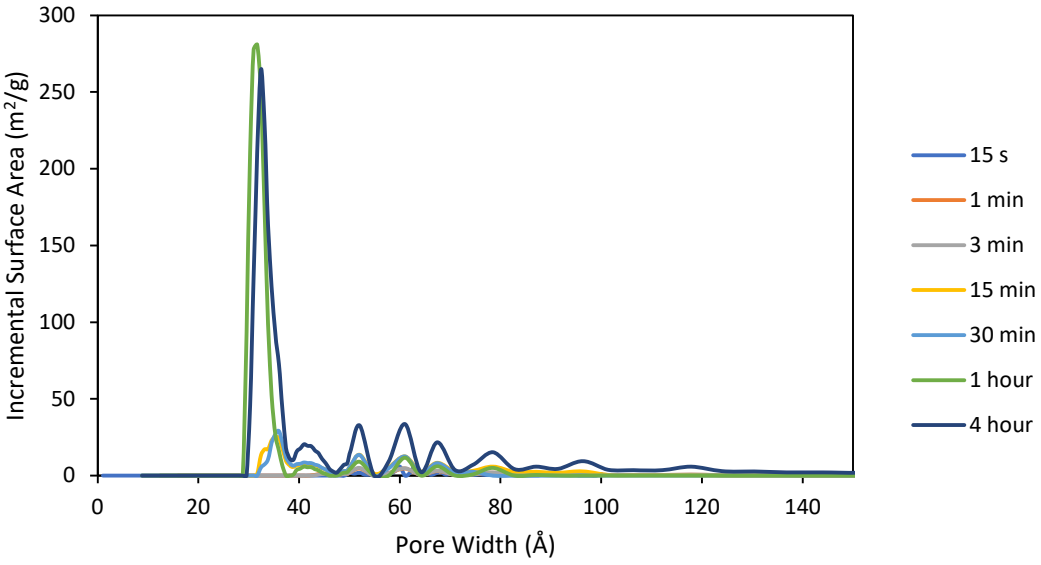


**Figure 3.36: TAPB-PDA COF pore size distribution versus reaction time.**

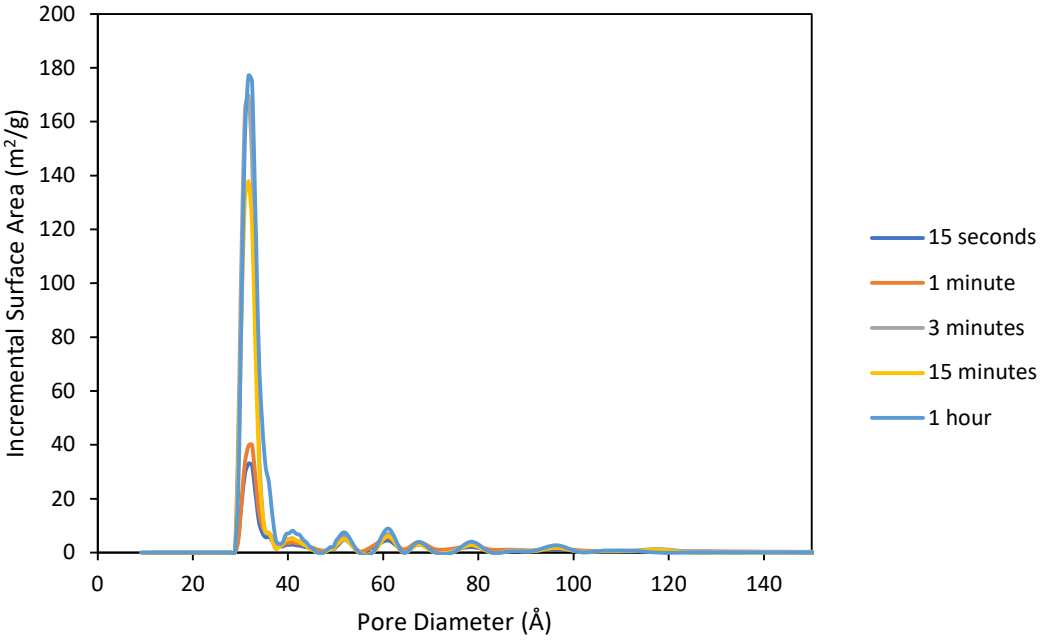


**Figure 3.37: TAPB-OMePDA pore size distribution versus reaction time.**

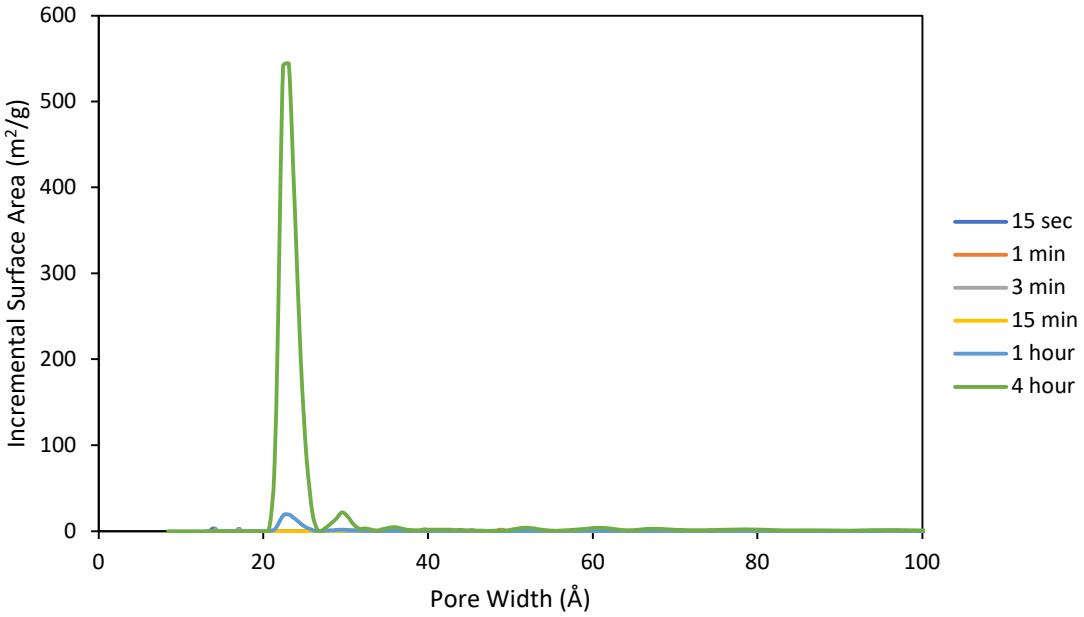


**Figure 3.38: TAPPy-PDA COF pore size distribution versus reaction time.**

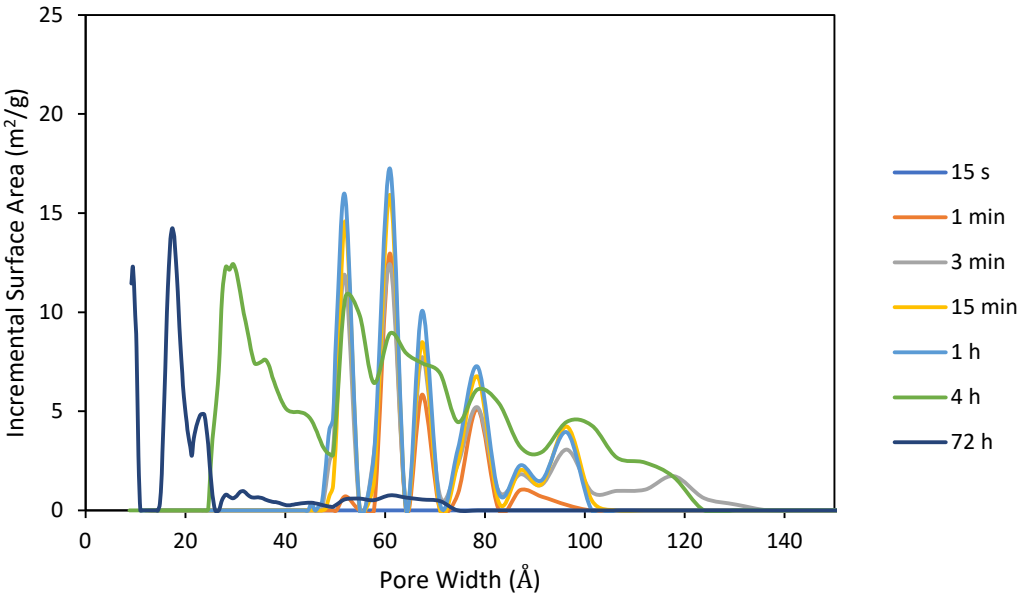


**Figure 3.39: TAPPy-OMePDA COF pore size distribution versus reaction time.**

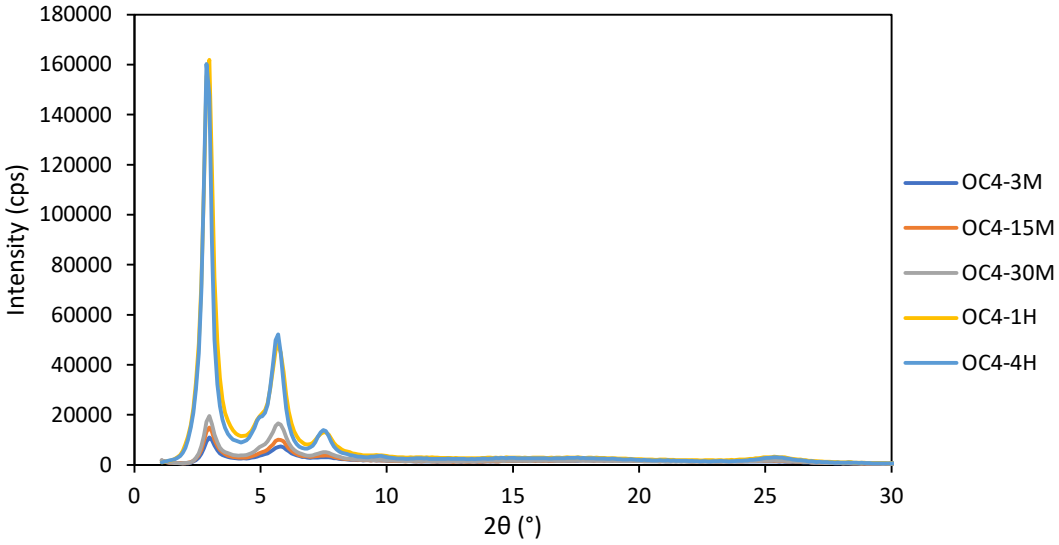


**Figure 3.40: TAPB-OBuPDA COF PXRD patterns versus reaction time.**

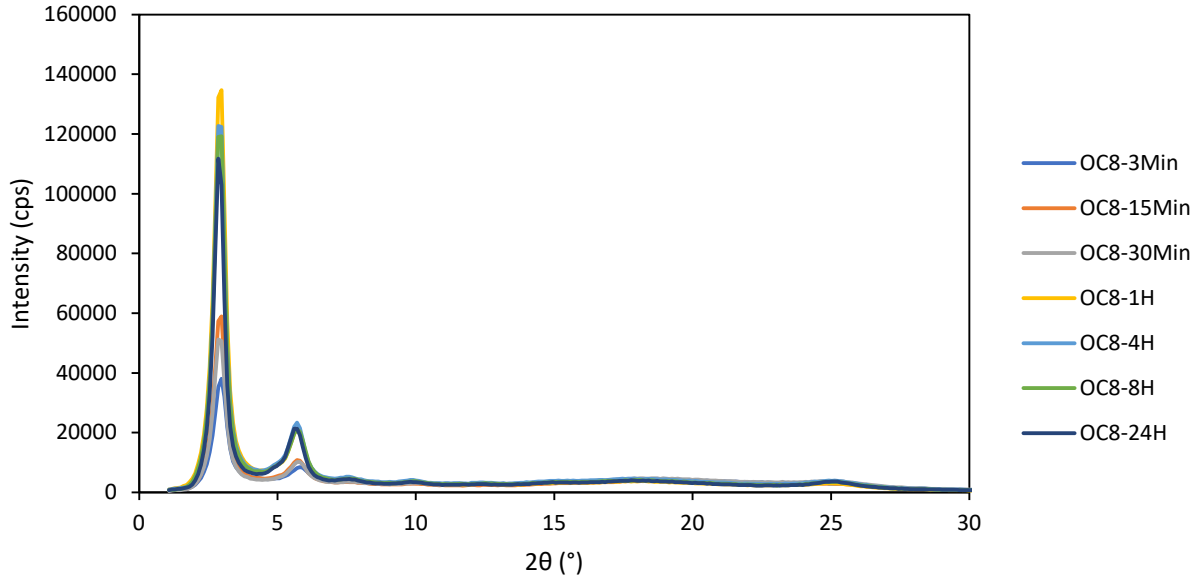


**Figure 3.41: TAPB-OOctPDA COF PXRD patterns versus reaction time.**

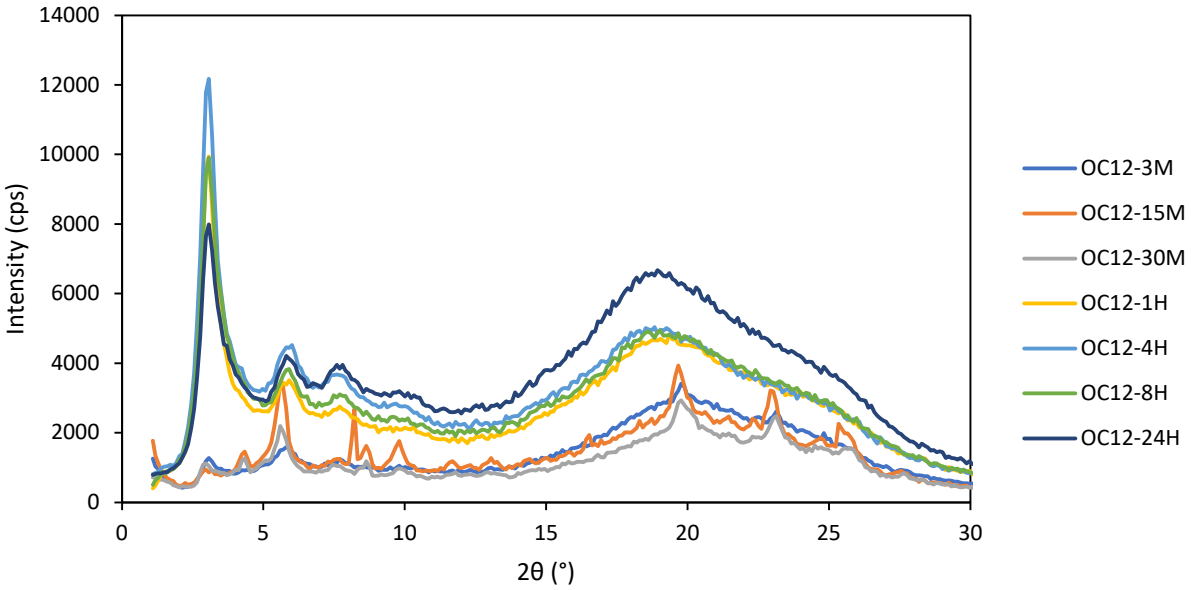


**Figure 3.42: TAPB-ODodecPDA COF PXRD patterns versus reaction time.**

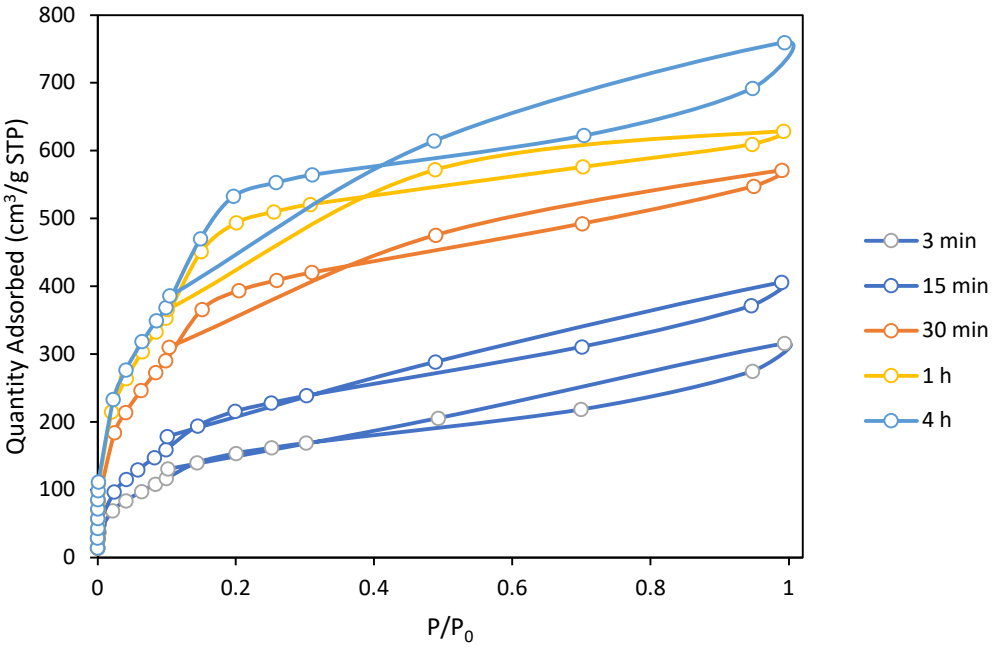


**Figure 3.43: TAPB-OBuPDA COF nitrogen adsorption/desorption isotherms versus reaction time.**

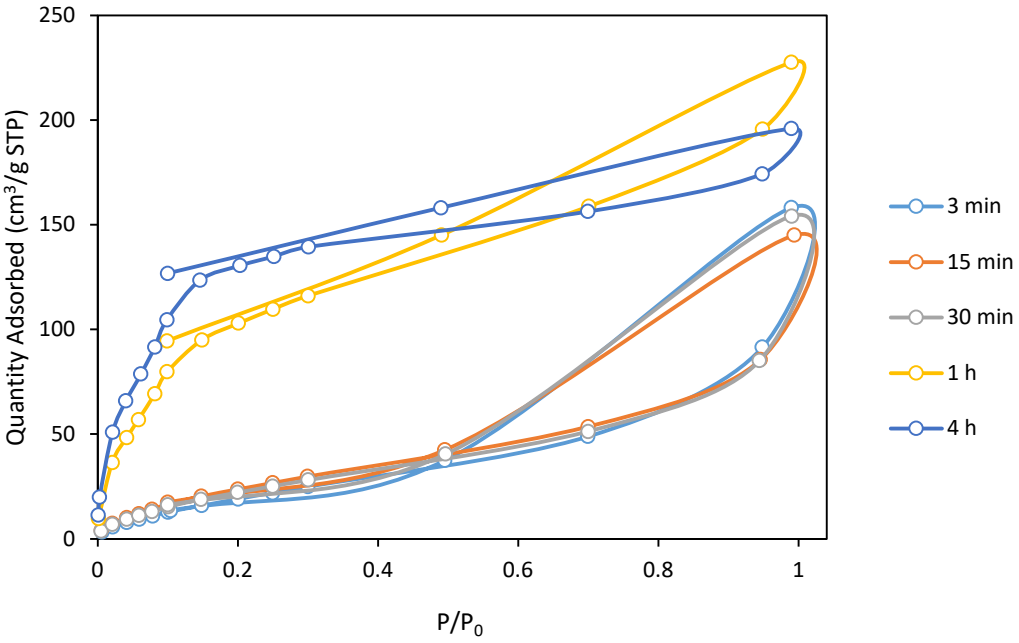


**Figure 3.44: TAPB-OOctPDA COF nitrogen adsorption/desorption isotherms versus reaction time.**

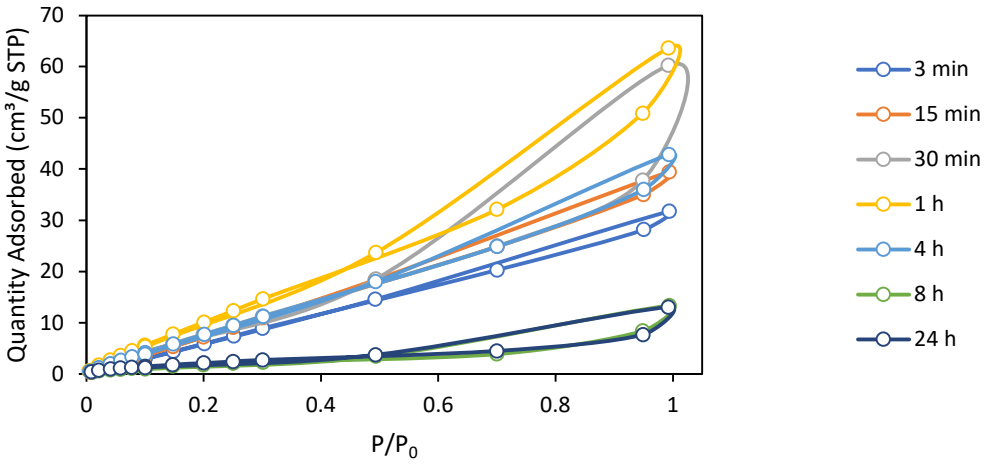


**Figure 3.45: TAPB-ODodecPDA COF nitrogen adsorption/desorption isotherms versus reaction time.**

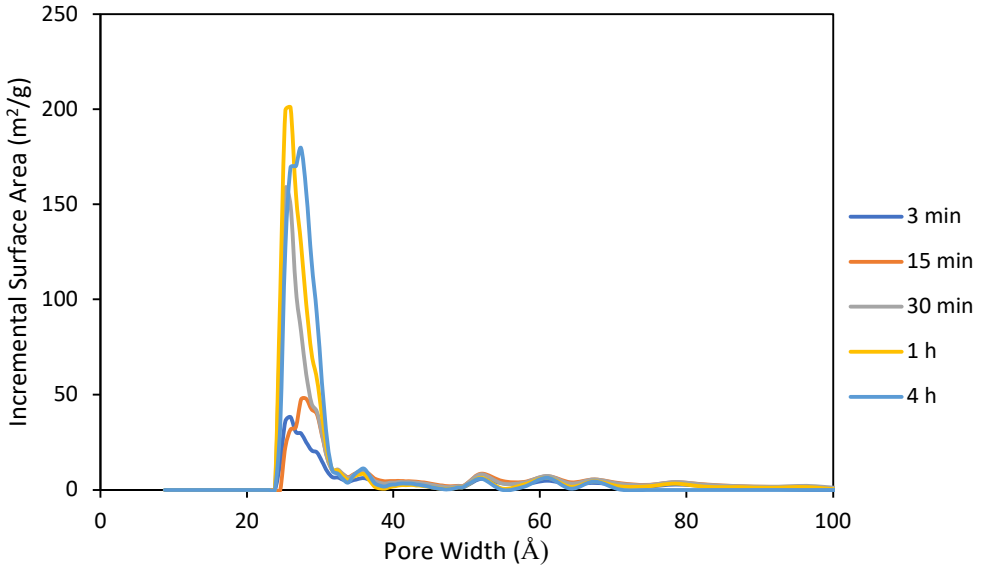


**Figure 3.46: TAPB-OBuPDA COF pore size distribution versus reaction time.**

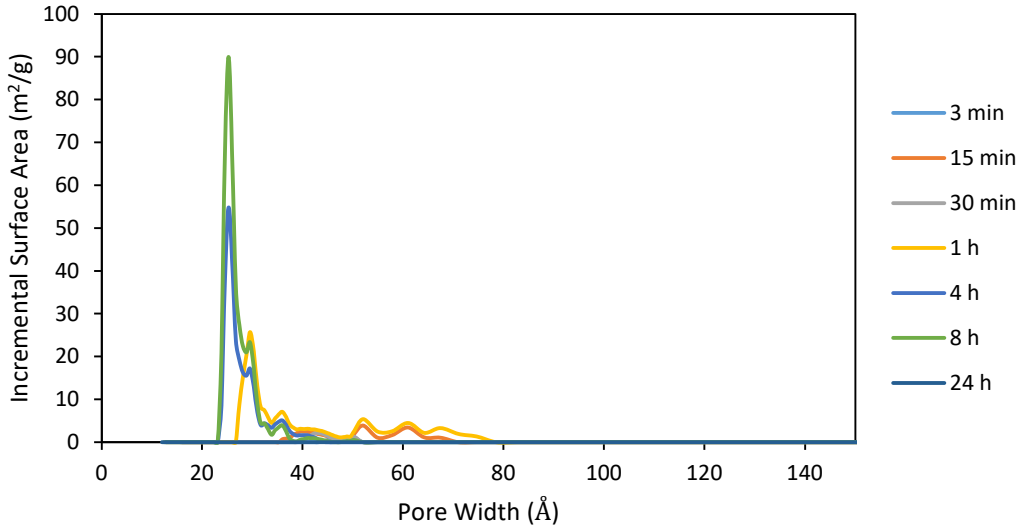


**Figure 3.47: TAPB-OOctPDA COF pore size distribution versus reaction time.**

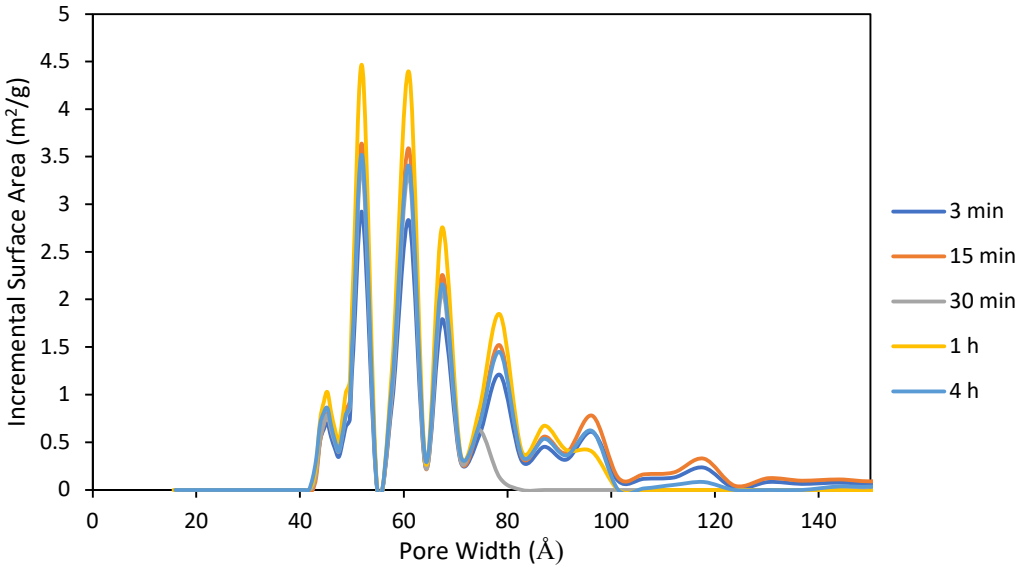


**Figure 3.48: TAPB-ODodecPDA COF pore size distribution versus reaction time.**

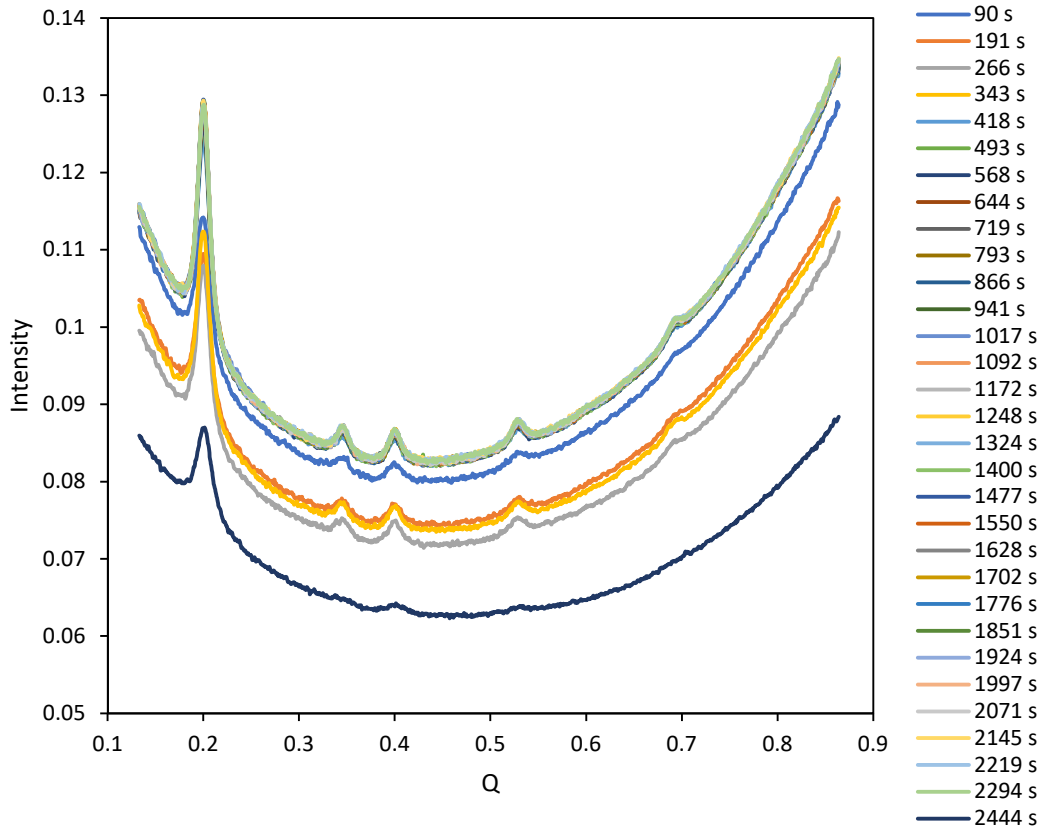


**Figure 3.49: TAPB-OMePDA COF *in situ* XRD diffraction raw data vs reaction time.**

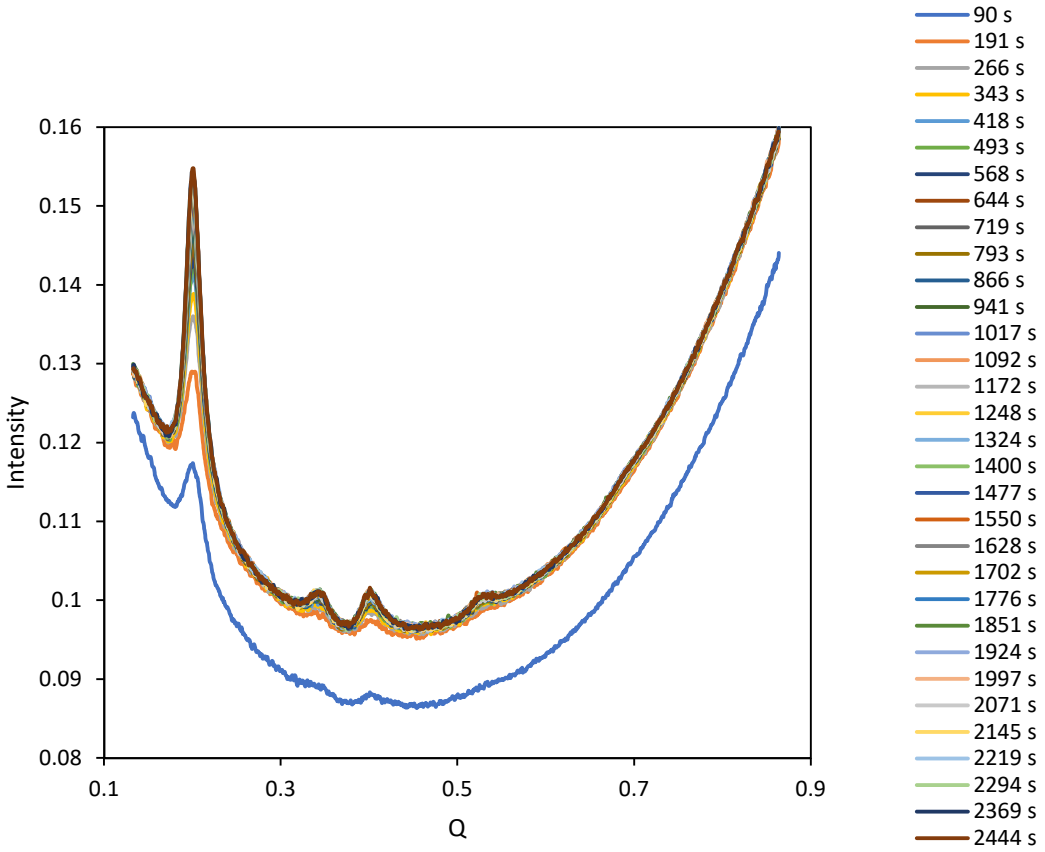


**Figure 3.50: TAPB-OBuPDA COF *in situ* XRD diffraction raw data vs reaction time.**

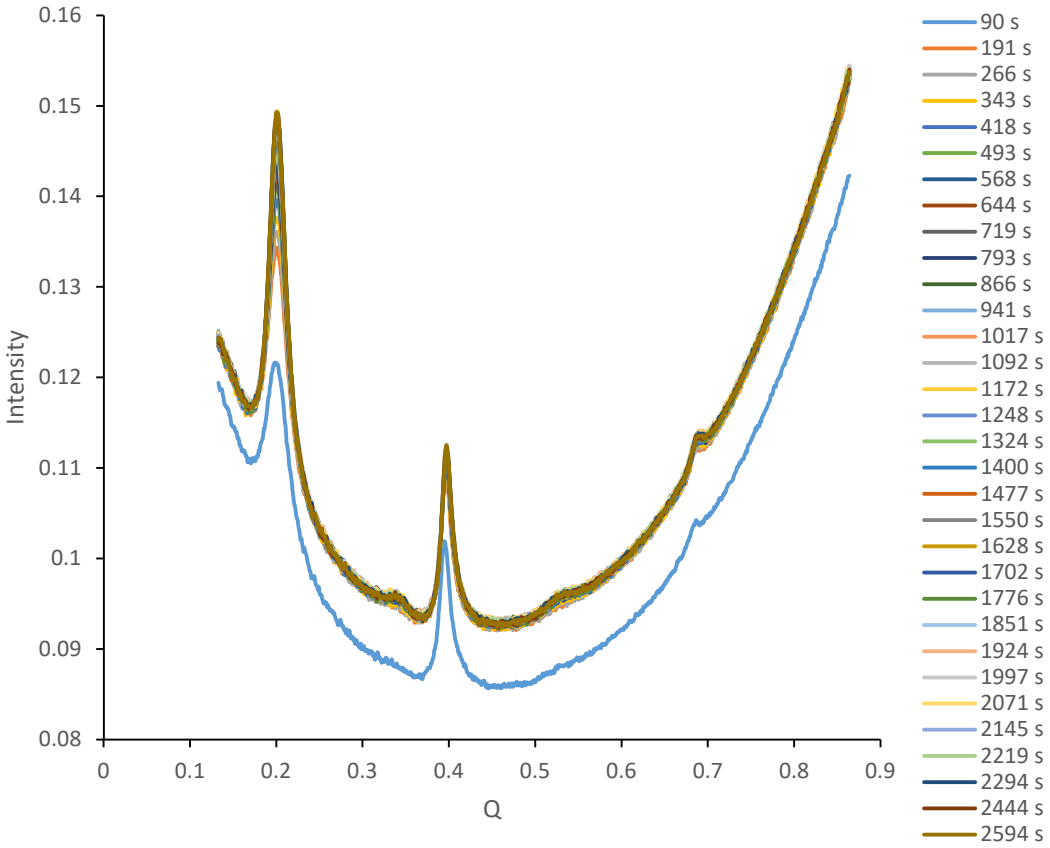


**Figure 3.51: TAPB-OOctPDA COF *in situ* XRD diffraction raw data vs reaction time.**

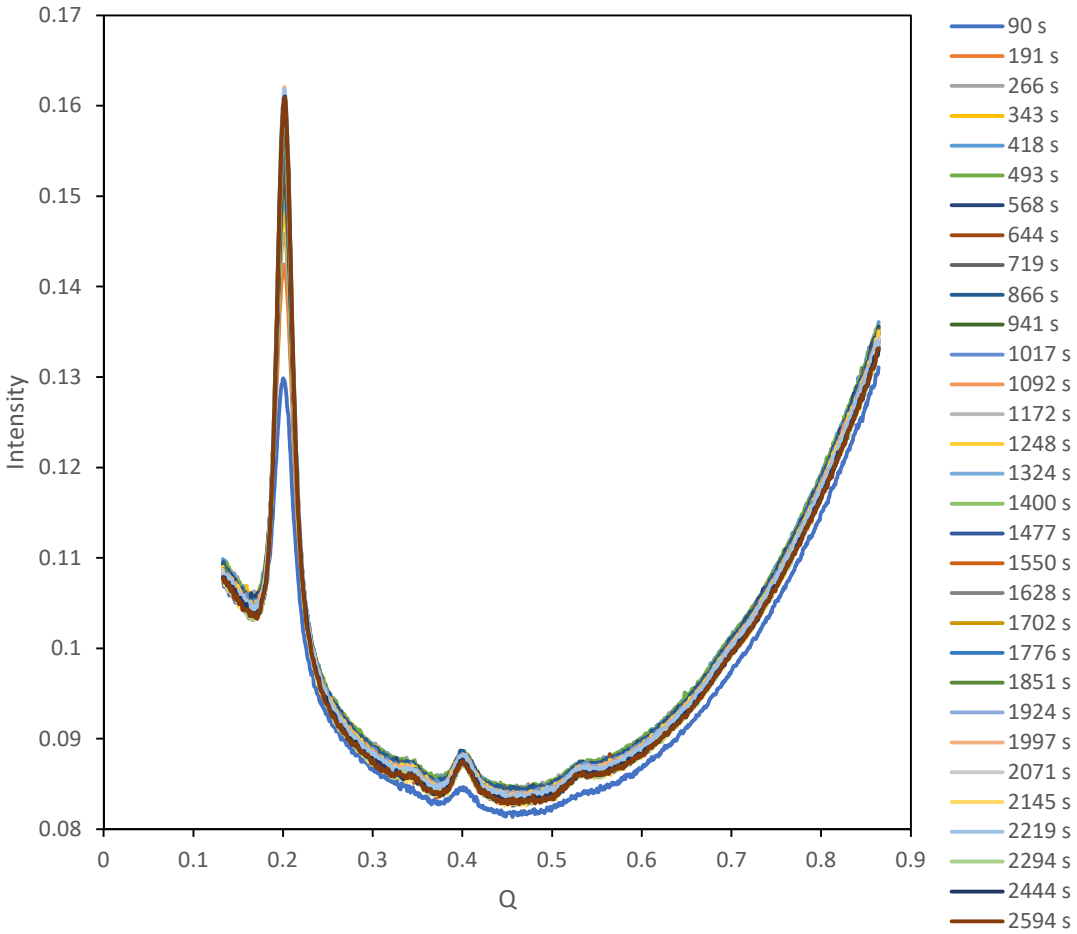


**Figure 3.52: TAPB-ODodecPDA COF in situ XRD diffraction raw data vs reaction time.**

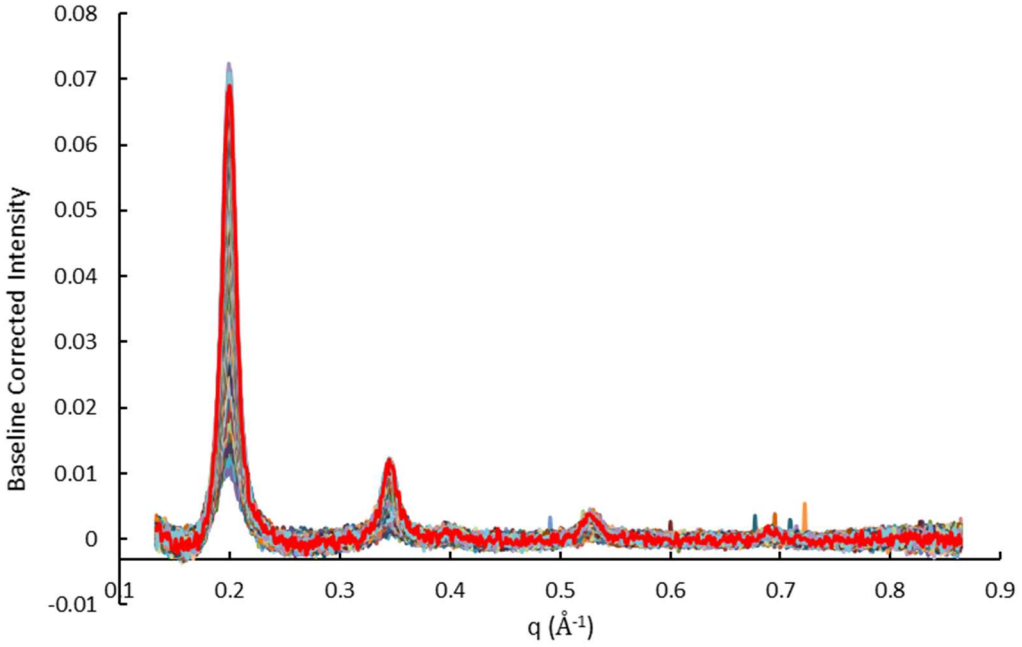


**Figure 3.53: Baseline corrected in situ XRD diffraction pattern for TAPB-PDA COF sample 3.7.A (original monomer concentration)**

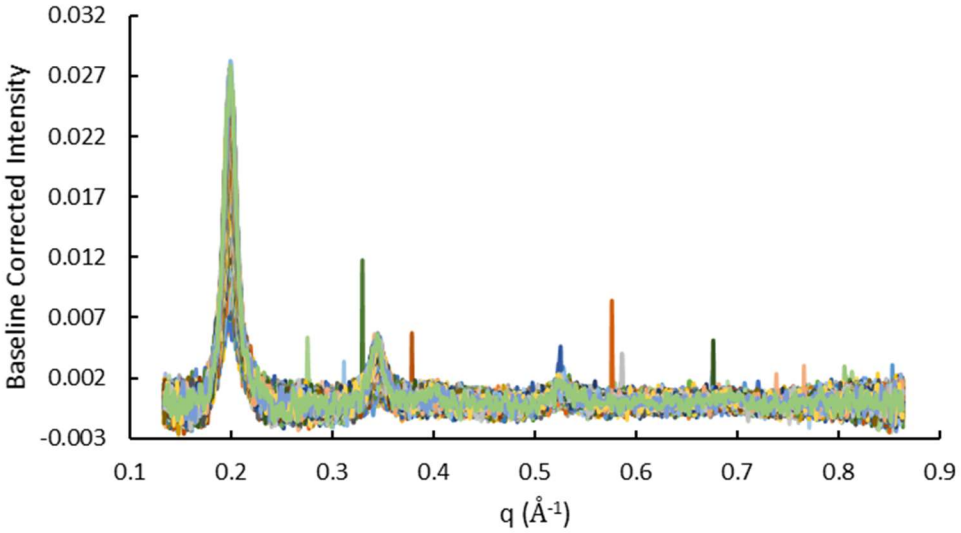


**Figure 3.54: Baseline corrected in situ XRD diffraction pattern for TAPB-PDA COF sample 3.7.B (1/2 monomer concentration)**

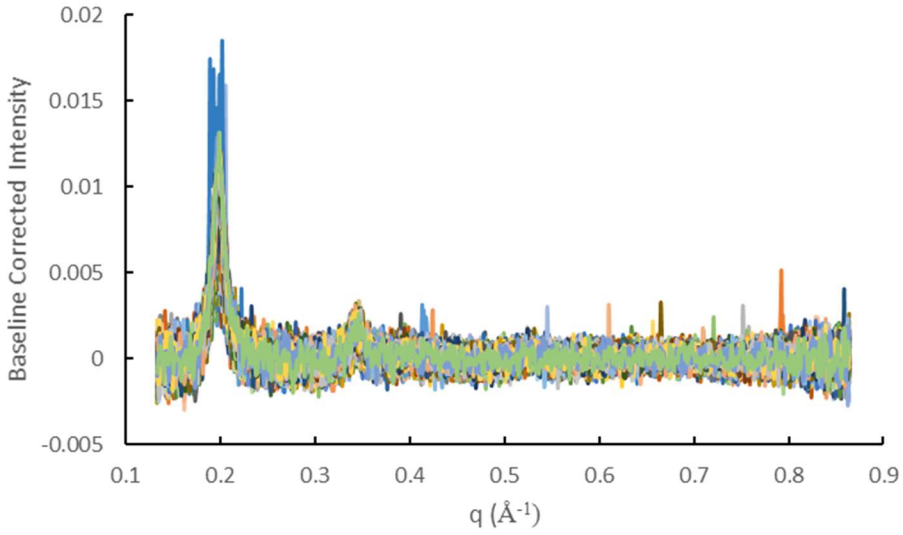


**Figure 3.55: Baseline corrected in situ XRD diffraction pattern for TAPB-PDA COF sample 3.7.C (1/4 monomer concentration)**

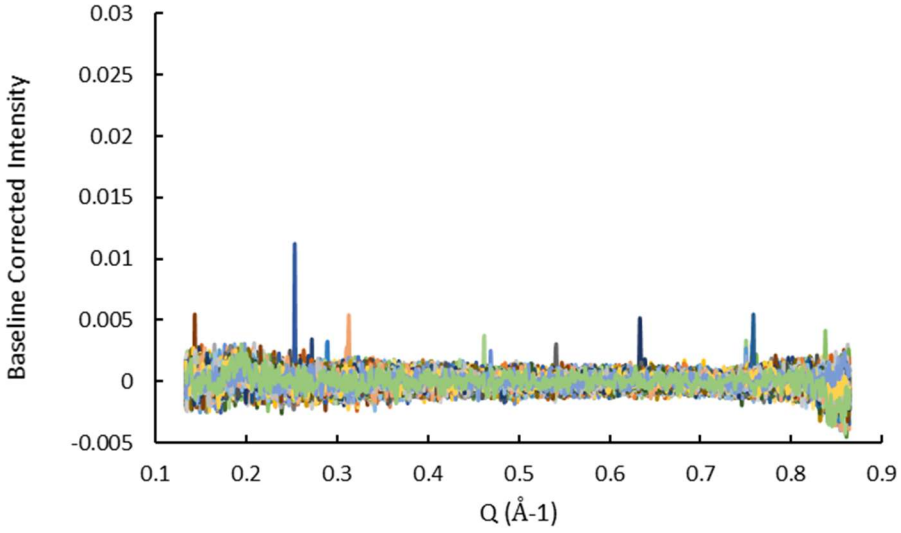


**Figure 3.56: Baseline corrected in situ XRD diffraction pattern for TAPB-PDA COF sample 3.7.D (1/8 monomer concentration)**

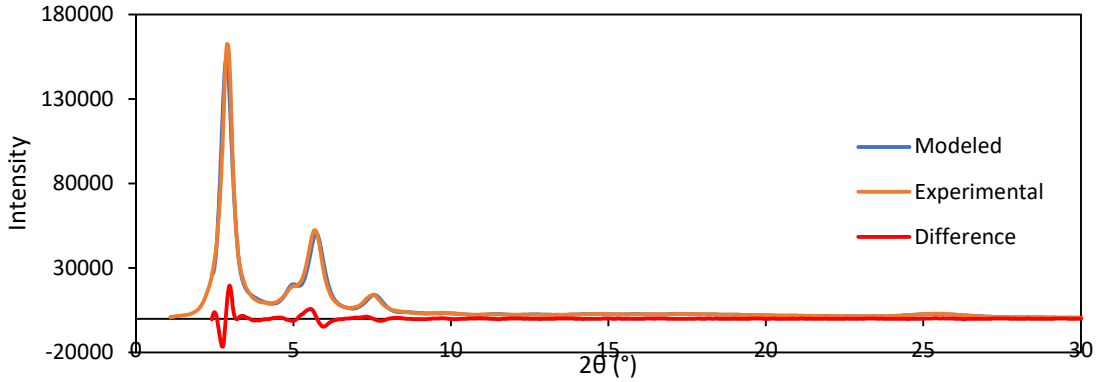


**Figure 3.57: Modeled PXRD versus experimental PXRD for TAPB-OBuPDA COF**

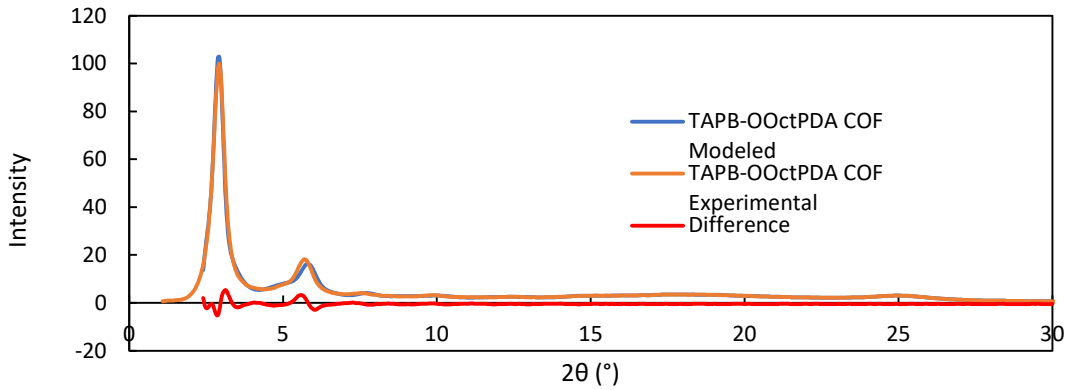


**Figure 3.58: Modeled PXRD versus experimental PXRD for TAPB-OOctPDA COF**

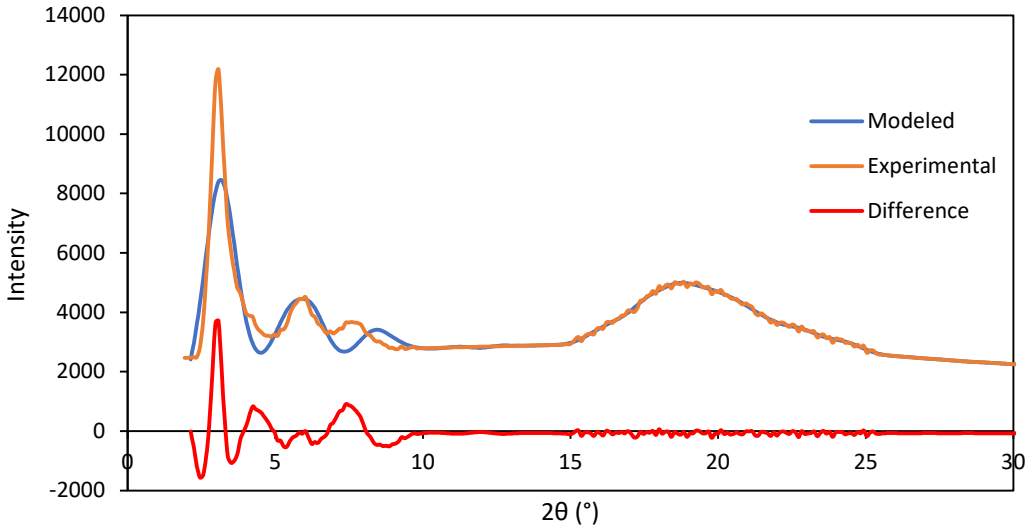


**Figure 3.59: Modeled PXRD versus experimental PXRD for TAPB-ODodecPDA COF**

**Table 3.4: Regression analysis statistics for linearized 1st order plots for TAPB-(2,5-dialkoxy)PDA COFs from Figure 3.24**

| COF | *m* | $R^2$ |
|---|---|---|
| TAPB-OMePDA COF | -0.0031 | 0.9114 |
| TAPB-OBuPDA COF | -0.0017 | 0.9431 |
| TAPB-OOctPDA COF | -0.0020 | 0.8622 |
| TAPB-ODodec PDA COF | -0.0021 | 0.8333 |

# CHAPTER 4. OUTLOOK, CONCLUSIONS, AND IMPACT

## 4.1 Overview

This thesis focused on the synthesis and isolation of 2D imine-linked COFs with the goal of providing insight into the effects of the activation process and the initial stages of COF synthesis as a means of expanding the fundamental knowledge about the formation of these materials.

Chapter 2 of this thesis examined the effects of three activation processes on the crystallinity, porosity and surface area of three different activation methods, vacuum activation, $scCO_2$ activation, and a new $N_2$-flow activation method. Three imine COFs were examined, showing a range of susceptibilities to degradation during vacuum activation, which is the most commonly applied activation technique reported for COF activation. The generalizability of these results was extended by examining three non-imine-linked COFs which showed different behavior compared to the imine COFs. Additionally, it was shown for a large variety of 2D imine-linked COF species that gentle activation using $scCO_2$ allowed for isolation of highly crystalline and porous materials at earlier times in the reaction.

Chapter 3 examined the initial stages of 2D imine-linked COF synthesis reactions catalysed by acetic acid through a combination of *in situ* and *ex situ* characterization techniques again as a means of extending the foundational knowledge of how imine-linked COFs transition from individual monomers, to an intermediate non-diffracting solid state, and ultimately to a final crystalline framework. 2D imine-linked COFs based on TAPB as a trifunctional

node were generally found to form crystalline structures very early in the synthesis reaction, some showing strong diffraction signals as early as ninety seconds after the addition of the acetic acid catalyst. Direct TEM imaging of sonicated TAPB-PDA and TAPB-OMePDA COF material during this time period showed crystalline sheets, which contradicts the previous theory presented by Smith *et al.* for imine-linked COF formation. A series of alkoxy-functionalized COFs with chains of increasing length were examined, showing that the length of the alkoxy chain does not significantly influence the COF formation, but does affect the interlayer spacing between COF sheets, reduce the available surface area proportionately to the size of the pendant chain, and in the case of long chains, affect the ability of the COF to stack precisely during the activation process.

Examined together, this work shows that 2D-imine linked COFs generally form crystalline sheet-like material more rapidly than was previously understood and are very dynamic materials during the activation process. The structure of the COF has a large effect on the stability of the COF during its formation and activation. This chapter describes the importance of the principal findings of this thesis on the COF field as a whole, suggests areas where the techniques and experiments presented here could be expanded into other areas of COF synthesis, and suggests areas where future work could be beneficial to the goal of better understanding imine COF synthesis and increasing the quality of the materials obtained.

## 4.2 Activation Induced Erroneous Conclusions in COF Literature Reports and Lessons Learned

Prior to the completion of this work, the effects of different activation methods on the structure and crystallinity of imine-linked COFs was not known, and COFs were commonly activated with vacuum to remove residual solvent and guest molecules. In Chapter 2, it was shown that vacuum activation can have detrimental effects on some imine linked COFs, as well as on an example azine COF. TAPB-PDA COF is an example of an imine-linked COF that is highly sensitive to vacuum activation, losing approximately 90% of its $S_{BET}$ and displaying dramatically reduced diffraction intensity when activated using vacuum activation at room temperature. In a communication by Smith *et al.* this phenomenon resulted in underestimation of the initial crystallinity of TAPB-PDA COF, which forms crystalline material much faster than the 72 hours reported.[3] This is one example where activation of an imine COF using vacuum resulted in drastically different conclusions due to degradation of the COF structure prior to analysis of the COF material.

There are other examples where vacuum activation may have caused similar errors. Xu *et al*. reported the synthesis of stable TAPB-OHPDA COF and TAPB-OMePDA COF in their work on COFs as chiral organocatalysts.[20] In this same work, Xu *et al.* report an unsuccessful synthesis of TAPB-PDA COF using the same synthesis conditions as TAPB-OHPDA COF and TAPB-OMePDA COF.[20] The reported data for this sample of TAPB-PDA COF showed a $S_{BET}$ of 16 $m^2/g$, and far less crystallinity than that reported for TAPB-OMePDA COF in this work.[20] Xu *et al.* posited that this difference in COF crystallinity was due to the increased interlayer interaction in TAPB-OMePDA COF.[20] Based on the results presented in Section 2.4 of this thesis, it is possible that the difference in COF

crystallinity reported between TAPB-PDA COF and TAPB-OMePDA COF is due to the vacuum activation method used in isolating the reported COFs.

The last example to be presented here comes from a report by Li *et al.* where a Salen-based COF, shown below in Figure 4.1, is tested as an organometallic catalyst for the Henry reaction, a coupling between a nitroalkane and an aldehyde or ketone.[21]

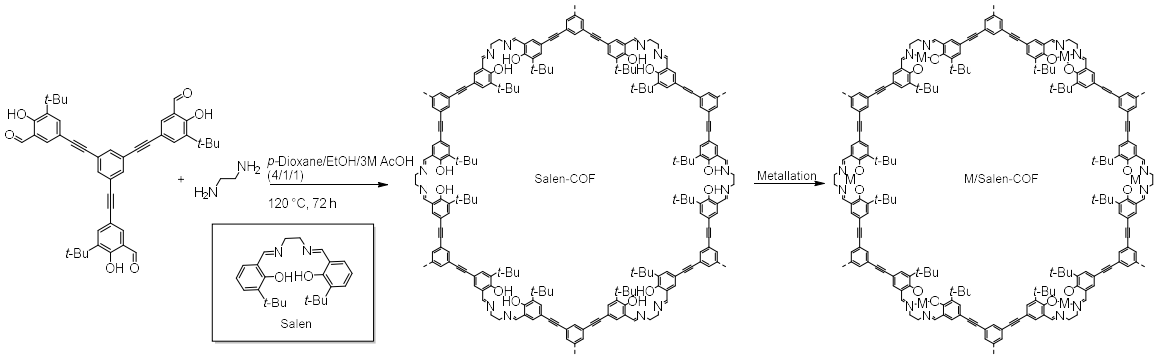


**Figure 4.1 Synthesis and Structure of Salen-COF and M/Salen-COF.[21]**

In this work the Salen-COF is shown to be stable to solvents and within a pH range of 1 to 13.[21] The specific aspect in question here is the recyclability test of the COF during its use as a catalyst; between each reaction, the COF solids are isolated from the reaction mixture using centrifugation, then dried using vacuum at 80 °C.[21] Over the course of four catalytic reactions, the product yield for the Henry reaction catalyzed by the COF decreases by 23%, the measured $S_{BET}$ for the COF decreases by 25% during these trials.[21] Since the COF is shown to be quite stable chemically, it is likely that the repeated isolation of the imine-linked Salen-COF is responsible for the reduction in porosity as assessed by the $S_{BET,}$ which

would restrict the ability of the COF to serve as an effective catalyst. The proportional reduction in the COF porosity, and the catalytic reaction yield supports this conclusion. This example also points to an important consideration when imine-linked COFs are applied as catalytic materials or as catalytic support, when the COF is intended to be recycled it will need to be isolated repeatedly. Any instability of the COF during activation will be exacerbated by multiple solvent removal and activation processes, as is seen for the reported Salen-COF.

These examples are presented here in order to contextualize the importance of fully understanding the activation process when studying COFs. Vacuum activation has the potential to severely disrupt the crystallinity and porosity of imine-linked COFs, and so the quality of the material that is synthesized can be mistakenly underestimated due to this phenomenon. Prior to forming conclusions about how structural changes in the COF framework affect the material properties, or the behavior of the COF during synthesis, it is imperative that the effects of the activation process be known. For novel COF materials, it is worthwhile to also investigate gentle activation methods such as $scCO_2$ activation or the nitrogen-flow activation reported in Section 2.5 to if the COF material in question is sensitive towards vacuum activation prior to relying on it as a routine isolation method. In this thesis, imine-linked COFs are shown to have varying susceptibilities to degradation of the COF crystallinity and porosity when activated by vacuum.[118] Azine-linked COFs may show similar activation behavior to that of partially vacuum-stable imine-linked COFs, such as TAPB-OMePDA COF, based on the results for HCOF-1 reported in Section 2.8.2. Section 2.6 examined literature reports of COFs displaying high surface areas when vacuum activated to identify COF structural features which may increase the stability of a

given COF towards vacuum activation, showing that strong π- π interactions between layers, and compact pore structures seem to correlate with increased stability. Within the COF literature there are a variety of reported COF species, which could all be directly tested to determine their relative stability towards vacuum in order to full understand this process. Relative stabilities of various COF structures aside, all the imine-linked COFs examined here showed at least some degradation during activation by vacuum. As COF research progresses, promoting awareness of the importance of the activation step within the COF community so that the changes the processes may cause in the COF structure are considered when designing experiments and drawing conclusions is critical to avoiding misleading conclusions in future COF research endeavors.

## 4.3 Gained Insight into the Formation of Imine Covalent Organic Frameworks under Solvothermal Conditions

The initial impetus for the study of COF behavior during the activation process began from an observation that TAPB-PDA COF was forming a highly crystalline material with intense diffraction peaks and a measured $S_{BET}$ approaching its theoretical Connolly surface area twelve times faster than the reported synthesis method for the COF would suggest.[3] Solvothermal synthesis methods for imine-linked COFs overwhelmingly reported a 72-hour synthesis time, which was far longer than the four hours found to be necessary to obtain highly crystalline material when gentle activation methods like $scCO_2$ or nitrogen-flow were applied. This finding indicated a deficiency in the knowledge of how imine COFs form, which was investigated via *ex situ* and *in situ* methods in Chapter 3.

In order to contextualize the potential importance of the findings presented here on the COF field it is beneficial to briefly summarize the principal findings of Chapter 3. First, it was found that TAPB-PDA COF, and several other tested Imine-linked COF species rapidly form crystalline networks within a few hours rather than the days implied by the commonly reported 72-hour solvothermal synthesis methods. From a COF screening standpoint, or from an optimization standpoint this is beneficial, since samples can be more rapidly synthesized and examined for the property of interest. The ability to synthesize, activate, and characterize a new imine-linked COF within the period of a single workday is a marked improvement over multi-day reaction methods.

Second, it was found that for TAPB-PDA COF and TAPB-OMePDA COF, crystalline material effectively exists from the start of the reaction, based on TEM images of isolated COF sheets obtained via the sonication of COF reaction precipitates which had only been allowed to react for one minute prior to sonication and isolation on the TEM grid. This shows that crystalline material exists very early in the reaction, potentially forming directly from discrete monomers as opposed to via an amorphous intermediate structure.

Third, it was demonstrated that the initial concentration of amine and aldehyde monomers has very limited, or no effect on the COF crystallization behavior in the first hour of the COF synthesis, indicating that screening the monomer concentration may not be necessary when attempting to synthesize new COFs, so long as there is sufficient monomer present to precipitate measurable amounts of solid material for analysis.

Fourth and finally it was found that the inclusion of alkoxy chains on the linear COF monomer affects the interlayer spacing of the COF material to a limited extent, however,

inclusion of very long chains may affect the ability of the COF to be isolated as a crystalline material due to stacking interference. Additionally, the inclusion of large alkoxy chains, or indeed any large pendant groups restricts the COF porosity proportionally to the size of the pendant chain. This indicates that attempts to control the COF stacking in this way may be fundamentally at odds with COF applications which rely on the porosity of the COF such as catalysis, adsorption, or separations.

## 4.3 Limitations of Current Characterization Techniques for Studying the Initial Crystallization Behavior of Imine-Linked COFs

While the results presented in Chapter 3 represent an incremental step forward in the understanding of the formation behavior of crystalline imine-linked COFs, there are significant unanswered questions remaining. It is unclear presently whether the initial precipitated species in imine COF synthesis is an amorphous gel, or disordered 2D COF sheets since both will appear amorphous to most analytical methods. *In situ* XRD shows the presence of crystalline material in the very first scan of the sample, which is not at a true starting time for the reaction. Due to the necessity of adding the acetic acid catalyst, ensuring sufficient mixing, and transferring a portion of the reaction mixture into an appropriate vessel for transmission XRD (glass capillary), this first scan occurs approximately 90 seconds after the reaction begins. *In situ* analysis of imine-linked COFs requires a sufficiently powerful photon source to provide *in situ* XRD scans with a sufficiently fast scan rate to obtain meaningful time-resolved data. This type of experiment is generally only possible at a synchrotron source, which have high demands placed on experimental time, as well as significant safety interlocks to maintain operator safety during analysis. Imine-linked COF reactions can produce rapid precipitation of solid

material when the acid catalyst is added to the COF monomer solution. Within a minute the COF has formed a viscous gel, and liquid can no longer flow freely within the reaction vessel. The critical initial stages of the COF precipitation are therefore challenging to observe *in situ* using current experimental setups. It may be beneficial for future experiments to develop an experimental setup where acid can be added and mixed remotely inside the XRD instrument in order to examine the first instances of crystallinity. Due to the necessity of a thin capillary as the sample holder, ensuring proper mixing will be an operation challenge during this approach.

Another possible tool for the analysis of the initial growth of imine COFs is liquid cell transmission electron microscopy (LCTEM), used by Smith *et al.* to examine the growth of colloidally synthesized COF-5 nanoparticles.[141] The technique has significant challenges when applied to COFs. The cumulative electron dose of the sample must be monitored to minimize radiolytic damage to the COF as it forms. Observing the growth of nanoparticles required the use of elevated temperature, which increased the sensitivity of the growing COF particles to damage from the electron bean, therefore individual snapshots were obtained rather than a continuous video.[141] Careful application of LCTEM to imine COFs could definitively show whether an imine COF initially produces individual nucleated particles, as opposed to a continuous gel-like structure. If individual imine-COF domains can be obtained, that opens the door to the use of a nucleation/growth strategy for obtaining single crystal 2D-imine COFs similarly to what has been demonstrated for 2D boroxine COFs.[119]

## 4.4 Computational Lessons Learned from COF-5 Applied to Imine-Linked COFs

The nucleation, growth, and mechanical characteristics of COF-5 have been well studied through computational methods.[142-145] Considering the initial growth mechanism proposed by Smith *et al.*, it would appear that conclusions about COF-5 which grows through relatively well-defined nucleation and growth steps would have very limited applicability to the initially-amorphous imine-linked COFs. However, results from Chapter 3 of this work suggest that the actual growth mechanism of imine-linked COFs like TAPB-PDA COF has COF sheets early in the reaction, and may proceed in a manner more similar to boronic ester-linked COFs than previously thought. Therefore, the existing computational literature could provide lessons applicable to imine-linked COFs.

COF-5 is shown to grow through the initial nucleation of oligomers, which upon attaining a certain size have a high likelihood of eventually growing into COF crystallites.[145] It is possible that imine COFs grow via the same mechanism, but the small crystallites present early in the reaction are not observable via *ex situ* measurements due to sheet-slipping effects upon activation as were observed in Chapter 2 of this work and in work by Sick *et al.*[127] Further, it has been shown computationally that individual COF sheets of COF-5 and TAPB-PDA COF are quite flexible compared to other 2D materials like graphene or transition metal dichalcogenides.[144] Defects, which are also very likely to be present in early COF sheets exacerbate this flexibility to the point that description of the resulting structures as 2D is charitable at best.[144] Multilayer COF sheets are more rigid, even when defects are present, therefore some amount of stacking may be necessary in order for COF sheets to remain ordered during the activation process and therefore be detected via *ex situ* analysis.

Further investigation of the growth of seeded COF-5 nanoparticles at low monomer concentrations identified the ideal monomer concentration for suppressing new nucleation of COF crystallites while allowing for controlled growth of the seeded particles to larger sizes.[143] This computational strategy would be very beneficial if applied to imine-linked COFs, since empirically determined reaction conditions preferentially identify conditions which rapidly precipitate COF material, instead of those allowing for slow growth of larger crystals. It is clear that the computational analysis of imine-linked COF growth is a very open, if admittedly challenging area, but existing work examining boronic ester-linked COFs provide a solid foundation.

## 4.5 Control of Interlayer Interactions in 2D Imine-Linked COFs as a Path to Larger Crystal Domains

Another significant challenge in the quest to synthesize 2D imine-linked COFs is the significant increase in interlayer interaction relative to boronic ester-linked COFs like COF-5. Lukose *et al.* calculate a stacking energy of 29.6 kJ/mol for COF-5 using Dispersion-Corrected Self-Consistent-Charge Density-Functional-Based Tight-Binding-Method.[146] Xu *et al.* calculated a crystal stacking energy of 393.6 kJ/mol for TAPB-PDA COF using a similar computational method to Lukose *et al.*, and cite this same work in discussing their findings. The molar mass of the monomer unit for the two COFs is comparable, with 525.65 g/mol for TAPB-PDA and 518.86 g/mol for COF-5. TAPB-PDA COF is therefore calculated to have approximately 13 times the interlayer stacking energy of COF-5. The COF sheets of an imine COF are therefore more likely to aggregate irreversibly, increasing the likelihood of disordered crystallite aggregation.

Nguyen *et al.* performed a thorough molecular dynamic simulation on a dispersed collection of hexahydroxytriphenylene and benzene diboronic acid monomers, which rapidly produced COF-5 like particles in the simulation.[147] During the performed simulations it was found that rapid bond formation produced particles with large amounts of topological defects such as five-membered rings, screw dislocations, and network interpenetration.[147] The bond-breaking dynamics of the boronic ester experimentally are responsible for the correction of these defects, but due to the short experimental timeframe for the simulation (1200 ns) these errors were found to be metastable during the simulation.[147] Also reported was an investigation on the importance of interlayer interactions in the COF formation process.[147] Nguyen *et al.* report that the simulation showed that even small oligomers are unstable against aggregation, and that there is a high driving force towards oligomer aggregation.[147] When this stacking interaction was lowered by a scaling factor, higher quality crystals were obtained in the simulation.[147] The highest quality of crystals was obtained when this stacking interaction was decreased by half compared to the calculated stacking parameters for experimental conditions from a mechanistic study by Smith *et al.*[141, 147] This phenomenon is one of the reasons for the careful selection of the COF reaction solvent system. This work finds that the minimization of the interlayer stacking is necessary to reduce the nucleation rate, minimize the number of COF nuclei in the reaction, and allow for error correction between crystalline domains.[147] Nguyen *et al.* investigated the ability of high-quality COF crystallites to undergo oriented attachment to one another, finding that COF-5 crystalline domains are able to correctly stack approximately 50% of the time.[147] Under current experimental conditions, these errors are effectively irreversible due to a prohibitively high energy

barrier. Other attachment errors, such as improper end-to-end attachment between sheets carried a similar energy penalty.[147] This work, in combination with other computational studies on COF-5 indicate that the suppression of new nucleation, and the prevention of disordered aggregation are necessary for controlled growth of COF materials.[119, 143, 145]

This study on COF-5 offers some insight into the magnitude of the challenge faced in the single crystal synthesis of 2D imine-linked COFs. As discussed before, the stacking energies between imine COF sheets are an order of magnitude stronger than those calculated for the boronic-ester linked COF-5. The orientation defects between aggregated imine-COF sheets will therefore be even more irreversible.

The key breakthrough allowing the synthesis of 2D imine-linked COFs with larger domain sizes, and potentially as single crystals will be the control of the initial nucleation process. The newly formed COF crystallites must be isolated from one-another, so that they can grow through the addition of monomers from the solution phase, rather than through aggregation with one-another. This can be achieved either through the minimization of interlayer interaction, as was attempted in Chapter 3 of this thesis through the incorporation of pendant side chains, or through manipulation of the synthesis conditions.

Graphene is the prototypical 2D material composed solely of $sp^2$-hybridized carbon atoms and shows a high interlayer stacking energy calculated to be 1.7 kJ/mol.[148] When the stacking energy is calculated by unit mass (necessary due to the far larger molar mass of the COF units compared to graphene) it is found that graphene shows approximately one half of the stacking energy per gram of TABP-PDA COF with 141.6 j/g for graphene and 394 j/g for TAPB-PDA COF.[20] Strategies which have been applied for the stabilization of

exfoliated graphene suspensions, which are suspensions of isolated 2D sheets may serve as inspiration for ways to stabilize newly-formed 2D imine-linked COF sheets during synthesis to increase the obtained domain size.

Suspensions of single and few layer graphene are commonly obtained through sonication of graphite, similar to efforts to isolate few and single layer samples of 2D COFs.[149-150] Ionic liquids are molten salts at room temperature, and have a variety of advantages over traditional organic solvents in many applications. Because of graphene's highly polarizable π-electrons dispersed across the entire planar sheet, ionic liquids can stabilize graphene sheets in suspensions.[151] Sonication of graphene in ionic liquids provided suspended exfoliated graphene, in stable suspensions ranging from single layer flakes to 30+ layer flakes with lateral dimensions of up to 440 nm depending on the selected ionic liquid and sonication conditions.[152] Surfactants, which are molecules which area amphiphilic molecules which are used as detergents, emulsifiers and dispersants, can also be used to stabilize graphene sheets in suspensions.[153-154] In addition to the stabilization of 2D graphene sheets, there is literature precedent for the use of surfactants to tune nucleation and suppress particle aggregation during MOF synthesis, resulting in higher quality crystals.[155-156]

However, there has thus far been limited application of these techniques to COFs. There are examples of COFs synthesized in ionic liquids; Guan *et al.* report the synthesis of three related 3D imine linked COFs with a high degree of interpenetration and crystallinity.[157] Guan *et al.* utlized 1-butyl-3-methylimidazolium bis((trifluoromethyl)sulfonyl)imide, shown in Figure 4.2 below.

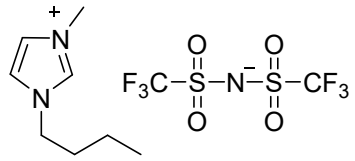

**Figure 4.2: Structure of 1-butyl-3-methylimidazolium bis((trifluoromethyl) sulfonyl)imide**

The use of this ionic liquid as the COF reaction solvent provided multiple advantages; These COFs were synthesized extremely quickly, one in as little as three minutes. The ionic liquid solvent was reusable for multiple COF synthesis reactions via simple filtration, and the reactions were carried out at room temperature under ambient air and atmospheric pressure.[157] This precedent alone would demonstrate dramatic potential for COF synthesis in ionic liquids, however there is also an example of the synthesis of a 2D imine-linked COF reported by Gao *et al.*[158] Here two 2D imine COFs, one based on tetrakis(4-formylphenyl)pyrene (TFPPy) and 1,4-phenylene diamine (PD), as well as another based on the aforementioned tetrakis(4-formylphenyl)pyrene (TFPPy) and TAPPy are reported in 1-butyl-3-methylimidazolium bis[(trifluoromethyl)sulfonyl]imide as well. The structures of these COFs are shown below in Figure 4.3.[158]

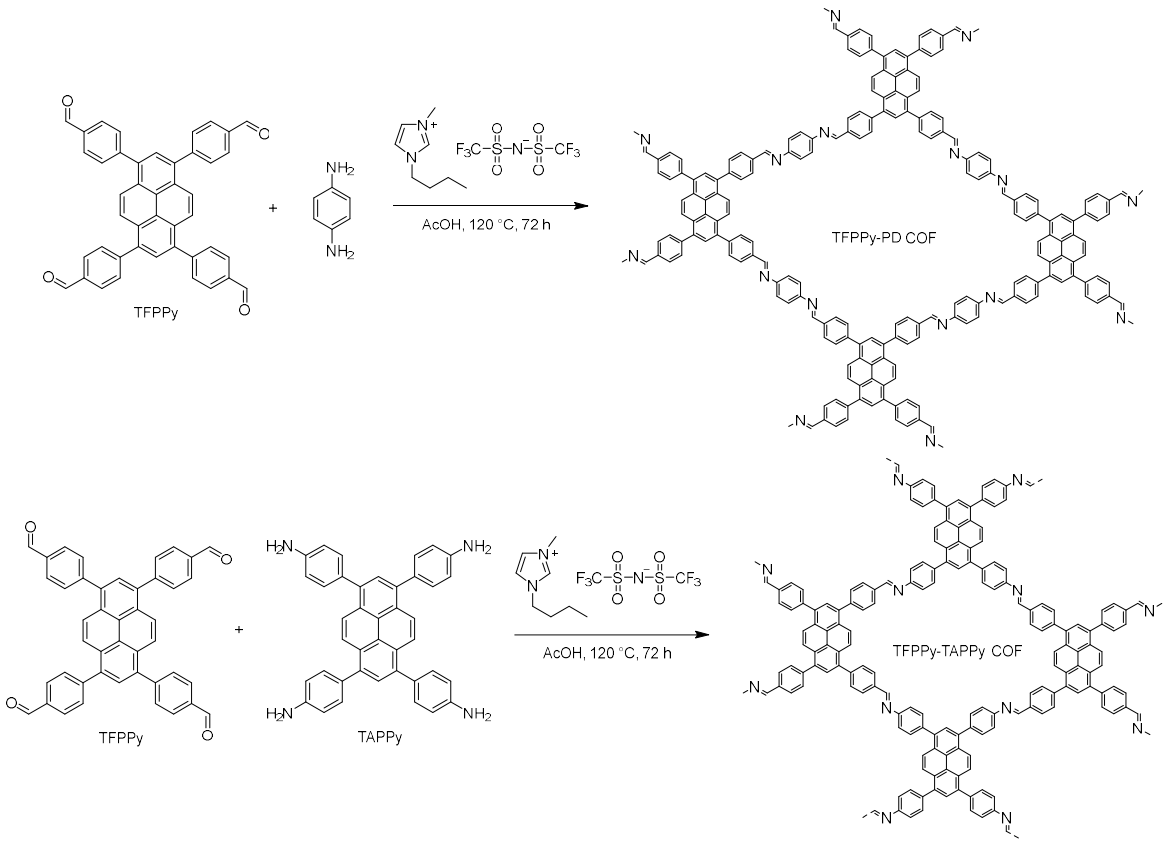


**Figure 4.3. Structures of TFPPy-PD COF and TFPPy-TAPPy COF synthesized in ionic liquid.[158]**

TFPPy-PD COF was isolated as rod-shaped crystallites with micrometer long lengths and 100 to 200 nm widths as compared to cubic crystals ranging from 30 to 70 nm obtained via a more traditional solvothermal method. TFPPy-TAPPy COF was isolated as 100 nm cubic crystals. These COFs displayed exceptionally high crystallinity, indicating that ionic liquids are beneficial for COF synthesis.[158]

Based on the very limited work performed so far, the ability of ionic liquids to synthesize high-quality COF samples is encouraging. A systematic investigation to determine if ionic

liquids are able to suppress nucleation and particle aggregation between 2D imine-linked COF sheets has the potential to be highly impactful in the goal of synthesizing high quality 2D imine-linked COF crystals. Similarly, an investigation into the efficacy of using surfactants to suppress COF sheet aggregation, thereby increasing crystallinity and crystallite size is potentially highly interesting to the COF field. The investigation of the effects of either ionic liquids or surfactants as applied to COFs could be undertake using *ex situ* measurement techniques to investigate the crystallinity, porosity and surface area of the isolated COF materials, or through the use of *in situ* measurements to investigate the effect of ionic liquids or surfactants on the nucleation and crystallization processes early in the reaction.

It is important to note that the mechanical characteristics of 2D COF sheets may inhibit the solution-state growth of single layer sheets. Computationally it was found that 2D single layer sheets of COF-5 and TAPB-PDA COF are very flexible compared to other 2D structures. This flexibility combined with the possibility of COFs forming stable structures like nanoscrolls[142] implies that single layer sheets may rapidly fold and crumple when growth is unsupported by a surface or interface. Multi-layer sheets have increased rigidity,[144] and may therefore be more synthetically accessible when stabilized by ionic liquids, surfactants, or other techniques or conditions.

In closing, it appears that the current solvothermal method for the synthesis of 2D-imine linked COFs may be fundamentally incompatible with the ultimate goal of providing single crystal COF samples for in-depth structural analysis, or high quality samples with large, defect free domains and minimized grain boundaries desirable for electronics applications. The mechanism of COF growth, whether it is taken to be the error-correction based

crystallization of amorphous gel-like imine-linked precipitates, the stacking and orientation of disordered 2D sheets, or a combination of both, appears to be very prone to the production of essentially irreversible errors caused by disordered aggregation of COF crystallites.

## 4.6 Conclusion

In Chapter 2 of this thesis it was shown that 2D imine-linked COFs and related azine COFs can undergo structural degradation and loss of crystallinity and porosity during vacuum activation processes. While the specific implications of this realization are discussed in Section 4.2 above, the importance of this knowledge warrants reiteration here. When analysing new COF materials, or when attempting to draw meaningful conclusions about experimental factors which impact the final COF structure or properties, it is imperative that the researcher insure that the activation method used for the particular COF in question is fully understood to insure that structural changes during the activation process do not influence the results of subsequent material analysis. When the activation method used is gentle towards the COF being isolated, advantages such as the rapid synthesis of imine-linked COFs demonstrated in Section 2.9 can be realized.

In Chapter 3 of this thesis it was shown that 2D imine-linked COFs can form crystalline material rapidly, potentially from the very first stages of the reaction. This challenges a prior theory on COF formation, by questioning the presence of a truly amorphous phase early in the reaction. In Section 3.5 and 3.6 the influence of COF topology was examined, with implications that the presence of multiple competing topologies may slow the observation of crystalline material. Additionally in Section 3.7 it was demonstrated that the

initial monomer concentration does not affect the rate of crystallization when TAPB-PDA COF was examined *in situ*, which implies that monomer concentration may not be a meaningful parameter when screening conditions for COF synthesis, due to the crystallization process being in the solid state after the monomers condense and precipitate. Finally, the effect of alkoxy chains on COF formation, crystallization, and properties was investigated. These results suggest paths for future investigation into COF formation, as well as strategies for obtaining higher quality COF samples by manipulating the initial formation of the COF, which are discussed in Section 4.4, above. Potentially the most impactful finding among those of Chapter 3 is that crystalline COF sheets exist and are isolatable via sonication, and probable via TEM, as early as one minute after the addition of acetic acid catalyst. The implications of this finding prompt reevaluation of the current conceptualization of 2D imine-linked COF formation, and hint that the strategies used for obtaining single crystal samples of boronic ester-linked COFs may be more applicable to 2D imine-linked COFs than previously thought.

The future work in the area of 2D-imine linked COFs will be comprised of fundamental studies on COF behaviour and formation, as well as the development of new designed materials comprised of interesting monomer components. However, while both fundamental studies and new material research have importance and merit, the research are which fundamentally advances the field is more likely to be the incremental investigation of COF formation leading to the complete understanding and eventual manipulation and control of 2D-imine linked COFs as they form. Once the way COFs form is fully understood, and can be controlled, then novel COF materials will be able to be synthesized and studied at their fullest potential.

# REFERENCES


1. Cote, A. P.; Benin, A. I.; Ockwig, N. W.; O'Keeffe, M.; Matzger, A. J.; Yaghi, O. M., Porous, crystalline, covalent organic frameworks. *Science* **2005,** *310*, 1166-70.

2. Yaghi, O. M.; O'Keeffe, M.; Ockwig, N. W.; Chae, H. K.; Eddaoudi, M.; Kim, J., Reticular synthesis and the design of new materials. *Nature* **2003,** *423*, 705-14.

3. Smith, B. J.; Overholts, A. C.; Hwang, N.; Dichtel, W. R., Insight into the crystallization of amorphous imine-linked polymer networks to 2D covalent organic frameworks. *Chem. Commun.* **2016,** *52*, 3690-3.

4. Uribe-Romo, F. J.; Hunt, J. R.; Furukawa, H.; Klock, C.; O'Keeffe, M.; Yaghi, O. M., A crystalline imine-linked 3-D porous covalent organic framework. *J. Am. Chem. Soc.* **2009,** *131*, 4570-1.

5. Zhu, L.; Zhang, Y. B., Crystallization of Covalent Organic Frameworks for Gas Storage Applications. *Molecules* **2017,** *22*.

6. Diercks, C. S.; Yaghi, O. M., The atom, the molecule, and the covalent organic framework. *Science* **2017,** *355*.

7. Feng, X.; Liu, L.; Honsho, Y.; Saeki, A.; Seki, S.; Irle, S.; Dong, Y.; Nagai, A.; Jiang, D., High-rate charge-carrier transport in porphyrin covalent organic frameworks: switching from hole to electron to ambipolar conduction. *Angew. Chem. Int. Ed. Engl.* **2012,** *51*, 2618-22.

8. Tian, Y.; Xu, S. Q.; Liang, R. R.; Qian, C.; Jiang, G. F.; Zhao, X., Construction of two heteropore covalent organic frameworks with Kagome lattices. *Crystengcomm* **2017,** *19*, 4877-4881.

9. Alahakoon, S. B.; Thompson, C. M.; Nguyen, A. X.; Occhialini, G.; McCandless, G. T.; Smaldone, R. A., An azine-linked hexaphenylbenzene based covalent organic framework. *Chem. Commun.* **2016,** *52*, 2843-5.

10. Furukawa, H.; Yaghi, O. M., Storage of hydrogen, methane, and carbon dioxide in highly porous covalent organic frameworks for clean energy applications. *J. Am. Chem. Soc.* **2009,** *131*, 8875-83.

11. Ma, H.; Ren, H.; Meng, S.; Yan, Z.; Zhao, H.; Sun, F.; Zhu, G., A 3D microporous covalent organic framework with exceedingly high C3H8/CH4 and C2 hydrocarbon/CH4 selectivity. *Chem. Commun.* **2013,** *49*, 9773-5.

12. Yang, Z. L.; Cao, D. P., Effect of Li Doping on Diffusion and Separation of Hydrogen and Methane in Covalent Organic Frameworks. *J. Phys. Chem. C* **2012,** *116*, 12591-12598.

13. Yang, C. X.; Liu, C.; Cao, Y. M.; Yan, X. P., Facile room-temperature solution-phase synthesis of a spherical covalent organic framework for high-resolution chromatographic separation. *Chem. Commun.* **2015,** *51*, 12254-7.

14. Lohse, M. S.; Stassin, T.; Naudin, G.; Wuttke, S.; Ameloot, R.; De Vos, D.; Medina, D. D.; Bein, T., Sequential Pore Wall Modification in a Covalent Organic Framework for Application in Lactic Acid Adsorption. *Chem. Mater.* **2016,** *28*, 626-631.

15. Wu, M.; Chen, G.; Liu, P.; Zhou, W.; Jia, Q., Polydopamine-based immobilization of a hydrazone covalent organic framework for headspace solid-phase microextraction of pyrethroids in vegetables and fruits. *J. Chromatogr. A* **2016,** *1456*, 34-41.

16. Dong, B.; Wang, L.; Zhao, S.; Ge, R.; Song, X.; Wang, Y.; Gao, Y., Immobilization of ionic liquids to covalent organic frameworks for catalyzing the formylation of amines with CO2 and phenylsilane. *Chem. Commun.* **2016,** *52*, 7082-5.

17. He, S. J.; Yin, B.; Niu, H. Y.; Cai, Y. Q., Targeted synthesis of visible-light-driven covalent organic framework photocatalyst via molecular design and precise construction. *Appl. Catal.* **2018,** *239*, 147-153.

18. Schwab, M. G.; Hamburger, M.; Feng, X.; Shu, J.; Spiess, H. W.; Wang, X.; Antonietti, M.; Mullen, K., Photocatalytic hydrogen evolution through fully conjugated poly(azomethine) networks. *Chem. Commun.* **2010,** *46*, 8932-4.

19. Xu, H.; Chen, X.; Gao, J.; Lin, J.; Addicoat, M.; Irle, S.; Jiang, D., Catalytic covalent organic frameworks via pore surface engineering. *Chem. Commun.* **2014,** *50*, 1292-4.

20. Xu, H.; Gao, J.; Jiang, D., Stable, crystalline, porous, covalent organic frameworks as a platform for chiral organocatalysts. *Nat. Chem.* **2015,** *7*, 905-12.

21. Li, L. H.; Feng, X. L.; Cui, X. H.; Ma, Y. X.; Ding, S. Y.; Wang, W., Salen-Based Covalent Organic Framework. *J. Am. Chem. Soc.* **2017,** *139*, 6042-6045.

22. Ascherl, L.; Evans, E. W.; Hennemann, M.; Di Nuzzo, D.; Hufnagel, A. G.; Beetz, M.; Friend, R. H.; Clark, T.; Bein, T.; Auras, F., Solvatochromic covalent organic frameworks. *Nat. Commun.* **2018,** *9*, 3802.

23. Jhulki, S.; Evans, A. M.; Hao, X. L.; Cooper, M. W.; Feriante, C. H.; Leisen, J.; Li, H.; Lam, D.; Hersam, M. C.; Barlow, S.; Bredas, J. L.; Dichtel, W. R.; Marder, S. R., Humidity Sensing through Reversible Isomerization of a Covalent Organic Framework. *J. Am. Chem. Soc.* **2020,** *142*, 783-791.

24. Li, Z.; Zhang, Y.; Xia, H.; Mu, Y.; Liu, X., A robust and luminescent covalent organic framework as a highly sensitive and selective sensor for the detection of Cu(2+) ions. *Chem. Commun.* **2016,** *52*, 6613-6.

25. Ding, S. Y.; Dong, M.; Wang, Y. W.; Chen, Y. T.; Wang, H. Z.; Su, C. Y.; Wang, W., Thioether-Based Fluorescent Covalent Organic Framework for Selective Detection and Facile Removal of Mercury(II). *J. Am. Chem. Soc.* **2016,** *138*, 3031-7.

26. Samanta, P.; Desai, A. V.; Anothumakkool, B.; Shirolkar, M. M.; Karmakar, A.; Kurungot, S.; Ghosh, S. K., Enhanced proton conduction by post-synthetic covalent modification in a porous covalent framework. *J. Mater. Chem. A* **2017,** *5*, 13659-13664.

27. Xu, H.; Tao, S.; Jiang, D., Proton conduction in crystalline and porous covalent organic frameworks. *Nat. Mater.* **2016,** *15*, 722-6.

28. Ma, H.; Liu, B.; Li, B.; Zhang, L.; Li, Y. G.; Tan, H. Q.; Zang, H. Y.; Zhu, G., Cationic Covalent Organic Frameworks: A Simple Platform of Anionic Exchange for Porosity Tuning and Proton Conduction. *J. Am. Chem. Soc.* **2016,** *138*, 5897-903.

29. Wan, S.; Gándara, F.; Asano, A.; Furukawa, H.; Saeki, A.; Dey, S. K.; Liao, L.; Ambrogio, M. W.; Botros, Y. Y.; Duan, X.; Seki, S.; Stoddart, J. F.; Yaghi, O. M., Covalent Organic Frameworks with High Charge Carrier Mobility. *Chem. Mater.* **2011,** *23*, 4094-4097.

30. Ma, L.; Wang, S.; Feng, X.; Wang, B., Recent advances of covalent organic frameworks in electronic and optical applications. *Chinese Chem. Lett.* **2016,** *27*, 1383-1394.

31. Yang, L.; Wei, D. C., Semiconducting covalent organic frameworks: a type of two-dimensional conducting polymers. *Chinese Chem. Lett.* **2016,** *27*, 1395-1404.

32. Jiang, Q.; Li, Y.; Zhao, X.; Xiong, P.; Yu, X.; Xu, Y.; Chen, L., Inverse-vulcanization of vinyl functionalized covalent organic frameworks as efficient cathode materials for Li–S batteries. *J. Mater. Chem. A* **2018,** *6*, 17977-17981.

33. Meng, Y.; Lin, G.; Ding, H.; Liao, H.; Wang, C., Impregnation of sulfur into a 2D pyrene-based covalent organic framework for high-rate lithium–sulfur batteries. *J. Mater. Chem. A* **2018,** *6*, 17186-17191.

34. Wu, Y.; Zhang, Z. Y.; Bandow, S.; Awaga, K., A Novel Strategy to Functionalize Covalent Organic Frameworks for High-Energy Rechargeable Lithium Organic Batteries via Graft Polymerization in Nano-Channels. *Bull. Chem. Soc. Jpn.* **2017,** *90*, 1382-1387.

35. Yang, D. H.; Yao, Z. Q.; Wu, D. H.; Zhang, Y. H.; Zhou, Z.; Bu, X. H., Structure-modulated crystalline covalent organic frameworks as high-rate cathodes for Li-ion batteries. *J. Mater. Chem. A* **2016,** *4*, 18621-18627.

36. Karak, S.; Kandambeth, S.; Biswal, B. P.; Sasmal, H. S.; Kumar, S.; Pachfule, P.; Banerjee, R., Constructing Ultraporous Covalent Organic Frameworks in Seconds via an Organic Terracotta Process. *J. Am. Chem. Soc.* **2017,** *139*, 1856-1862.

37. Matsumoto, M.; Valentino, L.; Stiehl, G. M.; Balch, H. B.; Corcos, A. R.; Wang, F.; Ralph, D. C.; Marinas, B. J.; Dichtel, W. R., Lewis-Acid-Catalyzed Interfacial Polymerization of Covalent Organic Framework Films. *Chem* **2018,** *4*, 308-317.

38. Yue, J. Y.; Liu, X. H.; Sun, B.; Wang, D., The on-surface synthesis of imine-based covalent organic frameworks with non-aromatic linkage. *Chem. Commun.* **2015,** *51*, 14318-21.

39. Campbell, N. L.; Clowes, R.; Ritchie, L. K.; Cooper, A. I., Rapid Microwave Synthesis and Purification of Porous Covalent Organic Frameworks. *Chem. Mater.* **2009,** *21*, 204-206.

40. Matsumoto, M.; Dasari, R. R.; Ji, W.; Feriante, C. H.; Parker, T. C.; Marder, S. R.; Dichtel, W. R., Rapid, Low Temperature Formation of Imine-Linked Covalent Organic Frameworks Catalyzed by Metal Triflates. *J. Am. Chem. Soc.* **2017,** *139*, 4999-5002.

41. Li, R. L.; Flanders, N. C.; Evans, A. M.; Ji, W.; Castano, I.; Chen, L. X.; Gianneschi, N. C.; Dichtel, W. R., Controlled growth of imine-linked two-dimensional covalent organic framework nanoparticles. *Chem. Sci.* **2019,** *10*, 3796-3801.

42. Garzon-Tovar, L.; Avci-Camur, C.; Rodriguez-San-Miguel, D.; Imaz, I.; Zamora, F.; Maspoch, D., Spray drying for making covalent chemistry II: synthesis of covalent-organic framework superstructures and related composites. *Chem. Commun.* **2017,** *53*, 11372-11375.

43. Zhang, M.; Li, L.; Lin, Q.; Tang, M.; Wu, Y.; Ke, C., Hierarchical-Coassembly-Enabled 3D-Printing of Homogeneous and Heterogeneous Covalent Organic Frameworks. *J. Am. Chem. Soc.* **2019,** *141*, 5154-5158.

44. Ding, S. Y.; Gao, J.; Wang, Q.; Zhang, Y.; Song, W. G.; Su, C. Y.; Wang, W., Construction of covalent organic framework for catalysis: Pd/COF-LZU1 in Suzuki-Miyaura coupling reaction. *J. Am. Chem. Soc.* **2011,** *133*, 19816-22.

45. Rabbani, M. G.; Sekizkardes, A. K.; Kahveci, Z.; Reich, T. E.; Ding, R.; El-Kaderi, H. M., A 2D mesoporous imine-linked covalent organic framework for high pressure gas storage applications. *Chemistry* **2013,** *19*, 3324-8.

46. Huang, N.; Krishna, R.; Jiang, D., Tailor-Made Pore Surface Engineering in Covalent Organic Frameworks: Systematic Functionalization for Performance Screening. *J. Am. Chem. Soc.* **2015,** *137*, 7079-82.

47. Gao, Q.; Bai, L.; Zhang, X.; Wang, P.; Li, P.; Zeng, Y.; Zou, R.; Zhao, Y., Synthesis of Microporous Nitrogen-Rich Covalent-Organic Framework and Its Application in $CO_2$ Capture. *Chin. J. Chem.* **2015,** *33*, 90-94.

48. Gao, Q.; Bai, L.; Zeng, Y.; Wang, P.; Zhang, X.; Zou, R.; Zhao, Y., Reconstruction of Covalent Organic Frameworks by Dynamic Equilibrium. *Chemistry* **2015,** *21*, 16818-22.

49. Gao, W. X.; Sun, X. Y.; Niu, H. L.; Song, X. J.; Li, K. G.; Gao, H. C.; Zhang, W. X.; Yu, J. H.; Jia, M. J., Phosphomolybdic acid functionalized covalent organic frameworks: Structure characterization and catalytic properties in olefin epoxidation. *Microporous Mesoporous Mater.* **2015,** *213*, 59-67.

50. Chen, X.; Addicoat, M.; Jin, E.; Zhai, L.; Xu, H.; Huang, N.; Guo, Z.; Liu, L.; Irle, S.; Jiang, D., Locking covalent organic frameworks with hydrogen bonds: general and remarkable effects on crystalline structure, physical properties, and photochemical activity. *J. Am. Chem. Soc.* **2015,** *137*, 3241-7.

51. de la Pena Ruigomez, A.; Rodriguez-San-Miguel, D.; Stylianou, K. C.; Cavallini, M.; Gentili, D.; Liscio, F.; Milita, S.; Roscioni, O. M.; Ruiz-Gonzalez, M. L.; Carbonell, C.; Maspoch, D.; Mas-Balleste, R.; Segura, J. L.; Zamora, F., Direct On-Surface Patterning of a Crystalline Laminar Covalent Organic Framework Synthesized at Room Temperature. *Chemistry* **2015,** *21*, 10666-70.

52. Kaleeswaran, D.; Vishnoi, P.; Murugavel, R., [3+3] Imine and β-ketoenamine tethered fluorescent covalent-organic frameworks for CO2 uptake and nitroaromatic sensing. *J. Mater. Chem. C* **2015,** *3*, 7159-7171.

53. Li, Z. J.; Ding, S. Y.; Xue, H. D.; Cao, W.; Wang, W., Synthesis of -C[double bond, length as m-dash]N- linked covalent organic frameworks via the direct condensation of acetals and amines. *Chem. Commun.* **2016,** *52*, 7217-20.

54. Leng, W.; Peng, Y.; Zhang, J.; Lu, H.; Feng, X.; Ge, R.; Dong, B.; Wang, B.; Hu, X.; Gao, Y., Sophisticated Design of Covalent Organic Frameworks with Controllable Bimetallic Docking for a Cascade Reaction. *Chemistry* **2016,** *22*, 9087-91.

55. Peng, Y. W.; Wong, W. K.; Hu, Z. G.; Cheng, Y. D.; Yuan, D. Q.; Khan, S. A.; Zhao, D., Room Temperature Batch and Continuous Flow Synthesis of Water-Stable Covalent Organic Frameworks (COFs). *Chem. Mater.* **2016,** *28*, 5095-5101.

56. Cai, S. L.; Zhang, K.; Tan, J. B.; Wang, S.; Zheng, S. R.; Fan, J.; Yu, Y.; Zhang, W. G.; Liu, Y., Rationally Designed 2D Covalent Organic Framework with a Brick-Wall Topology. *Acs Macro Lett.* **2016,** *5*, 1348-1352.

57. Zhang, J. Q.; Peng, Y. S.; Leng, W. G.; Gao, Y. A.; Xu, F. F.; Chai, J. L., Nitrogen ligands in two-dimensional covalent organic frameworks for metal catalysis. *Chinese J. of Catal.* **2016,** *37*, 468-475.

58. Dang, D.; Wu, P.; He, C.; Xie, Z.; Duan, C., Homochiral metal-organic frameworks for heterogeneous asymmetric catalysis. *J. Am. Chem. Soc.* **2010,** *132*, 14321-3.

59. Cao, X. C.; Qiao, Z. H.; Wang, Z.; Zhao, S.; Li, P. Y.; Wang, J. X.; Wang, S. C., Enhanced performance of mixed matrix membrane by incorporating a highly compatible covalent organic framework into poly(vinylamine) for hydrogen purification. *Int. J. Hydrogen Energ.* **2016,** *41*, 9167-9174.

60. Waller, P. J.; Lyle, S. J.; Osborn Popp, T. M.; Diercks, C. S.; Reimer, J. A.; Yaghi, O. M., Chemical Conversion of Linkages in Covalent Organic Frameworks. *J. Am. Chem. Soc.* **2016,** *138*, 15519-15522.

61. Yu, S. B.; Lyu, H.; Tian, J.; Wang, H.; Zhang, D. W.; Liu, Y.; Li, Z. T., A polycationic covalent organic framework: a robust adsorbent for anionic dye pollutants. *Polym. Chem.-Uk* **2016,** *7*, 3392-3397.

62. Peng, Y.; Huang, Y.; Zhu, Y.; Chen, B.; Wang, L.; Lai, Z.; Zhang, Z.; Zhao, M.; Tan, C.; Yang, N.; Shao, F.; Han, Y.; Zhang, H., Ultrathin Two-Dimensional Covalent Organic Framework Nanosheets: Preparation and Application in Highly Sensitive and Selective DNA Detection. *J. Am. Chem. Soc.* **2017,** *139*, 8698-8704.

63. Mu, M.; Wang, Y.; Qin, Y.; Yan, X.; Li, Y.; Chen, L., Two-Dimensional Imine-Linked Covalent Organic Frameworks as a Platform for Selective Oxidation of Olefins. *ACS Appl. Mater. Interfaces* **2017,** *9*, 22856-22863.

64. Haase, F.; Gottschling, K.; Stegbauer, L.; Germann, L. S.; Gutzler, R.; Duppel, V.; Vyas, V. S.; Kern, K.; Dinnebier, R. E.; Lotsch, B. V., Tuning the stacking behaviour of a 2D covalent organic framework through non-covalent interactions. *Mater. Chem. Front.* **2017,** *1*, 1354-1361.

65. Meri-Bofi, L.; Royuela, S.; Zamora, F.; Ruiz-Gonzalez, M. L.; Segura, J. L.; Munoz-Olivas, R.; Mancheno, M. J., Thiol grafted imine-based covalent organic frameworks for water remediation through selective removal of Hg(II). *J. Mater. Chem. A* **2017,** *5*, 17973-17981.

66. Vitaku, E.; Dichtel, W. R., Synthesis of 2D Imine-Linked Covalent Organic Frameworks through Formal Transimination Reactions. *J. Am. Chem. Soc.* **2017,** *139*, 12911-12914.

67. Rodriguez-San-Miguel, D.; Corral-Perez, J. J.; Gil-Gonzalez, E.; Cuellas, D.; Arauzo, J.; Monsalvo, V. M.; Carcelen, V.; Zamora, F., Sub-micron spheres of an imine-based covalent organic framework: supramolecular functionalization and water-dispersibility. *Crystengcomm* **2017,** *19*, 4872-4876.

68. Keller, N.; Bessinger, D.; Reuter, S.; Calik, M.; Ascherl, L.; Hanusch, F. C.; Auras, F.; Bein, T., Oligothiophene-Bridged Conjugated Covalent Organic Frameworks. *J. Am. Chem. Soc.* **2017,** *139*, 8194-8199.

69. Hou, Y. X.; Zhang, X. M.; Wang, C. M.; Qi, D. D.; Gu, Y. Q.; Wang, Z. G.; Jiang, J. Z., Novel imine-linked porphyrin covalent organic frameworks with good adsorption removing properties of RhB. *New J. Chem.* **2017,** *41*, 6145-6151.

70. Montoro, C.; Rodriguez-San-Miguel, D.; Polo, E.; Escudero-Cid, R.; Ruiz-Gonzalez, M. L.; Navarro, J. A. R.; Ocon, P.; Zamora, F., Ionic Conductivity and Potential Application for Fuel Cell of a Modified Imine-Based Covalent Organic Framework. *J. Am. Chem. Soc.* **2017,** *139*, 10079-10086.

71. Qian, H. L.; Dai, C.; Yang, C. X.; Yan, X. P., High-Crystallinity Covalent Organic Framework with Dual Fluorescence Emissions and Its Ratiometric Sensing Application. *ACS Appl. Mater. Inter.* **2017,** *9*, 24999-25005.

72. Alahakoon, S. B.; McCandless, G. T.; Karunathilake, A. A.; Thompson, C. M.; Smaldone, R. A., Enhanced Structural Organization in Covalent Organic Frameworks Through Fluorination. *Chemistry* **2017,** *23*, 4255-4259.

73. Bhunia, S.; Das, S. K.; Jana, R.; Peter, S. C.; Bhattacharya, S.; Addicoat, M.; Bhaumik, A.; Pradhan, A., Electrochemical Stimuli-Driven Facile Metal-Free Hydrogen Evolution from Pyrene-Porphyrin-Based Crystalline Covalent Organic Framework. *ACS Appl. Mater. Interfaces* **2017,** *9*, 23843-23851.

74. Xu, S. Q.; Liang, R. R.; Zhan, T. G.; Qi, Q. Y.; Zhao, X., Construction of 2D covalent organic frameworks by taking advantage of the variable orientation of imine bonds. *Chem. Commun.* **2017,** *53*, 2431-2434.

75. Rao, M. R.; Fang, Y.; De Feyter, S.; Perepichka, D. F., Conjugated Covalent Organic Frameworks via Michael Addition-Elimination. *J. Am. Chem. Soc.* **2017,** *139*, 2421-2427.

76. Kaleeswaran, D.; Antony, R.; Sharma, A.; Malani, A.; Murugavel, R., Catalysis and CO2 Capture by Palladium-Incorporated Covalent Organic Frameworks. *Chempluschem* **2017,** *82*, 1253-1265.

77. Ma, Y. X.; Li, Z. J.; Wei, L.; Ding, S. Y.; Zhang, Y. B.; Wang, W., A Dynamic Three-Dimensional Covalent Organic Framework. *J. Am. Chem. Soc.* **2017,** *139*, 4995-4998.

78. Lin, G.; Ding, H.; Chen, R.; Peng, Z.; Wang, B.; Wang, C., 3D Porphyrin-Based Covalent Organic Frameworks. *J. Am. Chem. Soc.* **2017,** *139*, 8705-8709.

79. Halder, A.; Karak, S.; Addicoat, M.; Bera, S.; Chakraborty, A.; Kunjattu, S. H.; Pachfule, P.; Heine, T.; Banerjee, R., Ultrastable Imine-Based Covalent Organic Frameworks for Sulfuric Acid Recovery: An Effect of Interlayer Hydrogen Bonding. *Angew. Chem. Int. Ed. Engl.* **2018,** *57*, 5797-5802.

80. Zhao, W.; Qiao, J.; Ning, T.-L.; Liu, X.-K., Scalable ambient pressure synthesis of covalent organic frameworks and their colorimetric nanocomposites through dynamic imine exchange reactions. *Chinese J. Polym. Sci.* **2017,** *36*, 1-7.

81. Ji, W.; Xiao, L.; Ling, Y.; Ching, C.; Matsumoto, M.; Bisbey, R. P.; Helbling, D. E.; Dichtel, W. R., Removal of GenX and Perfluorinated Alkyl Substances from Water by Amine-Functionalized Covalent Organic Frameworks. *J. Am. Chem. Soc.* **2018,** *140*, 12677-12681.

82. Braunecker, W. A.; Hurst, K. E.; Ray, K. G.; Owczarczyk, Z. R.; Martinez, M. B.; Leick, N.; Keuhlen, A.; Sellinger, A.; Johnson, J. C., Phenyl/Perfluorophenyl Stacking

Interactions Enhance Structural Order in Two-Dimensional Covalent Organic Frameworks. *Cryst. Growth Des.* **2018,** *18*, 4160-4166.

83. Gole, B.; Stepanenko, V.; Rager, S.; Grune, M.; Medina, D. D.; Bein, T.; Wurthner, F.; Beuerle, F., Microtubular Self-Assembly of Covalent Organic Frameworks. *Angew. Chem. Int. Ed. Engl.* **2018,** *57*, 846-850.

84. Albacete, P.; Martinez, J. I.; Li, X.; Lopez-Moreno, A.; Mena-Hernando, S. A.; Platero-Prats, A. E.; Montoro, C.; Loh, K. P.; Perez, E. M.; Zamora, F., Layer-Stacking-Driven Fluorescence in a Two-Dimensional Imine-Linked Covalent Organic Framework. *J. Am. Chem. Soc.* **2018,** *140*, 12922-12929.

85. Daugherty, M. C.; Vitaku, E.; Li, R. L.; Evans, A. M.; Chavez, A. D.; Dichtel, W. R., Improved synthesis of beta-ketoenamine-linked covalent organic frameworks via monomer exchange reactions. *Chem. Commun.* **2019,** *55*, 2680-2683.

86. Gao, Q.; Li, X.; Ning, G. H.; Leng, K.; Tian, B.; Liu, C.; Tang, W.; Xu, H. S.; Loh, K. P., Highly photoluminescent two-dimensional imine-based covalent organic frameworks for chemical sensing. *Chem. Commun.* **2018,** *54*, 2349-2352.

87. Li, X.; Zhang, C.; Cai, S.; Lei, X.; Altoe, V.; Hong, F.; Urban, J. J.; Ciston, J.; Chan, E. M.; Liu, Y., Facile transformation of imine covalent organic frameworks into ultrastable crystalline porous aromatic frameworks. *Nat. Commun.* **2018,** *9*, 2998.

88. Keller, N.; Calik, M.; Sharapa, D.; Soni, H. R.; Zehetmaier, P. M.; Rager, S.; Auras, F.; Jakowetz, A. C.; Gorling, A.; Clark, T.; Bein, T., Enforcing Extended Porphyrin J-Aggregate Stacking in Covalent Organic Frameworks. *J. Am. Chem. Soc.* **2018,** *140*, 16544-16552.

89. Pachfule, P.; Acharjya, A.; Roeser, J.; Langenhahn, T.; Schwarze, M.; Schomacker, R.; Thomas, A.; Schmidt, J., Diacetylene Functionalized Covalent Organic Framework (COF) for Photocatalytic Hydrogen Generation. *J. Am. Chem. Soc.* **2018,** *140*, 1423-1427.

90. Cifuentes, J. M. C.; Ferreira, B. X.; Esteves, P. M.; Buarque, C. D., Decarboxylative Cross-Coupling of Cinnamic Acids Catalyzed by Iron-Based Covalent Organic Frameworks. *Top. Catal.* **2018,** *61*, 689-698.

91. Liu, H. Y.; Chu, J.; Yin, Z. L.; Cai, X.; Zhuang, L.; Deng, H. X., Covalent Organic Frameworks Linked by Amine Bonding for Concerted Electrochemical Reduction of $CO_2$. *Chem* **2018,** *4*, 1696-1709.

92. Li, Y.; Chen, W. B.; Hao, W. J.; Li, Y. S.; Chen, L., Covalent Organic Frameworks Constructed from Flexible Building Blocks with High Adsorption Capacity for Pollutants. *ACS Appl. Nano Mater.* **2018,** *1*, 4756-4761.

93. Wang, J.; Si, L.; Wei, Q.; Hong, X.; Cai, S.; Cai, Y., Covalent Organic Frameworks as the Coating Layer of Ceramic Separator for High-Efficiency Lithium–Sulfur Batteries. *ACS Appl. Nano Mater.* **2017,** *1*, 132-138.

94. Waller, P. J.; AlFaraj, Y. S.; Diercks, C. S.; Jarenwattananon, N. N.; Yaghi, O. M., Conversion of Imine to Oxazole and Thiazole Linkages in Covalent Organic Frameworks. *J. Am. Chem. Soc.* **2018,** *140*, 9099-9103.

95. Zhang, G.; Tsujimoto, M.; Packwood, D.; Duong, N. T.; Nishiyama, Y.; Kadota, K.; Kitagawa, S.; Horike, S., Construction of a Hierarchical Architecture of Covalent Organic Frameworks via a Postsynthetic Approach. *J. Am. Chem. Soc.* **2018,** *140*, 2602-2609.

96. Han, X.; Huang, J.; Yuan, C.; Liu, Y.; Cui, Y., Chiral 3D Covalent Organic Frameworks for High Performance Liquid Chromatographic Enantioseparation. *J. Am. Chem. Soc.* **2018,** *140*, 892-895.

97. Kong, W.; Jia, W.; Wang, R.; Gong, Y.; Wang, C.; Wu, P.; Guo, J., Amorphous-to-crystalline transformation toward controllable synthesis of fibrous covalent organic frameworks enabling promotion of proton transport. *Chem. Commun.* **2018,** *55*, 75-78.

98. Qian, H. L.; Li, Y.; Yan, X. P., A building block exchange strategy for the rational fabrication of de novo unreachable amino-functionalized imine-linked covalent organic frameworks. *J. Mater. Chem. A* **2018,** *6*, 17307-17311.

99. Dong, J.; Li, X.; Peh, S. B.; Yuan, Y. D.; Wang, Y.; Ji, D.; Peng, S.; Liu, G.; Ying, S.; Yuan, D.; Jiang, J.; Ramakrishna, S.; Zhao, D., Restriction of Molecular Rotors in Ultrathin Two-Dimensional Covalent Organic Framework Nanosheets for Sensing Signal Amplification. *Chem. Mater.* **2018,** *31*, 146-160.

100. Wu, X. C.; Wang, B. W.; Yang, Z. Q.; Chen, L. G., Novel imine-linked covalent organic frameworks: preparation, characterization and application. *J. Mater. Chem. A* **2019,** *7*, 5650-5655.

101. Konavarapu, S. K.; Biradha, K., Luminescent Triazene-Based Covalent Organic Frameworks Functionalized with Imine and Azine: N2 and H2 Sorption and Efficient Removal of Organic Dye Pollutants. *Cryst. Growth Des.* **2018,** *19*, 362-368.

102. Li, Z. P.; Zhi, Y. F.; Shao, P. P.; Xia, H.; Li, G. S.; Feng, X.; Chen, X.; Shi, Z.; Liu, X. M., Covalent organic framework as an efficient, metal-free, heterogeneous photocatalyst for organic transformations under visible light. *Appl. Catal. B-Environ.* **2019,** *245*, 334-342.

103. Fischbach, D. M.; Rhoades, G.; Espy, C.; Goldberg, F.; Smith, B. J., Controlling the crystalline structure of imine-linked 3D covalent organic frameworks. *Chem. Commun.* **2019,** *55*, 3594-3597.

104. Luo, M.; Yang, Q.; Liu, K.; Cao, H.; Yan, H., Boosting photocatalytic H2 evolution on g-C3N4 by modifying covalent organic frameworks (COFs). *Chem. Commun.* **2019,** *55*, 5829-5832.

105. Guan, Q.; Fu, D. D.; Li, Y. A.; Kong, X. M.; Wei, Z. Y.; Li, W. Y.; Zhang, S. J.; Dong, Y. B., BODIPY-Decorated Nanoscale Covalent Organic Frameworks for Photodynamic Therapy. *iScience* **2019,** *14*, 180-198.

106. Bunaciu, A. A.; Udristioiu, E. G.; Aboul-Enein, H. Y., X-ray diffraction: instrumentation and applications. *Crit. Rev. Anal. Chem.* **2015,** *45*, 289-99.

107. Dollimore, D.; Spooner, P.; Turner, A., The bet method of analysis of gas adsorption data and its relevance to the calculation of surface areas. *Surface Technology* **1976,** *4*, 121-160.

108. Brunauer, S.; Emmett, P. H.; Teller, E., Adsorption of gases in multimolecular layers. *J. Am. Chem. Soc.* **1938,** *60*, 309-319.

109. Farokh Payam, A., Application of Atomic Force Microscopy to Study Metal–Organic Frameworks Materials and Composites. In *Futuristic Composites : Behavior, Characterization, and Manufacturing*, Sidhu, S. S.; Bains, P. S.; Zitoune, R.; Yazdani, M., Eds. Springer Singapore: Singapore, 2018; pp 37-73.

110. Suga, M.; Asahina, S.; Sakuda, Y.; Kazumori, H.; Nishiyama, H.; Nokuo, T.; Alfredsson, V.; Kjellman, T.; Stevens, S. M.; Cho, H. S.; Cho, M.; Han, L.; Che, S.; Anderson, M. W.; Schüth, F.; Deng, H.; Yaghi, O. M.; Liu, Z.; Jeong, H. Y.; Stein, A.; Sakamoto, K.; Ryoo, R.; Terasaki, O., Recent progress in scanning electron microscopy for the characterization of fine structural details of nano materials. *Prog. Solid State Ch.***2014,** *42*, 1-21.

111. Wiktor, C.; Meledina, M.; Turner, S.; Lebedev, O. I.; Fischer, R. A., Transmission electron microscopy on metal–organic frameworks – a review. *J. of Mater. Chem. A* **2017,** *5*, 14969-14989.

112. Lucier, B. E. G.; Chen, S.; Huang, Y., Characterization of Metal-Organic Frameworks: Unlocking the Potential of Solid-State NMR. *Acc. Chem. Res.* **2018,** *51*, 319-330.

113. Kortüm, G.; Braun, W.; Herzog, G., Principles and Techniques of Diffuse-Reflectance Spectroscopy. *Angew. Chem.* **1963,** *2*, 333-341.

114. Elgrishi, N.; Rountree, K. J.; McCarthy, B. D.; Rountree, E. S.; Eisenhart, T. T.; Dempsey, J. L., A Practical Beginner's Guide to Cyclic Voltammetry. *J. Chem. Educ.* **2017,** *95*, 197-206.

115. Oswald, S., X-Ray Photoelectron Spectroscopy in Analysis of Surfaces. In *Encyclopedia of Analytical Chemistry*, 2013.

116. Himpsel, F. J., Ultraviolet Photoelectron Spectroscopy. In *Characterization of Materials*, 2012; pp 1-13.

117. Sun, L.; Park, S. S.; Sheberla, D.; Dinca, M., Measuring and Reporting Electrical Conductivity in Metal-Organic Frameworks: Cd2(TTFTB) as a Case Study. *J. Am. Chem. Soc.* **2016,** *138*, 14772-14782.

118. Feriante, C. H.; Jhulki, S.; Evans, A. M.; Dasari, R. R.; Slicker, K.; Dichtel, W. R.; Marder, S. R., Rapid Synthesis of High Surface Area Imine-Linked 2D Covalent Organic Frameworks by Avoiding Pore Collapse During Isolation. *Adv. Mater.* **2020,** *32*, e1905776.

119. Evans, A. M.; Parent, L. R.; Flanders, N. C.; Bisbey, R. P.; Vitaku, E.; Kirschner, M. S.; Schaller, R. D.; Chen, L. X.; Gianneschi, N. C.; Dichtel, W. R., Seeded growth of single-crystal two-dimensional covalent organic frameworks. *Science* **2018,** *361*, 52-57.

120. Zhang, Y. B.; Su, J.; Furukawa, H.; Yun, Y.; Gandara, F.; Duong, A.; Zou, X.; Yaghi, O. M., Single-crystal structure of a covalent organic framework. *J. Am. Chem. Soc.* **2013,** *135*, 16336-9.

121. Ma, T.; Kapustin, E. A.; Yin, S. X.; Liang, L.; Zhou, Z.; Niu, J.; Li, L. H.; Wang, Y.; Su, J.; Li, J.; Wang, X.; Wang, W. D.; Wang, W.; Sun, J.; Yaghi, O. M., Single-crystal x-ray diffraction structures of covalent organic frameworks. *Science* **2018,** *361*, 48-52.

122. Langmuir, I., The Adsorption of Gases on Plane Surfaces of Glass, Mica and Platinum. *J. Am. Chem. Soc.* **1918,** *40*, 1361-1403.

123. Lastoskie, C.; Gubbins, K. E.; Quirke, N., Pore-Size Distribution Analysis of Microporous Carbons - a Density-Functional Theory Approach. *J. Phys. Chem.* **1993,** *97*, 4786-4796.

124. Connolly, M. L., Analytical Molecular-Surface Calculation. *J. Appl. Cryst.* **1983,** *16*, 548-558.

125. Dodson, R. A.; Wong-Foy, A. G.; Matzger, A. J., The Metal–Organic Framework Collapse Continuum: Insights from Two-Dimensional Powder X-ray Diffraction. *Chem. Mater.* **2018,** *30*, 6559-6565.

126. Nelson, A. P.; Farha, O. K.; Mulfort, K. L.; Hupp, J. T., Supercritical processing as a route to high internal surface areas and permanent microporosity in metal-organic framework materials. *J. Am. Chem. Soc.* **2009,** *131*, 458-60.

127. Sick, T.; Rotter, J. M.; Reuter, S.; Kandambeth, S.; Bach, N. N.; Doblinger, M.; Merz, J.; Clark, T.; Marder, T. B.; Bein, T.; Medina, D. D., Switching on and off Interlayer Correlations and Porosity in 2D Covalent Organic Frameworks. *J. Am. Chem. Soc.* **2019,** *141*, 12570-12581.

128. Auras, F.; Ascherl, L.; Hakimioun, A. H.; Margraf, J. T.; Hanusch, F. C.; Reuter, S.; Bessinger, D.; Doblinger, M.; Hettstedt, C.; Karaghiosoff, K.; Herbert, S.; Knochel, P.; Clark, T.; Bein, T., Synchronized Offset Stacking: A Concept for Growing Large-Domain and Highly Crystalline 2D Covalent Organic Frameworks. *J. Am. Chem. Soc.* **2016,** *138*, 16703-16710.

129. Lu, J.; Lin, F.; Wen, Q.; Qi, Q. Y.; Xu, J. Q.; Zhao, X., Large- scale synthesis of azine- linked covalent organic frameworks in water and promoted by water. *New J. Chem.* **2019,** *43*, 6116-6120.

130. Castano, I.; Evans, A. M.; Li, H.; Vitaku, E.; Strauss, M. J.; Bredas, J. L.; Gianneschi, N. C.; Dichtel, W. R., Chemical Control over Nucleation and Anisotropic Growth of Two-Dimensional Covalent Organic Frameworks. *ACS Cent. Sci.* **2019,** *5*, 1892-1899.

131. Kobaisi, M. A.; Bhosale, S. V.; Latham, K.; Raynor, A. M.; Bhosale, S. V., Functional Naphthalene Diimides: Synthesis, Properties, and Applications. *Chem. Rev.* **2016,** *116*, 11685-11796.

132. Sun, Q.; Aguila, B.; Perman, J.; Earl, L. D.; Abney, C. W.; Cheng, Y.; Wei, H.; Nguyen, N.; Wojtas, L.; Ma, S., Postsynthetically Modified Covalent Organic Frameworks for Efficient and Effective Mercury Removal. *J. Am. Chem. Soc.* **2017,** *139*, 2786-2793.

133. Jin, S.; Sakurai, T.; Kowalczyk, T.; Dalapati, S.; Xu, F.; Wei, H.; Chen, X.; Gao, J.; Seki, S.; Irle, S.; Jiang, D., Two-dimensional tetrathiafulvalene covalent organic frameworks: towards latticed conductive organic salts. *Chemistry* **2014,** *20*, 14608-13.

134. Wang, B.; Wasielewski, M. R., Design and Synthesis of Metal Ion-Recognition-Induced Conjugated Polymers: An Approach to Metal Ion Sensory Materials. *J. Am. Chem. Soc.* **1997,** *119*, 12-21.

135. Cai, S.; Sun, B.; Li, X.; Yan, Y.; Navarro, A.; Garzon-Ruiz, A.; Mao, H.; Chatterjee, R.; Yano, J.; Zhu, C.; Reimer, J. A.; Zheng, S.; Fan, J.; Zhang, W. G.; Liu, Y., Reversible Interlayer Sliding and Conductivity Changes in Adaptive Tetrathiafulvalene-Based Covalent Organic Frameworks. *ACS Appl. Mater. Interfaces* **2020**.

136. Yang, Z.; Chen, H.; Wang, S.; Guo, W.; Wang, T.; Suo, X.; Jiang, D. E.; Zhu, X.; Popovs, I.; Dai, S., Transformation Strategy for Highly Crystalline Covalent Triazine Frameworks: From Staggered AB to Eclipsed AA Stacking. *J. Am. Chem. Soc.* **2020**.

137. Wang, S.; Chavez, A. D.; Thomas, S.; Li, H.; Flanders, N. C.; Sun, C.; Strauss, M. J.; Chen, L. X.; Markvoort, A. J.; Bredas, J.-L.; Dichtel, W. R., Pathway Complexity in the Stacking of Imine-Linked Macrocycles Related to Two-Dimensional Covalent Organic Frameworks. *Chem. Mater.* **2019,** *31*, 7104-7111.

138. Nagai, A.; Guo, Z.; Feng, X.; Jin, S.; Chen, X.; Ding, X.; Jiang, D., Pore surface engineering in covalent organic frameworks. *Nat. Commun.* **2011,** *2*, 536.

139. Chen, L.; Furukawa, K.; Gao, J.; Nagai, A.; Nakamura, T.; Dong, Y.; Jiang, D., Photoelectric covalent organic frameworks: converting open lattices into ordered donor-acceptor heterojunctions. *J. Am. Chem. Soc.* **2014,** *136*, 9806-9.

140. Murthy, N. S.; Correale, S. T.; Minor, H., Structure of the Amorphous Phase in Crystallizable Polymers - Poly(Ethylene-Terephthalate). *Macromolecules* **1991,** *24*, 1185-1189.

141. Smith, B. J.; Parent, L. R.; Overholts, A. C.; Beaucage, P. A.; Bisbey, R. P.; Chavez, A. D.; Hwang, N.; Park, C.; Evans, A. M.; Gianneschi, N. C.; Dichtel, W. R., Colloidal Covalent Organic Frameworks. *ACS Cent. Sci.* **2017,** *3*, 58-65.

142. Li, H.; Brédas, J.-L., Nanoscrolls Formed from Two-Dimensional Covalent Organic Frameworks. *Chem. Mater.* **2019,** *31*, 3265-3273.

143. Li, H.; Evans, A. M.; Castano, I.; Strauss, M. J.; Dichtel, W. R.; Bredas, J. L., Nucleation-Elongation Dynamics of Two-Dimensional Covalent Organic Frameworks. *J. Am. Chem. Soc.* **2020,** *142*, 1367-1374.

144. Li, H.; Bredas, J. L., Large Out-of-Plane Deformations of Two-Dimensional Covalent Organic Framework (COF) Sheets. *J. Phys. Chem. Lett.* **2018,** *9*, 4215-4220.

145. Li, H.; Chavez, A. D.; Li, H.; Li, H.; Dichtel, W. R.; Bredas, J. L., Nucleation and Growth of Covalent Organic Frameworks from Solution: The Example of COF-5. *J. Am. Chem. Soc.* **2017,** *139*, 16310-16318.

146. Lukose, B.; Kuc, A.; Heine, T., The structure of layered covalent-organic frameworks. *Chemistry* **2011,** *17*, 2388-92.

147. Nguyen, V.; Grunwald, M., Microscopic Origins of Poor Crystallinity in the Synthesis of Covalent Organic Framework COF-5. *J. Am. Chem. Soc.* **2018,** *140*, 3306-3311.

148. Mostaani, E.; Drummond, N. D.; Fal'ko, V. I., Quantum Monte Carlo calculation of the binding energy of bilayer graphene. *Phys. Rev. Lett.* **2015,** *115*, 115501.

149. Coleman, J. N., Liquid exfoliation of defect-free graphene. *Acc. Chem. Res.* **2013,** *46*, 14-22.

150. Amiri, A.; Naraghi, M.; Ahmadi, G.; Soleymaniha, M.; Shanbedi, M., A review on liquid-phase exfoliation for scalable production of pure graphene, wrinkled, crumpled and functionalized graphene and challenges. *Flatchem* **2018,** *8*, 40-71.

151. Bordes, E.; Douce, L.; Quitevis, E. L.; Padua, A. A. H.; Costa Gomes, M., Ionic liquids at the surface of graphite: Wettability and structure. *J. Chem. Phys.* **2018,** *148*, 193840.

152. Bordes, E.; Morcos, B.; Bourgogne, D.; Andanson, J. M.; Bussiere, P. O.; Santini, C. C.; Benayad, A.; Costa Gomes, M.; Padua, A. A. H., Dispersion and Stabilization of Exfoliated Graphene in Ionic Liquids. *Front. Chem.* **2019,** *7*, 223.

153. Lotya, M.; King, P. J.; Khan, U.; De, S.; Coleman, J. N., High-concentration, surfactant-stabilized graphene dispersions. *ACS Nano* **2010,** *4*, 3155-62.

154. Fernandez-Merino, M. J.; Paredes, J. I.; Villar-Rodil, S.; Guardia, L.; Solis-Fernandez, P.; Salinas-Torres, D.; Cazorla-Amoros, D.; Morallon, E.; Martinez-Alonso, A.; Tascon, J. M. D., Investigating the influence of surfactants on the stabilization of aqueous reduced graphene oxide dispersions and the characteristics of their composite films. *Carbon* **2012,** *50*, 3184-3194.

155. Zhao, J.; Liu, X.; Wu, Y. P.; Li, D. S.; Zhang, Q. C., Surfactants as promising media in the field of metal-organic frameworks. *Coord. Chem. Rev.* **2019,** *391*, 30-43.

156. Feng, L.; Wang, K. Y.; Powell, J.; Zhou, H. C., Controllable Synthesis of Metal-Organic Frameworks and Their Hierarchical Assemblies. *Matter.* **2019,** *1*, 801-824.

157. Guan, X.; Ma, Y.; Li, H.; Yusran, Y.; Xue, M.; Fang, Q.; Yan, Y.; Valtchev, V.; Qiu, S., Fast, Ambient Temperature and Pressure Ionothermal Synthesis of Three-Dimensional Covalent Organic Frameworks. *J. Am. Chem. Soc.* **2018,** *140*, 4494-4498.

158. Gao, Y.; Wang, C.; Hu, H.; Ge, R.; Lu, M.; Zhang, J.; Li, Z.; Shao, P.; Jiang, D., Synthesis of Two-Dimensional Covalent Organic Frameworks in Ionic Liquids. *Chemistry* **2019,** *25*, 15488-15492.